EXTENDED STORAGE AND TRANSPORTATION: EVALUATION OF DRYING ADEQUACY

Prepared for

U.S. Nuclear Regulatory Commission
Contract NRC–02–07–006

Prepared by

Hundal Jung[1]
Pavan Shukla[1]
Tae Ahn[2]
Lynn Tipton[1]
Kaushik Das[1]
Xihua He[1]
Debashis Basu[1]

[1]Center for Nuclear Waste Regulatory Analyses
San Antonio, TX

[2]U.S. Nuclear Regulatory Commission
Washington, DC

June 2013

CONTENTS

FIGURES

TABLES

EXECUTIVE SUMMARY

This study examines potential impacts of residual water remaining inside a dry storage cask[1] for spent nuclear fuel (SNF) after the drying process. Residual water could cause chemical degradation of SNF, cladding, and other internal components inside the cask, such as SNF baskets and neutron absorbing plates. Scoping analyses were conducted to assess potential impacts of residual water on cask internals, flammability, and criticality. The analyses evaluated potential degradation mechanisms, including oxidation and hydration of SNF, cladding unzipping, oxidation and hydrogen-absorption-induced damage of cladding, and corrosion of internal structural materials. The evaluation also included the potential for a flammable canister environment resulting from hydrogen and oxygen generated by radiolytic decomposition of water (i.e., radiolysis). In addition to possible effects on cask performance during storage, degradation of canister internals and potential flammability of the canister environment would complicate retrieval of SNF assemblies from the cask, transport, and ultimate disposal.

For the conditions analyzed, the overall conclusion is that degradation of cladding, fuels, and other internal components is not expected to be significant over the analyzed period, up to 300 years of storage time. With no significant degradation of cladding, fuel, and internal components, criticality safety is not affected. At the higher end of analyzed range of residual water, and for relatively low initial temperature and backfill pressure, the canister environment could meet the condition of flammability in terms of the amount of hydrogen and available oxygen present, given a source of ignition.

The study made several assumptions to constrain the conditions analyzed and the structure of the models used. The analyses assumed that the canister remained sealed and that no air entered or backfill gas was lost. Based on information found in the literature, the analyses assumed that the amount of residual water in the canister yields a range from 5.5 to 55 moles (0.1 to 1 liter (L) (3.5 to 35 ounces (oz))) of water, mostly in the vapor phase. This residual water could undergo radiolysis as a result of the radiation field, producing oxidizing species, such as oxygen and hydrogen, prone to interact chemically with cladding, SNF, and cask internals. The radiolysis analysis also considered the recombination of hydrogen and oxygen via intermediate species. This study developed models for time-dependent relative humidity of the in-canister environment for vapor corrosion and the radiolysis rate of water, as well as models for SNF and cladding oxidation. These models were coupled in another model, referred to as the integration model, for each time step to estimate (1) relative humidity of the canister environment, (2) extent of SNF and cladding oxidation, and (3) amount of residual oxygen, water, and hydrogen in the canister, as a function of initial residual water amount, SNF and cladding temperature conditions, initial cladding failure, and radiation field. This study used the data from the integration model to estimate the extent of hydrogen absorption by the cladding and evaluate conditions for flammability. Qualitative analyses evaluated the extent of corrosion-induced damage of internal structural materials resulting from the residual water and the potential decrease in criticality safety margins.

[1] Several different designs of dry cask storage systems are in use. In some systems, the spent fuel is confined within a welded canister stored within a separate concrete shielding structure. In other designs, the confinenment and shielding components are integrated into a single structure with a bolted sealed lid. In this report, the term “canister” is used in a generic sense to refer to the component or system that provides confinement for the spent fuel.

The integration model yielded the following five observations:

(1) The extent of cladding oxidation is limited to a few micrometers of cladding; nonetheless, cladding oxidation can consume most of the oxygen produced by radiolysis.

(2) Exposed SNF could get oxidized to U_3O_8 when located in hotter parts of the canister and the radiolysis of residual water is sufficiently fast to decompose within a decade or two for the amounts of residual water considered.

(3) The cask environment could become flammable in the presence of ignition provided a sufficient amount of residual water undergoes radiolysis and not all of the generated oxygen is consumed by SNF and cladding oxidation.

(4) Only a small fraction of residual water would condense provided radiolysis of residual water occurs over several decades.

(5) Any significant hydrogen absorption by cladding is unlikely to occur in the canister environment.

Given 5.5 to 55 moles (0.1 to 1 L (3.5 to 35 oz)) of residual water, degradation of cladding, SNF, and other internal components is not significant over the analyzed period, up to 300 years of storage time. This study evaluated the aqueous corrosion of the canister internal structures when a fraction of residual water condenses or results in high relative humidity for vapor corrosion. Internal structures considered included the SNF basket, neutron absorbers, SNF assembly materials, and canister walls. The combined effects of the radiolysis rate and the temperature in the canister determine the conditions at which a fraction of residual water would condense or high humidity would be present. Water condensed or relative humidity went up in the numerical simulations when a significant amount of residual water (e.g., 55 moles) underwent slow radiolysis and SNF and cladding temperatures were low. Neither general nor localized corrosion of internal components is likely to cause structural damage. Other potential corrosion modes, such as galvanic and shadow corrosion (a form of galvanic corrosion), are limited and also unlikely to affect the integrity of any component. Data are insufficient to support a finding of potential stress-corrosion cracking (SCC) at lower temperatures over a longer time.

Above 17.4 moles (i.e., the log mean of 5.5 and 55 moles) (0.32 L (11.2 oz)) of residual water, the canister environment would meet the condition of flammability (in the presence of ignition) in terms of the amount of hydrogen and available oxygen present. This condition is anticipated for radiolysis via linear decomposition of water with time in 72.62 years, given the low-end of initial temperature of SNF and cladding and 1 atmosphere (14.7 pounds per square inch) of backfill pressure. The qualitative analysis performed on the potential impact on criticality due to incomplete drying shows that since the conditions resulting from incomplete drying are not expected to cause significant degradation of internals, a significant impact on criticality safety is not anticipated.

ACKNOWLEDGMENTS

This report documents work performed by the Center for Nuclear Waste Regulatory Analyses (CNWRA®) for the U.S. Nuclear Regulatory Commission (NRC) under Contract No. NRC-02-07–006. The studies and analyses reported herein were performed on behalf of the NRC, Office of Nuclear Material Safety and Safeguards, Division of Spent Fuel Alternative Strategies. The report is an independent product of the CNWRA and does not necessarily reflect the view or regulatory position of the NRC. The NRC staff views expressed herein are preliminary and do not constitute a final judgment or determination of the matters addressed in the report, or of the acceptability of a license application related to the activities addressed in the report.

The authors gratefully acknowledge O. Pensado and J. Stamatakos for their technical and programmatic reviews, respectively; L. Mulverhill for her editorial review; and B. Street for her administrative support. The authors also gratefully acknowledge the stimulating comments and suggestions of R. Einziger, J. Rubenstone and H. Gonzalez at the NRC.

Quality of Data, Analyses, and Code Development

DATA: All CNWRA-generated data contained in this report meet the quality assurance requirements described in the Geosciences and Engineering Division's Quality Assurance Manual. Sources of other data should be consulted for determining the quality level of those data. Computational calculations have been recorded in Das and Basu (2011), Jung (2011), and Shukla (2011).

ANALYSES AND CODES: None.

References

Das, K. and D. Basu. "Analytical Support for Regulation of Extended Spent Fuel Storage: Task 2." Scientific Notebook No. 1087E. San Antonio, TX: CNWRA. 2011. ADAMS Accession No. ML13144A149.

Jung, H. "Evaluation of Drying Adequacy for Extended SNF Dry Storage—Cladding and Fuel Oxidation and Amount of Residual Water." Scientific Notebook No. 1093E. San Antonio, TX: CNWRA. pp. 1–16. 2011. ADAMS Accession No. ML13144A147.

Shukla, P. "Development of an Integration Model to Evaluate Effect of Residual Water on Fuel and Cladding Oxidation." Scientific Notebook No. 1098E. San Antonio, TX: CNWRA. pp. 1–87. 2011. ADAMS Accession No. ML13144A148.

1. INTRODUCTION

1.1 Background

The U.S. Nuclear Regulatory Commission (NRC) is evaluating the safety and security of spent nuclear fuel (SNF) stored in dry casks for extended time periods before transportation to a location where the SNF is further processed or permanently disposed. Regulations at Title 10 of the *Code of Federal Regulations* (10 CFR) Part 72, "Licensing Requirements for the Independent Storage of Spent Nuclear Fuel, High-Level Radioactive Waste, and Reactor-Related Greater Than Class C Waste," require that dry storage casks function to ensure that (1) radioactive releases do not exceed specified limits, (2) there is sufficient shielding to keep direct radiation dose rates below specified limits, (3) subcritical conditions can be maintained under credible scenarios, and (4) SNF assemblies can be retrieved when necessary.

Following accepted procedures, spent fuel is typically loaded into dry storage casks underwater. The cask is then removed from the pool, drained, dried, backfilled with inert gas, and sealed to the atmosphere. These procedures may leave some limited amount of water may remain in the cask, even under normal operations. If residual water remains after drying and sealing, several physicochemical processes can affect the cask and its contents, and potentially compromise the capabilities of the cask to function properly.

Potential effects of residual water include degradation of SNF rod cladding, oxidation of exposed SNF pellets, and corrosion of internal components inside the canister (e.g., SNF basket, neutron absorber plates). Radiolysis of residual water can create reactive oxygen species which can oxidize cladding, other metallic components, and uranium dioxide (UO_2) exposed by cladding breaches. This effect would be most pronounced at the higher temperatures present earlier in the storage period. If a significant fraction of UO_2 in an SNF rod is oxidized to U_3O_8, swelling of the SNF pellets can rupture the cladding and release SNF particles into the canister. Contamination of the inside of the canister complicates transport, retrieval, and other handling of SNF assemblies. At later times, when the intensity of the radiation diminishes and the high temperatures generated by radioactive decay heat decrease, potential condensation of liquid water on metallic components could initiate aqueous corrosion. If the canister gas composition includes oxygen generated by radiolysis that was not consumed by chemical reactions and radiolysis-generated hydrogen, the gas mixture in the canister may be flammable if a source of ignition is present.

1.2 Purpose and Scope

The purpose of this study is to assess potential impacts of residual water on the integrity of the SNF and canister internals, flammability, and criticality, for extended time periods. For this study, the time period selected for the analysis and calculations was up to 300 years of storage time. At the initial phase of this study, a review of relevant literature information was conducted. The review identified four potential damage states that may result from incomplete canister drying: (1) SNF rod collapse caused by oxidation-induced thinning of the cladding, (2) cladding unzipping caused by oxidation and swelling of SNF exposed by cladding defects, (3) flammability conditions resulting from hydrogen and oxygen gas generated by water radiolysis, and (4) aqueous and vapor corrosion-induced failure of internal structural components. All four damage states may affect retrievability of SNF assemblies.

The analyses evaluated potential degradation mechanisms, including oxidation and hydration of SNF, cladding unzipping, oxidation and hydrogen-absorption-induced damage of cladding, and corrosion of internal structural materials. The evaluation also included a flammable canister environment resulting from hydrogen and oxygen generated by radiolytic decomposition of water (i.e., radiolysis). Degradation of canister internals and potential flammability of the canister environment would complicate recovery of SNF assemblies, transport, and ultimate disposal.

1.3 Methods and Assumptions

This study considered (1) the evolution of environmental conditions in the cask, (2) the important physicochemical processes that affect degradation of the materials within the cask, and (3) the potential damage states that may result from these conditions and processes.

The study considered the following set of cask environmental conditions: (1) the quantity of residual water after drying, (2) internal temperature fields and their decrease over time, and (3) the strength of the internal radiation field. The analyses assumed that the canister remained sealed and that no air entered. The study also evaluated the effect of the fraction of SNF rods with breached cladding on the number of SNF rods damaged by oxidation of SNF pellets. The quantity of residual water will affect the mass of cladding, SNF, and other components that are degraded by oxidation. Temperature controls the rate of the oxidation reactions, the phase composition of water, and, to a lesser extent, the rate at which water vapor is radiolyzed. The strength of the radiation field controls the radiolysis rate of residual water. Section 2 and Sections A1 and A2 in the appendix to this report provide detailed descriptions of the environmental conditions in the canister.

Generation of oxygen from radiolysis of residual water is modeled considering first-order kinetics for depletion of residual water and uncertainties such as the radiolytic decomposition of the products of the residual water, recombination of hydrogen and oxygen, and oxidation of SNF and cladding. The cladding and SNF oxidation mass action equations are modeled in five distinct temperature zones inside the cask's internal volume. At each time step in the integrated assessment, the total amounts of hydrogen and oxygen produced by radiolysis are recalculated. For each zone, the oxidized surface area of cladding and the exposed SNF are tracked. Available oxygen reacts with the cladding and exposed SNF at the temperature for that zone. Oxygen not consumed in a colder zone is transferred to the adjacent warmer zone. This sequence of calculations continues until the oxidation reactions are complete for that time step. Section 3 and Section A2 in the appendix to this report provide detailed descriptions of the physicochemical process models that control the extent and rate of the degradation. In addition, this study qualitatively assessed the potential effect of degraded conditions on criticality safety margins, considering changes to the geometry of the fuel and removal of neutron poisons as well as the presence of residual water as a moderator. Section 4 and Sections A4 and A5 in the appendix to this report provide detailed descriptions of the damage states that result from residual water-induced degradation.

2. CANISTER ENVIRONMENTS AND SPENT NUCLEAR FUEL ROD INTEGRITY

2.1 Quantity of Water Remaining after Drying

NRC regulations do not prescribe accepted canister drying procedures. NUREG–1536, "Standard Review Plan for Dry Cask Storage Systems," issued July 2010 (NRC, 2010), provides guidance in this area. NUREG–1536 indicates that vacuum drying methods similar to those recommended in Pacific Northwest Laboratories (PNL)–6265 (Knoll and Gilbert, 1987) can be used, and provides temperature and pressure limits for the drying process. Cask vendors have developed loading, draining, drying, and helium backfilling procedures specific to their canister to meet the specified maximum temperature of 400 degrees Celsius (°C) (752 degrees Fahrenheit (°F)) for the cladding under normal conditions (NRC, 2003) and the specified internal canister pressure of 4.0×10^{-4} megapascal (MPa) (5.8×10^{-2} pounds per square inch (psi)) after drying (NRC, 2010, Section 9.5.1). However, as indicated in American Society for Testing and Materials (ASTM) C1553, "Standard Guide for Drying Behavior of Spent Nuclear Fuel," issued in 2008 (ASTM International, 2008), and NUREG–1536 (NRC, 2010, Section 9.5.1), vendor-recommended drying procedures, as implemented, may not completely remove all water from the canister. Water can remain within the canister as unbound residual liquid water, unbound water vapor, and water chemically bound to hydroxide and hydrate species. In order to assess the effect of this uncertainty, this study evaluated a greater amount of water than the approximately 1 to 5 moles (0.02 to 0.1 L (0.7 to 3.5 oz)) which had been previously considered for normal vacuum drying conditions. This study assumes the presence of up to 55 moles (approximately 1 L (35 oz)). No detailed analysis was done for the upper limit of 55 moles (approximately 1 L (35 oz)), and the confirmation of current vacuum drying methods is recommended as a future work. Nevertheless, it is useful to review the nature of the uncertainties associated with the water amount from the incomplete drying, as summarized below. This review helped the staff to understand how residual water can react with heat and radiation and, subsequently, how SNF, cladding, and internal components degrade.

2.1.1 Unbound Residual Water

Unbound water can be present as either liquid or gas (water vapor) that is not physically or chemically bound (physisorbed or chemisorbed) to another species (e.g., surfaces of SNF UO_2, cladding or metal components). Based on the experiment conducted and reported by Kohli, et al. (1985), the amount of unbound water in both phases, including the additional water from a waterlogged SNF rod, could range from 1.4 to 11 moles (25 milliliters (ml) to 0.2 L (0.88 to 7 oz)). Their results are extrapolated to a CASTOR V/21 cask in Section A1.1.1 in the appendix to this report. In theory, ice could form during the drying process where suctions as low as 3 Torr are employed. However, final vacuum pressures are reached by a sequence of small vacuum steps that are sufficiently separated in time to allow residual heat to melt accumulated ice. At the temperatures and pressures expected in the canister over the extended storage period, ice might form, although it could quickly melt depending on detailed drying procedures.

2.1.1.1 Liquid Phase

Unbound liquid phase water can exist at capillary pressures in pores, cracks, and spaces in crud and sludge; in thin, wetted surface films on internal components; and in breached rods that have become waterlogged in the SNF pool. Based on the pressure-temperature phase

equilibrium diagram for water, the mass of water existing in the capillary state will generally be considered less than vapor phase water contained elsewhere in the canister.

Peehs et al. (1986) reported that the total amount of water collected from one waterlogged breached SNF rod heated at 160 °C (320 °F) for 7 hours and 200 °C (392 °F) for 24 hours ranged from 0.1 to 0.2 moles (1.9 to 3.8 ml (0.067 to 0.134 oz)). During 2 months of storage at 400 °C (752 °F) following drying, an additional 0.03 to 0.23 moles (0.5 to 4.1 ml (0.018 to 0.144 oz)) of water was collected. Kohli et al. (1985) reported similar observations for a moisture release experiment on a waterlogged boiling-water reactor (BWR) SNF rod. During the moisture release experiment conducted at 325 °C (617 °F), an additional 0.08 moles (1.5 ml (0.053 oz)) of water was released. Under vacuum and applied heat, the waterlogged BWR rod continued to outgas water vapor. Even when the cladding breaches were large, significant evaporation of water occurred during the vacuum drying process with temperatures up to 130 °C (266 °F) for 1 hour. Outgassing continued for up to 650 hours when the SNF rods were heated to 325 °C (617 °F).

As shown in these experiments, significant water can remain in the canisters and casks. For example, assuming a 1-percent cladding failure and 0.23 moles (4.1 ml (0.144 oz)) of water released from one waterlogged breached rod, the amount of water present in a CASTOR V/21 cask would be 11 moles (0.2 L (7 oz)). This calculation assumes the CASTOR V/21 houses 21 Westinghouse 15 × 15 assemblies with 50 of the 5,000 rods breached. The amount of residual water would be 1.1 or 0.1 moles (0.02 or 0.002 L (0.7 or 0.07 oz)) for a cladding failure of 0.1 or 0.01 percent, respectively. The cladding failure of 1 percent was estimated for older SNF designs and cladding materials. More modern light-water reactor (LWR) SNF rods have shown a lower average cladding failure of only 0.1 to 0.01 percent (CRWMS M&O, 2000). These estimates of residual water are based on available data, and reflect conditions favorable for water trapping. It is recognized that water evaporation is rapid in the open system. However, if vacuum pumping is less effective than the open system, uncertainty is associated with more water potentially coming from slow drying kinetics.

2.1.1.2 Vapor Phase

The ideal gas law provides a means to estimate the amount of unbound water in the vapor phase after drying, but before backfilling with helium. The nominal gas pressure limit in NUREG–1536 of 4.0×10^{-4} MPa (5.8×10^{-2} psi) (3 Torr) after drying could result in approximately 0.34 moles (6.03 ml (0.205 oz)) of water within a cask void volume of 2.1 cubic meters (m^3) (74 cubic feet (ft^3)) at 25 °C (77 °F). However, the pressure inside the cask could be higher than measured if the pressure gauge is connected to the canister by a tube through which there is a pressure drop during the drying process. Measurements taken under these conditions would not indicate that actual canister pressures are higher than the gauge pressure. In this case, the amount of residual water in the vapor phase could be higher as well. For example, if the canister pressure were actually 15 Torr (0.29 psi), the amount of residual water in the vapor phase would be 1.7 moles (31 ml (1.1 oz)) (i.e., 0.34 moles × 15 Torr/3 Torr).

2.1.2 Bound Water

Physisorbed water can be dried easily during the vacuuming process. Chemisorbed water, which can exist as a hydroxide or hydrate in the native oxides or corrosion products on the fuel, cladding, or the canister's structural materials, is more difficult to remove. If hydroxides or hydrates are decomposed by dehydration, water will be released from their chemisorbed lattice

structures. It is rare to find hydroxides and dehydration of hydroxides in zirconium. An analog of zirconium, aluminum cases, are reviewed first. Dehydration of hydroxides has been observed for aluminum-cladding fuels at temperatures ranging from 120 to 350 °C (248 to 662 °F) (ASTM International, 2008). From a survey on Advanced Test Reactor SNF plates, the maximum amount of chemisorbed water in the form of boehmite, γ-AlO(OH), was estimated to be 94 moles (1.7 L (60 oz)), assuming a hydroxide thickness of 34 micrometers (μm) (0.00134 inches (in.) and a density of 3.01 grams per cubic centimeter (g/cm^3) (0.91 pounds per cubic inch ($lb/in.^3$)) for a cladding surface area of 108 square meters (m^2) (1,163 square feet (ft^2)) (see ASTM C1553 (ASTM International, 2008)).

Zirconium cladding can form hydrated zirconium oxides, such as $ZrO(OH)_2$. Under irradiation conditions, zirconium can preferentially form zirconium hydroxides, such as $Zr(OH)_4$ or $Zr_4(OH)_8(H_2O)_{16}$ (ASTM International, 2008; Guipponi et al., 2012). Powers and Gray (1973) reported that the dehydration of zirconium oxide octahydrates ($ZrOCl_2 \cdot 8H_2O$) could begin above 150 °C (302 °F) and be complete at 700 °C (1,292 °F). Although the temperatures attained during the canister vacuum drying process may be high enough (i.e., greater than 150 °C (302 °F)) to remove the water present as zirconium hydroxides or hydrates, the duration of the drying process may not be sufficient to remove all chemisorbed water. Peak temperatures attained during dry storage could be sufficiently high for subsequent release of chemisorbed water if present on the Zircaloy surface.

The approach used to estimate the amount of chemisorbed water on aluminum cladding can be applied to zirconium cladding. It is assumed that a zirconium hydroxide ($ZrO(OH)_2$) thickness of 10 μm (0.000394 in.) may form from the oxide present from reactor discharge or during pool storage. The typical hydrated phase has a low density of 2.0 g/cm^3 (0.603 $lb/in.^3$). This leads to an amount of water that could be present of approximately 1.1 to 85 moles (0.02 to 1.5 L (0.68 to 52 oz)) based on the fraction of zirconium hydroxides and hydrates decomposed ranging from 0.01 to 1, respectively, for a 600-m^2 (6,458-ft^2) surface area of zirconium cladding (see Section A2.1.3.2 in the appendix to this report).

Although this estimate was made considering aluminum and zirconium oxide, there is little data on the potential quantity of chemisorbed water present on the zirconium cladding as a result of dehydration of hydroxides or their hydrates. Therefore, uncertainty exists regarding the amount of chemisorbed water. The uncertainties that could affect the amount of chemisorbed water include the (1) initial amount and distribution of zirconium hydroxides or hydrates on the cladding surface after drying and placement in the canister, (2) decomposition fraction at varying temperature and duration of drying, and (3) effect of cladding geometry on the amount and distribution of hydroxide or hydrates (e.g., cracks, pinholes). The quantitative uncertainty analysis for the chemisorbed water amount is outside the scope of this report.

2.1.3 Total Residual Water

Available data on unbound or free residual water supplemented by calculations indicate that the amount of unbound water in a canister, including additional water from a single waterlogged rod, could range from 1.4 to 11 moles (25 ml to 0.2 L (0.88 to 7 oz)). Data on the amount of chemisorbed bound water on the zirconium cladding are rare and highly uncertain. An analog estimate based on aluminum cladding suggests the quantity of chemisorbed bound water ranges from 1.1 to 85 moles (20 ml to 1.6 L (0.7 to 54 oz)). Together, these data and analyses show that the total amount of residual water could range from 1.1 to 96 moles (20 ml to 1.8 L (0.7 to 61 oz)), adding 11 and 85 moles. Because of the lack of data on

zirconium cladding, this scoping assessment assumed a residual water amount between 5.5 and 55 moles, which is equivalent to 0.1 to 1.0 L (3.5 to 35 oz) of liquid water at 25 °C (77 °F) and 1 atmosphere (atm) (115 lb/in.^{2}).

2.2 Temperature Conditions

Temperature distributions in the canister and their rate of decrease over time control the phase and spatial distribution of water, the reaction rates of oxidation processes, and the material properties of metallic components. Decay heat transfer in the storage canister and resulting temperature distributions are complicated by geometry, variations in the material properties of the canister and its contents, and the multiple modes of heat transfer involved. Two primary dry storage cask designs are used to store SNF. In the first configuration, SNF assemblies are placed in a basket that is directly loaded into a metal cask. There is no gap between the cask's inner surface and the basket assembly, and the cask is closed and sealed using a bolted lid. In this design, the principal mode of heat transfer is through convection at the outermost surface of the cask. In the second configuration, the SNF assemblies are placed in a basket within a canister that is sealed using a welded lid. The SNF canister is subsequently inserted into an overpack, leaving an annular gap between the outer wall of the canister and inner wall of the overpack for air circulation. In this configuration, the primary mechanism of heat transfer from the canister is through natural convection of air through the gap. Cooler air enters the passage near the bottom of the gap, flows upwards from increased buoyancy as it warms, and the hot air exhausts near the top of the cask.

This study used the cask configuration with the annular ventilation gap. Temperature fields from a detailed numerical heat transfer and fluid flow model (Figure 2-1) were averaged within five semi-ellipsoidal, nested shell-shaped zones starting at the hottest zone at the center of the SNF basket and extending radially outward to the inner surface of the canister (Figure 2-2).

The temperature in each zone is assumed to be uniform at any given time. Simple exponential decay models were used to define the change in the uniform temperature profile with time for each zone.

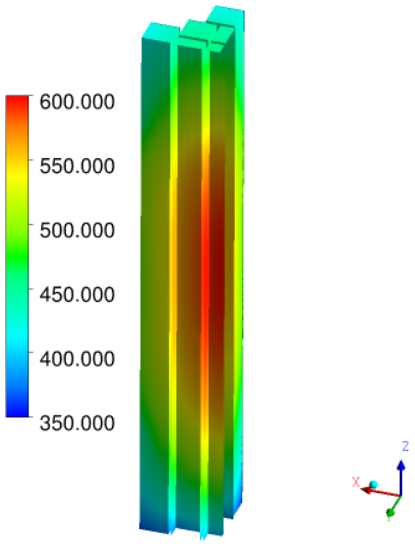

Figure 2-1 Temperature distribution in the SNF basket assembly. The temperature scale

is in Kelvin (K) (°F = 1.8 × K − 459.4).

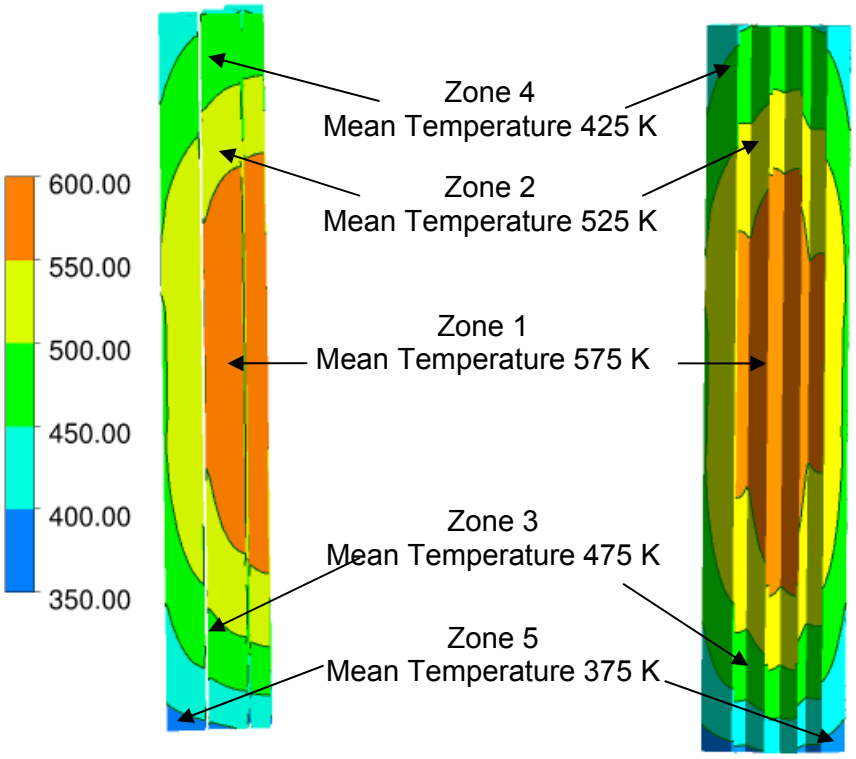

Figure 2-2 Location of the five temperature zones in the SNF basket assembly. The temperature scale is in K (°F = 1.8 × K − 459.4).

To account for uncertainties, four temperature-versus-time profiles were developed for each zone. These profiles represent combinations of high and low initial cladding and SNF temperatures and high and low temperature decay rates (Figures 2-3 and 2-4). The model for the time-dependent temperature is as follows:

$$T(t) = (T_{mean} - 309)\exp(-at) + 309 \quad (2\text{-}1)$$

where T_{mean} is the initial mean temperature (K) of a temperature zone and a is a thermal decay constant. The assumed value of the decay constant (a) is either 0.023 or 0.064. The temperature values listed in Table 2–1 are used as T_{mean} in Equation 2-1 to calculate SNF and cladding temperatures in a zone as a function of time. The listed values in Table 2–1 in the range of 375 to 575 K (215.3 to 575.3 °F) and 481 to 673 K (406.1 to 751.7 °F) are referred to as low and high temperature conditions, respectively.

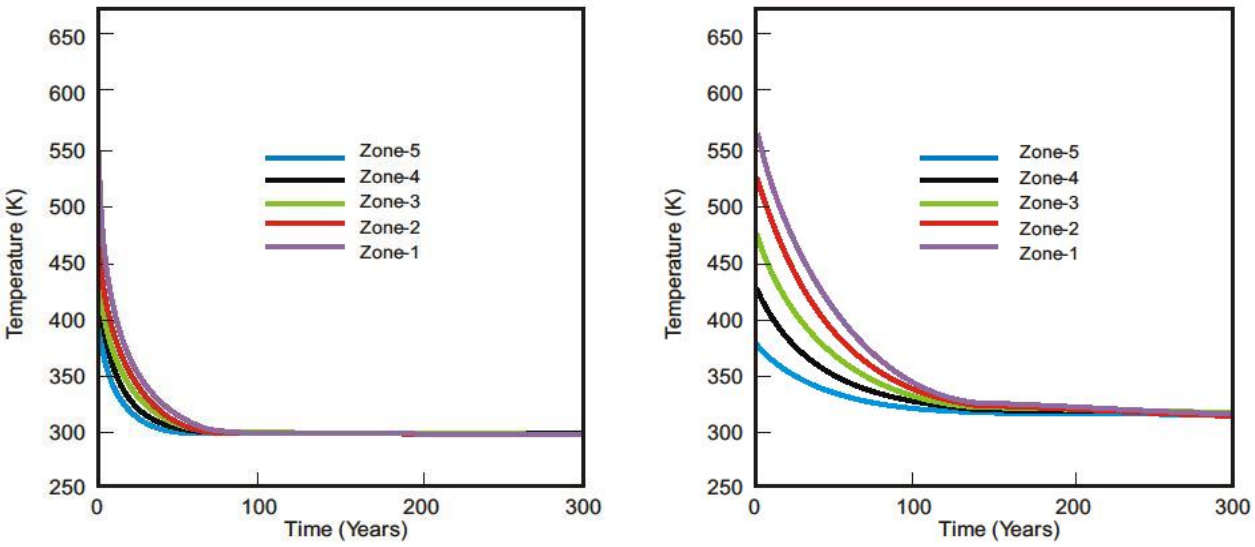

(a) (b)

Figure 2-3 SNF and cladding in the five zones calculated using mean values of low-end SNF and cladding initial temperatures with decay constants (a) 0.064 and (b) 0.023 (°F = 1.8 × K − 459.4)

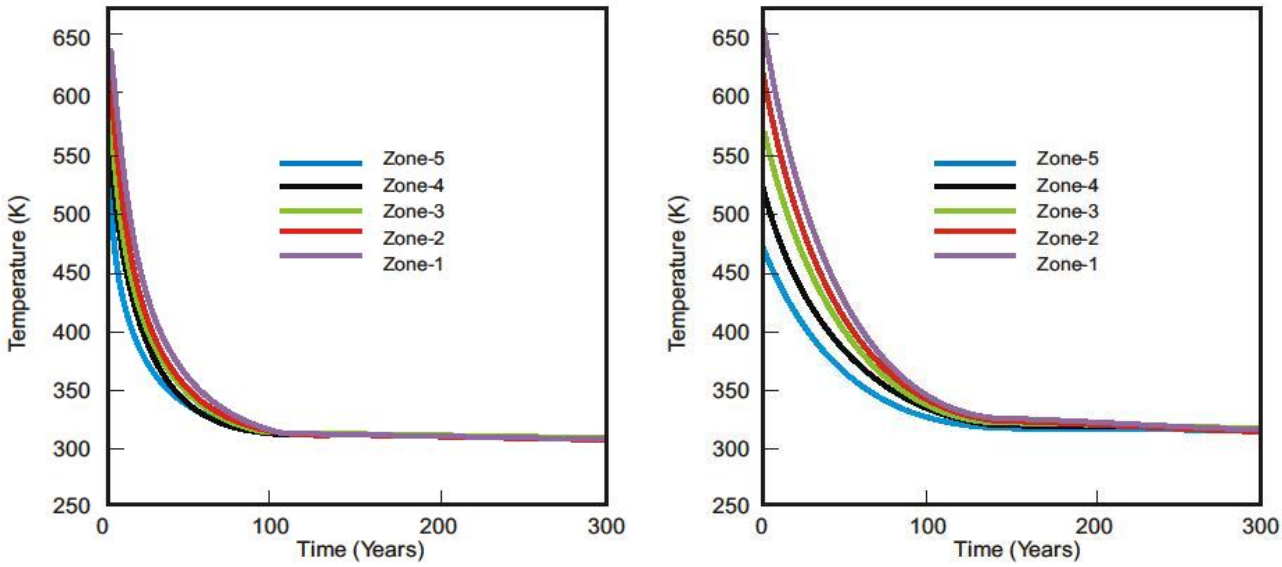

(a) (b)

Figure 2-4 SNF and cladding in the five zones calculated using mean values of high-end SNF and cladding initial temperatures with decay constants (a) 0.064 and (b) 0.023 (°F = 1.8 × K − 459.4)

Table 2-1 Mean Temperatures (i.e., T_{mean}) in Equation 2-1 and Percentage of Volume of Five Temperature Zones			
Zone Number	**Mean Values of Low-End SNF and Cladding Initial Temperature K (°C) (°F)**	**Mean Values of High-End SNF and Cladding Initial Temperature K (°C) (°F)**	**Percentage of Total Volume of SNF Basket**
1	575 (301.9) (575.3)	673 (400.0) (751.7)	18.95
2	525 (251.9) (485.3)	623 (350.0) (661.7)	33.00
3	475 (201.9) (395.3)	573 (300.0) (571.7)	33.72
4	425 (151.9) (305.3)	523 (250.0) (481.7)	12.38
5	375 (101.8) (215.3)	481 (208.0) (406.1)	1.95

2.3 Radiation Field and Dose Rates

Estimates of radiation energy deposition rates inside waste packages and canisters containing twenty-one 15 × 15 Babcock and Wilcox PWR SNF assemblies were based on dose rates reported in BSC (2001). BSC (2001) provides dose rates for conditions ranging from 75 gigawatt days per metric ton of uranium (GWd/MTU) burnup for 5.5-percent initial uranium(U)-235 enrichment and 5-year cooling time to 48 GWd/MTU burnup, 4.0-percent initial U-235 enrichment, and 21-year cooling time. Although the dose rates presented in BSC (2001a) vary by location within the waste package, combined gamma and neutron doses generally range from 10^2 to 10^3 grays per hour (Gy/h) (10^4 and 10^5 rad/h).

Similar information regarding radiation energy deposition and dose rates for thirty-two 17 × 17 Westinghouse PWR SNF assemblies placed in a canister were obtained from Radulescu (2011). Radulescu (2011) assumed 60 GWd/MTU burnup, 5-percent initial enrichment, and 20-year cooling period and included a map of the dose rate values for a cross-section through the center of a modeled HI-STAR 100 cask. Based on the dose rate map, two representative dose rates were selected: (1) 1.18×10^2 Gy/h (1.18×10^4 rad/h) and (2) 1.69×10^3 Gy/h (1.69×10^5 rad/h). These two values are representative of the dose rate range in the canister volume. The selected values are consistent with those reported in BSC (2001a).

The dose rate in units of rad/h can be converted to units of eV/g/s according to the following conversion factor:

$$1 \text{ rad/h} = 1.7338\times10^{10} \text{ eV/g/s} \qquad (3\text{-}1)$$

The unit of electronvolt per gram per second (eV/g/s), also referred as radiation energy deposition rate, is valid for moist air (Radulescu, 2011) and was used for the canister environment. Using the conversion factor, the corresponding radiation energy deposition rates are 2×10^{14} and 3×10^{15} eV/g/s for the dose rates of 1.18×10^2 and 1.69×10^3 Gy/h, respectively.

2.4 Cladding Defects and Breaches

The physical condition of the SNF rods and assemblies at the time they are placed into dry storage is virtually unchanged from when they are removed from the reactor because degradation during storage in the SNF pool is minimal (CRWMS M&O, 2000). Some SNF rods can have initial defects, such as manufacturing microdefects; handling-induced defects, including small, partial-depth cladding wall cracks; weld defects; moisture or organic

contamination of cladding or pellets; and excessive gaps at spacers that permit vibration and fretting. During reactor operations, cladding can fail by pellet-cladding interactions, SCC, and debris-induced fretting.

Data from studies of Zircaloy-based cladding failure from 1968 to 1973 indicate that one in 100 SNF rods (1 percent) had cladding failures (CRWMS M&O, 2000; Locke, 1974). A later study reported that the overall cladding failure had decreased to 0.36 percent for BWR and 0.04 percent for PWR SNF rods as a result of design and material performance improvements (Cohen & Associates, 1999). From the measurement of krypton (Kr)-85 leaking from approximately 26,500 rods currently in dry storage, the overall observed failure is estimated to be 0.045 percent (CRWMS M&O, 2000).

3. PHYSICAL AND CHEMICAL PROCESSES IN THE CANISTER

3.1 Radiolysis of the Residual Water

Radiolysis of the residual water in the canister would generate various products (e.g., hydrogen and oxygen) that may affect backfill gas pressure, flammability limits, and degradation of internal components. As noted previously, this study assumed that the canister seals remain intact and that no air or moisture enters once the canister has been sealed after the drying process. Thus, chemically aggressive species such as nitric acid are not present.

Complete decomposition of the residual water by radiolysis could occur within a few years or over several decades. The dominant radiolysis products are hydrogen and oxygen. Other chemical species, such as hydrogen peroxide, could also be produced, but were not included in the analysis because hydrogen peroxide readily (spontaneously) decomposes to hydrogen and oxygen at the temperatures expected in the cask (see Section A2.1.3 in the appendix to this report).

A single forward rate of water vapor decomposition by radiolysis was estimated using a G-value of G_{water} = 7.4 particles per 100 eV (see Section A2.1.2 in the appendix to this report). Two time constants for decomposition of residual water were estimated using this G-value and the two values of the radiation energy deposition rates—2.0×10^{14} and 3×10^{15} eV/g/s.

Assuming that water decomposes to produce only hydrogen and oxygen, the decomposition rate for water R_D in units of molecules per second was calculated as follows:

$$R_D = R_{ED} m_{water} G_{water} \tag{3-1}$$

where R_{ED} is the rate of energy deposition in units of eV/g/second, m_{water} is the mass of water in grams, and G_{water} is the G-value in units of molecules of water (H_2O) decomposed per 100 eV. The radiation energy deposition rates are assumed to be uniform, irrespective of water vapor location in the canister, and time independent. Note that the rates would decrease with time as the total radiation level decreases in the canister.

Following the law of mass action, m_{water} can be expressed as follows:

$$m_{water}(t) = m_0 exp\left(-\frac{R_{\mathrm{ED}} G_{\mathrm{w}} MW}{N_A} t\right) = m_0 exp\left(-\frac{t}{\tau}\right) \tag{3-2}$$

where *t* is time (year), m_0 is the initial amount of the residual water, MW is the molar mass of water, N_A is Avogadro's number, and time constant, τ, is defined as follows:

$$\tau = \frac{N_A}{R_{ED} G_W MW} \tag{3-3}$$

Equation 3-2 can be rewritten as follows:

$$n_{water}(t) = n_0 exp\left(-\frac{t}{\tau}\right) \tag{3-4}$$

where n_{water} is the moles of water and n_0 is the initial moles of the residual water. Using the higher and lower values of radiation energy deposition rates, the values of the time constants are equal to 4.77 and 71.62 years for the radiation energy deposition rates equal to 2.0×10^{14} and 3×10^{15} eV/g/s, respectively. Additional analysis presented in Section A2 in the appendix to this report suggests that recombination could change the water decomposition rate. Under the assumption that the recombination reaction is limited because of oxygen consumption by cladding and SNF, and that nearly all the water decomposes in one time constant, Equations 3-5 and 3-6 were adopted for the amount of remaining water as a function of time. Section A2 in the appendix to this report provides a detailed justification for these assumptions.

$$n_{water}(t) = n_0 exp(-1.929\ t) \tag{3-5}$$

for a time constant equal to 4.77 years, and

$$n_{water}(t) = n_0 exp(-0.129\ t) \tag{3-6}$$

for a time constant equal to 71.62 years. To explore the effect of functional form of the decomposition model, the following two linear functions were also used to compute the amount of remaining water as function of time:

$$n_{water}(t) = n_{water}\left(1 - \frac{t}{4.77}\right) \tag{3-7}$$

and

$$n_{water}(t) = n_{water}\left(1 - \frac{t}{71.62}\right) \tag{3-8}$$

Both the exponential and linear function radiolysis equations for the two time constants are reasonable for this scoping study given the uncertainty in the parameters and the wide range of radiation doses.

3.2 Cladding Oxidation

SNF burnup affects the oxide thickness and other cladding properties, including the amount of absorbed hydrogen, fission gas production, and crud buildup. It has been observed that peak oxide thickness of Zircaloy increases as burnup extends to 75 GWd/MTU (Garde, 1991; Van Swam et al., 1997; EPRI, 2007). In particular, measurements of more than 4,400 commercial SNF rods from reactors around the world show that the average oxide thickness on Zircaloy-4 was 100 μm (0.00394 in.) for burnups in the range of 60 to 65 GWd/MTU (EPRI, 2007), while for low burnup conditions (less than 45 GWd/MTU), the average oxide thickness was 40 μm (0.00157 in.).

Hillner et al. (1994) analyzed weight data from long-term autoclave tests of Zircaloy-2 and Zircaloy-4. The tests were conducted in degassed pure water for 10,507 days at temperatures ranging from 250 to 360 °C (482 to 680 °F). Twenty-two different tests were analyzed, and specimens with different heat treatment and preoxidized surface conditions were included. Based on their analysis, Hillner et al. (1994) developed Equation 3-9 to describe weight gain resulting from cladding oxidation as a function of temperature and time:

$$\Delta W = A\ t\ exp\ (-Q/RT) \tag{3-9}$$

where

ΔW — specimen weight gain in milligrams per decimeter square (mg/dm^2)
A — preexponential constant in milligrams per decimeter square per day ($mg/dm^2/day$)
t — time in days
Q — activation energy in calories per mole (cal/mole)
R — gas constant in calories per mole per Kelvin (cal/mole/K)
T — absolute temperature in K

Nine independent cladding oxidation studies report distinct values for the activation energy and preexponential constant in Equation 3-9. Figure 3-1 illustrates the oxide thickness growth curves, using the *A* and *Q* values from those nine studies, for a temperature profile and unlimited oxidizing environment. The following temperature profile was used to calculate the oxide layer thickness presented in Figure 3-1:

$$T(t) = (575 - 309)\frac{[exp(-0.023t) + exp(-0.064t)]}{2} + 309 \quad (3\text{-}10)$$

where $T(t)$ is the temperature (K) as a function of the time. The calculated maximum oxide thickness ranges from 1.2 μm to 4 μm (4.724×10^{-5} to 1.6×10^{-4} in.). Sections A3.1 and A4.4.1 in the appendix to this report provide additional details regarding the cladding oxidation. The integration model used the *A* and *Q* values associated with the highest thickness of cladding oxidation.

3.3 Spent Nuclear Fuel Oxidation

When cladding is breached, irradiated UO_2 SNF can react with oxidants formed by radiolysis of the residual water present inside the canister. The UO_2 could be oxidized to form U_4O_9, U_3O_7, and U_3O_8 in dry air (less than 40 percent RH) or form hydrated uranium oxides, such as schoepite ($UO_3 \cdot xH_2O$, x = 0.5 to 2), in humid air (greater than 40 percent RH) or in an aqueous environment (Ahn, 1996; Einziger et al., 1992; Einziger and Strain, 1986; Einziger and Cook, 1985; EPRI, 1986; McEachern and Taylor, 1998; Taylor et al., 1995; Wasywich et al., 1993).

The extent of SNF oxidation and hydration is controlled by the reaction kinetics of SNF oxidation and the amount of available oxidants (oxygen and water vapor) present in the canister. For example, if reaction rates are slow and oxidants abundant, kinetics will control overall reaction progress. However, for fast reaction kinetics and limited amounts of oxidants, overall reaction progress will be controlled by the net production rate of the oxidant. Table 3-1 summarizes the SNF oxidation model adopted in the integrated analysis.

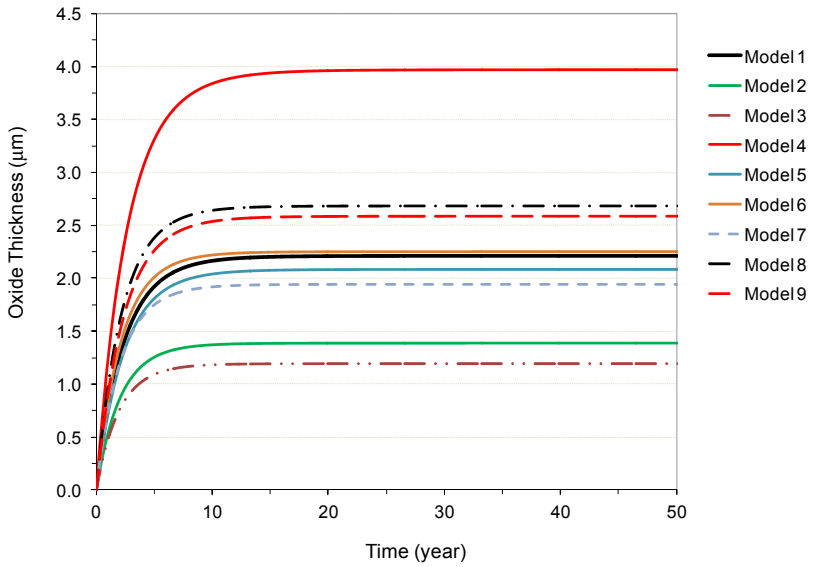

Figure 3-1 Calculated additional oxide thickness on cladding surface during the dry storage period according to nine different values of parameters *Q* and *A* for the temperature profile given by Equation 3-10 in unlimited oxidizing environment. (See Section A3.1.3, Figure A3-1, in the appendix to this report for more details on the nine models.)

Table 3-1 Criteria for Temperature and RH for SNF Oxidation and Hydration in the Canister Environment

Temperature and Relative Humidity		Primary Phase Considered	Applicable Kinetic Equation and Comments
T ≥ 230 °C (T ≥ 446 °F) (independent of RH)		U_3O_8	The equation for $UO_{2.4}$, $w = (2kt)^{0.5}$ (Eq. A3-4) is used assuming all $UO_{2.4}$ is fully convert to U_3O_8.
150 ≤T <230 °C (302 ≤T <446 °F)	RH* <40%	$UO_{2.4}$†	$w = (2kt)^{0.5}$
	RH >40%	U_3O_8	U_3O_8 is not normally observed below 230 °C (446 °F) in dry air with RH < 40%. U_3O_8 can eventually form over a long term at high RH (no clear time at which formation starts) based on observations of U_3O_8 formation for unirradiated UO_2 and used CANDU SNF tested at 150 °C ≤ T < 230 °C (302 °F ≤ T < 446 °F) with a high moisture level. The equation $w = (2kt)^{0.5}$ is applicable assuming conversion of UO_2 to U_3O_8.
T <150 °C (T <302 °F)	RH <40%	$UO_{2.4}$‡	$w = (2kt)^{0.5}$
	RH >40%	$UO_3 \cdot xH_2O$ (x < 2)	The kinetics to form schoepite or other hydrate forms can be used as the dissolution rate obtained from the aqueous condition.† The rate ranges from 0.01 to 6.85 mg/m^2/d.

* relative humidity

† $UO_{2.4}$ could be a quasi-stable intermediate phase that can be eventually converted to U_3O_8 only when the oxygen is available to react with $UO_{2.4}$ to form U_3O_8 during a long-term conversion time (e.g., 1.16×10^4 years required at 150 °C (305 °F)) (see Table A3-2)

‡ In NUREG–1914, "Dissolution Kinetics of Commercial Spent Nuclear Fuels in the Potential Yucca Mountain Repository Environment," issued in 2008 (Agencywide Documents Access and Management System Accession No. ML083120074,), the kinetics assume sufficient oxidants are present. Otherwise, the supply of oxidants can control the kinetics.

The calculated times for complete conversion from UO_2 to $UO_{2.4}$ (non-stoichiometric) and from UO_2 to U_3O_8 as functions of temperature show that the conversion time decreases exponentially with increasing temperature (Figure 3-2). Note that the time for conversion to U_3O_8 could be observed only for temperatures above 230 °C (446 °F) (as marked with a dotted line in the figure), although U_3O_8 could form continuously at below 230 °C (446 °F). The U_3O_8 phase was not typically observed below 230 °C (446 °F) in experiments conducted in dry air. Below 230 °C (446 °F) for dry air oxidation at low RH (e.g., less than 40 percent of RH), $UO_{2.4}$ was the predominant phase. Sections A3.2 and A4.4.2 in the appendix to this report present additional details regarding SNF oxidation.

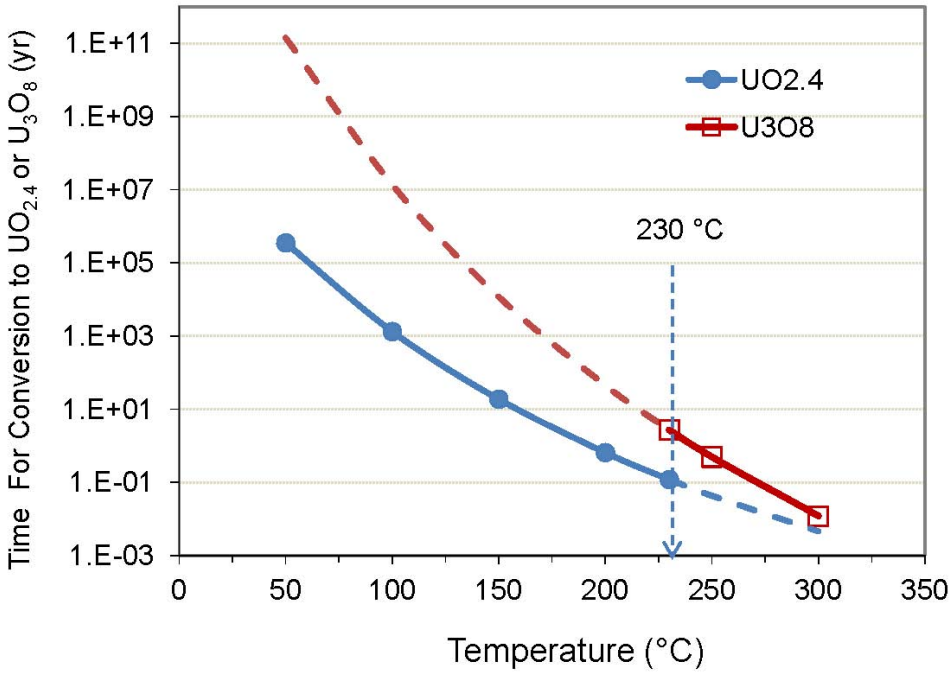

Figure 3-2 Time for conversion from UO_2 to $UO_{2.4}$ and from UO_2 to U_3O_8 as a function of temperature

4. CONSEQUENCE ASSESSMENT

Based on the environmental conditions presented in Section 2 and using the physicochemical process models described in Section 3, this study performed an integrated quantitative assessment of the consequences of residual water on the degradation of the cask and its contents. The following sections discuss specific details of various degradation mechanisms and their effects, and Table 4-1 presents a detailed summary of results.

4.1 Cladding Thinning

Data from the integration model presented in Section A4.4.1 in the appendix to this report indicate that additional cladding oxidation is insignificant compared to the original cladding oxide layer thickness generated in the reactor. Cladding oxidation caused by radiolysis-generated oxygen is not expected to be a concern because the additional layer of cladding oxide that would form during extended storage is expected to be no more than 7.5 μm (0.00025 in.), whereas the original cladding thickness ranges between 0.6 and 0.9 mm (0.0236 and 0.0355 in.) (Bailey and Tokar, 1982). Thus, the loss of cladding material from oxidation in the canister environment is expected to be less than 1 percent. Therefore, the formation of the ZrO_2 layer resulting from cladding oxidation is not expected to affect the strength of the cladding.

4.2 Spent Nuclear Fuel Oxidation and Cladding Unzipping

Oxidation of spent nuclear SNF would be of concern if one or more UO_2 SNF pellets fully oxidize to U_3O_8. SNF pellets swell up to 36 percent by volume when UO_2 is fully oxidized to U_3O_8. Expansion of the SNF pellets increases the stress on the cladding, which will split the cladding (in a process commonly referred to as unzipping) if the resulting strain reaches a 6.5-percent threshold for a 3.5-centimeter (cm) (1.4-inch (in.))-long initial cladding defect (Einziger and Cook, 1985). When the strain exceeds this threshold, preexisting defects (crack, pinhole) on the cladding could become wider than 1 mm (0.039 in.). This could result in release of U_3O_8 SNF particulates (NRC, 2007), thus contaminating the canister environment and complicating SNF retrieval, transport, and ultimate disposal. Available data suggest the threshold strain may be less than 1 percent, but this threshold value also depends on the shape of the defect as well as the cladding composition. To evaluate cladding rupture, this scoping study used a 6.5-percent threshold strain criterion along with an assumed 1-mm (0.039-in.) crack width.

Once the SNF rod splits at a defect caused by SNF swelling, cracks can propagate quickly at high temperature. Continued oxidation of the pellets causes swelling, mechanical loading, and continued crack growth. An initial defect (3.5 cm (1.4 in.) long and 1 mm (0.039 in.) wide), assuming rod rupture, was used to estimate the total number of pellets near the defect that are fully oxidized. Data suggest that SNF pellets within a linear zone extending 3 cm (1.2 in.) beyond both ends of the initial 3.5-cm (1.4-in.) defect will be oxidized to U_3O_8.

Results from the integrated scoping assessment described in Section A4.4.2 in the appendix to this report indicate that exposed SNF pellets could be completely oxidized to U_3O_8 if the SNF rod is located in the high-temperature zone of the canister, sufficient residual water is available,

Table 4-1 Effect of Residual Water Amount on SNF and Cladding Oxidation, Flammability, Hydrogen-Induced Damage, Aqueous Corrosion of the Canister Components, and Decrease in Criticality Safety Margin

Mechanism/ Effect	Component	Criteria for Concern†	Environmental Conditions*					Detailed Analysis
			Radiation Dose Rate (H, L)	Initial Temperature (H, L)	Residual Water Amount (moles) 5.5	17.4	55	
Oxidation	Spent Nuclear Fuel	One or more UO_2 SNF pellet fully oxidizes to U_3O_8, causing cladding unzipping because the strain exceeds the threshold (e.g., 6.5%) at the defect location. When the strain exceeds the threshold, preexisting defects (crack, pinhole) can propagate to expose more U_3O_8 to the canister atmosphere (Einziger and Cook, 1985). Grossly breached SNF cladding is considered to be any cladding breach of greater than the 1 mm (0.039 in.) crack width required to release U_3O_8 SNF particulates (NRC, 2007). Radiological dose is not considered in determining this criterion, which is unlikely significant.	H	H	†	†	†	4.2, A3.2, A4.4.2
				L	†	†	†	
			L	H	—	—	†	
				L	—	†	†	
	Cladding	Loss of cladding thickness equal or greater than 17% with respect to the original cladding thickness. As defined in 10 CFR 50.46(b)(2), the maximum cladding oxidation limit (i.e., oxidation thickness) must be no more than 17% of the original cladding thickness (Meyer, 2000).	H	H	—	—	—	4.1, A3.1, A4.4.1
				L	—	—	—	
			L	H	—	—	—	
				L	—	—	—	
Flammability	N/A	When oxygen and hydrogen mole fractions are equal to or more than 5% (Zlochower and Green, 2009; NRC, 1999) and source of ignition present. Flammability is affected by the canister's void volume and backfill pressure. This criterion is evaluated for 1 atm (14.7 lb/in.^{2}) of backfill pressure and 2,100 L (74.2 ft^3) of void volume.	H	H	—	—	√	4.3, A4.4.4
				L	—	—	√	
			L	H	—	—	√	
				L	—	√	√	
Hydrogen-Induced Damage	Cladding	Most of the hydrogen generated from radiolysis of the residual water is absorbed by the cladding and results in formation hydrides. When all of the hydrogen generated by 55 moles of residual water is absorbed, the hydrogen concentration in the cladding would be an additional 25 ppm.	H	H	—◊	—◊	—◊	4.4.1, A5.1
				L	—◊	—◊	—◊	
			L	H	—◊	—◊	—◊	
				L	—◊	—◊	—◊	
	Canister Internals	Absorbed hydrogen concentration is equal to or more than 10 ppm in steel components (Okada, 1977). Mechanical properties of steel components would degrade when hydrogen concentration is more than 10 ppm.	H	H	—♦	—♦	—♦	4.4.2, A5.2
				L	—♦	—♦	—♦	
			L	H	—♦	—♦	—♦	
				L	—♦	—♦	—♦	
Aqueous Corrosion‡	Cladding	Corrosion of cladding resulting in formation of throughwall cracks.	H	H	—‡	—‡	—‡	4.5, A5.2
				L	—‡	—‡	—‡	
			L	H	—‡	—‡	—‡	
				L	—‡	—‡	—‡	

Table 4-1 Effect of Residual Water Amount on SNF and Cladding Oxidation, Flammability, Hydrogen-Induced Damage, Aqueous Corrosion of the Canister Components, and Decrease in Criticality Safety Margin (continued)

Mechanism/ Effect	Component	Criteria for Concern†	Environmental Conditions*					Referral Sections for Detailed Analysis
			Radiation Dose Rate (H, L)	Initial Temperature (H, L)	Effect of Residual Water Amount (moles)			
					5.5	17.4	55	
Aqueous Corrosion‡ (continued)	Canister Internals	Throughwall stress-corrosion cracks form on structural components creating a passage for ambient atmosphere to interact with canister internals. In addition, one or more internal structural components collapse as a result of loss of material.‡	H	H	—	—	—	4.5, A5.2
				L	—	—	—	
			L	H	—	—	—	
				L	—	—	±	
Decrease in Criticality Margin*	N/A	In general, based on the limited degradation expected for dry cask storage system components, a significant impact on criticality safety is not anticipated. However, if specific degradation mechanisms are identified, development of more detailed models would likely be required to address each potential issue.	N/A	N/A	N/A	N/A	N/A	4.5, A6

* For environmental conditions, the following values, or ranges of values, were considered:
Radiation Dose Rate: Low (L) = 1.18×10^{2} Gy/h (1.18×10^{4} rad/h), corresponding to an energy deposition rate of 2×10^{14} eV/g/s; High (H) = 1.69×10^{3} Gy/h (1.69×10^{5} rad/h), corresponding to an energy deposition rate of 3×10^{15} eV/g/s
Initial Temperature (SNF and cladding): L = 375–575 K (215.3–575.3 °F); H = 481–673 K (406.1–751.7 °F)

† For criteria of concern, the following symbols are used:
√: Significant impact (in the presence of ignition).
†: Measurable impact.
±: Signifies that the criteria of concern (third column) for the given combination of environmental conditions (fourth column) examined was met. Relevant literature data are insufficient to support a finding of potential SCC at longer time and lower temperatures.
—: Signifies that the criteria of concern for the given combination of environmental conditions examined was not met.
◊: Signifies that the criterion was never met because oxide layer on cladding prevents hydrogen absorption. Only a small (less than 1%) fraction of the water is absorbed.
♦: Signifies that the criterion was never met because hydrogen partial pressure in canister was too low to induce hydrogen absorption.
‡: Signifies that the potential damage mechanism was qualitatively assessed.

water undergoes complete radiolysis in a relatively short period, and diffusion of oxygen occurs along and through grain boundaries in the SNF. The integration model data indicates the following:

- SNF oxidation is a concern for any amount of residual water ranging 5.5 to 55 moles for energy deposition rate of 3×10^{15} eV/g/s corresponding to a time constant of 4.77 years. However, the concern did not consider the radiological dose consequence which is unlikely significant, as stated in Table 4-1. This is applicable for the two temperature conditions listed in Table 2-1.

- Radiolysis kinetics is slower for the lower value of the radiation energy deposition rate of 2×10^{14} eV/g/s compared to the higher value. It takes several decades to decompose the residual water at the lower energy deposition rate. Under this scenario, uncertainties in the radiolysis kinetics affect the extent of SNF oxidation. For example, when the residual water decomposes slowly (e.g., according to the exponential function given in Equation 3-6), the integration model data indicate that SNF oxidation is a concern for 17.4 and 55 moles of residual water for the low-end temperature condition. On the other hand, SNF oxidation is only a concern when 55 moles of residual water decomposed via the linear model given in Equation 3-8, within 71.62 years for the high-end temperature condition. Thus, the amount of residual water is a key uncertainty affecting SNF oxidation for the lower radiation energy deposition rate. If the amount of residual water is fixed, the key process affecting the extent of SNF oxidation is the radiolysis rate.

4.3 Flammability

The cladding will not absorb radiolysis-generated hydrogen because the hydrogen will be in a molecular form that cannot diffuse through the oxide layer on the cladding surface at temperatures expected in the canister (see details in Section 4.4.1). Radiolysis-generated hydrogen will, therefore, exist as gas in the canister void volume and may pose a flammability risk if a source of ignition is present. The flammability criterion in NUREG-1609, "Standard Review Plan for Transportation Packages for Radioactive Material," issued March 1999 (NRC, 1999), requires the volume fraction of any flammable gas to be less than 5 percent. This report also considered the presence of an oxidizer (i.e., oxygen).

Oxygen gas is necessary for hydrogen to become flammable; however, no criterion exists that specifies the ratio of oxygen to hydrogen needed for the flammability of hydrogen with helium as an inert gas. Zlochower and Green (2009) conducted experiments to determine oxygen concentration limits for the flammability of hydrogen in the presence of nitrogen as an inert gas. The limiting oxygen concentration is defined as the minimum amount of oxygen that can support flame propagation.

Zlochower and Green (2009) determined that the limiting oxygen concentration is close to 5 mole percent for a hydrogen mole fraction varying between 4 and 76 mole percent. It is assumed that the limiting oxygen concentration value that Zlochower and Green (2009) determined applies to hydrogen mixed with helium as an inert gas. The amount of oxygen needed to achieve the criterion of 5 mole percent in the canister is estimated using the following equation:

$$\frac{n_{oxygen}}{n_{oxygen} + n_{hydrogen} + n_{helium}} = 0.05 \qquad (4\text{-}1)$$

where n_{oxygen}, $n_{hydrogen}$, and n_{helium} denotes moles of oxygen, hydrogen, and helium in the canister. The moles of helium in the canister are calculated using the ideal gas law:

$$n_{helium} = \frac{PV}{RT} \tag{4-2}$$

where P is equal to either 1 or 5 atm (14.7 or 73.5 lb/in.^{2}), V is equal to the canister void volume (i.e., 2,100 L (74.2 ft^3)), and T is equal to 298 K (77 °F). However, there is uncertainty regarding the gas temperature when the canister is being backfilled, and it is expected that the gas temperature would be higher than 298 K (77 °F). Assuming a higher temperature results in an underestimate of the moles of helium (but only by 10 to 25 percent) when the temperature is less than 373 K (212 °F). Thus, estimates based on lower temperatures are reasonable.

According to Equation 4-2, the oxygen concentration exceeds 5 mole percent only when the residual oxygen is more than 4.8, 5.4, and 7.4 moles for 5.5, 17.4, and 55 moles of residual water, respectively, and the backfill pressure is 1 atm (14.7 lb/in.^{2}). Similarly, at a backfill pressure of 5 atm (73.5 lb/in.^{2}), the oxygen concentration exceeds 5-mole percent when residual oxygen is more than 22.8, 24.4, and 25.7 moles for 5.5, 17.4, and 55 moles of residual water, respectively. Note that these values of oxygen amounts are for a 2,100-L (74.2-ft^3) canister void volume and both backfill pressures at room temperature of 25 °C (77 °F).

The integration model indicates that conditions for flammability could be met (in the presence of ignition) for 55 moles of residual water and 1 atm (14.7 lb/in.^{2}) of backfill pressure and for the two temperature and radiation conditions considered in this study. The data also indicate that the canister environment would meet the conditions of flammability when 17.4 moles of residual water undergoes radiolysis via linear decomposition in 71.62 years, given the low-end SNF and cladding initial temperature condition and 1 atm (14.7 lb/in.^{2}) of backfill pressure. The conditions of flammability are never met when backfill pressure is 5 atm (73.5 lb/in.^{2}) and the residual water amount is 55 moles or less.

4.4 Hydrogen-Absorption-Induced Damage

4.4.1 Cladding

The hydrogen generated by the radiolytic decomposition of water would be in molecular form. The absorption of the molecular hydrogen through zirconium oxide into zirconium is expected to be limited at temperatures below 400 °C (752 °F) as governed by Sievert's law. Further, hydrogen solubility in zirconium oxide is very low (10^{-5} to 10^{-4} moles of hydrogen per mole oxide) (Miyake et al., 1999). Consequently, the presence of the oxide film on the cladding significantly impedes hydrogen absorption (Steinbrück, 2004). Therefore, molecular hydrogen generated by the radiolysis is not expected to be absorbed by the cladding. If the oxide is damaged, zirconium will be instantly repassivated forming the oxide in water. With maximum possible hydrogen from 55 moles of water, the increase of hydrogen concentration in cladding is insignificant compared with the amount of initially existing hydrogen.

Hydrogen could also be absorbed by the cladding when water directly reacts with cladding, through the process shown in Figure A5–1 in the appendix to this report. This would occur if water contacting the cladding material is either in the liquid phase or the RH is above 20 percent. Detailed analysis presented in Section A5.1 of the appendix to this report indicates

that the increase of hydrogen concentration in the cladding would be less than 1 part per million (ppm). This suggests that hydrogen absorption by the cladding in the canister environment is not a concern with 55 moles of water.

4.4.2 Canister Internals

In an extended storage environment, most of the hydrogen is generated by radiolysis of water. The subsequent absorption of hydrogen into the metal matrix can affect and may degrade the mechanical properties of the stainless steel basket and canister when the concentration exceeds a critical hydrogen concentration in the metal matrix. Okada (1977) reported that the critical hydrogen concentration dissolved in the iron matrix needs to be 10 ppm to cause appreciable mechanical degradation by blistering and cracking. The hydrogen concentration in alpha iron was estimated to be 0.9 part per billion (ppb) at room temperature in contact with 0.1 MPa (14.5 lb/in.^{2}) H_2 pressure by estimating with Sievert's law. With increasing temperature, the concentration will increase following an Arrhenius temperature relationship. Oriani (1970) estimated that the maximum hydrogen concentration in iron was less than 1 ppm at 300 °C (572 °F) at 8 MPa (1,160.3 lb/in.^{2}) of H_2 pressure. This information indicates that the hydrogen absorption in any ferrous-based alloy is expected to be insignificant in the canister environment. Even with this mechanism, the absorbed hydrogen is expected to be less than 1 ppm, much below the limit of 10 ppm. Based on this information, hydrogen absorption by the canister internals is not a concern.

4.5 Aqueous Corrosion

Aqueous corrosion could occur in vapor when the RH is greater than a threshold value. For internal structural components and the SNF cladding, the threshold value is greater than 20 percent. Below is an assessment made assuming that the RH is high enough for vapor corrosion or vapor condensation. In the early period of storage, the RH is mostly below 20 percent, as fully described in Section A5 of the appendix to this report.

General corrosion of the canister's internal structural components is unlikely to cause any structural damage to those components. Localized corrosion either in the form of pitting or crevice corrosion of the structural components is unlikely to occur. Galvanic corrosion would commence only when residual water condenses inside the canister. However, the extent of damage to the components is expected to be limited and is unlikely to affect the integrity of any component.

SCC of the canister's internal structural components, especially those composed of carbon and stainless steel, could occur during extended storage. SCC-induced cracks could become throughwall even in the presence of a sufficient amount of oxidants, which could occur even in 1 mole of liquid-phase water in the canister environment. Liquid-phase water could exist in the canister when the canister humidity reaches saturation or sufficient amounts of residual oxygen combine with hydrogen to produce water. Given this possibility, as well as the RH of the canister environment summarized in Table A5-1 (see Appendix A to this report), SCC of steel components may need to be considered when the residual water amount is 55 moles and the low-end temperature condition is present. However, relevant data are insufficient to support a finding of potential SCC of carbon steel and stainless steel at longer time and lower temperatures.

Shadow corrosion (a form of galvanic corrosion) between cladding and spacer-grid material could occur when residual water condenses in the canister. However, the effect of shadow

corrosion on cladding is expected to be limited and is not expected to affect more than a few SNF rods. Shadow corrosion is unlikely to cause the formation of throughwall cracks and holes on the SNF rods.

4.6 Perspectives on the Potential Impact of Incomplete Drying on Criticality Safety Margins

Maintaining subcritical conditions for stored SNF assemblies is an important safety requirement for dry cask storage systems. For incomplete cask drying, there are several important considerations for criticality safety margins, including (1) the impact of water (a moderating material for neutrons) directly on system reactivity and (2) the potential corrosive effects of water on system components that maintain the physical configuration of the fuel. NUREG/CR-6835, "Effects of Fuel Failure on Criticality Safety and Radiation Dose for Spent Fuel Casks," issued September 2003 (Elam et al., 2003) and Povetko et al. (2008) provide examples of bounding scenarios and assess their effects on the criticality safety margin if severe degradation occurred. Section A6 of the appendix to this report includes a more detailed description of the criticality safety considerations, as well as the references, scenarios, and dry cask storage system components considered.

Based on the review of scenarios from Elam et al. (2003) and the work by Povetko et al. (2008), several insights on the effects of various degraded conditions were developed. The conditions considered for the case of incomplete cask drying included removal of neutron absorber materials from the SNF basket and removal of SNF rods from the SNF assembly or relocation of SNF pellets. In general, the removal of a single SNF rod (or possibly a few rods) may not make a large contribution for criticality concerns. In the case of SNF relocation, it is possible for a significant contribution to system reactivity. The scenario considered in Elam et al. (2003) is expected to be a bounding case for SNF relocation in a dry storage cask. With regard to removal of neutron absorber panels, several important insights can be drawn from Povetko et al. (2008), including a significant reduction in safety margin. However, the scenarios in Povetko et al. (2008) considered complete removal of neutron absorber panels, which would constitute removal of a large quantity of neutron-absorbing material. The complete removal of the panels requires a significant degradation of the neutron absorber materials.

With limited degradation expected for dry cask storage system components (Section 4.5), no significant impact on criticality safety is anticipated from SNF and neutron absorber reconfiguration. The presence of 55 moles of water is not expected to affect criticality margins since this amount of water would fill less than 0.05 percent of the 2,100-L (74.2-ft^3) void volume of the canister. In addition, criticality is not expected to be a concern because significant degradation of cask system components does not occur in this situation.

5. OBSERVATIONS AND CONCLUSIONS

The paragraphs below provide the overall conclusion, as well as topical observations, derived from the consequence analysis of the residual water from incomplete SNF drying. Table 4-1 also summarizes the analysis results.

The overall conclusions are stated as follows:

Degradation of cladding, fuels, and other internal components is not expected to be significant over the analyzed period, up to 300 years of storage time, for conditions in the range of 5.5 to 55 moles (0.1 to 1 L (3.5 to 35 oz)) of residual water analyzed in this study,. Above 17.4 moles (log mean of 5.5 and 55 moles) (0.32 L (11.2 oz)) of residual water, the canister environment would meet the condition of flammability in terms of the amount of hydrogen and available oxygen present, given a source of ignition. This condition is anticipated for radiolysis via linear decomposition of water with time in 72.62 years for the low end of the initial temperature of SNF and cladding and for 1 atm (14.7 lb/in.^{2}) of backfill pressure. The uncertainty associated with the maximum water amount needs to be assessed.

The qualitative assessment performed on the potential impact on criticality due to residual water indicates that the conditions resulting from incomplete drying are not expected to cause significant degradation of internals; therefore, no significant impact on criticality safety is anticipated.

The following are topical observations from this study:

The potential amount of unbound residual water in a canister, including additional water from a waterlogged rod, could range from roughly 1.4 to 11 moles (25 ml to 0.2 L (0.88 to 7 oz)). There is uncertainty associated with more water potentially resulting from slow drying kinetics. The amount of chemisorbed bound water present on the cladding surface remains uncertain because of a lack of data. With these considerable uncertainties, the analysis of the residual water effect assumes a range from 1 to 55 moles.

Calculations indicate that complete decomposition of the residual water by radiolysis will occur within a few years to several decades. The dominant long-term radiolysis products are likely to be hydrogen and oxygen.

Cladding oxidation is not expected to be a concern because the additional amount of cladding oxide that would form during extended storage is expected to be less than 7.5 μm (2.7×10^{-2} in.) thick, whereas the original cladding thickness ranges between 0.6 and 0.9 mm (0.0236 and 0.0355 in.). Thus, the loss of cladding material resulting from its oxidation is expected to be less than 1 percent.

One or more exposed SNF pellets could be completely oxidized to U_3O_8, if the exposed pellets are located in the hotter parts of the canister (approximately 302 °C (576 °F)), the amount of residual water is sufficiently high (near 55 moles), water undergoes complete radiolysis in a relatively short period (near 4.77 years), and oxygen is diffused through grain boundaries.

With an assumption of an initial crack size for cladding gross rupture (i.e., a crack 3.5 cm (1.38 in.) long and 1 mm (0.039 in.) wide), the crack can further propagate to the affected area of plus or minus 3 cm (1.18 in.) in the axial direction with a complete conversion of the exposed fuel

pellets to U_3O_8. The analysis of crack propagation did not consider the radiological dose consequence, which appears unlikely to be significant.

In regards to flammability of the canister environment caused by residual water, a significant amount of residual hydrogen generated by radiolysis could be left inside a storage cask when a sufficient quantity of the residual water undergoes radiolytic decomposition. A flammable environment could form with residual oxygen (in the presence of ignition).

Any significant amount of hydrogen absorption by the cladding is unlikely. Radiolysis-generated hydrogen is expected to be in molecular form, which would not be absorbed through oxide. If the oxide is damaged, zirconium will be instantly repassivated forming the oxide in water. With maximum possible hydrogen from 55 moles of water, the increase of hydrogen concentration in cladding is insignificant compared to the amount of initially existing hydrogen. No significant amount of hydrogen is expected to be absorbed by other canister components.

Under the study assumptions and from review of available literature data, general corrosion of the internal structural components is unlikely to cause any structural damage to those components. Localized corrosion either in the form of pitting or crevice corrosion is unlikely to occur. Galvanic corrosion could commence only when residual water condenses inside the canister. However, the extent of damage is expected to be limited and is unlikely to affect the integrity of any component. In addition, data are insufficient to support a finding of potential SCC of carbon steel and stainless steel at longer time and lower temperature. SCC of stainless steel in pure water was observed only at higher temperatures, typically 290 °C (554 °F. No data are available for carbon steel. In the storage canister, relative humidity is very low at this high temperature and the aqueous corrosion condition will not form. Shadow corrosion could occur, but the effect on cladding is expected to be limited.

6. REFERENCES

Ahn, T. NUREG–1565, "Dry Oxidation and Fracture of LWR Spent Fuels." Washington, DC: U.S. Nuclear Regulatory Commission. 1996. ADAMS Accession No. ML040150720.

ASTM International. "Standard Guide for Drying Behavior of Spent Nuclear Fuel." ASTM C1553–08. West Conshohocken, PA: ASTM International. 2008.

Bailey, J.C. and M. Tokar. NUREG/CR–3001, "Fuel Performance Annual Report for 1981." PNL–4342. Washington, DC: U.S. Nuclear Regulatory Commission. December 1982.

BSC. "Dose Rate Calculation for the 21–PWR UCF Waste Package." CAL–UDC–NU–000002, Rev. 01. ACC: MOL.20000223.0507. Las Vegas, NV: Civilian Radioactive Waste Management Systems, Management and Operations. 2001. ADAMS Accession No. ML040550509.

Cohen & Associates. "Effectiveness of Fuel Rod Cladding as an Engineered Barrier in the Yucca Mountain Repository." Contract No. 68D70073. Washington, DC: U.S. Environmental Protection Agency. 1999.

CRWMS M&O. "Initial Cladding Condition." ANL–EBS–MD–000048, Rev. 00 ICN 01. Las Vegas, NV: Civilian Radioactive Waste Management Systems, Management and Operations. 2000.

Einziger, R.E. and J.A. Cook. "Behavior of Breached Light Water Reactor Spent Fuel Rods in Air and Inert Atmospheres at 229 °C." *Nuclear Technology*. Vol. 69. pp. 55–71. 1985.

Einziger, R.E. and R.V. Strain. "Behavior of Breached Pressurized Water Reactor Spent-Fuel Rods in an Air Atmosphere between 250 and 360 °C." *Nuclear Technology*. Vol. 75. pp. 82–95. 1986.

Einziger, R.E., L.E. Thomas, H.C. Buchanan, and R.B. Stout. "Oxidation of Spent Fuel in Air At 175 to 195 °C." *Journal of Nuclear Materials*. Vol. 190. pp. 53–60. 1992.

Elam, K.R., J.C. Wagner, C.V. Parks, and C.J. Withee. NUREG/CR–6835, "Effects of Fuel Failure on Criticality Safety and Radiation Dose for Spent Fuel Casks." Washington, DC: U.S. Nuclear Regulatory Commission. September 2003.

EPRI. "Spent Fuel Transportation Applications—Assessment of Cladding Performance, A Synthesis Report—Final Report." EPRI-TR-1015048. Palo Alto, CA: Electric Power Research Institute. 2007.

EPRI. "Oxidation of Spent Fuel between 250 and 360 °C." EPRI NP–4524. Palo Alto, CA: Electric Power Research Institute. 1986.

Garde, A.M. "Enhancement of Aqueous Corrosion of Zircaloy-4 Due to Hydride Precipitation at the Metal-Oxide Interface." *Proceedings of the Zirconium in the Nuclear Industry: 9th International Symposium*. C.M. Eucken and A.M. Garde, eds. ASTM STP 1132. West Conshohocken, PA: ASTM International. pp. 566–594. 1991.

Guipponi, C., N. Millard-Pinard, N. Bérerd, E. Serris, M. Pijolat, V. Peres, and V. Wasselin-Trupin. "Modification of Oxidized Zircalloy-4 Surface in Contact with Radiolysed Wet Air." *Nuclear Instruments and Methods in Physics Research*. Vol. B 272. pp. 222–226. 2012.

Hillner, E., D.G. Franklin, and J.D. Smee. "The Corrosion of Zircaloy-Clad Fuel Assemblies in a Geological Repository Environment." WAPD-3173. West Miffin, PA: Bettis Atomic Power Laboratory. 1994.

Kohli, R., D. Stahl, V. Pasupathi, A.B. Johnson, and E.R. Gilbert. "The Behavior of Breached Boiling Water Reactor Fuel Rods on Long-Term Exposure to Air and Argon at 598 K." *Nuclear Technology.* Vol. 69. pp. 186–197. 1985.

Knoll, R.W., and E. R. Gilbert. "Evaluation of Cover Gas Impurities and Their Effects on the Dry Storage of LWR Spent Fuel. PNL-6365. Richland, WA: Pacific Northwest Laboratory. 1987.

Locke, D.H. "Review of Experience With Water Reactor Fuels—1968–1973." *Nuclear Engineering and Design*. Vol. 33. pp. 94–124. 1974.

McEachern, R.J. and P. Taylor. "A Review of the Oxidation of Uranium Dioxide at Temperatures below 400 °C." *Journal of Nuclear Materials*. Vol. 254. pp. 87–121. 1998.

Meyer, R.O. "NRC Activities Related to High Burnup, New Cladding Types, and Mixed-Oxide Fuel." *Proceedings of the 2000 International Topical Meeting on Light Water Reactor SNF Performance, Park City, UT, April 10–13, 2000*. Published on CD-ROM. La Grange Park, IL: American Nuclear Society. 2000.

Miyake, M., M. Uno, S. Yamanaka. "On the Zirconium-Oxygen-Hydrogen Ternary System." *Journal of Nuclear Materials*. Vol. 270. pp. 233–241. 1999.

NRC. NUREG–1536, "Standard Review Plan for Dry Cask Storage Systems." Rev. 1. Washington, DC: U.S. Nuclear Regulatory Commission. July 2010.

NRC. Interim Staff Guidance–1, "Classifying the Condition of Spent Nuclear Fuel for Interim Storage and Transportation Based on Function." Rev. 2. Washington, DC: U.S. Nuclear Regulatory Commission. 2007.

NRC. Interim Staff Guidance–11, "Cladding Considerations for the Transportation and Storage of Spent Fuel, Revision 3." Washington, DC: U.S. Nuclear Regulatory Commission. 2003.

NRC. NUREG–1609, "Standard Review Plan for Transportation Packages for Radioactive Material." Washington, DC: U.S. Nuclear Regulatory Commission. March 1999.

Okada, H. "Stress Corrosion Cracking and Hydrogen Cracking of Structural Steels." In *Proceedings, Stress Corrosion Cracking and Hydrogen Embrittlement of Iron Base Alloys, NACE-5.* Houston, TX: NACE International. pp. 124–134. 1977.

Oriani, R.A. "The Diffusion and Trapping of Hydrogen in Steel." *Acta Metallurgica*. Vol. 18. pp. 147–157. 1970.

Peehs, M., R. Bokelmann, and J. Fleisch. "Spent Fuel Dry Storage Performance in Inert Atmosphere." *Proceedings of the 3rd International Spent Fuel Storage Technology Symposium/Workshop, Seattle, WA, April 8–10, 1986*. CONF-860417. Vienna, Austria: International Atomic Energy Agency. pp. S–215 to S–230. 1986.

Povetko, O., S. Whaley, and A. Kouznetsov. "Neutronic Reactivity Effect of Removed Neutron Absorber Plates." Presentation to the ASTM C26—Nuclear Fuel Cycle C260300 Subcommittee on Neutron Absorber Materials, Washington, DC, June 24, 2008. Washington, DC: U.S. Nuclear Regulatory Commission. 2008. ADAMS Accession No. ML081760149.

Powers, D.A. and B. Gray. "Characterization of the Thermal Dehydration of Zirconium Oxide Halide Octahydrate." *Inorganic Chemistry*, Vol. 12, No. 11. pp. 2,721–2,726. 1973.

Radulescu, G. "Radiation Transport Evaluations for Repository Science." ORNL/LTR–2011/294. Oak Ridge, TN: Oak Ridge National Laboratory. 2011.

Steinbrück, M. "Hydrogen Absorption by Zirconium Alloys at High Temperatures." *Journal of Nuclear Materials*. Vol. 334. pp. 58–64. 2004.

Taylor, P., D.D. Wood, and D.G. Owen. "Microstructures of Corrosion Films on UO_2 Fuel Oxidized in Air-Steam Mixtures at 225 °C." *Journal of Nuclear Materials*. Vol. 223. pp. 316–320. 1995.

Van Swam, L.F., G.M. Bain, W.C. Dey, D.D. Davis, and H. Heckermann. "BWR and PWR Fuel Performance at High Burnup." *Proceedings of the 1997 International Topical Meeting on LWR Performance, Portland, OR, March 2–6, 1997*. La Grange Park, IL: American Nuclear Society. pp. 3–10. 1997.

Wasywich, K.M., W.H. Hocking, D.W. Shoesmith, and P. Taylor. "Differences in Oxidation Behavior of Used CANDU Fuel during Prolonged Storage in Moisture-Saturated Air and Dry Air at 150 °C." *Nuclear Technology*. Vol. 104. pp. 309–329. 1993.

Zlochower, I.A. and G.M. Green. "The Limiting Oxygen Concentration and Flammability Limits of Gases and Gas Mixtures." *Journal of Loss Prevention in the Process Industries*. Vol. 22, No. 4. pp. 499–505. 2009.

APPENDIX A

SCOPING EVALUATION OF TECHNICAL ISSUES

CONTENTS

Figures

Tables

A1. SPENT NUCLEAR FUEL AND CLADDING TEMPERATURES IN THE CANISTER DURING EXTENDED STORAGE

The spent nuclear fuel (SNF) and cladding temperatures in the storage cask[2] are expected to influence the consumption of the residual water and any oxidants that could be produced from radiolysis of the residual water. Therefore, it is necessary to estimate the time-dependent SNF and cladding temperatures in the canister environment. This section explains the development of the methodology used to estimate the SNF and cladding temperatures. The section also describes a model to estimate the relative humidity (RH) of the canister environment.

A1.1 Spatial Temperature Distribution of Spent Nuclear Fuel Storage Systems—Spatial Profiles during Extended Storage

Heat transfer in the storage cask is a complex process because of the storage cask geometry and the multiple modes of heat transfer involved. The specifics of the heat transfer mechanisms depend on a number of factors, including the cask's configuration and material properties. Presently, two primary dry storage cask configurations are used to store SNF. In the first configuration, SNF assemblies are placed within a basket that is directly loaded into a metal cask. There is no gap between the cask surface and the basket assembly, and the cask is closed and sealed using a bolted lid. In this configuration , the principal mode of heat transfer is through convection at the outermost surface of the cask. In the second configuration, the SNF assemblies are placed in a basket within a canister that is sealed using a welded lid. The canisterized SNF is subsequently put in an overpack, with an annular gap between the outer periphery of the canister and inner periphery of the overpack for air circulation. In this configuration, the primary mechanism of heat transfer from the canister is through the natural convection of airflow through the gap, where cooler air enters the air passage near the bottom of the gap and flows vertically upwards as it absorbs decay heat and the low density hot air exits the system near the top of the cask. For the present analysis, the thermal analysis performed for the second type of configuration (with annular gap and ventilation) has been used for subsequent calculations.

A1.1.1 Literature Information

McKinnon and DeLoach (1993) performed a detailed experimental study to understand the thermal behavior of seven different combinations of cask designs and SNF characteristics, including the following:

(1) Ridihalgh, Eggers & Associates REA 2023 cask with a 7 × 7 boiling-water reactor (BWR) SNF assembly

(2) Gesellschaft fur Nuklear Service CASTOR-V/21 cask with a 15 × 15 pressurized-water reactor (PWR) SNF assembly

[2] Several different designs of dry cask storage systems are in use. In some systems, the spent fuel is confined within a welded canister stored within a separate concrete shielding structure. In other designs, the confinenment and shielding components are integrated into a single structure with a bolted sealed lid. In this report, the term "canister" is used in a generic sense to refer to the component or system that provides confinement for the spent fuel.

(3) Transnuclear, Inc. TN-24P cask with a general 15 × 15 PWR SNF assembly

(4) Transnuclear, Inc. TN-24P cask with a consolidated 15 × 15 PWR SNF assembly

(5) Westinghouse MC–10 cask with a 15 × 15 PWR SNF assembly

(6) NUTECH horizontal modular storage system with a general 15 × 15 PWR SNF assembly

(7) Sierra Nuclear Corporation ventilated vertical concrete storage cask (VSC-17) with a consolidated 15 × 15 PWR SNF assembly

The experimental study was conducted for three canister backfill scenarios with nitrogen and helium as backfill gas and a near-vacuum condition. The experimental data obtained from the study showed spatial temperature variation along different cask components (e.g., the SNF assemblies, outer surface, and the SNF basket). In addition to the experimental study, two thermal hydraulic codes, COBRA-SFS (Lombardo et al., 1986) and HYDRA (McCann and Lowery, 1987), were used to calculate the spatial temperature distribution. A subsequent cask demonstration project, performed at Idaho National Laboratory and Argonne National Laboratory, used the experimental study as its foundation. A series of reports (McKinnon, 1995; McKinnon and Doherty, 1997; Bare and Torgerson, 2001; EPRI, 2002) describes subsequent study and progress related to the cask demonstration project.

Detailed experimental and numerical studies of SNF storage systems have been carried out to explore the physics and mechanism of heat dissipation characteristics of such systems. In general, most studies have indicated that SNF heat generation rate, thermal boundary condition, canister backfill media, and cask orientation with respect to gravity (which dictates natural convection patterns) are the major contributing factors in determining the heat transfer and the spatial temperature distribution pattern of an SNF storage system. Investigations by Arya and Keyhani (1990) and Cannan and Klein (1998) mainly focused on the natural convection pattern within the SNF assemblies. A recent investigation by Heng et al. (2002) found that the dominant heat transfer mode changes from conduction to convection with an increase in the Rayleigh number. That study also indicated that, within the limit of the turbulent Rayleigh number, convective heat transfer is so strong that the temperature change mainly occurs near the wall of the cask, and the natural convection plays a more important role on a local scale than on of a global scale. Araya and Greiner (2007) conducted a two-dimensional simulation of a BWR SNF assembly within a nitrogen- and helium-filled enclosure to understand the effect of internal convection pattern on overall heat transfer. The study concluded that the effect of natural convection is significant only at lower basket temperatures with nitrogen backfill, whereas for helium backfill, natural convection has a negligible impact on the overall heat transfer rate.

Wataru et al. (2008) performed heat transfer analyses of reinforced concrete storage casks and concrete-filled steel casks using the FIT-3D® thermal hydraulics code and the commercial solver PHOENICS®. Comparison of their computed results with the experimental data of Takeda et al. (2008) indicates that a hybrid computational fluid dynamics (CFD) and thermal-hydraulic analysis will provide a reasonable temperature estimate. Lee et al. (2009) performed a detailed experimental and computational analysis of a vertical storage system that was composed of a stainless steel canister with a concrete overpack under both normal and off-normal conditions. The off-normal condition was simulated by blocking the storage system coolant air vent. Lee et al. (2009) demonstrated that the storage cask cooling capacity was adequate for safe operation under both normal and off-normal conditions.

In this report, the Sierra Nuclear Corporation's VSC-17 is used to gain an understanding of the spatial temperature distribution in the SNF assembly and other cask components. Section A1.1.2 of this appendix describes the cask. McKinnon et al. (1992) measured temperatures along different cask components to provide a partial understanding of spatial temperature distributions within the cask. The VSC-17 cask was selected because detailed surface temperature distribution for the different cask components is available from previous studies (see Zigh and Solis (2008); Das et al. (2008)). A detailed surface temperature distribution is necessary to calculate the localized condensation condition and the relative extent of the wet surfaces. This study adopted the computational model developed by Zigh and Solis (2008) and later used by Das et al. (2008). The computed surface temperature distributions on the SNF assembly were used as the starting point of the condensation analysis.

A1.1.2 Description of the Storage System

VSC-17 is a canisterized SNF storage system that uses buoyancy-driven natural convection as the primary mechanism to dissipate decay heat. It has the capacity to store 17 assemblies of consolidated SNF. The VSC-17 system consists of two major components: a multiassembly sealed basket (MSB) and a ventilated concrete cask (VCC). The MSB has a cylindrical steel vessel that holds an arrangement of guide sleeves. The consolidated SNF assemblies are placed within these guide sleeves. The open MSB cavity is backfilled with either nitrogen or helium gas to create an inert atmosphere. A composite shield lid seals the MSB contents. The sealed MSB is placed within the VCC overpack, with an annular gap between the outer surface of the MSB and inner surface of the VCC. Inlet and outlet openings for this gap are provided through the VCC structure. Ambient coolant air enters the system through an inlet at the bottom, flows vertically upwards as it absorbs thermal energy from the MSB outer surface, and exhausts at the top. The VCC is a concrete shell with an inner steel liner and a weather cover. Figure A1–1 highlights the major components of the VSC-17 storage system. McKinnon et al. (1992) and McKinnon and DeLoach (1993) evaluated detailed configuration geometry and the system description.

A1.1.3 Computational Thermal Analysis of the Vertical Concrete Storage Cask-17 System

Das et al. (2008) and Das et al. (2010) conducted a detailed computational analysis of the VSC-17 cask system, which is used in this report to understand the pattern of spatial temperature distribution of the SNF and cladding. The previous study (Das et al., 2008) was based on the computational framework that Zigh and Solis (2008) developed for analyzing the VSC-17 cask. The following section briefly discusses the computational techniques and results.

A1.1.3.1 Model Development

This report uses the commercial CFD package FLUENT® Version 6.3 (Fluent, Inc., 2007a). A solution was obtained for the steady-state incompressible Navier-Stokes equations. The pressure-based solver of FLUENT® was used in conjunction with a Green-Gauss, cell-based gradient option. An implicit time-marching scheme was used for faster convergence. The SIMPLE algorithm was used to obtain pressure velocity coupling.

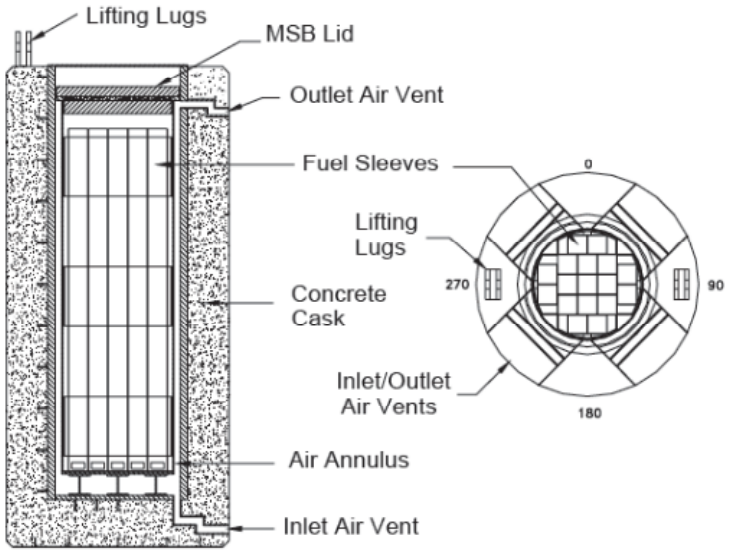

Figure A1-1 Components of the Sierra Nuclear Corporation's ventilated vertical concrete storage cask-17 dry storage system (McKinnon and DeLoach, 1993)

Details of the governing equations and numerics can be found in the FLUENT® Theory Guide and User's Manual (Fluent, Inc., 2007a, b).

A single quadrant of the whole circular cross-section of the cask was considered as the computational domain because the heat load distribution is almost the same in each quadrant. A symmetry boundary condition was assumed on the quadrant edges Figures A1-2 and A1-3 provide a schematic of the domain and distribution of the cross-sectional grid in the quadrant, respectively. The computational domain did not include the surrounding ambient environment. The computational grid consisted of 1,038,794 cells and 1,166,560 nodes.

Radiation heat transfer was modeled using the discrete ordinate method. The calculated Reynolds number for the flow was in the transitional range, and a number of turbulence models were studied, including the standard k-ω model, the renormalization group k-ε model, the shear stress transport k-ω model, and the realizable k-ε model. The results presented in the report were generated using the realizable k-ε turbulence model; these results had the best agreement with the experimental data. The realizable k-ε model considers all the pertinent physics involved in these flows, and the model is widely accepted as the best turbulence model for complex turbulent flow and heat transfer simulations. Convection within the tightly packed consolidated SNF assemblies was neglected. This region was modeled as a homogeneous solid with uniform heat generation. A customized, temperature-dependent, orthotropic, effective thermal conductivity for this region was derived using an auxiliary two-dimensional simulation of an individual SNF assembly. The effective thermal conductivity is used to represent the entire heat transfer by radiation and conduction within this region (Bahney and Lotz, 1996). The decay heat value for every SNF assembly that was obtained from experimental observation was applied as a uniform volumetric heat generation rate throughout the homogeneous region; it was modified only to include an axial power profile based on the measured axial power distribution. Customized user-defined functions were used to incorporate the source terms within the CFD solver.

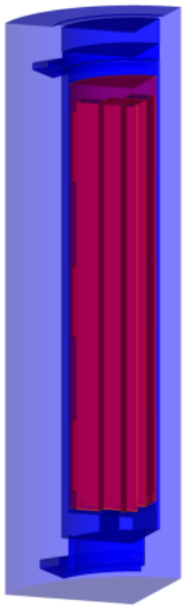

Figure A1-2 Sectional view of the Sierra Nuclear Corporation's ventilated vertical concrete storage cask-17 dry storage system used in computation

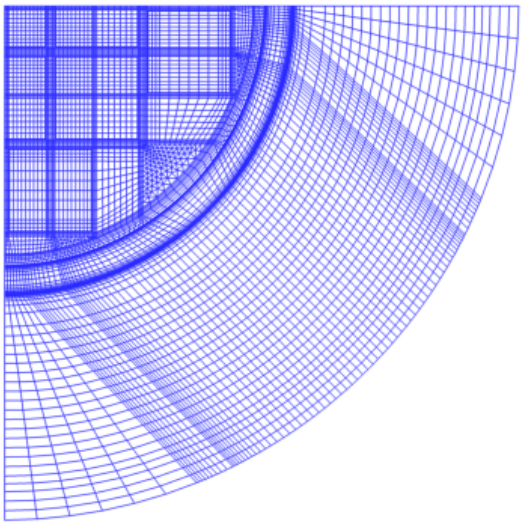

Figure A1-3 Cross-sectional grid of the domain

A1.1.3.2 Model Results

Though the numerical study was conducted for a number of test cases, this section presents only selected results to highlight the pattern of temperature distribution within the cask. Specifically, this section presents results from simulations based on input conditions corresponding to Test 1 of the experimental study (McKinnon et al., 1992). Under this test condition, the MSB cavity was filled with helium at below atmospheric pressure. No blockages of the inlet or exit air vents were assumed. The computational domain did not include the surrounding atmospheric air, and a pressure boundary condition was assumed at the inlet vent. The ambient temperature was 296 Kelvin (K) (75.13 degrees Fahrenheit (°F)), and the pressure was 101.33 kilopascals (KPa) (14.7 pounds per square inch (psi)).

Figures A1-4(a) and (b) show the temperature contours on different VSC-17 components. It is clear that the SNF basket assembly has a considerably higher temperature than other components. The peak temperature region within the domain is located approximately near the center of the basket assembly. In the present study, individual SNF rods and claddings were not modeled explicitly. Instead, the SNF assembly was treated as a homogeneous solid with a uniform heat generation rate and an effective thermal conductivity representing the total heat transfer. Hence, the peak temperature within the basket assembly volume is an approximate estimate of cladding surface temperature. The location of the calculated high temperature region is consistent with the experimental observations of McKinnon et al. (1992).

Figure A1-5 shows the temperature contours for the outside concrete surface and the coolant air flowing through the annular gap between the steel MSB liner and VCC. Compared to the temperature of the basket assembly, as shown in Figures A1-4 (a) and (b), the VCC and the air temperatures are substantially lower. It can also be observed that the coolant air temperature increases as it flows vertically upwards from inlet to outlet. The temperature of the outer concrete shell also changes with increased vertical distance above the VCC inner floor.

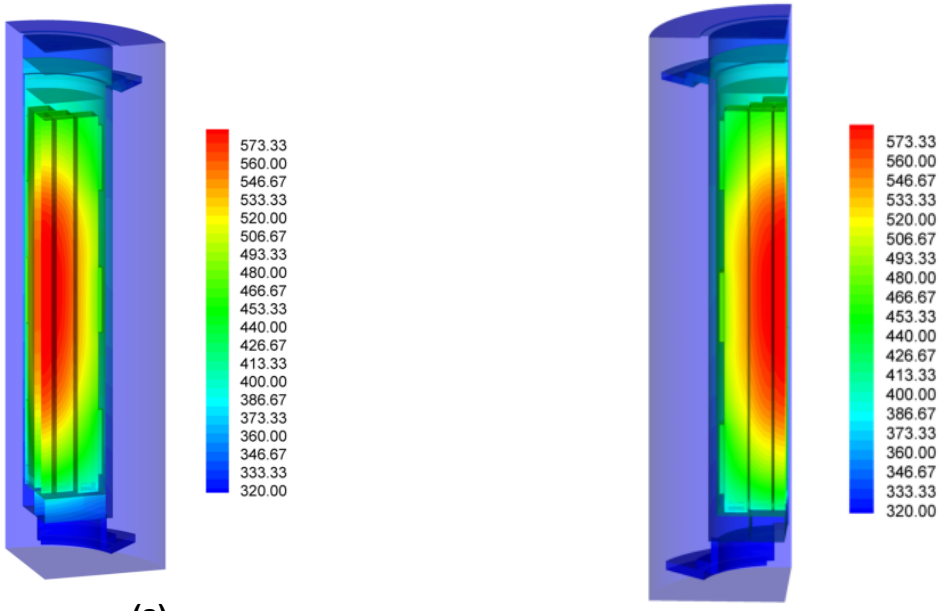

(a) (b)

Figure A1-4 Temperature contours in the Sierra Nuclear Corporation's ventilated vertical concrete storage cask-17 components. The temperature scale are in Kelvin (°F = 1.8 × K − 459.4).

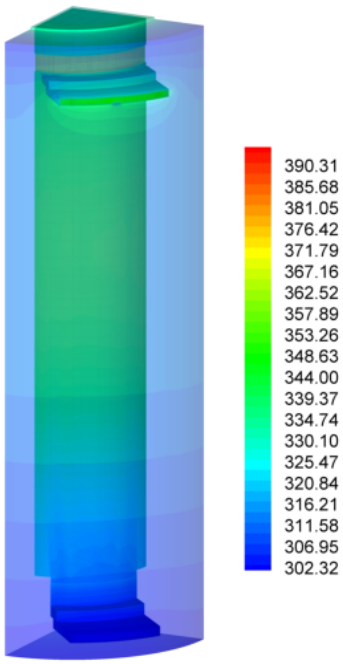

Figure A1-5 Temperature contours in the air passage and concrete shell. The temperature scale is in Kelvin. (°F = 1.8 × K − 459.4).

In the experimental setup (McKinnon et al., 1992), lances with multiple thermocouples were placed at seven different locations along the SNF assembly canisters (identified by the lance number). Temperature results along SNF assembly baskets from McKinnon et al. (1992) are reproduced in Figure A1-6 and presented alongside the computed data. At every lance location, the temperature was observed to first increase to a maximum and then decrease with increasing vertical elevation. It can be observed that the peak temperature is slightly overpredicted for all three locations by about 1 to 2 percent; however, the predicted temperature distribution shows qualitative agreement with the experimental data and follows the same pattern and trend.

Figure A1-7 highlights the computed axial temperature distribution and experimental data along the steel liner and MPC wall. Like the results computed for SNF assemblies, the results for the steel liner and MSB overpredict temperature by 5 percent even though the predicted temperature qualitatively agreed with the experimental observations. In general, such deviations between computed and experimental data are attributed to both modeling and parametric uncertainty of the numerical model, as well as to experimental uncertainties. Modeling uncertainties include geometric approximations made to construct the domain and geometry and parametric uncertainties related to material selection and specification of material properties.

A1.1.3.3 Development of Temperature Zones

One focus of the present study is to determine the extent of SNF and cladding oxidation during the extended storage period. To this end, temperature evolution of cladding, temperature gradient, and RH in the MSB cavity is needed.

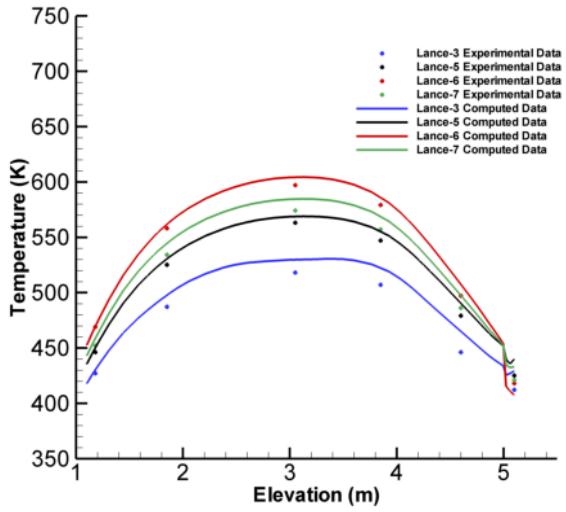

Figure A1-6 Axial temperature distribution along the SNF assembly baskets (°F = 1.8 × K − 459.4)

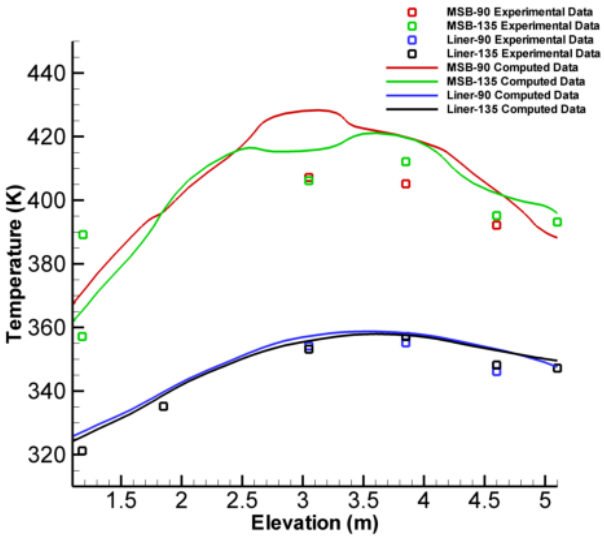

Figure A1-7 Axial temperature distribution along the steel liner and the multiassembly sealed basket (°F = 1.8 × K − 459.4)

Ideally, a series of quasi-steady numerical simulations with time-varying thermal loading that reflects the decay heat characteristics during the storage period would provide evolving spatial temperature distribution. Such an exercise is computationally expensive and outside the scope of this report. As an approximation, information presented in the previous section was used as the initial estimate of the spatially dependent SNF and cladding temperatures within the VSC-17. This information is coupled with an analytical expression from another study (EPRI, 2002) to estimate time-dependent temperature variations. The main component of interest, the SNF basket, is divided into five subvolumes; mean temperatures of the subvolumes are used. The computed temperature range in the five SNF basket assembly subvolumes is divided into five equal intervals. Sections of the SNF basket assembly volume that have computed temperatures within the same interval are considered to be part of a same single subvolume. The mean temperature of each range is used as the representative value for that subvolume and for subsequent calculation of time-temperature variations. Each subvolume with constant mean temperature is referred to as a zone, and a number is designated for identification.

The maximum and minimum temperatures within the SNF basket assembly for the VSC-17 cask under test condition one (McKinnon et al., 1992) are 598 and 366 K (616 °F and 199 °F), respectively. Figure A1-8 shows the temperature distribution in the basket assembly.

Figure A1-9 shows the five temperature zones developed for this analysis, as viewed from two different angles. Each color band is denoted as a temperature zone. The lowest temperature zone is at the bottom, and the highest temperature zone is located near the center of the SNF basket. The zonal temperature distributions based on the CFD calculation are treated as the lower initial temperature limit.

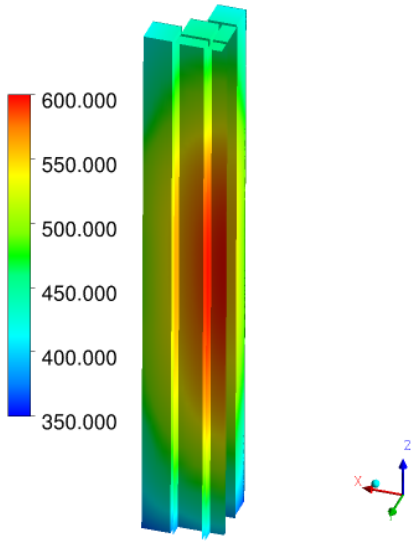

Figure A1-8 Temperature distribution in the SNF basket assembly. The temperature scales is in Kelvin. (°F = 1.8 × K − 459.4).

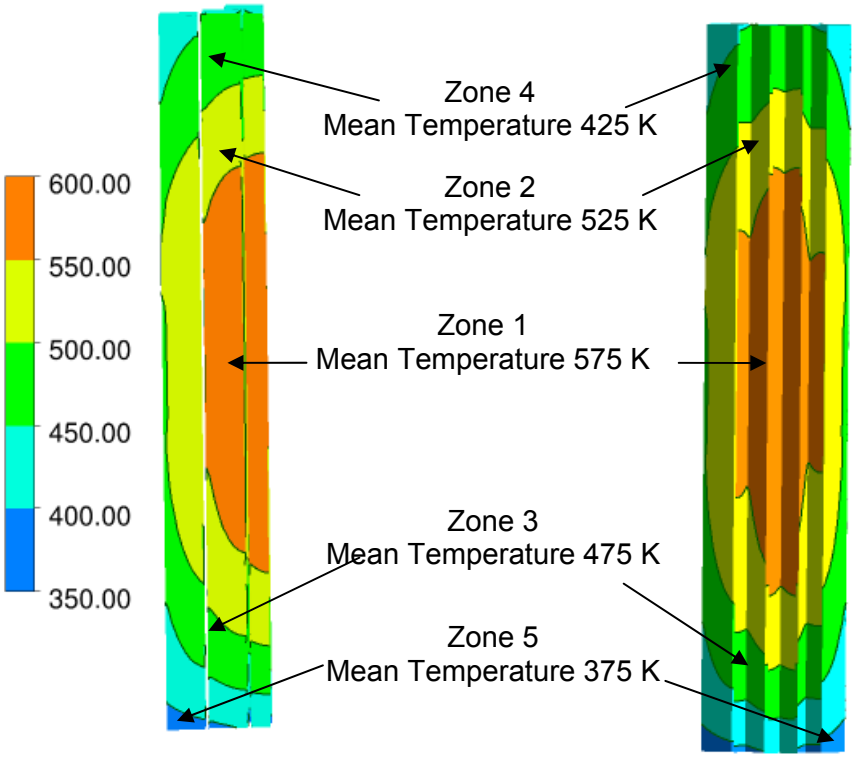

Figure A1-9 Location of the five temperature zones in the SNF basket assembly. The temperature scale is in Kelvin. (°F = 1.8 × K − 459.4).

The heat transfer computations were done for a constant heat load of SNF assemblies. It is recognized that changing the SNF heat load will change the mean temperatures. The maximum temperature of the hottest zone, however, should not exceed the allowable SNF cladding temperature of 673 K (751.7 °F), in accordance with Title 10 of the *Code of Federal Regulations* (10 CFR) Part 72, "Licensing Requirements for the Independent Storage of Spent Nuclear Fuel, High-Level Radioactive Waste, and Reactor-Related Greater Than Class C Waste." A high end of initial temperature distribution for every zone was developed by increasing the highest temperature of the hottest central zone to the maximum allowable limit and then adjusting the temperature of the other zones accordingly. This information was used to parametrically study the effect of temperature during extended storage on SNF and cladding oxidation. Note, however, that the volume fraction of each temperature zones was not changed.

Table A1-1 lists the mean temperature of each zone and its volume fraction.

A1.2 Time-Dependent Temperature Profile

This section describes the methodology used to estimate the evolution of SNF and cladding temperatures in the five zones. The time-dependent temperature is estimated using the correlations that were obtained from experimental data and known SNF characteristics (EPRI, 2002). Section A1.2.1 briefly discusses these correlations and the basis for their use. Section A1.2.2 discusses the assumptions associated with this study.

A1.2.1 Expression for Estimating Time-Dependent Temperature

Two bounding estimates of temperature evolutions were proposed as a part of the dry storage characterization project (EPRI, 2002). The CASTOR-V/21(Gesellschaft fur Nuklear Service) cask with a 15 × 15 PWR SNF assembly was used for dry storage characterization. McKinnon et al. (1992) and EPRI (2002) describe this cask. The CASTOR-V/21cask is a direct-loaded storage system. The main components of this cask include a ductile cast iron canister body, a stainless steel SNF basket assembly, and stainless steel primary and secondary lids. The cask body is a cylindrical structure, 4.9 meters (m) (16 feet (ft)) tall and 2.4 m (8 ft) in diameter, which has 73 heat transfer fins placed circumferentially around the cask. To provide neutron shielding, polyethylene moderator rods are placed within the cask, but outside the canister wall body, in two concentric rows distributed around the cask perimeter. Two lifting trunnions are bolted at each end of the cask body. The SNF basket assembly is made of stainless steel plates and a borated stainless steel plate with a boron content of approximately 1 percent for criticality control. The basket can hold 21 SNF assemblies. Figures A1-10 and A1-11, respectively, show a cross-sectional view of the cask and the basket assembly. The stainless steel primary lid was sealed using metallic O-rings and 44 bolts. A number of penetrations were made on the primary lid for inserting probes and other devices necessary for the experiment. The stainless steel secondary lid, which is part of the CASTOR V/21 cask, was not used during the experiment because it was necessary to regularly access the probes and other devices inserted into the system.

In the experiment conducted for the dry storage characterization project, the CASTOR V/21 cask was loaded to its full SNF holding capacity of 21 SNF assemblies. Each assembly contained Westinghouse 15 × 15 PWR SNF discharged from the Surry-1 facility of Virginia Power (presently Dominion Power). Stored SNF burnup ranged from 24 to 35 gigawatt days per metric ton of uranium (GWd/MTU), and the out-of-reactor cooling period ranged from 2.2 to 3.8 years. The per-assembly heat load varied between 1 to 1.8 kilowatts (kW) (1 to 1.71 British thermal units per second (BTU/s)), and the total heat load of the cask was 28.4 kW (26.9 BTU/s).

Table A1-1 Mean Temperatures and Percentage of Volume of Five Temperature Zones			
Zone Number	**Mean Values of Low End SNF and Cladding Initial Temperature K (°C) (°F)**	**Mean Values of High End SNF and Cladding Initial Temperature K (°C) (°F)**	**Percentage of Total Volume of SNF Basket**
1	575 (301.9) (575.3)	673 (400.0) (751.7)	18.95
2	525 (251.9) (485.3)	623 (350.0) (661.7)	33.00
3	475 (201.9) (395.3)	573 (300.0) (571.7)	33.72
4	425 (151.9) (305.3)	523 (250.0) (481.7)	12.38
5	375 (101.8) (215.3)	481 (208.0) (406.1)	1.95

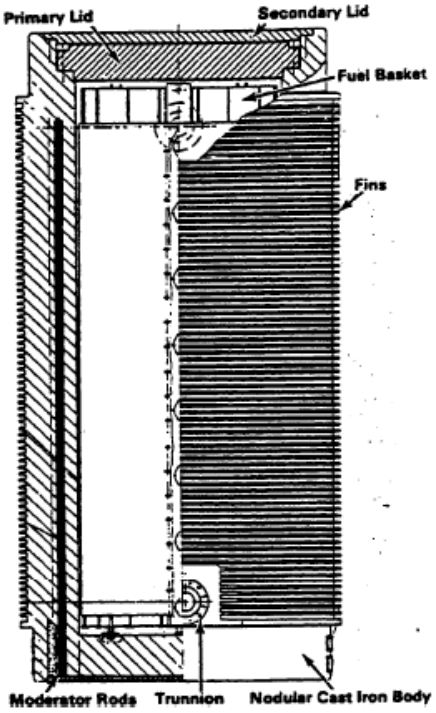

Figure A1-10 Sectional view of the CASTOR V/21 cask (EPRI, 2002)

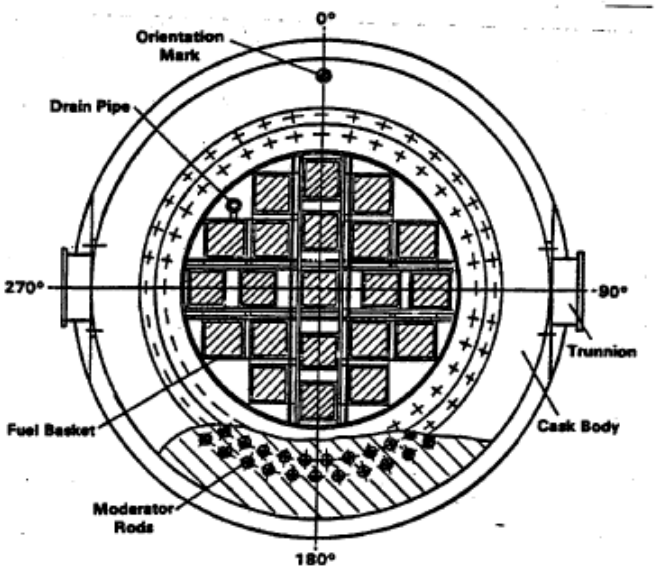

Figure A1-11 Sectional view of the basket assembly of the CASTOR V/21 cask (EPRI, 2002)

McKinnon et al. (1992) recorded detailed spatial temperature measurements along the SNF assembly basket for the CASTOR V/21 cask before the characterization study. These measurements were recorded using thermocouples inserted through the penetrations in the primary lid. At the end of the 14.2-year characterization study, another set of temperature measurements was recorded. The measurements were, however, not recorded at the same locations as those made in the initial study and were made with the primary lid open.

EPRI (2002) developed two different methods for modeling the temperature profile based on the recorded temperatures and SNF characteristics. The first method assumed three temperature points. The initial temperature at time = 0.0 years was fixed at 617 K (651 °F); the temperature

at the end of the cask characterization study at time = 14.8 years was fixed at 428 K (311 °F); and it was assumed that at time = 100 years, the entire system will be at an atmospheric temperature of 311 K (100 °F). The following equation was obtained using these temperature points:

$$T(t) = 308\exp(-0.064\,\mathrm{t}) + 309 \quad \text{(A1-1)}$$

where T is the temperature in Kelvin, and t is the time in years.

Because the primary lid was open during temperature measurement at the end of the characterization study (i.e., after 14.8 years), it was expected that the recorded temperature would be lower than the actual temperature within the closed cask. Hence, the correlation based on this temperature is used as the low end of temperature distribution.

The second method was based on the assumption that temperature is first proportional to the exponentially decreasing decay heat and is subsequently dominated by the ambient temperature at later times. As indicated in EPRI (2002), cesium (Cs)-137 and strontium (Sr)-90 are the main contributors to decay heat. For the model expression, the half-life of Cs-137 was used as the reference decay heat load because both Cs-137 and Sr-90 have similar half-lives. The initial temperature was fixed at 617 K (650.93 °F). The following equation represents the analytical expression of temperature profile obtained using this method:

$$T(t) = 308\exp(-0.023\,\mathrm{t}) + 309 \quad \text{(A1-2)}$$

Because the half-life of Cs-137 is longer than that for Sr-90 and was used in deriving Equation A1–2, the amount of heat retained in the system will be overestimated. In turn, Equation A1–2 is expected to bound the actual temperature conditions that were present for the EPRI study. The present assessment uses Equation A1–2 at the high end of the temperature distribution.

A1.2.2 Assumptions and Modified Equations

Equations A1–1 and A1–2 were derived based on experimental data for the CASTOR V/21 cask. A number of assumptions and approximations were made to adopt the equations for the VSC-17 cask, which the present study uses. These assumptions include the following:

- The temperature distribution within any cask largely depends on the SNF characteristics and the SNF decay heat. As both the CASTOR V/21 and VSC-17 casks use 15 × 15 Westinghouse PWR SNF assemblies, it is assumed that the time-dependent temperatures between the two casks are analogous. Hence, it is assumed that the temperatures of VSC-17 cask components also exhibit the exponential decay, as highlighted in Equations A1-1 and A1-2. This implies that the exponential term in Equations A1-1 and A1-2 is adopted to model the time-dependent temperature profile in each zone of VSC-17.

- For calculating low end temperatures, it is assumed that, after 100 years of storage, the temperature within the cask will reach the near-ambient thermal condition (309 K (96.53 °F)). Hence, the final low end temperatures after 100 years are the same for both the VSC-17 and CASTOR V/21 casks. The estimated upper temperature bound follows the SNF decay curve of the SNF and is based on the same assumptions used to derive Equation A1-2.

- The initial temperature used to derive Equations A1-1 and A1-2 is fixed at 617 K (650 °F). This is not the case for the present analysis, where different temperature zones in the VSC-17 SNF assembly will have different initial temperatures. Hence, Equations A1-1 and A1-2 are modified to accommodate the difference in initial temperatures. Equations are adjusted so that the initial temperature difference decreases exponentially with time. Furthermore, it is assumed that the decay in this temperature difference is similar to the decay in temperature (i.e., the same exponential decay constants are used for calculating the decay in temperature difference).

Equation A1-3 represents the adopted model for the time-dependent temperature as follows:

$$T(t) = (T_{mean} - 309)\exp(-at) + 309 \quad \text{(A1-3)}$$

where T_{mean} is the mean temperature (K) of a temperature zone, and a is a thermal decay constant. The value of the decay constant (a) is either 0.023 or 0.064. Equation A1-3 is used in the integration model in Section A4. Equation A1-3 uses the temperature values listed in Table A1-1 as T_{mean} to calculate SNF and cladding temperatures in a zone as a function of time. This provides both temporal and spatial variation of SNF and cladding temperatures in the canister.

A1.2.3 Time-Dependent Temperature Profile

Figure A1–12(a) shows the temperature for the five zones listed in Table A1-1. The temperature profiles have been calculated using the decay constant equal to 0.064 in Equation A1-3 and the mean values of the low end SNF and cladding initial temperatures listed in Table A1–1. As can be seen in the figure, the temperatures decrease exponentially with time and reach the ambient temperature of 311 K (100 °F) after 100 years. It can also be observed that the temporal gradient of temperature increases with increased initial temperature. As a result, the Zone 1 temperature distribution curve is steeper for the first 100 years as compared to Zone 5. This is because Equation A1-3 was developed with an approximation that a fixed temperature at the end of 100 years will be attained by all of the components. During inservice storage, it is likely that various canister components will reach the ambient condition at a different point in time, with the hottest region attaining the ambient temperature at the end. Hence, the slopes of the temperature curves will likely be more uniform. Figures A1-12(a) and (b) show the temperature distribution for different zones using Equation A1-3 and the decay constant values of 0.064 and 0.023, respectively. Figures A1-13(a) and (b) show temperature distributions of different zones for the high end SNF and cladding initial temperatures using the decay constants at 0.064 and 0.023, respectively. As can be seen, the trend of temperature variations is similar to that in Figure A1-12.

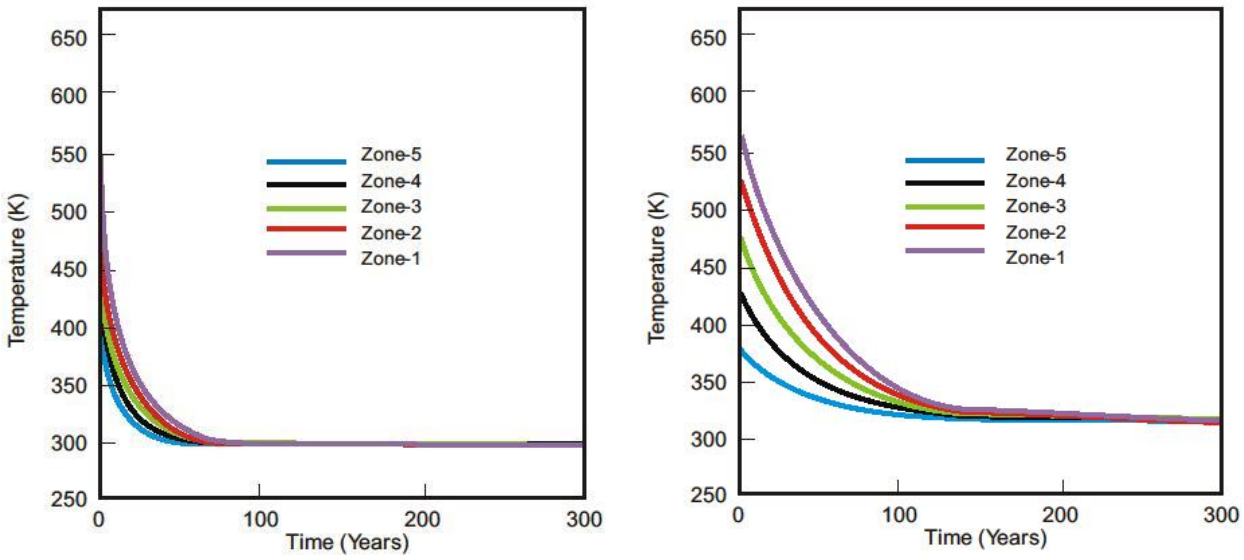

Figure A1-12 SNF and cladding in the five zones calculated using Equation A1-3. Mean values of low-end SNF and cladding initial temperatures in Table A1-1 are used to calculate these temperature profiles. The value of the decay constant is (a) 0.064 and (b) 0.023. (°F = 1.8 × K − 459.4)

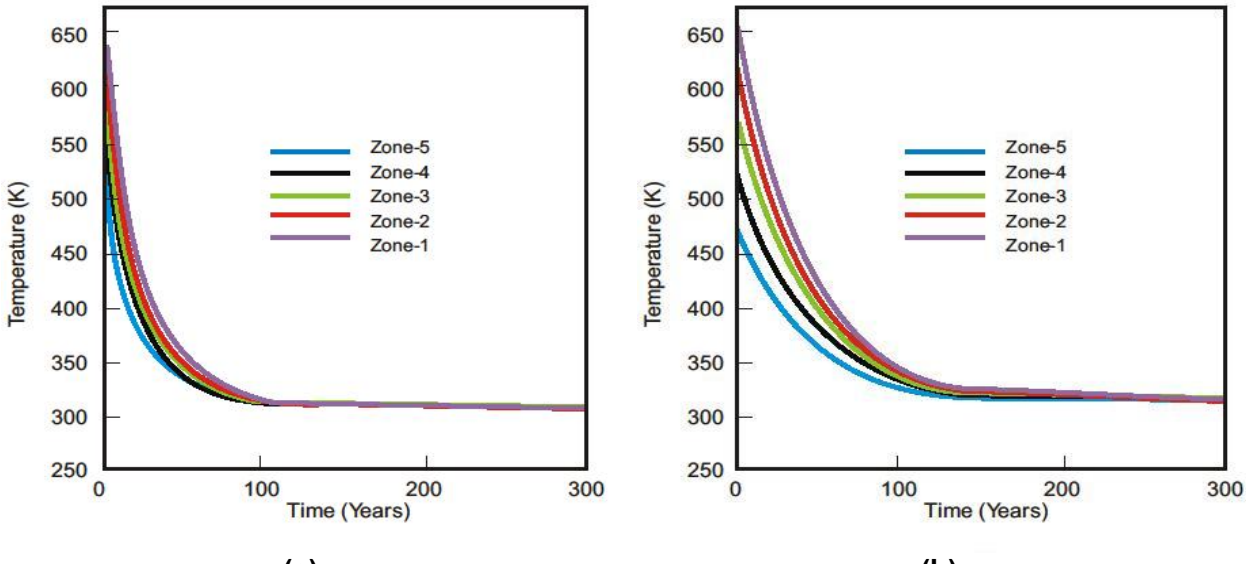

Figure A1-13 SNF and cladding in the five zones calculated using Equation A1-3. Mean values of high-end SNF and cladding initial temperatures in Table A1-1 are used to calculate these temperature profiles. The value of the decay constant is (a) 0.064 and (b) 0.023. (°F = 1.8 × K − 459.4)

A1.3 Relative Humidity

As a result of imperfect and incomplete drying, some residual water may remain within the canister. At relatively high temperatures, this residual water will remain in the vapor state. As the temperature starts to decrease, RH within the canister starts to increase. If the temperature of any surface within the container drops below the saturation temperature, the local RH will be at 100 percent and water will condense into the liquid phase.

This study investigates the evolution of RH and potential condensation within the sealed canister of the VSC-17 system. The study did not consider detailed movement of water vapor within the canister cavity and localized condensation on any internal surface. Instead, an analytical approach was developed to estimate the local RH and condensation rate using the mean temperatures for the five zones listed in Table A1-1.

A1.3.1 Assumptions

The study used the following assumptions to estimate the RH in a zone:

- The internal open volume of the canister cavity is fixed at 2.1 cubic meters (m^3) (74 cubic feet (ft^3)). The total volume occupied by other significant components, such as the SNF assembly basket, was deducted from the total cavity volume. This value is approximate because the volume calculation did not consider some of the smaller components, such as steel support beams.

- A lumped parameter approach is adopted for analytical formulation, and spatial distribution of temperature within the volume is not considered.

- The fluid inside the canister was assumed to be a binary mixture of the backfill gas and water vapor. It was assumed that any noncondensable component of the backfill gas, if present, does not affect condensation.

- An equilibrium condition was assumed within the system. This means that when the enclosed volume reached RH of 100 percent, any water that would have caused supersaturation of the fluid will completely condense to form liquid water.

- The analysis has been done for the five zones in isolation. This means that the mean temperature profile of each zone is used to calculate the RH in that zone, and no vapor transport occurs between any zones.

- Pressure of the gas phase does not change after condensation. Initial analysis indicated that most of the residual water is expected to undergo radiolysis. Moreover, water would condense when radiolysis is slow and temperature is low enough. The results indicate that condensation would occur only for a limited set of conditions, and only a small fraction of the residual water would condense.

- The gas temperature is assumed to be unaffected by condensation even though heat transfer would occur during condensation.

A1.3.2 Relative Humidity Model and Condensation

Relative humidity is calculated using Equation A1-4:

$$RH = 100 \times \frac{P_{vp}(T)}{P_{vp,sat}(T)} \quad \text{(A1-4)}$$

where RH is the relative humidity in percent, $P_{vp}(T)$ is the partial pressure of water vapor at the temperature T, and $P_{vp,sat}(T)$ is the saturation vapor pressure of water vapor at the temperature, T.

Equation A1-5 (Keenan et al., 1969) is used to obtain the saturation vapor pressure as a function of temperature:

$$P_{vp,sat}(T) = 217.99 \times e^{\left[\frac{0.01}{T}(647.3-T)\sum_{k=0}^{7} F_k (3.38-0.01T)^k\right]} \quad \text{(A1-5)}$$

where

F_0 = −741.9242
F_1 = −29.721
F_2 = −11.55286
F_3 = −0.8685635
F_4 = 0.1094098
F_5 = 0.439993
F_6 = 0.2520658
F_7 = 0.05218684
$P_{vp,sat}$ = water vapor saturation pressure in atmosphere (atm) (1 atm = 14.7 psi)
T = the temperature in Kelvin (K)

Equation A1-5 applies to temperatures ranging from 273 to 647 K (32 to 705 °F). This relationship was primarily chosen because it is valid for the temperature range that is expected in a normally functioning cask over time. The primary interest is the temperature range when condensation is likely to happen, which is within the validity limit of the cask system. Figure A1-14 illustrates the variation of saturation vapor pressure with temperature.

At any point in time, the moles of condensate water were calculated using Equation A1-6:

$$n_{cond}(t) = n(t) - n_{sat}[T(t)] \quad \text{(A1-6)}$$

where $[T(t)]$ is the temperature at time t, $n_{cond}(t)$ is the moles of condensate water at time t, $n(t)$ is the moles of water vapor at that point in time t, and $n_{sat}[T(t)]$ is the moles of water vapor in the saturation condition at temperature $[T(t)]$.

Equation A1-7 can be used to calculate the number of moles of water vapor in the saturation condition at temperature, T:

$$n_{sat}[T(t)] = \frac{P_{vp,sat}[T(t)] \times V}{R[T(t)]} \quad \text{(A1-7)}$$

where V is the open cavity volume and R is the gas constant. Any excess water will have to be condensed to maintain equilibrium. Equations A1-6 and A1-7 will determine the water vapor

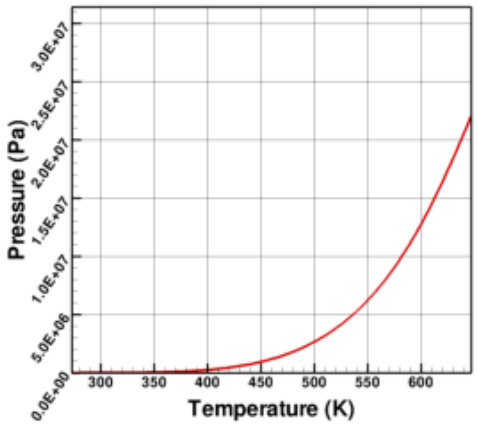

Figure A1-14 Variation of saturation vapor pressure with temperature (1 Pa = 1.45×10^{-4} psi; °F = 1.8 × K − 459.4)

remaining in the system. Once it reaches the saturation limit, the water vapor content will remain at the saturation value. Because the amount of water may be affected by radiolysis, the actual variation of RH and water remaining in the system will be discussed after addressing the radiolysis effect on residual water in Section A2.

A2. RADIOLYTIC DECOMPOSITION OF RESIDUAL WATER AND THE RELATIVE HUMIDITY PROFILE IN THE CANISTER

This section discusses radiolytic decomposition of residual water. In addition, a model for radiolytic decomposition of the residual water is proposed to support the scoping analyses. The discussion in Section A1.3 on RH is also extended.

A2.1 Radiolysis

A2.1.1 General Discussion of Radiolysis in the Canister and Assumptions for Radiolysis Model

Radiolysis of the residual water in the canister would lead to generation of various products (e.g., hydrogen and oxygen), which may affect pressurization, flammability limits, and degradation of internal components. The environment inside of a canister is subject to a number of dynamic factors, including radiation and temperatures, within a complicated geometry composed of several materials and components. Detailed modeling of these factors and radiolytic processes within a canister environment is complex and would require significant effort. The present assessment is scoping in nature, with an intent to develop a simplified, approximate model for radiolytic decomposition of residual water in a canister based on limited information and allowing for quantitative analysis over a range of conditions. To achieve this goal, researchers made a number of simplifying assumptions, discussed below, to make the problem tractable.

For the present discussion, the cask seal (e.g., canister welding) is assumed to be intact, the environment is inert, and additional atmospheric air and moisture are not introduced into the canister interior once it has been sealed and the drying process has been completed. Therefore, for the present case, species like nitric acid are assumed to be negligible because of the limited availability of nitrogen.

In the canister, it is expected that the residual water will be initially distributed in the form of vapor because of high temperatures from residual SNF assembly decay heat. At later times, the SNF assembly decay heat could reduce sufficiently for temperatures to reach low enough levels for condensation to occur, if residual water remains. In the present discussion, only radiolysis of the water in vapor phase is considered. The study examined the model for the cask temperature zones (presented in Section A1), and the amount of water that would be expected to condense (presented in Section A5.1) is much less in comparison to the vapor phase water. Furthermore, water condensation is expected to occur only in the coolest region (Zone 5) when relatively slow radiolytic decomposition of the residual water occurs and SNF and cladding temperatures are sufficiently low. Radiolysis of the liquid phase is not expected to have a large impact; however, ignoring this process in the present model is a recognized uncertainty. Detailed modeling would be required to assess how much liquid water would have a significant impact on system components and may require accounting for the difference in water mass balance, radiolysis yields (e.g., G-values for liquid water versus vapor), and strength of the radiation field for locations where liquid water is condensing.

A2.1.2 Parameters and Assumptions for Modeling Decomposition of Water

For the sake of the scoping nature of this work, simplified, approximate models for radiolytic decomposition of residual water in the canister environment were developed to estimate the

quantity of residual water decomposed as a function of time. It was assumed that the decomposition only results in production of hydrogen and oxygen. To develop the water decomposition models, G-values and the radiation field and dose rate were considered and uncertainties noted.

To estimate the rate of decomposition of water and production of radiolysis products, several factors need to be known. G-values are typically used to estimate the rate of production of chemical species or molecular decomposition as a result of ionizing radiation. For a given system, the measured G-values depend on a number of interdependent reactions between chemical species produced from radiolysis and reactions within the system's environment. For example, in a dry cask system, this could include interactions between water vapor, its decomposition products, and cask components (including exposed SNF and cladding). These values are determined experimentally and reported in units of molecules produced or decomposed per energy deposited from ionizing radiation. The values used in the present assessment were those selected in Arkhipov et al. (2007), including a G-value for the decomposition of water of G_{H2O} = 7.4 particles per 100 electronvolts (eV). The G-values selected in Arkhipov et al. (2007) were assumed to be independent of irradiation conditions in a wide range of conditions, including temperatures up to 900 Kelvin (K) (1,160 degrees Farenheit (°F)), pressure from 10^4 to 10^6 pascals (Pa), and absorbed dose rate up to 10^{12} grays per second (Gy/s) (10^{14} rad/s). The value selected for decomposition of water vapor from Arkhipov et al. (2007) is considered reasonable for the present assessment. The model does not consider detailed radiolysis kinetics and reactions that would take place in the canister environment. This is recognized as a model uncertainty and may need to be considered in future refined assessments.

An estimate for the expected rate of energy deposition was also needed for the canister internal environment. To assess rough values for radiation (and expected energy deposition) in the canister environment, values were selected based on those presented in Radulescu (2011) and from a comparison with dose rates reported in the U.S. Department of Energy's calculation for the 21 PWR uncanistered SNF (UCF) waste packages (BSC, 2001a) and Jenks (1972). Radulescu (2011) reported values of total dose rates for a representative cask model. The model for the representative cask was developed for a HI-STAR 100 cask with 32 PWR Westinghouse 17 × 17 optimized SNF assemblies that have a burnup of 60 GWd/MTU and a 5 weight-percent (wt%) initial uranium (U)-235 enrichment. The report also includes a map of the dose rate values for a cross-section through the center of the cask (Radulescu, 2011, Figure 2). The source term Radulescu (2011) used for this model includes neutron and gamma radiation, and the model calculations were made using MAVRIC (Peplow, 2011) for dose rate values. Based on this figure, it is clear that the range of dose rates in the canister volume can vary significantly depending on the location in the volume (e.g., proximity to SNF assemblies).

Two representative dose rates were selected based on the ranges of dose rates which cover the majority of the canister volume. The values selected from the figure were 1.18×10^2 and 1.69×10^3 grays per hour (Gy/h) (1.18×10^4 and 1.69×10^5 rad/h). To convert from dose rate in rad/h to units of electronvolt per gram per second (eV/g/s) for moist air, the relationship of 1 rad/h = 1.7338×10^{10} eV/g/s was used as a surrogate for the canister environment. This is assumed reasonable in the present work. As stated in Radulescu (2011), the conversion to energy deposition rate from the dose rates is assumed applicable to moist air of varying density because the flux-to-dose rate found in American National Standards Institute/American Nuclear Society (ANSI/ANS)-6.1.1-1991, "Neutron and Gamma-Ray Fluence-to-Dose Factors" (ANSI/ANS, 1991), was used in the MAVRIC dose rate calculations. In BSC (2001b), these calculations lead to slightly higher energy absorption for moist air. Using this conversion factor,

the corresponding dose rates in units of eV/g/s are 2.04×10^{14} eV/g/s for 1.18×10^{2} Gy/h (1.18×10^{4} rad/h) and 2.93×10^{15} eV/g/s for 1.69×10^{3} Gy/h (1.69×10^{5} rad/h). For use in the model, these values were rounded to 2×10^{14} eV/g/s and 3×10^{15} eV/g/s.

For comparison purposes, the dose rates reported in BSC (2001a) were examined, and it was corroborated that the selected values for dose rate are reasonable. In BSC (2001a), 21 PWR Babcock and Wilcox 15 × 15 assemblies are modeled in a UCF waste package. The UCF waste package was a previous disposal cask design considered for a potential geologic disposal site. Although the UCF package design differs from dry cask systems (e.g., external wall thickness, use of a borated stainless steel basket), the SNF configuration, inert environment, and SNF loading (source term) are similar, and the model is considered applicable for comparison purposes. For the present application, the BSC (2001a) calculation listed the dose rate values for a bounding case of SNF burnup (SNF burnup of 75 GWd/MTU, 5.5-wt% initial U-235, and 5-year decay time) and an average case (SNF burnup of 48 GWd/MTU, 4.0-wt% initial U-235, and 21-year decay time). The reported results also included cases when the SNF basket is assumed not to be present. In this case, the SNF assemblies are modeled in the same location, and basket components (stainless steel alloyed with natural boron) would not contribute to reducing radiation in regions outside of the basket.

Table A2-1 includes a selection of the dose rates reported in BSC (2001a). In this case, it is assumed that 1 sievert per hour (Sv/h) (100 rem/h) is equivalent to 1 Gy/h (100 rad/h) because the dose is predominantly from gamma radiation (with a quality factor of 1). The data in Table A2-1 indicate that the dose rates vary over a wide range depending on the SNF characteristics (e.g., burnup and age of fuel) and location. For example, at the bottom of the waste package cavity, the dose rate was calculated in close proximity to the fuel. This, along with streaming of radiation through channels in the SNF basket, would contribute to the high dose rates in this region. As can be seen for the bounding case, the dose rates can vary between approximately 1×10^{2} and 1×10^{3} Gy/h (1×10^{4} and 1×10^{5} rad/h). For the low-burnup case (48 GWd/MTU), the values reported are generally lower, with the exception that dose at the bottom of the waste package is comparable to the lower value in the range of doses—1×10^{2} Gy/h (1×10^{4} rad/h). In general, there is good overlap between the reported dose rates from Radulescu (2011) and BSC (2001a).

Table A2-1 Selected Dose Rate Values Reported in BSC (2001)*

Reference Model and Location	Dose Rate Gamma in Sv/h (rem/h)	Dose Rate Neutron in Sv/h (rem/h)	Total (Gamma + Neutron) in Sv/h (rem/h)
Table 17*: dose rate on inner surface of interior compartment enclosing SNF for bounding source with basket present, segment 6 (axial center of SNF region)	4.6887×10^{2} (4.6887×10^{4})	6.8477×10^{-1} (6.8477×10^{1})	4.6955×10^{2} (4.6955×10^{4})
Table 23*: dose rate on inner surface of interior compartment enclosing SNF for bounding source without basket present, segment 6 (axial center of SNF region)	1.2808×10^{3} (1.2808×10^{5})	9.1498×10^{-1} (9.1498×10^{1})	1.2861×10^{3} (1.2861×10^{5})

Table A2-1 Selected Dose Rate Values Reported in BSC (2001)* (continued)			
Reference Model and Location	**Dose Rate Gamma in Sv/hr (rem/h)**	**Dose Rate Neutron in Sv/h (rem/h)**	**Total (Gamma + Neutron) in Sv/h (rem/h)**
Table 28*: dose rate on inner surface of interior compartment enclosing SNF for bounding case with basket present, segment 10 (bottom of the WP† cavity)	1.1857×10^{3} (1.1857×10^{5})	7.7908×10^{-1} (7.7908×10^{1})	1.1864×10^{3} (1.1864×10^{5})
Table 28*: dose rate on inner surface of interior compartment enclosing SNF for bounding case without basket present, segment 10 (bottom of the WP cavity)	1.8324×10^{3} (1.8324×10^{5})	1.1248 (1.1248×10^{2})	1.8336×10^{3} (1.8336×10^{5})
Table 35*: dose rate on inner surface of interior compartment enclosing SNF for average source with basket present, segment 6 (axial center of SNF region)	9.5141×10^{1} (9.5141×10^{3})	1.0393×10^{-1} (1.0393×10^{1})	9.5247×10^{1} (9.5247×10^{3})
† waste package			

For the radiation dose rates, several uncertainties exist. The dose rates were selected to represent those that may exist in a canister after loading. Depending on the dry cask system design and SNF age and loading characteristics, the dose rates can vary. This additional source of uncertainty should be considered in refined future modeling efforts. For example, the work by Jenks (1972) reports a higher dose rate of $2x10^{7}$ Gy/h ($2x10^{5}$ rad/h) at the boundary of the canister for SNF with 5.0 kW (4.7 BTU/s) of energy loading. Furthermore, the values selected from Radulescu (2011) are at 20 years of decay. Provided the cask loading criteria could be met, the dose rate at earlier times would be expected to be higher, and the dose rates in regions near the SNF assemblies would be expected to be higher than those in other regions of the canister interior volume. However, the selected dose range is wide and intended to allow assessment of a range of conditions arising from incomplete drying. In the water decomposition model, the dose rate is considered constant, even though it would decline with time. For future refined efforts, detailed modeling of the radiation field for the cask interior environment, structures, and at potential SNF loading configurations should be considered to reduce uncertainty and allow for consideration of the change of the radiation field with time.

A2.1.3 Radiolysis Model

It is assumed that the water decomposes to produce oxygen and water according to the following chemical equation:

$$2H_2O \leftrightarrow 2H_2 + O_2 \qquad \text{(A2-1)}$$

Intermediate species such as H_2O_2 will decompose readily (spontaneously) to be hydrogen (H_2) and oxygen (O_2). The decomposition rate for water, R_D, in units of molecules per second was calculated using the following equation:

$$R_D = R_{ED} m_{water} G_{water} \quad \text{(A2-2)}$$

where R_{ED} is the rate of energy deposition in units of eV/g/s, m_{water} is the mass of water in grams, G_{water} is the G-value in units of molecules of water (H_2O) decomposed per 100 eV. Following the law of mass action, m_{water} can be expressed as follows:

$$m_{water}(t) = m_0 exp\left(-\frac{R_{\mathrm{ED}} G_{\mathrm{w}} MW}{N_A} t\right) = m_0 exp\left(-\frac{t}{\tau}\right) \quad \text{(A2-3)}$$

where *t* is time (year), m_0 is the initial amount of the residual water, MW is the molecular mass of water, N_A is Avogadro's number, and τ is a time constant defined as follows:

$$\tau = \frac{N_A}{R_{ED} G_W MW} \quad \text{(A2-4)}$$

Equation A2-3 can be rewritten as follows:

$$n_{water}(t) = n_0 exp\left(-\frac{t}{\tau}\right) \quad \text{(A2-5)}$$

where n_{water} is the moles of water, and n_0 is the initial moles of the residual water. Using the higher and lower values of radiation energy deposition rates, the values of the time constants are equal to 4.77 and 71.62 years for the radiation energy deposition rates equal to 2.0×10^{14} and 3×10^{15} eV/g/s, respectively. These two times were at ($n_{water}(\tau)/n_0$) equal to 37 percent (i.e., 1/e). The criterion, 1/e, is a normal practice for the time of complete reaction in kinetic exercises. Equation A2-5 is a global approximation without considering detailed reaction kinetics with time among intermediate species (e.g., Van Konynenburg, 1986, Table 9 and Equation 2). The quantitative information on the detailed kinetics is unavailable, which could affect the effective G_W values with time as the water amount decreases with time. It is generally considered that reaction rates of intermediate species embedded in various reaction formula (e.g., Van Konynenburg, 1986) possibly decrease as the water amount decreases with time based on the Le Chatelier's principle of chemical kinetics. Therefore, it is assumed that the kinetic curve of Equation A2-5 will become steeper moving forward in shorter times until the remaining water amount becomes negligible (i.e., 0.01 percent). The scoping analyses uses this assumption based on conservatism (i.e., faster component degradation and formation of flammability condition) and consistency with the normal practice for the time of complete reaction in kinetic exercises (i.e., 1/e). With $n_{water}(\tau)$ = 0.0001n_o and the completion times of 4.77 and 71.62 years, new time constants were computed below in Equations A2-6 and A2-7:

$$n_{water}(t) = n_0 exp(-1.929\, t) \quad \text{(A2-6)}$$

for a time constant equal to 4.77 years, and

$$n_{water}(t) = n_0 exp(-0.129\, t) \quad \text{(A2-7)}$$

for a time constant equal to 71.62 years.

The values τ for 4.77 and 71.62 years are obtained by calculating the inverse of Equation A2-4 with G = 7.4 molecules per 100 eV, the rate of energy deposition given and 1 year = 3.15×10^7 seconds. Then, the constants of Equations A2-6 and A2-7 are obtained by the Ln[0.0001 (99.99 percent)] = - constant × (4.77 or 71.62).

The uncertainty associated with this approximation is justified because the conclusion drawn (see Table 4-1 and Section 5 in the main body of the report) regarding the effect of residual water on the SNF and component degradation will not change with the uncertainty. For example, in Equation A2-5, to decrease the percentage of remaining water amount from 37 percent to 10 percent, the radiolysis time needs to increase to 10.99 years. In this increased time of 10.99 years, all oxygen produced by radiolysis will be consumed because of higher temperatures (e.g., Figure 3-1 in the main body of the report). At 10 percent, the remaining water from 55 moles becomes 5.5 moles, which does not pose any new issues of component degradation or flammability condition by separate analyses (see Table 4-1 in the main body of the report).

Overall, the assumed fast radiolysis is conservative in terms of the issues of component degradation and flammability condition, as shown in Section 5 of the main body of the report. As stated in Section A2.1.3.2, the more realistic radiation strength is likely to be higher than the current example case because of the availability of more design information. The higher radiation strength decreases the radiolysis time. The numerical analysis given in this report is only a representative example case, which lacks the benefit of detailed radiolysis kinetics.

The following two equations were also used where water is assumed to decompose completely within a time constant following a linear function of time:

$$n_{water}(t) = n_0(1 - t / 4.77) \quad \text{(A2-8)}$$

and

$$n_{water}(t) = n_0(1 - t / 71.62) \quad \text{(A2-9)}$$

These equations are reasonable given the uncertainty in the parameters with time, the wide range of radiation dose considered, and the scoping nature of this assessment. Equations A2-6 to A2-9 are used to analyze the effects of residual water on various canister components.

A2.1.3.1 Effect of Recombination Reaction

The paper by Arkhipov et al. (2007) lists more than 20 chemical equations to model radiolytical decomposition of the vapor-phase water. Several of those reactions involve reaction between hydrogen and oxidizing species to produce water. This indicates that recombination reaction between hydrogen and oxygen could occur via a complex reaction pathway leading to the production of water in the canister. Recombination could change the water depletion rate embedded in Equation A2-5. The discussion that follows is a simplified analysis of potential changes in the depletion rate arising from recombination.

Considering together the recombination effect , Equation A2-2, and the stoichiometry of Equation A2-1, the following equation represents a modified mass-balance for water in the canister:

$$\frac{d[H_2O]}{dt} = -\frac{[H_2O]}{\tau} + k[H_2]^2[O_2] \quad \text{(A2-10)}$$

where

$[H_2O]$	=	water concentration in the canister = $n_{water}(t)/V$
$[H_2]$	=	hydrogen concentration in the canister = $n_{hydrogen}(t)/V$
$[O_2]$	=	oxygen concentration in the canister = $n_{oxygen}(t)/V$
k	=	rate constant for the recombination reaction in units of inverse square of molar per second ($M^{-2}s^{-1}$)
V	=	canister volume

and the symbols $n_{hydrogen}(t)$ and $n_{oxygen}(t)$ denote molecular amounts of hydrogen and oxygen as functions of time. Based on the stoichiometry of Equation A2-1, the following equations are valid in the canister environment:

$$[O_2] = \frac{[H_2]}{2} \tag{A2-11}$$

and

$$[H_2] = [H_2O]_0 - [H_2O] \tag{A2-12}$$

where $[H_2O]_0$ is initial water concentration. Equations A2-11 and A2-12 mean that the only source for H_2 and O_2 is water decomposition, and that reactions with uptake O_2 and H_2 are ignored, such as oxidation of SNF and cladding. Equation A2-10 can be rewritten as follows:

$$\frac{d[H_2O]}{dt} = -\frac{[H_2O]}{\tau} + \frac{k}{2}([H_2O]_0^3 - 3[H_2O]_0^2[H_2O] + 3[H_2O]_0[H_2O]^2 - [H_2O]^3) \tag{A2-13}$$

In the canister environment, $[H_2O]_0$ is equal to 0.026 molar (M) for 55 moles of residual water and
2,100 liter (L) void volume; therefore, in general the concentration $[H_2O]$ is small. A limit analysis (Equation A2-13) is provided to compare the rate of water depletion with respect to Equation A2-5. First, a case of slow chemical kinetics is considered.

Slow Recombination Reaction (i.e., Small k)

Because $[H_2O]$ is small, the first order term with respect to $[H_2O]$ would dominate in Equation A2-13 for the canister environment for small k values. Therefore, neglecting second and third order terms with respect to $[H_2O]$, the following approximation is valid:

$$\frac{d[H_2O]}{dt} = -[H_2O]\left(\frac{1}{\tau} + \frac{3k[H_2O]_0^2}{2}\right) + \frac{k}{2}[H_2O]_0^3 = -\frac{[H_2O]}{\tau_{eff}} \tag{A2-14}$$

where effective time constant τ_{eff} considering the recombination reaction, in the limit of small k, is the following:

$$\tau_{eff} = \frac{2\tau}{2 + 3k[H_2O]_0^2\tau} \tag{A2-15}$$

Equation A2-15 indicates that τ_{eff} is less than τ, or that recombination would expedite water depletion in the limit of small k, with respect to the depletion rate implied in Equation A2-5. Therefore, an assumption of 99.99 percent of the residual water within one time constant is reasonable.

Fast Recombination Reaction (i.e., Large k)

For large k, Equation A2-13 can be approximated as follows:

$$\frac{d[H_2O]}{dt} = \frac{k}{2}([H_2O]_0^3 - 3[H_2O]_0^2[H_2O] + 3[H_2O]_0[H_2O]^2 - [H_2O]^3) \quad \text{(A2-16)}$$

At steady state, this equation has the following trivial solution:

$$[H_2O](t) = [H_2O]_0 \quad \text{(A2-17)}$$

This solution is intuitive—in the limit of very fast chemical kinetics, any water decomposed by radiolysis is immediately reconstituted by the recombination reaction, leaving the amount of water unchanged. Thus, based on the limiting Equation A2-17, as k increases, the rate of water depletion is slowed down compared to the depletion rate embedded in Equation A2-5.

Based on the limiting analysis for small and large k, recombination can accelerate or slow down water depletion compared to the depletion rate in Equation A2-5. To account, in a simplistic manner, for radiolysis and chemical kinetics, perturbations to Equation A2-5 were examined in the form of Equations A2-6 to A2-9.

A2.1.3.2 Oxygen Consumption and Rationale for Recombination Effects

Radiolysis-generated oxygen can react with cladding and SNF and other internal components. Interaction of radiolysis-driven chemical reactions, such as $2H_2O \rightarrow 2H_2+O_2$, with metal oxidation reactions can affect the rate of recombination reactions (e.g., the balance assumed in Equation A2-11 would be altered if metal oxidation is considered). Thus, the overall rate of water decomposition (in which radiolysis and chemical kinetics play a role) can be a function of oxidation rates of metallic system components. Oxygen generated by radiolysis will be consumed fast by the oxidation of cladding and SNF and other internal components, which have a large surface area (e.g., approximately 580 m^2 (54 ft^2) of cladding). This fast oxygen consumption will substantially slow down the recombination rate of oxygen and hydrogen (and generally for all species generated).

Furthermore, compared with the decomposition of water, the recombination will require additional time for molecular collisions before the recombination reaction itself. This collision time is long because of long mean free path, as stated below. In other words, the collision rate is much lower by greater than 5 orders of magnitude than the radiolysis rate. This additional collision process slows down the recombination process for all species involved in about 10 to 20 possible reactions (Arkhipov et al., 2007; Van Konynenburg, 1986). Therefore, the recombination is likely to be insignificant, as was the case presented in the subsection entitled, "Slow Recombination Reaction," in Section A2.1.3.1. In the literature, water radiolysis showed linear kinetics in the sealed environment without saturation, indicating insignificant recombination (Lewis and Warren, 1990; Sowden, 1963).

The mean free path of gaseous molecules, as an example, is approximately 1.6×10^{-7} m (6.3×10^{-8} inch (in.)) compared with the molecular separation—approximately 3×10^{-10} m

(8×10^{-10} in.) at 177 degrees Celsius (°C) (350 °F) and 1.0 atm (14.7 pounds per square inch ($lb/in.^2$)), which is equivalent to 55 moles (1 L (35 ounces (oz)) of water in 2,100 L (21,009 oz)). This implies that the collision process will not impede a normally expected diffusion. The usual gaseous diffusion distance is greater than 1 centimeter (cm) for a second, which is a statistically averaged moving distance of molecules colliding each other. This distance is greater, in orders of magnitude, than the oxygen penetration for zirconium oxidation for 1 second. The oxygen consumption rate from Figure A3-2 is well below the oxygen diffusion rate toward the cladding surface. Therefore, on the surface of cladding and SNF and internal components, oxygen is always available as the radiolysis proceeds. In addition, the oxygen consumption rate is faster than the radiolysis rate, as seen in Section A3.1.2. Therefore, the recombination of oxygen by radiolysis would be limited. This relative kinetic consideration suggests that the oxygen accumulation for recombination at the initial high temperatures will not occur.

Alternatively, at the same temperature, water amount, and canister volume, the molecular collision frequency is 5×10^{9}/s, which is equivalent to 8×10^{-15} moles/s. In the radiolysis model of Section A2.1.3, the rates range from 3×10^{-8} to 4×10^{-7} moles/s, which are much higher than the collision frequency. The collision frequency is insignificant and will not impede the radiolysis rate. The recombination is insignificant, as well. Generally, this type of rate assessment is equally applicable to all intermediate radiolysis species. The net results, including all of the species, will not change because the species are involved in both the radiolysis and recombination processes.

Perturbations are used in Equations A2-8 and A2-9, with respect to Equations A2-6 and A2-7, by adopting linear time kinetics in reference to exponential time kinetics. This perturbation will cover some uncertainties associated with using simple mathematics (Equations A2-2 and A2-3) considering all of the species involved (e.g., Arkhipov et al., 2007; Van Konynenburg, 1986). The linear kinetics represents cases of slower decomposition. This perturbation approach allows more water to be present and later oxygen accumulation. These cases were observed at lower temperatures and high water volumes (near 55 moles) with slower radiolysis kinetics (e.g., Figure A4-5).

Finally, as discussed in Section A2.1.2, the level of radiation in the canister could be more than an order of magnitude higher than the level used in this study if the SNF loading is increased above 5 kW (4.7 BTU/s) per assembly. The realistic determination of the radiation level is one uncertainty identified in the current literature. If the radiation level increases, expected lower G values from recombination will result in a similar amount of water decomposed presented in the current model exercise using higher G values. The literature (Ausloos, 1968) reports G values an order of magnitude lower.

A2.1.3.3 Conservatism of Current Radiolysis Model for Component Degradation

If the recombination is significant, it is expected that water vapor will remain in the canister. However, the temperature at which the oxidation with water (i.e., aqueous corrosion with a thicker adsorbed water layer) occurs normally has RH above a threshold value (e.g., approximately 20 percent for cladding as discussed in Sections 3.3 and 4.5 of the main body of this report) for aqueous corrosion. In 10 years, with 55 moles (1 L (35 oz)) of water, RH decreases to 11 percent at 450 K (351 °F), 4 percent at 500 K (441 °F), and 2 percent at 550 K (499 °F), under these RH conditions, it is dry without oxidation with water. At lower temperatures, RH may increase but the corrosion rate will become low. Therefore, no degradation would occur with significant recombination—only hydrogen and oxygen would be produced very slowly. One could envision an exceptional case in which continuous aqueous

(electrochemical) corrosion may occur at lower temperatures. However, this scenario has not been proven. In this case, only hydrogen will be produced. Overall, only the fast radiolysis discussed in this section induces degradation of cladding/SNF and components and the early, complete hydrogen formation. Regarding hydrogen flammability, more oxygen produced by slower radiolysis kinetics may be detrimental. However, as shown in Section A4.4.4, a sufficient amount of oxygen may only be obtained with a greater amount of water (e.g., 17.4 and 55 moles), as Table 4-1 presents. Flammability also requires ignition.

A2.2 Relative Humidity Considering Radiolysis

This section presents relative humidity calculations considering radiolysis. Calculations were performed for temperature Zone 5, which has the lowest initial temperature and the maximum potential for condensate to form. Because the other zones have higher initial temperatures, the potential for condensate formation is less when compared to Zone 5. Section A5 summarizes the RH trends of the canister environment.

The RH profiles are calculated for exponential decomposition of the residual water, with decomposition periods of 4.77 and 71.62 years, as shown in Figures A2-1(a) and (b), respectively. The amount of residual water is 55 moles (1 L (35 oz)) in the canister. The RH values will change with the residual water amount. The curves were obtained using the expression for RH described in Equation A1-4. The temperature values needed to calculate relative humidity were obtained using Equation A1-3.

As can be seen, in several cases, RH drops rapidly within the first several years and does not exceed 5 percent. This phenomenon is a combined effect of water amount and temperature variation in the canister. These results also indicate that radiolysis decomposes most of the residual water, and not enough water is available to saturate in the gas phase when the mean value of the SNF and cladding initial temperature is 575 K (576 °F). Section A5 provides additional details on the RH of the canister environment considering radiolysis.

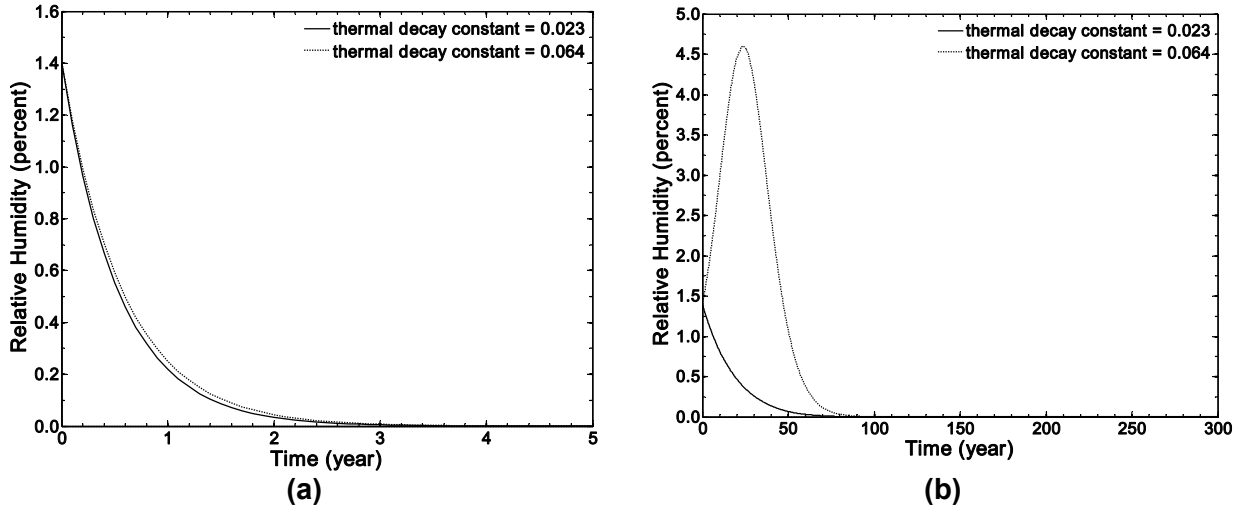

Figure A2-1 RH in Zone 1 of the canister environment considering radiolysis. The RH values are calculated using the decay constant equal to 0.023 and 0.064, and T_{mean} equal to 375 K in Equation A1-3. The exponential decomposition of the residual water in (a) is 4.77 years and in (b) is 71.62 years.

A3. CLADDING OXIDATION AND SPENT NUCLEAR FUEL OXIDATION AND HYDRATION MODELS

A3.1 Cladding Oxidation

Zirconium-based alloys were introduced as SNF cladding material in the early 1950s because of their high corrosion resistance and low thermal neutron absorption cross-section. The excellent corrosion resistance of zirconium alloys results from the formation of an extremely adherent (i.e., nearly perfect electrical insulator), protective, and thermodynamically stable zirconium oxide layer. Most cladding materials used in nuclear reactors are the traditional zirconium-based alloys, such as (1) Zircaloy-2 (Zr-1.5Sn-0.12Fe-0.1Cr-0.05Ni in weight-percent (wt%)), which is predominantly used to clad the SNF in BWRs, and (2) Zircaloy-4 (Zr 1.5Sn-0.2Fe-0.1Cr in wt%), which is predominantly used to clad SNF in PWRs. As reactor SNF cycles are extended leading to higher SNF burnup, new alloys, such as Westinghouse's optimized ZIRLO™ (Zr-1.0Sn-0.1Fe-1.1Nb in wt%)) (Cornstock et al., 1996) and Areva's M5® (Zr-0.03Fe-1.0Nb in weight-percent) (Mardon et al., 2000), have been developed to reduce corrosion and hydrogen pickup by the cladding materials.

Cladding oxidation could occur as a result of residual water during extended storage in the canister. Moisture and water radiolysis products (i.e., oxygen and highly oxidizing species such as $OH^{\bullet}$ or H_2O_2) present in the canister can react with zirconium cladding to form zirconium oxide on the exposed cladding surfaces. A thicker zirconium oxide layer tends to be more porous in the outer oxide layer and less protective compared to the thinner and compact inner oxide layer. Thus, oxide growth can reduce cladding wall thickness with more porous oxide formation that can be more susceptible to mechanical breakage as a result of a thinner metallic wall.

Several environmental factors can affect the oxidation and oxide growth on the cladding, including temperature, RH, irradiation, and oxygen partial pressure. In addition, other factors, such as cladding alloy composition and SNF burnup level, affect the extent of cladding oxidation during the storage.

A3.1.1 Effect of Spent Nuclear Fuel Burnup (Initial Condition for Storage)

SNF burnup affects the oxide thickness and other properties, including the amount of absorbed hydrogen, fission gas production, and crud buildup. It has been generally observed that the peak oxide thickness of Zircaloy increased as the burnup increased up to approximately 75 GWd/MTU (Garde, 1991; Van Swam et al., 1997; EPRI, 2007). In particular, measurements of more than 4,400 commercial SNF rods irradiated in reactors worldwide show that the average oxide thickness on Zircaloy-4 was as great as 100 micrometers (μm) (0.00394 in.) for burnups in the range of 60 to 65 GWd/MTU (EPRI, 2007). At low burnup (less than 45 GWd/MTU), the average oxide thickness was 40 μm (1.57×10^{-3} in.).

For SNF rods having an average burnup of 52.5 GWd/MTU, the average peak oxide thickness for ZIRLO was 31 μm (1.22×10^{-3} in.), which was approximately 27.5 percent of the average peak oxide thickness for conventional and optimized Zircaloy-4 (Sabol et al., 1994). However, compared to the large size of the database for Zircaloy cladding, the data for new alloys necessary to confirm the range of oxide thickness at the high burnup regime are still lacking, as indicated in Cheng et al. (2000).

Concerning the integrity of the cladding during reactor operation, 10 CFR Part 50, "Domestic Licensing of Production and Utilization Facilities," defines the maximum cladding oxidation limit (i.e., oxidation thickness) to be no more than 17 percent of the original cladding thickness (Meyer, 2000). The current regulatory burnup limit for dry storage is 62.5 GWd/MTU (Brach, 2003).

A3.1.2 Cladding Failure (Initial Condition for Storage)

The initial physical condition of the SNF rods and assemblies at the time that they are placed into dry storage is closely related to their condition when taken out of the reactor because degradation during wet storage is minimal (CRWMS M&O, 2000). Some SNF rods can have initial defects, such as manufacturing microdefects, handling-induced defects (including small partial depth cladding wall cracks), weld defects, moisture or organic contamination of cladding or pellets, and excessive gaps at spacers leading to vibration and fretting. During reactor operations, cladding can fail through various degradation mechanisms, such as pellet-cladding interaction, SCC, and debris-induced fretting.

Data from studies of Zircaloy-based cladding failure from 1968 to 1973 indicate that 1 in 100 SNF rods (1 percent) had cladding failure (CRWMS M&O, 2000; Locke, 1974). A later study reported that the overall cladding failure had decreased to 0.36 percent for BWR and 0.04 percent for PWR SNF rods as a result of design and material performance improvements (Cohen & Associates, 1999). From the measurement of Kr-85 leaking from approximately 26,500 rods currently in dry storage, the overall observed failure was estimated to be 0.045 percent (CRWMS M&O, 2000).

A3.1.3 Effect of Temperature

Zirconium cladding can be oxidized in the canister environment according to the following chemical reactions: $Zr + O_2 = ZrO_2$ for dry air and $Zr + 2H_2O = ZrO_2 + 2H_2$ for water or humid air (e.g., steam).

The oxidation rate of cladding materials has a strong positive dependence on temperature. Corrosion of zirconium and its alloys—in particular, Zircaloy-2 and Zircaloy-4—has been extensively studied in water and steam, and a large database exists as a result of the broad experience with LWRs (Cox, 1988, 1976; Rothman, 1984; Hillner et al., 1994) and in dry air (Suzuki and Kawasaki, 1986). Note that the oxidation rates of Zircaloy were independent of the type of oxidants. The rates were almost identical when exposed to different oxidants (e.g., oxygen, water, and vapor) (Cox, 1988; Rothman, 1984).

Only limited information is publicly available regarding oxidation rates of ZIRLO and M5. The available data suggest that ZIRLO and M5 oxidation rates are almost half of other Zircaloys (Mardon et al., 1997; Wilson et al., 1997; Duriez et al., 2008). Because most experiment data regarding cladding oxidation rate is for Zircaloy-4, the cladding oxidation assessment in this study is based on Zircaloy-4. To evaluate oxidation behavior of new alloys that follow a temperature-dependent rate equation, a simple comparison with Zircaloy is made as described below.

Hillner et al. (1994) conducted detailed analysis of weight measurement data from long-term autoclave tests of Zircaloy-2 and Zircaloy-4. The tests were conducted in degassed pure water for 10,507 days at temperatures ranging between 250 and 360 degrees Celsius (°C) (482 and 680 degrees Farenheit (°F)). Twenty-two different tests were analyzed, and specimens

with different heat treatment and preoxidized surface conditions were included. Based on their data, Hillner et al. (1994) proposed the following equation for reaction kinetics as a function of temperature:

$$\Delta W = A\, t \exp\left(-Q/RT\right) \quad \text{(A3-1)}$$

where

ΔW = specimen weight gain in mg/dm^2
A = preexponential constant in mg/dm^2/d
t = time in days
Q = activation energy in cal/mole
R = gas constant in cal/mole/K
T = absolute temperature in K

A number of other investigators also conducted similar oxidation tests in autoclaves and established their own values in terms of activation energy and preexponential constant (Table A3-1).

To select the cladding model from the listed models in Table A3-1, bounding calculations for cladding oxide thickness can be conducted as presented in Section A4. To this end, the oxide thickness that could form on Zircaloy during the dry storage period is estimated. To evaluate these temperature-dependent models, a scoping calculation was conducted to estimate an additional oxide thickness using the temperature profile in Equation A3-2 for the case of the low-end SNF and cladding temperature:

$$T(t) = (575 - 309)\frac{[\exp(-0.023t) + \exp(-0.064t)]}{2} + 309 \quad \text{(A3-2)}$$

where $T(t)$ is the temperature (K) as a function of the time. It is assumed that the oxygen supply is not a limiting factor in this calculation. Based on this assumption, the additional oxide thickness that could form during the storage period was calculated from several models of oxide growth and is presented in Figure A3-1. Note that 15 mg/dm^2 (0.49 oz/ft^2) of weight gain corresponded approximately to 1 μm (4×10^{-5} in.) of oxide and 0.66 μm (2.6×10^{-5} in.) of metal consumed by the oxidation reaction (Garzarolli et al., 1982; Rothman, 1984).

As seen in Figure A3-1, all models exhibit similar trends. Most of the cladding oxidation occurs during the first 10 years of storage. The oxide thickness can increase rapidly because of the relatively high temperatures during this period. However, no substantial oxide growth occurs beyond 10 years because oxidation rate decreases as a result of lower temperatures. Depending on the model used, the maximum calculated thickness ranges from 1.2 to 4.0 μm (4.724×10^{-5} to 1.6×10^{-4} in.).

Table A3-1 Values of A and Q/R in Equation A3-1 from Models of Different Investigators for Zircaloy Oxidation			
Model No.	**Investigators**	**A (mg/dm^2/d)**	**Q/R (K)**
1	Hillner (1977)	1.12×10^{8}	12,529
2	Van der Linde (1965)	2.30×10^{9}	14,451
3	Dyce (1964)	6.53×10^{9}	15,109
4	Daalgard (1976)	1.84×10^{7}	11,222
5	Billot et al. (1989)	1.13×10^{8}	12,567
6	Garzaolli et al. (1982)	1.18×10^{9}	13,815
7	Stehle et al. (1975)	2.21×10^{9}	14,242
8	Peters (1984)	8.12×10^{8}	13,512
9	Hillner et al. (1994)	2.46×10^{8}	12,877

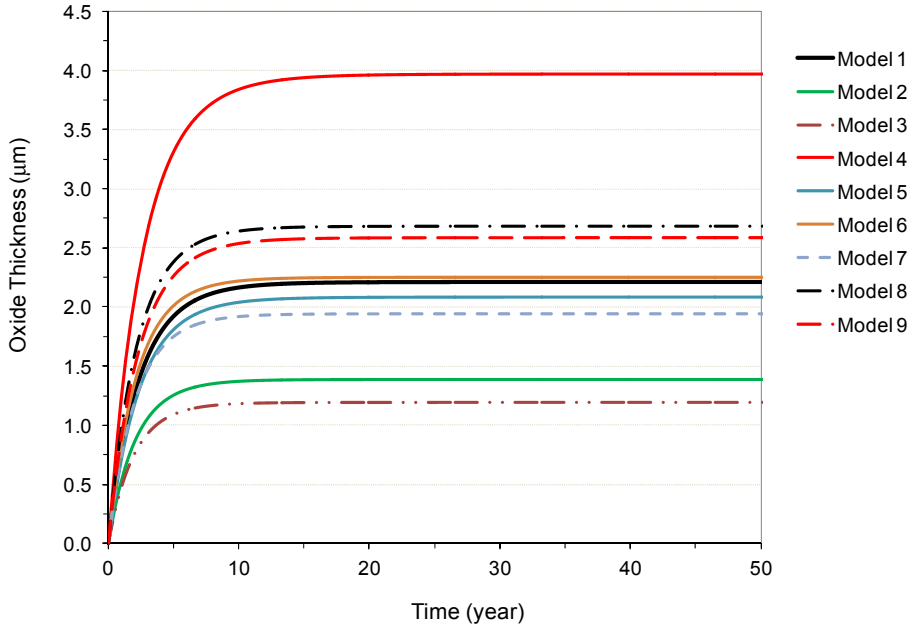

Figure A3–1 Calculated additional oxide thickness on cladding surface during the dry storage period according to different selections of parameters *Q* and *A* from different investigators at the temperatures of 250 and 360 °C (482 and 680 °F)

Because of the high corrosion resistance of the new cladding alloys, it is expected that the percentage of cladding thickness oxidized would be lower than that of the traditional Zircaloy alloys.

Figure A3-2 presents the estimated thinning of cladding using a Pilling-Bedworth factor (i.e., a ratio of the volume of metal oxide formed to the volume of the corresponding metal matrix consumed) of 1.75 for zirconium (Van Swam et al., 1997). Because the density of zirconium oxide is lower than the zirconium matrix and contains voids, the amount of metal loss from the cladding is equivalent to 57 percent of the oxide thickness, which is the inverse of the Pilling-Bedworth factor of 1.75.

A3.1.4 Heat Transfer Degradation of Cladding

During reactor operation, cladding tubes are subjected to a high heat flux at a high core temperature (e.g., higher than 1,000 °C (1,832 °F)). Under a heat flux condition, the metal cladding temperature at the metal surface and oxide layer interface can increase as a result of crud deposits from the coolant and zirconium oxide growth. Stehle et al. (1975) hypothesized that the increase of weight under heat flux conditions was controlled by the protective oxide barrier layer on the metal surface which acts as a thermal barrier. Because the thermal conductivity of the zirconium oxide (e.g., approximately 2 Watts per meter per Kelvin (W/m-K)) is considerably lower than that of the zirconium metal (e.g., 20 W/m-K), the oxide layer formed on the zirconium cladding surface may act as a thermal barrier and result in a large temperature gradient across the oxide layer. In the reactor, the growth of the insulating oxide layer can lead to an increase in temperature at the metal–oxide interface. Thus, the increase in temperature at the interface can

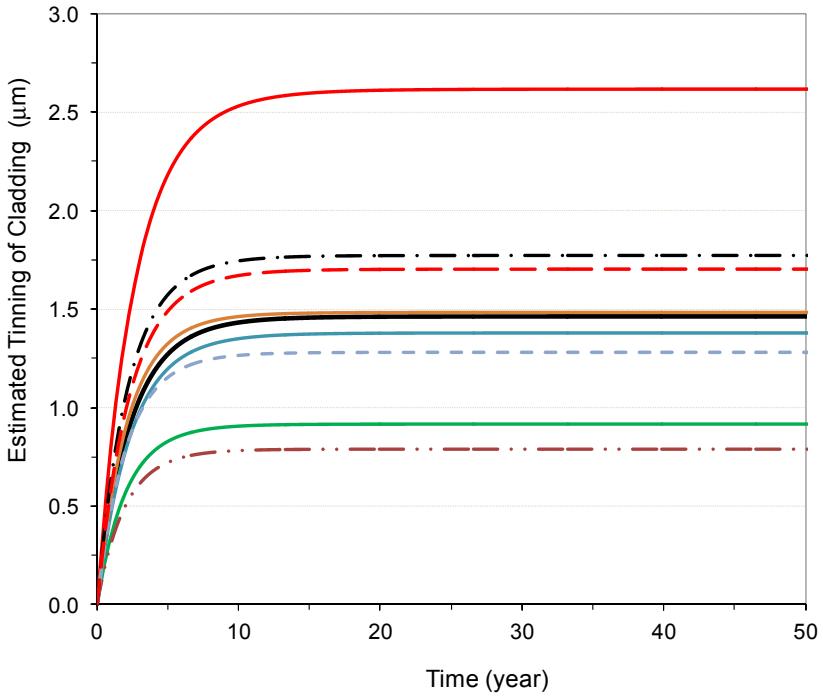

Figure A3–2 Calculated additional cladding thinning during the dry storage period according to different selections of parameters *Q* and *A*

accelerate the metal matrix corrosion by increasing the rate at which oxidants (e.g., oxygen) diffuse from the oxide layer into the metal matrix.

However, the temperature of an SNF assembly inside the canister during extended dry storage will be much lower (e.g., maximum of 400 °C (752 °F)) than that in the reactor core and will decrease with time as shown in Figure A1-12. Moreover, the environment inside the canister would contain a limited mass of oxidants, which would limit further oxidation. It is unlikely that this small increase of oxide thickness at the relatively low canister temperature and less corrosive environment will significantly affect cladding degradation.

Another mechanism that may cause cladding degradation during extended dry storage is the significant temperature difference along the cladded SNF rods as distributed into the five temperature zones (see Figure A1-9 and Table A1-1). The data suggest that the temperature variation along an SNF rod could reach up to 200 °C (392 °F). In gas transmission pipelines (Saji, 2009), it is well known that temperature-driven corrosion (so called thermogalvanic corrosion) can occur when a pipe has a hot zone, which serves as the anode, and a cool zone, which functions as a cathode. In pipelines, the compressed hot gas area of the pipe can corrode by acting as an anode with respect to the relatively large area of cathode of the cooler part. Note that thermogalvanic corrosion can only occur when the anode is very small compared to the large area of cathode. This is called the anode-to-cathode area effect.

However, as seen in Table A1-1, the volume (area) of the hot Zone 1 is comparable to other zones and even larger than that of the cold Zone 5. This suggests that the area difference between the small anode and large cathode required to cause thermogalvanic corrosion will not be established. Therefore, temperature-driven thermogalvanic corrosion of cladding is not expected to occur in the canister during the extended storage period.

A3.1.5 Other Factors Affecting Cladding Oxidation

Other environmental factors, such as RH, irradiation, and oxygen pressure, can affect cladding oxidation. There is little information in the literature on the effect of RH on oxidation of zirconium or its alloys. Unfortunately, the threshold values of RH on oxidation of zirconium or its alloys have not been reported in the literature to the author's knowledge. However, aluminum alloy cladding oxidation data may indicate the effect of RH on zirconium oxidation. Lam et al. (1997) conducted oxidation tests for aluminum alloys in the range of 80 to 200 °C (176 to 392 °F) to compare the oxidation rate in air at different RH values (0 to 100 percent). For aluminum cladding, the minimum RH required to sustain detectable oxidation was approximately 20 percent at 150 °C (302 °F). Because aluminum and zirconium have been shown to have a similar thermodynamic and practical nobility based on Pourbaix classification of the nobility order (Ghali, 2010) and they exhibit a similar corrosion performance with the formation of a protective oxide film, a threshold RH of 20 percent can also be assumed for zirconium-based cladding materials.

To investigate the effect of irradiation on cladding oxidation rates, Hillner et al. (1994) compared the oxidation rate of irradiated Zircaloy to unirradiated Zircaloy in degassed pure water in an autoclave. The test results revealed that the irradiated cladding oxidation rate was almost twice that of the unirradiated rate after 185 days of exposure at 325 °C (617 °F). However, the authors observed a gradual decrease of the difference in the oxidation rate between irradiated and unirradiated samples and anticipated a similar range of oxidation rates for both types of samples. Garzarolli et al. (1982) confirmed this. In a moist environment, Woo et al. (2000) reported the same oxidation rates for both unirradiated and irradiated Zircaloy-2 samples at 300 °C (572 °F).

A number of researchers have studied the effects of oxygen partial pressure on the oxidation rate of Zircaloy (Cox, 1963; Nakamura et al., 1993; Causey et al., 2005). In the temperature range of 350 to 500 °C (662 to 932 °F), it has been shown that, as the partial pressure increased by four orders of magnitude, the rate of oxidation increased, at most, less than two times.

A3.2 Spent Nuclear Fuel Oxidation and Hydration

When cladding breaches are present, irradiated UO_2 SNF can react with oxidants (e.g., oxygen, water vapor, or other radiolytic products) formed by radiolysis and evaporation of residual water present inside a canister. The UO_2 could be oxidized to form U_4O_9, U_3O_7, and U_3O_8 in dry air (e.g., less than 40 percent RH) or could also form hydrated uranium oxides, such as schoepite ($UO_3 \cdot xH_2O$, x = 0.5 to 2) in humid air (e.g., greater than 40 percent RH) or an aqueous environment (Ahn, 1996; Einziger et al., 1992; Einziger and Strain, 1986; Einziger and Cook, 1985; EPRI, 1986; McEachern and Taylor, 1998; Taylor et al., 1995; Wasywich et al., 1993).

In particular, irradiated LWR SNFs with typical burnup of 20 to 50 GWd/MTU have been shown to be oxidized via the two-step reaction in air, as in Equation A3-3 (Hanson, 1998; Einziger et al., 1992; Thomas et al., 1989; Thomas et al., 1993):

$$UO_2 \rightarrow U_4O_9 \rightarrow U_3O_8 \quad \text{(A3-3)}$$

LWR SNF is first oxidized by a rapid formation of nonstoichiometric U_4O_9 preferentially along the grain boundaries to reach an oxygen-to-metal (O/M) ratio of approximately 2.4 (often represented as U_4O_{9+x} or $UO_{2.4}$). Grain boundary openings associated with the presence of fission gas at the grain boundaries in the LWR SNF may facilitate oxygen diffusion through grain boundaries (Einziger et al., 1992; Thomas et al., 1989). $UO_{2.4}$ then grows into UO_2 grains. As depicted in Figure A3-3, uniform grain boundary oxidation of the LWR SNF (burnup of 28 GWd/MTU) has occurred starting from outside. With increased exposure time, the oxidation front moves into the grain. The results of x ray diffraction analysis revealed that the oxidized phase was U_4O_9. With preferential oxidation along the grain boundary to form $UO_{2.4}$, all individual grains can be further oxidized to U_3O_8 without producing an intermediate phase compound, such as U_3O_7 (Hanson, 1998; Thomas et al., 1993). For the case of used Canada deuterium uranium (CANDU) fuel, two oxidation models were observed: a grain model and a fragment model (Wasywich et al., 1993). In a fragment model, the oxidation occurred along the fracture-free surface of the fragments and expanded to the grain, as discussed in Section A3.1.3. However, in a moisture environment, the CANDU SNF was oxidized by preferential diffusion of oxygen along the grain boundaries. As an alternative to the base case of a grain model, a fragment model can be explored.

The extent of SNF oxidation and hydration can be correlated with two controlling parameters: the chemical reaction kinetics of the SNF oxidation and the amount of available oxidants (oxygen and water vapor) present in the canister. For example, if the kinetics is slow and oxidant is abundant, kinetics can control the overall reaction. However, for the opposite case (i.e., fast kinetics and limited amount of oxidant), the overall reaction will be controlled by the rate of the radiolysis process and consumption rate of oxidant with time.

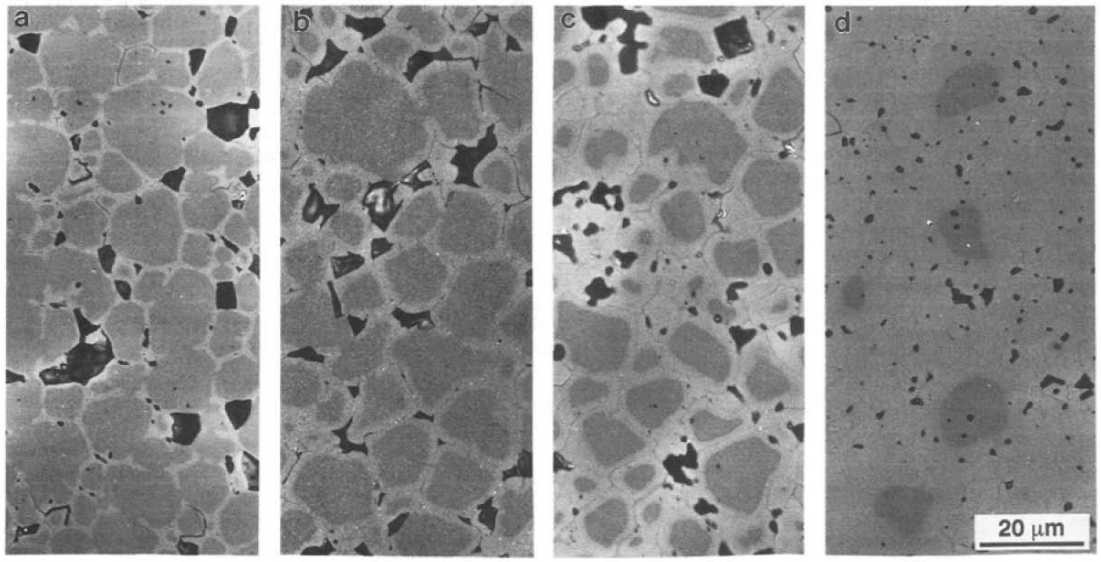

Figure A3-3 Grain boundary oxidation of americium-105 SNF to U_4O_9. Optical ceramographs, as polished: (a) 95 h, Bulk O/M = 2.05; (b) 420 h, Bulk O/M = 2.17; (c) 775.5 h, Bulk O/M = 2.24; and (d) 1,677 h, Bulk O/M = 2.31. (Einziger et al., 1992)

Important factors that affect the UO_2 oxidation and hydration may include temperature, RH, and SNF type (e.g., burnup and enrichment). The next section discusses the effects of these factors on SNF oxidation.

A3.2.1 Temperature

Temperature strongly affects the SNF oxidation rate. Below 230 °C (446 °F) in a dry air environment, U_4O_9 (or $UO_{2.4}$) is generally observed in LWR SNF because the kinetics of U_3O_8 formation is believed to be too slow to be detected on a reasonable laboratory time scale (McEachern and Taylor, 1998; Thomas et al., 1993). The time for conversion of UO_2 into $UO_{2.4}$ has been shown to have Arrhenius dependence with temperature and is represented by the following equation (Einziger et al., 1992; Ahn, 1996):

$$t_{2.4}(\text{yr}) = 2.97 \times 10^{-13} \exp\left(\frac{26.6\ \text{kcal}}{RT}\right) \quad \text{(A3-4)}$$

where

R = gas constant
T = temperature (K)

Assuming oxygen diffusion through a layer of U_4O_9 from the individual grain surface to inside the grain to be the rate-controlling step, the growth kinetics of the oxidized width is represented by the following equation (Einziger et al., 1992):

$$w\ (\mu\text{m}) = (2kt)^{0.5} \quad \text{(A3-5)}$$

where

t = oxidation time (hour)
k = rate constant

Equation A3-6 represents the rate constant measured in the temperature range of 175 to 195 °C (347 to 383 °F):

$$k\left(\frac{\mu m^2}{hr}\right) = 1.04 \times 10^8 \exp\left(\frac{-24.0\ kcal}{RT}\right) \quad \text{(A3-6)}$$

where

R = gas constant
T = temperature (K)

Equations A3-4 to A3-6 were developed using the weight gain measurement tests of the LWR SNF to reach an O/M ratio of nearly 2.4 when individual grains oxidized close to 100 percent to U_4O_9, as seen in Figure A3-3.

Above 230 °C (446 °F), as observed by Einziger and Cook (1985), a higher oxidation phase of U_3O_8 could be a primary oxide phase. The formation of U_3O_8 has been shown to follow a nucleation-and-growth mechanism and displays a sigmoidal trend for reaction kinetics (McEachern and Taylor, 1998). Because of the less dense structure of U_3O_8 (density of 8.35 grams per cubic centimeter (g/cm^3) (0.301 pounds per cubic inch ($lb/in.^3$) compared to that of UO_2 (density of 10.96 g/cm^3 (0.396 $lb/in.^3$), a significant net volume expansion (36 percent) based on the crystallographic volumes per uranium atom can occur when the fluorite structure of UO_2 transits to the orthorhombic structure of U_3O_8 (Taylor et al., 1989). The swelling of SNF can then exert a hoop stress to the cladding and eventually lead to fracture, such as rod rupture by splitting (unzipping). This would occur when the stress and ensuing strain reaches a threshold value. Einziger and Cook (1985) reported the threshold strain on the cladding to be about 6.5 percent with a formation of about 100 percent U_3O_8 underneath the initial cladding crack based on measuring the diametrical increase necessary to propagate the defects (e.g., crack or holes) for the BWR SNF. The results of x ray diffraction analysis of the oxidized SNF samples revealed that only U_3O_8 was observed for the case of the highest dilation area at the defect present on the SNF rod. The experiments were conducted at 229 °C (444 °F) in air and for a hole size of 0.76 millimeters (mm) (0.0299 in.). The cladding was observed to have crack lengths of 11.3 or 55.1 mm (0.449 or 2.169 in.) after 2,235 or 5,962 hours of exposure, respectively.

The incubation time is defined as the time for full conversion of $UO_{2.4}$ plus the time required for enough U_3O_8 to form and initiate crack propagation along an existing defect on the cladding.

Equation A3-7 can be used to estimate the incubation time (Einziger and Strain, 1986; Stout and Leider, 1994; Ahn, 1996):

$$t_{U3O8}(yr) = 1.56 \times 10^{-19} \exp\left(\frac{44.1\ kcal}{RT}\right) \quad \text{(A3-7)}$$

Figure A3-4 presents the calculated times for complete conversion from UO_2 to $UO_{2.4}$ and from UO_2 to U_3O_8 as functions of temperature using Equations A3-4 and A3-7, respectively. As seen in the figure, the time for conversion decreases exponentially with increasing temperature. Note

that the time for conversion to U_3O_8 could be valid only for temperatures above 230 °C (446 °F) (as marked with a dotted line in the figure), assuming U_3O_8 is the primary phase at this high temperature because U_3O_8 was not normally observed below 230 °C (446 °F) when experiments were conducted in dry air. Below 230 °C (446 °F) for dry air oxidation at low RH (e.g., less than 40 percent RH), $UO_{2.4}$ was normally observed as a primary phase. As mentioned previously, because the kinetics of U_3O_8 formation is believed to be very slow, it could be difficult to detect its formation on a reasonable laboratory time scale (McEachern and Taylor, 1998; Thomas et al., 1993).

Table A3-2 lists the calculated times required to convert to $UO_{2.4}$ or U_3O_8 at various temperatures. The conversion time is relatively short at high temperature (e.g., less than 1 year above 250 °C (482 °F) for U_3O_8). The time is significantly longer for complete conversion to high oxidation phases at low temperature (e.g., more than 1,000 years at 100 °C (212 °F) for $UO_{2.4}$).

Considering that an average grain size has approximately a 10- to 20-µm (3.94×10^{-4} to 7.87×10^{-4} in.) radius for irradiated LWR SNF, individual grains can be fully oxidized to U_3O_8 within several days at high temperature (e.g., 32 days at 300 °C (572 °F)), provided there is enough oxygen present to react. As described earlier, rapid grain boundary oxidation can result in simultaneous matrix oxidation of all grains to U_3O_8.

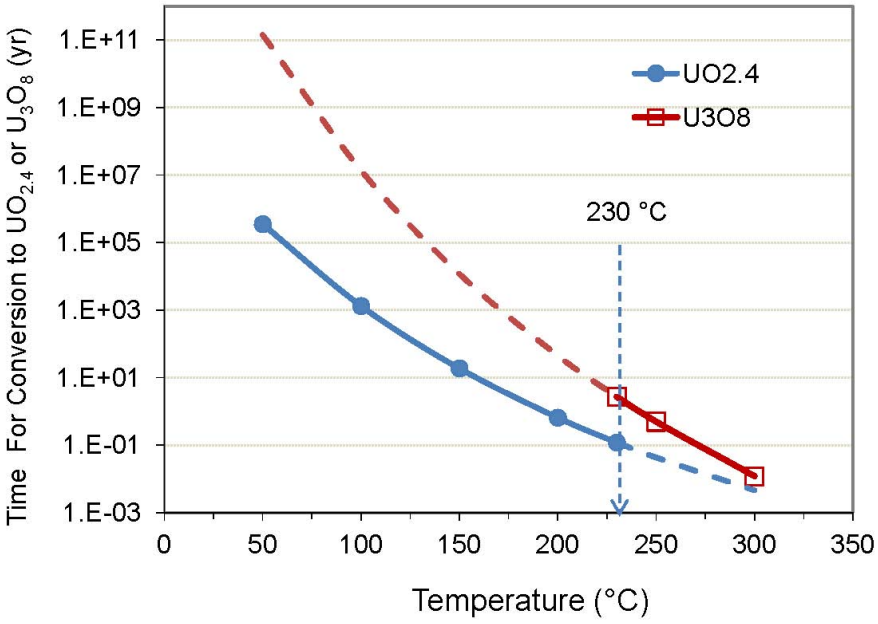

Figure A3-4 Time for conversion from UO_2 to $UO_{2.4}$ and from UO_2 to U_3O_8 as a function of temperature

Table A3-2 Summary of the Calculated Times for Conversion to $UO_{2.4}$ or U_3O_8 as a Function of Temperature		
T (°C)	$t_{2.4}$ (yr)	t_{U3O8} (yr)
50	3.46×10^{5}	1.40×10^{11}
100	1.31×10^{3}	1.35×10^{7}
150	1.86×10^{1}	1.16×10^{4}
200	6.46×10^{-1}	4.44×10^{1}
230	1.19×10^{-1}	2.67
250	4.27×10^{-2}	4.92×10^{-1}
300	4.54×10^{-3}	1.20×10^{-2}

A3.2.2 Relative Humidity

Moisture can affect UO_2 oxidation and hydration. The presence of moisture can lead to production of U_3O_8 or compounds such as UO_3-H_2O hydrates (e.g., schoepite and other UO_3-H_2O compounds). The moisture can also enhance the extent of grain boundary oxidation, as compared to dry air oxidation (Taylor et al., 1995; Wasywich et al., 1993; McEachern and Taylor, 1998). The degree of the moisture effect depended on the moisture content (i.e., RH).

According to Taylor et al. (1995), at low RH (e.g., less than 40 percent), the bulk products of UO_2 oxidation were almost the same as in the case of dry air oxidation (e.g., U_3O_7/U_4O_9 or U_3O_8). The experiments by Taylor et al. (1995) used unirradiated UO_2 in an autoclave under controlled RH and temperature ranging from 200 to 225 °C (392 to 437 °F). At high RH (e.g., greater than 40 percent), the unirradiated UO_2 presented a mixture of U_3O_8 and dehydrated schoepite ($UO_3 \bullet 0.8H_2O$).

Wasywich et al. (1993) conducted a long-term oxidation test (up to 99.5 months) of a used CANDU SNF rod with a 3 mm (0.11811 in.) hole drilled in the cladding both in dry air and moisture-saturated air at 150 °C (302 °F). To attain moisture-saturated air, 100 ml (3.52 oz) of distilled water was added to the testing vessel at 150 °C (302 °F). Surface and microstructure analysis results revealed that, in a moisture environment, the used CANDU SNF was oxidized to mostly dehydrated schoepite with a small amount of U_3O_8. Oxidation occurred through the length of the SNF rod and was preceded by preferential diffusion of oxygen along the grain boundaries. In dry air, oxidation was localized to the defect area, and a 3-mm (0.11811-in.) hole occurred along the fracture free surface of the fragments and expanded into the grain from the surface. The used SNF consisted of mainly U_3O_7 with a small amount of U_3O_8. The authors explained that the different oxidation behavior of the used CANDU SNF in a moisture environment could be the result of radiolytically generated oxidizing radicals, $OH^{\bullet}$, O_2^{-}, H_2O_2, and nitric acid.

Hastings et al. (1985) have estimated that the used CANDU SNF can undergo about 15 percent conversion to U_3O_8 on the SNF surface before sheath splitting occurs. The 15-percent conversion to U_3O_8 was considered to be sufficient to produce the 2-percent diametrical increase required to split the cladding. As compared to the strain threshold for the LWR SNF (6.5 percent) from Einziger and Cook (1985), the threshold value of the used CANDU SNF (2 percent) is quite low and could be associated with the lower burnup of CANDU fuel, resulting in a different structure and chemistry of the SNF as compared to the LWR fuel. Sections A3.4 and A3.5 discuss some insights on the strain and crack propagation in the cladding.

A3.2.3 Spent Nuclear Fuel Burnup

SNF burnup may affect the oxidation behavior of SNF since the structure and chemistry of the SNF can change with burnup level. It is generally observed that SNF is more porous with more grain boundary openings and contains more fission products as burnup increases.

At relatively low temperature, Thomas et al. (1993) and Einziger et al. (1992) previously showed no clear correlation of burnup with oxidation rate of UO_2 to $UO_{2.4}$ in a burnup range of 27 to 48 GWd/MTU at 175 to 195 °C (347 to 383 °F) in air. At high temperature, however, Hanson (1998) reported an incubation time increase for a full conversion to $UO_{2.4}$ with increasing burnup of LWR fragments tested at 305 °C (581 °F). The incubation time increased from about 10 hours to 100 hours for 16 and 42 GWd/MTU, respectively. Hanson (1998) has proposed a possible retardation effect of substitutional cations, such as uranium to plutonium, and fission products to delay or hinder U_3O_8 formation. Herranz and Feria (2009) presented a similar dependence of the incubation time on the burnup for CANDU and LWR fuels (8 to 27 GWd/MTU). The higher burnup delayed U_3O_8 formation at the temperature of 200 to 400 °C (392 to 752 °F). Einziger and Strain (1986) reported an increase in the time required for spallation with powdered U_3O_8 formation, with increased burnup (22.1 to 26.7 GWd/MTU) at 295 °C (563 °F) for PWR fragments.

Note that at burnup values higher than 45 GWd/MTU, a unique rim layer structure is normally observed on the outmost surface of the LWR fuels and could expand to the grain. This rim structure has unique microstructure and chemistry characteristics compared to that of the SNF body in the center. The rim layer is represented by submicron grain size, high porosity with many micropores, and high concentrations of actinides and fission gases (Manzel and Walker, 2002; Rondinella and Wiss, 2010; Bruno and Ewing, 2006). Such a significant change in the rim layer may affect the overall oxidation behavior of the high burnup fuel. However, there are no reported oxidation experiments on fuels with burnup greater than 45 GWd/MTU.

A3.2.4 Temperature and Relative-Humidity-Dependent Spent Nuclear Fuel Oxidation Model

As discussed previously, oxidation or hydration behavior of SNF can depend on the temperature and RH in terms of reaction kinetics and formation of the oxide phase. To delineate the effect of temperature and RH on SNF oxidation and hydration in the canister environment, the following three temperature ranges are defined: $T \geq 230$ °C (446 °F); $150 \leq T < 230$ °C ($302 \leq T < 446$ °F); and $T < 150$ °C (302 °F).

Above 230 °C (446 °F), the primary phase will be U_3O_8 irrespective of the RH, and the oxidized SNF can be assumed to be fully converted to U_3O_8 once $UO_{2.4}$ forms, considering relatively short conversion times at high temperature (e.g., less than 1 year above 250 °C (482 °F) for U_3O_8), as shown in Table A3-2. When temperature ranges between $150 \leq T < 230$ °C ($302 \leq T < 446$ °F), the UO_{2+x} primary phase can be either $UO_{2.4}$ when RH is less than 40 percent or U_3O_8 when RH is greater than 40 percent. Below 150 °C (302 °F), $UO_{2.4}$ can be the primary phase when RH is less than 40 percent, while schoepite ($UO_3 \cdot xH_2O$) will be more prevalent when RH is greater than 40 percent. Table A3-3 summarizes this SNF oxidation model along with the applicable kinetic equations.

Table A3-3 Criteria for Temperature and RH for SNF Oxidation and Hydration in This Study			
Temperature and Relative Humidity		**Primary Phase Considered**	**Applicable Kinetic Equation and Comments**
$T \geq 230$ °C ($T \geq 446$ °F) (independent of RH)		U_3O_8	The equation for $UO_{2.4}$, $w = (2kt)^{0.5}$ (Equation A3-4) can be used, assuming all $UO_{2.4}$ can fully convert to U_3O_8.
$150 \leq T < 230$ °C ($302 \leq T <$ 446 °F)	RH* <40%	$UO_{2.4}$†	$w = (2kt)^{0.5}$
	RH >40%	U_3O_8	Even an appreciable amount of U_3O_8 for the LWR SNF is not normally observed below 230 °C (446 °F) in dry air. There is an indication that eventually U_3O_8 can form in a long-term period with high RH (no clear cutoff period) based on observations of U_3O_8 formation for unirradiated UO_2 and used CANDU SNF tested at $150 \leq T < 230$ °C ($302 \leq T < 446$ °F) with a high moisture level. The equation $w = (2kt)^{0.5}$ can be applicable assuming conversion to U_3O_8 from UO_2.
T <150 °C (T <302 °F)	RH <40%	$UO_{2.4}$†	$w = (2kt)^{0.5}$
	RH >40%	$UO_3 \cdot xH_2O$ ($x < 2$)	The kinetics to form schoepite or other hydrate forms can be used as the dissolution rate obtained from the aqueous condition.‡ The rate ranges from 0.01 to 6.85 mg/m^2/d.

* Relative humidity

† $UO_{2.4}$ could be a quasi-stable intermediate phase that can be eventually converted to U_3O_8 only when the oxygen is available to react with $UO_{2.4}$ to form U_3O_8 during such a long-term period of conversion time (e.g., 1.16×10^4 years required at 150 °C (305 °F)) (see Table A3-2).

‡ In NUREG-1914, "Dissolution Kinetics of Commercial Spent Nuclear Fuels in the Potential Yucca Mountain Repository Environment," issued in 2008 (ADAMS Accession No. ML083120074), the kinetics assume sufficient oxidants are present. Otherwise, the supply of oxidants can control the kinetics.

A3.2.5 Strain Estimate Caused by Spent Nuclear Fuel Swelling

As discussed in Section A3.2.1, oxidation of UO_2 to U_3O_8 can generate stress on cladding as U_3O_8 swells (36 percent when there is 100-percent conversion to U_3O_8). This can split the cladding and propagate the crack once the strain reaches the threshold value of 6.5 percent of strain with 100-percent conversion to U_3O_8 at the defected area on the LWR SNF rod (Einziger and Cook, 1985). In Einziger and Cook (1985), a volume expansion of 5.1 percent was correlated with approximately 25 percent conversion of UO_2 to U_3O_8. A strain of 2 percent was also correlated to a 50-percent conversion.

As expected and also observed from the previously described experiments, the strain produced on the cladding was closely related to the amount of U_3O_8 formed in the SNF pellet. Thus, the present study made an attempt to estimate the strain as a function of conversion fraction to U_3O_8 using a grain size model.

Because the volume (V) of a sphere shape of grain is proportional to the cube of grain radius (r) (i.e., $V = 4/3\ \pi \times r^3$), a ratio of the grain radius when there is an increase from r_1 to r_2 can be expressed as follows:

$$\text{ratio of grain radius} = r_2/r_1 = (V_2/V_1)^{1/3} \quad \text{(A3-8)}$$

where

r_1 and r_2 = grain radius before and after volume increase with U_3O_8 formation, respectively
V_1 and V_2 = volume before and after volume increase with U_3O_8 formation, respectively

Assuming a linear increase in the volume with the U_3O_8 conversion fraction of δ based on a 36-percent increase when UO_2 to U_3O_8 conversion is 100 percent, the volume increase ($\Delta V = V_2 - V_1$) in percent can be calculated as follows:

$$\Delta V = \delta \times 0.36 \times 100 \quad \text{(A3-9)}$$

Thus, a radius increase in percent is expressed below:

$$\Delta r = (\Delta V^{1/3} - 1) \times 100 \quad \text{(A3-10)}$$

Table A3-4 lists the calculated volume and radius increases as a function of conversion fraction according to Equations A3-9 and A3-10, respectively.

As seen in Table A3-4, with 100-percent conversion to U_3O_8, the grain radius can increase up to 10.8 percent and the volume can increase 36 percent. If a linear increase in radius based on the grain size model in this study can represent a strain on the SNF pellet, the radius increase of 10.8 percent should be high enough to split the cladding, as estimated from the LWR SNF rod experiment of Einziger and Cook (1985). However, as mentioned previously, the strain required to split and propagate the defects was estimated to be 6.5 percent with 100-percent conversion for LWR fuel, which is less than the value of 10.8 percent calculated in this study. Similarly, the strains associated with conversion to 20 and 50 percent were estimated to be about 1 and 2 percent, respectively, in the same literature. These are consistently lower than the strains of 2.3 and 5.7 percent for conversion to 20 and 50 percent, respectively, calculated in this study.

Table A3-4 Volume and Radius Increases in a Grain as a Function of Conversion Fraction to U_3O_8

Conversion Fraction to U_3O_8 δ (no unit)	Volume Increase ΔV (%)	Radius Increase Δr (%)
1.00	36.0	10.8
0.86	31.0	9.4
0.58	20.9	6.5
0.50	18.0	5.7
0.25	9.0	2.9
0.20	7.2	2.3
0.15	5.4	1.8

It is not surprising to present such a relatively low strain from the real SNF pellet compared to the strain based on the grain size model in this study. There are several reasons for the differences in strain values between those determined from measurements on SNF pellets and the theoretical estimate based on a grain size. The difference could be the result of an appreciable amount of porosity in the SNF pellet, normally 5 percent (Bailey and Tokar, 1982). It is most likely that the free space with porosity can accommodate a certain amount of net volume increase (mathematically as high as 5 percent) to reduce a stress buildup from U_3O_8 formation. An intermediate phase of U_4O_9 that is not considered in the grain size model can play a role in determining the strain because the density of U_4O_9 (11.30 g/cm^3 (0.408/in.^{3})) is slightly higher than that of UO_2 (10.96 g/cm^3 (0.396 lb/in.^{3})), leading to a volume reduction (approximately 2 percent) when oxidized from UO_2 to U_4O_9 (BSC, 2005). Other features present in the irradiated fuel, such as cracks and grain boundary openings with burnup, can also dissipate stresses.

A3.2.6 Crack Propagation

Defects (e.g., pinholes or throughwall hairline crack) in the cladding can grow if the exposed SNF is oxidized to form more U_3O_8 near the defect. EPRI (1986) estimated crack growth rates for LWR SNFs (8 to 38 GWd/MTU burnup) when defects of 8 to 760 μm (3.15×10^{-4} to 2.99×10^{-2} in.) long are present. The growth rate ranged from 3×10^{-4} to 2.3×10^{-3} centimeter per minute (cm/min) (1.18×10^{-4} to 9.06×10^{-4} inch per minute (in./min)) at temperatures of 250 to 360 °C (482 to 680 °F). The strain required for crack propagation was estimated to be 6.5 percent for a large-size defect (i.e., 760 μm (2.99×10^{-2} in.)). For a relatively small size of defect (i.e., 8 to 37 μm (0.32 to 1.46×10^{-3} in.)), the threshold strain was estimated to be less than 1 percent. The difference in the threshold strain value was not clearly stated. For the case of CANDU fuels, Hastings et al. (1985) have estimated that about a 2-percent strain could be a threshold for cladding splitting, corresponding to a 15-percent conversion to U_3O_8 on the outermost SNF surface. Novak et al. (1983) reported that about a 2-percent strain was necessary for initiation of crack growth on the used CANDU fuel. Even though no reported studies explain why such a difference in the strain required for splitting the cladding was observed, many factors, such as low burnup of CANDU SNF and defect shape and size, can result in different observations. Because the SNF in the United States is LWR fuel, the evaluation of the crack propagation is based on the strain for the LWR SNFs estimated in EPRI (1986) for this study.

Adopting the Arrhenius-type equation for crack propagation, the crack propagation by the oxide formation front velocity can be expressed as follows (BSC, 2007):

$$V\ (\mathrm{cm/min}) = V_o(\mathrm{cm/min}) \times \exp\left(\frac{104.8\ \mathrm{kJ}}{RT}\right) \qquad \text{(A3-11)}$$

where

V_o = coefficient (4.98×10^6 cm/min (1.96×10^6 in./min))
R = gas constant
T = temperature (K)

Figure A3-5 presents the calculated velocity according to Equation A3-11. As shown in this figure, the velocity at high temperatures (e.g., 230 °C (446 °F)) is high enough to propagate the defects (hole or crack) within a relatively short time once the strain reaches the threshold value, such as 6.5 percent for the case of the 0.76-mm (2.99×10^{-2}-in.) hole. For example, the crack

can propagate to 10 cm (3.9 in.) in 2,560 hours (0.3 year) at 230 °C (446 °F). Thus, if the oxidation can continue with enough oxygen to form U_3O_8, the crack can grow further in length and width to the maximum extent possible. However, the amount of oxidants (i.e., oxygen) in the canister would be limited because of the finite amount of residual water.

Depending on the available amount of oxidant (oxygen), the amount of U_3O_8 formed at the defect area will vary. If the growth, as modeled using Equation A3-5, to form U_3O_8 is slow enough and the oxidant is abundant, the growth kinetics will control the rate of U_3O_8 formation. But if the oxidant is limited because of a limited amount of oxygen, the production rate of oxidant from the radiolysis process and subsequent reactions will control the overall reaction to form U_3O_8.

In NRC (2007), grossly breached SNF cladding is considered to be any cladding breach of a few micrometers (4×10^{-5} in.), such as greater than 1 mm (4×10^{-2} in.) in crack width. The width is determined by converting strain to the circular length of the rod. The increment of the circular length from the initial circular length is crack width. This appears to be conservative in terms of release because the experiment and modeling of the SNF fragments showed that at least 2 to 3 mm (7.89×10^{-2} to 1.18×10^{-1} in.) is required to release SNF fines. Kohli et al. (1985) reported that the initial crack size of the damaged LWR SNF ranged from 0.4 to 7 cm (0.157 to 2.76 in.), and the average length was 3.5 cm (1.38 in.). After 2,100 hours of exposure in air at 325 °C (617 °F), the crack propagated up to about 10 cm (3.9 in.) in the axial direction. Einziger and Cook (1985) have reported a crack width increase for the initial defect size of the 0.76-mm (2.99×10^{-2} in.) hole on the BWR SNF.

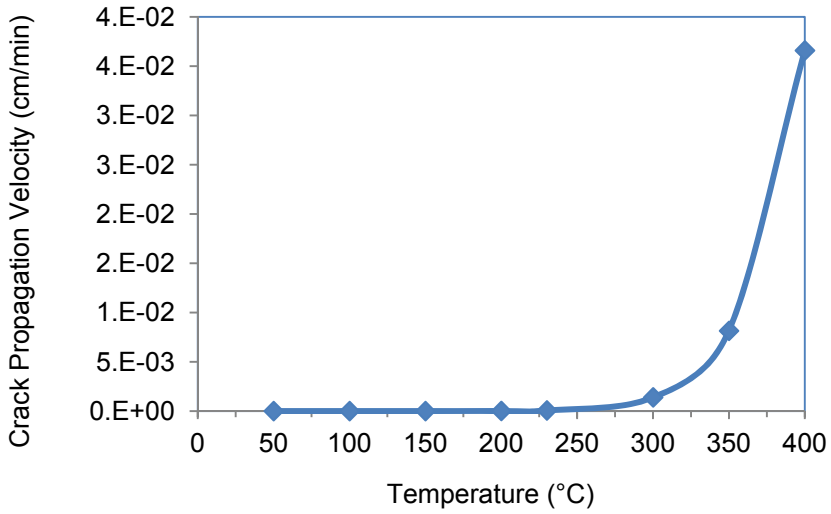

Figure A3-5 Crack propagation velocity as a function of time for LWR SNF (BSC, 2007)

With oxidation of the SNF rods in air at 229 °C (444 °F), the rods were breached at the defect sites, and the crack width from the two different locations of the holes increased either 1.37 mm (0.054 in.) in width by 1.128 cm (0.444 in.) in length after 2,235 hours or 4.55 mm (0.179 in.) in width by 5.51 cm (2.17 in.) in length after 5,962 hours. The area affected by formation of U_3O_8 near the defect was estimated to be approximately plus or minus 3 cm (plus or minus 1.2 in.) in the axial direction when tested at 229 °C (446° F) after 5,962 hours of exposure in air. Once the SNF rod splits at a defect from SNF swelling, cracks can propagate quickly at high temperature. The initial crack size of 3.5 cm (1.4 in.) long and 1 mm (4×10^{-2} in.) wide, assuming rod rupture, could be an example of the crack size that can be used in estimating the number of pellets affected (oxidized) near the crack. Limited data suggest that an affected area of approximately plus or minus 3 cm (plus or minus 1.2 in.) in the axial direction will have a crack width of a few millimeters with 6.5 percent of the strain threshold. Assuming that gross rupture can occur underneath an initial cladding defect area (when U_3O_8 formation is complete) and reach a crack width of a few millimeters, further crack propagation can give insights into whether there will be significant SNF matrix dispersion (i.e., retrievability concern).

A4. INTEGRATED ANALYSIS OF CLADDING AND SPENT NUCLEAR FUEL OXIDATION CAUSED BY RADIOLYSIS OF THE RESIDUAL WATER

The objective of the integrated analysis is to estimate the extent of cladding and SNF oxidation that could occur as a result of residual water in the canister. The amount of residual water will decrease with time primarily because of radiolysis and consumption of radiolysis products by cladding and SNF oxidation. As outlined in Section A2, the rate of radiolysis depends on the SNF burnup and the radiation field, which is expected to have both temporal and spatial variations. The radiolysis product of water would include hydrogen, oxygen, hydrogen peroxide, and other intermediate species. It is assumed that the radiolysis of the water produces primarily hydrogen and oxygen. Most intermediate species are short lived, including spontaneous decomposition after radiolysis (e.g., hydrogen peroxide) (Van Konynenburg, 1986). Data in the oxidation of SNF and cladding are similar both with and without intermediate species. For example, tests were done with and without the intermediate species, including corrosion of unirradiated cladding and cladding corrosion in reactor (Hillner et al., 1994; Nishino et al., 1997) and oxidation of irradiated SNF. Therefore, this work assumes that the oxygen would oxidize the cladding and any exposed fuel. The extent of SNF and cladding oxidation resulting from the presence of oxygen in the canister is estimated using the quantitative analysis.

A4.1 Integration Model

The SNF and cladding oxidation models, presented in Section A3, are implemented using a computer code developed in MATLAB® in each time step of the integration. This is referred to as the integration model. This model accounts for both temporal and spatial variation of temperature and RH and their effects on cladding and SNF oxidation. The model is used in each time step to simulate various cases to assess the uncertainties in water content, rate of radiolysis, and thermal characteristics of the cask system (i.e., temperature) on the SNF and cladding oxidation. Section A4.1 describes the model, and Section A4.2 describes the model parameters. The model is simulated for various cases, which Section A4.3 describes. The model's results, which Section A4.4 presents, include an evaluation of flammability. Section A4.5 discusses and summarizes the model results. This section also defines the model assumptions, wherever applicable.

A4.1.1 Inputs

The model inputs include cask parameters, SNF temperature at the time of loading, residual water amount, cask internal volume, number of SNF assemblies, SNF rods per SNF assembly, dimensions of each SNF rod and SNF pellet, number of fragments per pellets, size of each grain in an SNF pellet, density of various UO_{2+x} phases, and void fraction in each SNF pellet. Because the SNF and cladding temperatures are expected to vary spatially, the canister inside the cask volume is divided into five zones, as detailed in Section A1. The inputs also include the radiolysis rate of water over the assumed storage time of 300 years. In each zone, it is assumed that the SNF and cladding temperatures are uniform. It is also assumed that the SNF temperature asymptotically approaches the ambient temperature in 300 years. The initial SNF and cladding temperatures and volume fraction of each zone are input to the model. A fraction of failed cladding percentage is also input. This fraction is used to calculate the number of exposed SNF pellets available for oxidation. For example, a failed cladding fraction of 0.1 percent amounts to failure of one SNF rod out of 1,000. The failed rod is assumed to have a crack of a certain length that is specified in the model.

A4.1.2 Calculation Sequences

In the initial step, storage time is divided into several time steps. Before conducting sequential calculations as a function of time, the following calculations are conducted:

(1) Cladding surface areas in each zone are estimated based on the volume fraction in each zone. Cladding surface areas are estimated by multiplying the zone volume fraction by the total surface area of the cladding. The number of SNF rods in each zone is also estimated by multiplying the zone volume fraction with total rods in a canister.

(2) The number of failed SNF rods in each zone is estimated by multiplying the number of SNF rods in each zone with the failure, which is the same as the failure of the cladding. The model inputs include cladding failure of 0.1 and 0.01 percent and 4,368 SNF rods. The cladding failure of 0.1 and 0.01 percent yield four and one failed rods, respectively. It is assumed that there is one failed rod in each of the hotter zones (i.e., Zones 1 to 4) for the case of 0.1 percent failure. Similarly, for the 0.01 percent failure, the failed rod is assumed to be located in Zone 1.

(3) The number of affected SNF pellets exposed to the canister environment resulting from failed cladding in a zone is estimated. The literature (Einziger and Cook, 1985) indicates that the affected SNF pellets with a crack of a specified length in an SNF rod include pellets located 3 cm (1.2 in.) on either side of the crack, as well as all pellets directly underneath the axial length of the crack. Thus, effective crack length for SNF oxidation is equal to the dimension of the crack along the length of the SNF rod plus 6 cm (2.4 in.). Figure A4-1 presents a schematic diagram depicting a crack oriented axially along an SNF rod. As seen in the figure, the effective crack length for SNF oxidation exceeds the crack length. The number of affected SNF pellets in a zone is calculated as follows:

$$N_{pellets\_zone} = floor\left(\frac{\text{effective crack length}}{\text{pellet length}} \times \text{number of failed SNF rods in a zone}\right) \qquad \text{(A4-1)}$$

where $N_{pellets\_zone}$ denotes the number of affected pellets in a zone. The *floor* function in Equation A4-1 rounds the calculated number within the parentheses down to the lowest integer.

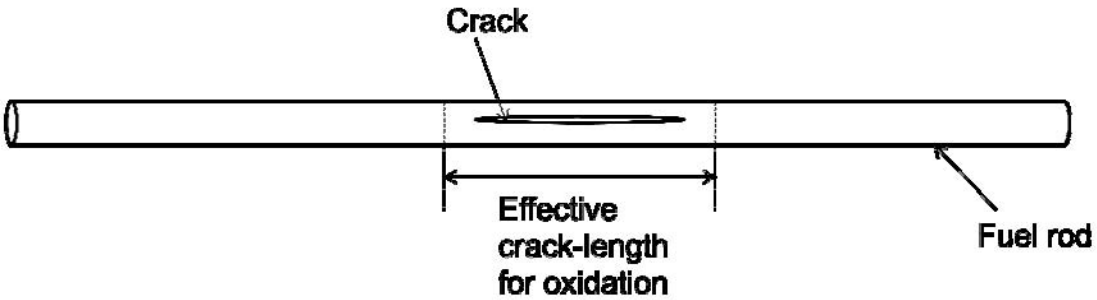

Figure A4-1 Schematic representation of a crack oriented along the length of the SNF rod. The effective crack length for SNF oxidation Is equal to crack length plus 6 cm (2.36 in.).

(4) The literature (Einziger and Cook, 1985) also indicates that SNF pellets directly underneath a crack tend to be oxidized sooner than SNF pellets not directly exposed but underneath the effective crack length for oxidation. Considering this, it is assumed that the SNF pellets directly underneath the crack undergo oxidation before the other SNF pellets. It is also assumed that the oxidation of the other pellets begins only after the directly exposed SNF pellets have been completely oxidized. The number of directly exposed SNF pellets in a zone is determined as follows:

$$N_{directly-exposed\_pellets\_zone} = floor\left(\frac{\text{crack length}}{\text{pellet length}} \times \text{number of failed SNF rods in a zone}\right) \quad \text{(A4-2)}$$

where $N_{directly-exposed\_pellets\_zone}$ denotes the number of directly exposed SNF pellets in a zone. The number of other SNF pellets in a zone is calculated by subtracting the number of directly exposed SNF pellets from the number of affected SNF pellets.

(5) The exposed area for SNF oxidation is also estimated. An SNF pellet is expected to fragment into 10 to 30 pieces during the reactor operation. There are two possible mechanisms for oxygen contacting the exposed fuel: (1) oxygen diffuses through grain boundaries and thus each SNF grain is oxidized simultaneously and (2) contact occurs through the exposed surface of each SNF fragment. For the LWR fuel, the first case is referred to as the base case, whereas the second case is considered for uncertainties associated with the SNF oxidation model described in Section A3.2. For the first mechanism (i.e., base case), the surface area for SNF oxidation per pellet is calculated by determining the number of grains per pellet and then multiplying it by the surface area of each grain. The number of grains per pellet is calculated as follows:

$$N_{grains\_per\_pellet} = floor\left[\frac{V_{pellet} \times (1 - f_{void})}{V_{grain}}\right] \quad \text{(A4-3)}$$

where

$N_{\text{grains}\_per\_pellet}$ = number of grains per pellet
V_{pellet} = volume of a pellet
V_{grain} = volume of a grain
f_{void} = void volume fraction in a pellet

The corresponding surface area per pellet for SNF oxidation for the first mechanism is calculated as follows:

$$A_{oxidation\_per\_pellet\_fm} = N_{grains\_per\_pellet} \times A_{grain} \quad \text{(A4-4)}$$

where

$A_{oxidation\_per\_pellet\_fm}$ = surface area for SNF oxidation per pellet for the first mechanism
A_{grain} = surface area of each grain

For the second mechanism of oxygen contacting each SNF fragment, the surface area for SNF oxidation per pellet is determined as follows:

$$A_{oxidation\_per\_pellet\_sm} = N_{fragments\_per\_pellet} \times A_{fragment} \quad \text{(A4-5)}$$

where

$A_{oxidation\_per\_pellet\_sm}$	=	surface area for SNF oxidation per pellet for the second mechanism
$A_{fragment}$	=	surface area of a fragment

Each cylindrical SNF pellet is assumed to be fragmented into $N_{fragments\_per\_pellet}$. Figure A4-2 presents a schematic diagram depicting a fragmented SNF pellet. As seen in the figure, the pellet fragments along the azimuthal direction.

(6) The temperature of each zone is calculated as a function of time (see Section A1.2.3).

(7) It is implicitly assumed that the amount of residual water does not affect the SNF and cladding temperatures. The SNF and cladding temperatures are assumed to vary with time according to Equation A4-6, which is the same as Equation A1-3. Section A1 details the justification for using the equation.

$$T_{fuel\_cladding\_zone} = (T_{mean} - T_{ambient})exp(-at) + T_{ambient} \quad \text{(A4-6)}$$

where

$T_{fuel\_cladding\_zone}$	=	temperature of SNF and cladding in a zone
T_{mean}	=	mean value of initial temperature in a zone at the time of SNF loading
$T_{ambient}$	=	ambient temperature
a	=	thermal decay constant

(8) Before going to the next time step, the RH in each zone is also calculated at the time of loading and at the first time step. It is assumed that the water is distributed in each zone according to the following equation:

$$n_{water\_zone} = n_{water} \times f_{zone} \quad \text{(A4-7)}$$

where

n_{water_zone}	=	moles of water in a zone
n_{water}	=	moles of water in the canister
f_{zone}	=	volume fraction of a zone

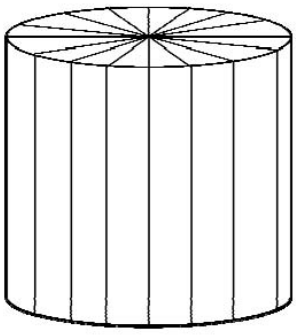

Figure A4-2 Schematic representation of a cylindrical SNF pellet fragmented into 16 pieces

The partial pressure of water in each zone is calculated using the ideal gas law, and RH is calculated by dividing the partial pressure by the saturated pressures. Section A1 further details the RH calculations.

(9) The calculations continue in the next time steps. The following calculations are conducted at each time step:

(a) The amount of oxygen produced by radiolysis between the two time steps is calculated. The SNF and cladding temperatures between the two time steps in a zone are assumed to be equal to the average of the temperatures at the two time steps. Similarly, RH in a zone between the two time steps in a zone is assumed to be equal to the average of the relative humidities at the two time steps.

(b) The amount of oxygen consumed by the SNF pellets and cladding between the two time steps using the rate models in each zone is calculated. If the total oxygen produced by radiolysis is more than the oxygen consumed by SNF and cladding oxidation in all of the zones, the calculations are continued to the next time step. However, if the total oxygen consumed by SNF and cladding oxidation in all of the zones is more than the oxygen generated by the radiolysis, the radiolysis-controlled SNF and cladding oxidation model is applied. This is explained in the next step.

(c) In the radiolysis-controlled oxidation model, the amount of oxygen SNF and cladding oxidation consumed in Zone 5, the coldest zone, is estimated. If the moles of oxygen generated from radiolysis in Zone 5 are less than the amount needed for SNF and cladding oxidation, the amount of oxygen generated between the two time steps is divided between the SNF and cladding according to Equations A4-8 and A4-9 as follows:

$$n_{oxygen\_fuel\_oxidation\_zone\_5} = \left(\frac{A_{exposed\_fuel\_zone\_5}}{A_{exposed\_fuel\_zone\_5} + A_{clad\_zone\_5}}\right) \times n_{oxygen\_generated\_zone\_5} \quad \text{(A4-8)}$$

$$n_{oxygen\_clad\_oxidation\_zone\_5} = \left(\frac{A_{clad\_zone\_5}}{A_{exposed\_fuel\_zone\_5} + A_{clad\_zone\_5}}\right) \times n_{oxygen\_generated\_zone\_5} \quad \text{(A4-9)}$$

where

$n_{oxygen\_fuel\_oxidation\_zone\_5}$	=	moles of oxygen consumed by SNF oxidation in Zone 5
$n_{oxygen\_clad\_oxidation\_zone\_5}$	=	moles of oxygen consumed by cladding oxidation in Zone 5
$n_{oxygen\_generated\_zone\_5}$	=	moles of oxygen generated between two time steps in Zone 5
$A_{exposed\_fuel\_zone\_5}$	=	surface area of the exposed SNF in Zone 5
$A_{clad\_zone\_5}$	=	surface area of cladding in Zone 5

However, if the moles of oxygen generated from radiolysis in Zone 5 are greater than the oxygen needed for SNF and cladding oxidation, the leftover oxygen in Zone 5 is calculated as follows:

$$n_{oxygen\_leftover\_zone\_5} = n_{oxygen\_generated\_zone\_5} - n_{oxygen\_fuel\_oxidation\_zone\_5} - n_{oxygen\_clad\_oxidation\_zone\_5} \quad \text{(A4-10)}$$

where $n_{oxygen\_leftover\_zone\_5}$ denotes moles of oxygen not consumed by cladding and SNF oxidation in Zone 5. These moles of oxygen are added to the moles of oxygen generated in Zone 4. These effective moles of oxygen present in Zone 4 between the two time steps are represented by the values determined by Equation A4-11 as follows:

$$n_{oxygen\_present\_zone\_4} = n_{oxygen\_generated\_zone\_4} + n_{oxygen\_leftover\_zone\_5} \quad \text{(A4-11)}$$

where

$n_{oxygen\_present\_zone\_4}$	=	moles of oxygen present in Zone 4 for SNF and cladding oxidation
$n_{oxygen\_generated\_zone\_4}$	=	moles of oxygen generated by radiolysis in Zone 4 between two time steps

Again, the moles of oxygen consumed by SNF and cladding oxidation in Zone 4 are calculated. If the moles of oxygen present in Zone 4 are less than the amount needed for SNF and cladding oxidation, the moles of oxygen are partitioned between the cladding and SNF according to Equations A4-12 and A4-13 as follows:

$$n_{oxygen\_fuel\_oxidation\_zone\_4} = \left(\frac{A_{exposed\_fuel\_zone\_4}}{A_{exposed\_fuel\_zone\_4} + A_{clad\_zone\_4}}\right) \times n_{oxygen\_present\_zone\_4} \quad \text{(A4-12)}$$

$$n_{oxygen\_clad\_oxidation\_zone\_4} = \left(\frac{A_{clad\_zone\_4}}{A_{exposed\_fuel\_zone\_4} + A_{clad\_zone\_4}}\right) \times n_{oxygen\_present\_zone\_4} \quad \text{(A4-13)}$$

where

$n_{oxygen\_fuel\_oxidation\_zone\_4}$	=	moles of oxygen consumed by SNF oxidation in Zone 4
$n_{oxygen\_clad\_oxidation\_zone\_4}$	=	moles of oxygen consumed by cladding oxidation in Zone 4
$A_{exposed\_fuel\_zone\_4}$	=	surface area of the exposed SNF in Zone 4
$A_{clad\_zone\_4}$	=	surface area of cladding in Zone 4

Otherwise, the excess moles of oxygen are transferred to Zone 3. This process is repeated for the remaining three zones.

(d) A counter is used to keep track of the moles of oxygen produced by radiolysis and consumed by cladding and SNF oxidation throughout the preceding time steps. If the moles of oxygen produced by radiolysis reach a plateau, and the difference between moles of oxygen produced by radiolysis and the total moles of oxygen consumed by SNF and cladding oxidation is less than a specified tolerance limit, calculations are stopped.

(e) When the criterion to stop the calculations is not met, a computational check is conducted to determine whether the directly exposed SNF pellets in a zone have been completely oxidized. If the directly exposed SNF pellets have been completely oxidized in a zone, the other SNF pellets undergo oxidation in the next time step. A computational check is also conducted to determine whether the affected SNF pellets (i.e., the directly exposed and other SNF pellets) have been completely oxidized in a zone. If the affected SNF pellets have been completely oxidized, only cladding oxidation is implemented in the next time step.

(f) Steps (a) through (e) are repeated until the net oxygen production criterion is met and the calculations are stopped.

A4.1.3 Outputs

The integrated model calculates the extent of SNF and cladding oxidation and the moles of oxygen consumed by both SNF and cladding in each zone. The model also calculates SNF and cladding temperatures; RH; and the moles of oxygen, hydrogen, and water in the canister as a function of time.

A4.2 Model Parameters

This section provides the values of the different parameters used in the model. Some of parameters are fixed while others are varied in the model. Table A4-1 lists the model parameters with fixed values.

The model results are presented for several potential scenarios that account for uncertainties in the amount of residual water, radiolysis kinetics, decay heat of the SNF loaded in the canister, rate of temperature decay of fuel, and mechanisms for oxygen contacting the exposed fuel. The following sections describe these uncertainties and the inputs used to model them.

A4.2.1 Residual Water Amount (Section A2.1)

The residual water amount could vary between 1 and 55 moles. The model used specific values of 5.5, 17.4, and 55 moles of residual water. The next section discusses the potential effects of residual water when the amount is less than 5.5 moles.

A4.2.2 Radiolysis Kinetics (Section A2.1.3)

The residual water could be completely decomposed within 4.77 to 71.62 years. The rate of radiolysis would determine the rate of production of oxidizing species, such as oxygen and hydrogen peroxide. Moreover, because the oxidizing species are consumed during SNF and

Table A4-1 Cladding, Fuel, and Canister Parameter Values Used in the Integration Model	
Parameter	**Values**
Canister void volume	2.1 m^3 (74.2 ft^3)
Number of SNF assemblies	21
SNF rods per assembly	208 in 15 × 15 Babcock & Wilcox SNF Assembly
SNF rod length	3.9 m (10.2 ft)
SNF rod outer diameter	10.92 mm (0.43 in.)
Pellet diameter	9.36 mm (0.37 in.)
Pellet length	15.24 mm 0.6 in.)
Axial length of a crack on a failed rod	3.5 cm 1.38 in.)
SNF pellet void volume	5%
UO_2 density	10.96 g/cm^3 (684 lb/ft^3)
$UO_{2.4}$ density	11.30 g/cm^3 (705 lb/ft^3)
U_3O_8 density	8.35 g/cm^3 (521 lb/ft^3)
$UO_3 \cdot xH_2O$* (x<2) density	4.89 g/cm^3 (305 lb/ft^3)
UO_2 grain shape	spherical
UO_2 grain radius	10 μm (3.9×10^{-4} in.)
Volume fraction Zones 1, 2, 3, 4, and 5	19, 33, 33.7, 12.4, and 1.9%, respectively
ZrO_2 density	5.6 g/cm^3 (350 lb/ft^3)
* In the integration model simulation, x is assumed to be zero.	

cladding oxidation, the rate of radiolysis is affected by the SNF and cladding oxidation. Considering this, the rate of radiolysis as discussed in Section A2.2 is input using linear and exponential kinetic rates. For the linear rate, the water, oxygen, and hydrogen concentrations are calculated using Equations A4-14, A4-15, and A4-16 as follows:

$$n_{water}(t) = n_{water}(1 - bt) \quad \text{(A4-14)}$$

$$n_{oxygen}(t) = \frac{n_{water} - n_{water}(t)}{2} \quad \text{(A4-15)}$$

$$n_{hydrogen}(t) = n_{water} - n_{water}(t) \quad \text{(A4-16)}$$

where

$n_{water}(t)$ = moles of water at time *t*
n_{water} = moles of residual water
b = constant
t = time in years
$n_{oxygen}(t)$ = moles of oxygen at time *t*
$n_{hydrogen}(t)$ = moles of hydrogen at time *t*

The values of b are 1/4.77 and 1/71.62 for the decomposition periods of 4.77 and 71.62 years, respectively. The values of b are selected such that complete radiolytic decomposition of the residual water occurs either in 4.77 years or 71.62 years. For the exponential kinetic rate, the amount of water is calculated using Equation A4-17 as follows:

$$n_{water}(t) = n_{water} exp(-ct) \quad \text{(A4-17)}$$

where c is a constant with values input as −1.9290 and −0.12860 for 99.99 percent decomposition of the residual water in 4.77 years and 71.62 years, respectively. Equations A4-15 and A4–16 are used to calculate oxygen and hydrogen moles for the exponential kinetic rates.

A4.2.3 Spent Nuclear Fuel and Cladding Temperature (Sections A1.1.3.2 and A1.1.3.3)

The SNF temperature could significantly affect the SNF and cladding oxidation in the dry storage cask system. The model considers this uncertainty by inputting two sets of SNF and cladding initial temperatures in different zones. These values are assumed to be SNF and cladding temperatures at the time of canister loading and are referred to as low- and high-end SNF and cladding initial temperatures. These values, provided in Table A1–1, are relisted in Table A4-2 for convenience. These two conditions are referred to as low- and high-end temperature conditions.

A4.2.4 Decay Rate of Spent Nuclear Fuel and Cladding Temperature (Section A1.2)

Equation A4-6 is used to model the evolution of SNF and cladding temperatures. Uncertainties in the thermal characteristics of a storage cask system would affect the evolution of SNF and cladding temperatures. To account for this uncertainty, two values of the thermal decay constant are input to the model. The value of a in Equation A4-6 is set equal to either 0.023 or 0.064. Section A1 provides detailed justification for the two values of a in Equation A4-6. The SNF and cladding temperatures decrease more slowly with time for a equal to 0.023 than 0.064.

A4.2.5 Initial Cladding Failure

The model uses cladding failure values of 0.1 and 0.01 percent. These values are based on the information on cladding failure presented in Section A3.

A4.2.6 Mechanisms for Oxygen Contacting the Exposed Spent Nuclear Fuel

The integrated model use one of the following two processes for oxygen contacting the exposed fuel (for chemical reaction): (1) oxygen diffuses through grain boundaries (also referred to as the base case) and thus each grain is oxidized simultaneously and (2) oxygen diffuses through the surface of each SNF fragment. These two processes are used to model uncertain surface areas exposed for oxidation.

Table A4-2 Values of Low- and High-End SNF and Cladding Mean Initial Temperature (T_{mean} in Equation A4-6) in the Model

Zone	Mean Values of Low-End SNF and Cladding Initial Temperatures, K (°F)	Mean Values of High-End SNF and Cladding Initial Temperatures, K (°F)
1	575 (575.3)	673 (751.7)
2	525 (485.3)	623 (661.7)
3	475 (395.3)	573 (571.7)
4	425 (305.3)	523 (481.7)
5	375 (215.3)	481 (406.1)

A4.3 Model Simulations

The model is run with various combinations of the parameters listed in Table A4-3 to evaluate several cases. These cases, which are listed in Table A4-4, correspond to various uncertainties discussed previously.

Table A4-3 List of Varying Parameters and Their Values in the Integrated Model

Parameter	Value
SNF and cladding initial temperature	Low- or high-end SNF and cladding initial temperature (as listed in Table A4-2)
Initial cladding failure	0.1 or 0.01%
Radiolysis kinetics	Exponential decomposition in 4.77 years, linear decomposition in 4.77 years, exponential decomposition in 71.62 years, and linear decomposition in 71.62 years
Residual water amount*	5.5, 17.4, or 55 moles
Thermal decay constant	a equal to 0.023 or 0.064
Mode of oxygen contacting the fuel	Either through grain boundaries or fragment surface
* The analysis did not consider 1 mole of water.	

Table A4-4 Values of Varying Parameters and Corresponding Cases for Presenting the Simulation Data of the Integrated Model

Case No.	Values of Varying Parameters Listed in Table
1	The residual water amounts of 5.5, 17.4, and 55 moles. Cladding failure of 0.1 and 0.01. Low- and high-end initial SNF temperature. Oxygen diffusion through grain boundaries and contacting each grain simultaneously (i.e., the base case). Thermal decay constant a equal to 0.023. Exponential decomposition of the residual water in 4.77 years from radiolysis.
2	All parameters are the same as Case 1 except linear decomposition of the residual water in 4.77 years from radiolysis.
3	All parameters are the same as Case 1 except exponential decomposition of the residual water in 71.62 years from radiolysis.
4	All parameters are the same as Case 1 except linear decomposition of the residual water in 71.62 years from radiolysis.
5	17.4 moles of residual water. Cladding failure of 0.1 percent. Low-end initial SNF temperature. Oxygen diffusion through grain boundaries (i.e., the base case). Linear decomposition of the residual water in 71.62 years from radiolysis. Thermal decay constant a equal to 0.064. Case 4 data are used for comparison.
6	17.4 moles of residual water. Cladding failure of 0.1 percent. Low-end initial SNF and cladding temperatures. Exponential decomposition of the residual water in 4.77 years from radiolysis. Thermal decay constant a equal to 0.023. Oxygen diffusion through the surface of SNF pellet fragments. An SNF pellet is considered to have fragmented into 10 pieces. Case 1 data are used for comparison.

The only difference between the first four cases is the selection of the radiolysis model. Cases 1 to 4 can be seen as combinations of several subcases because each case includes a number of varying parameters.

Case 5 is constructed to highlight the effect of the thermal decay constant on cladding and SNF oxidation. In this case, the radiolysis kinetic model of linear decomposition of the residual water in 71.62 years is selected because the decay constant is expected to maximally influence SNF and cladding oxidation when water decomposes over longer periods. This is expected because SNF and cladding temperatures decay more rapidly when a equals 0.064 compared to a being equal to 0.023 during the decomposition period of 71.62 years. Because SNF and cladding temperatures influence SNF and cladding oxidation rates, the extent of SNF and cladding oxidation for the two values of the decay constant is expected to differ. Case 4 data are used for comparison and highlight the effect of the thermal decay constant on cladding and SNF oxidation.

Case 6 is constructed to estimate the effect of the mode by which oxygen contacts the fuel. Case 1 data are used for comparison.

A4.4 Model Results

Cladding failure would be expected to cause an SNF rod to develop a crack. The cladding failure and length of the crack per failed rod parameter values are used to determine the number of exposed SNF pellets in each zone. Table A4-5 summarizes the calculated number of failed rods and corresponding exposed SNF pellets. As long as cladding failure is specified in a case, the number of failed rods and corresponding number of exposed pellets remain unchanged.

Similarly, the surface areas of the exposed cladding in each zone also remain unchanged within a simulation. The surface area of the cladding in each zone is directly proportional to the volume fraction of each zone. The exposed cladding surface area was calculated by multiplying the total surface area by the volume fraction of each zone. Table A4-6 provides the exposed surface area of the cladding in each zone.

Table A4–5 The Calculated Number of Failed Rods in Each Zone and Corresponding Exposed SNF Pellets Directly underneath a 3.5-cm (1.38-in.)-Long Crack and for underneath the Extended Crack Length (i.e., Crack Length Plus 6 cm (2.36 in.) on the Failed Rods)

	Cladding Failure of 0.1%			Cladding Failure of 0.01%		
Zone	Failed Rods	Number of Exposed Pellets Directly underneath the 3.5-cm (1.38-in.)-Long Crack	Number of Pellets Underneath the Extended Length of the Crack*	Failed Rods	Number of Exposed Pellets Directly underneath the 3.5-cm (1.38-in.)-Long Crack	Number of Pellets underneath the Extended Length of the Crack*
1	1	2	4	1	2	4
2	1	2	4	0	0	0
3	1	2	4	0	0	0
4	1	2	4	0	0	0
5	0	0	0	0	0	0

* The SNF pellets underneath the extended length are not directly exposed.

Table A4-6 Exposed Cladding Surface Area in Each Zone					
Zone	1	2	3	4	5
Surface Area m^2 (ft^2)	111 (1,194.8)	192.9 (2,076.4)	196.9 (2,119.4)	72.5 (780.4)	11.1 (119.5)

Various tables present the simulation data for SNF and cladding oxidation for the six cases. The cladding oxidation data are presented in terms of the thickness of the zirconium oxide layer. The SNF oxidation data are presented in terms of the amount of UO_{2+x} phase that would form from exposure to oxygen produced by radiolysis. The SNF oxidation data also include the extent of oxidation, which is equal to the percentage of the exposed SNF pellets that have undergone oxidation to a particular UO_{2+x} phase. The extent of oxidation is separately calculated for the directly exposed SNF pellets and the SNF pellets in the extended crack length that are not directly exposed.

Tables A4-16 to A4-19, respectively, list the cladding oxidation data for Cases 1 to 4. These tables appear at the end of this section. Note that the cladding oxidation model by Daalgard (1976) was used in the simulations. The analysis presented in Section A3 indicates that the cladding oxidation model by Daalgard (1976) is expected to provide the highest cladding oxidation rates compared to the other models. The cladding oxidation model by Daalgard (1976) was selected because it is expected to provide a bounding (with respect to cladding oxidation) assessment of (1) the cladding oxidation in the limited oxidizing environment in the canister and (2) the SNF oxidation in the canister. Regarding the second consideration, when cladding consumes most of the available oxygen, the extent of SNF oxidation of any exposed SNF is expected to represent a lower bound (with respect to SNF oxidation). The next subsection provides the cladding oxidation data for Cases 5 and 6 and discusses the effects of various varying parameters on cladding oxidation.

Tables A4-20 to A4-23, respectively, list the SNF oxidation data for Cases 1 to 4. These tables appear at the end of this section. The data from these tables are selected to highlight the effects of varying parameters. The data for Cases 5 and 6 are presented in Sections A4.4.2.5 and A4.4.2.6, and tables A4-13 and A4-14.

A4.4.1 Cladding Oxidation

A4.4.1.1 Spent Nuclear Fuel and Cladding Initial Temperatures

The cladding (chemical) oxidation data from Case 1 (i.e., exponential in 4.77 years) are extracted to illustrate the effect of SNF and cladding initial temperatures. Figure A4-3 presents the cladding oxidation data for 17.4 moles of residual water, 0.1 percent cladding failure, and the low- and high-end SNF and cladding initial temperatures.

More cladding oxidation is observed when SNF and cladding temperatures are lower in certain parts of the canister. For example, in Figure A4-3, the cladding oxide thickness from Zones 2 to 4 for low-end initial temperatures of SNF and cladding are less compared to the high-end initial temperatures of SNF and cladding; however, this trend is reversed for Zone 1 (i.e., more cladding oxidation occurs at the low-end initial temperatures of SNF and cladding compared to the high-end initial temperatures of SNF and cladding).

The reason for the aforementioned observation is the following. In the canister, the rates of cladding and SNF oxidation not only depend on temperature (for chemical reaction) but also on

the rate of radiolysis of water and the amount of available oxygen. The amount of available oxygen in a zone is affected by the transfer of oxygen between the zones in the integration model. In Figure A4-3, cladding oxidation rates for Zones 2 to 5 are lower for the low-end initial temperature condition of SNF and cladding compared to the high-end initial temperature condition of SNF and cladding. This results because a sufficient amount of oxygen is available for both temperature conditions. Therefore, more oxidation of cladding occurs for Zones 2 through 5 for the high-end temperature condition. However, in Zone 5, the rate of cladding oxidation depends on the amount of oxygen in a given time step. Since more oxygen is available for the low-end temperature condition in the integration model, more oxidation occurs for Zone 1 cladding for the low-end compared to the high-end temperature condition. This trend is observed in the cladding oxidation data for Cases 1, 2, and 3 (see Tables A10-1 to A10-3).

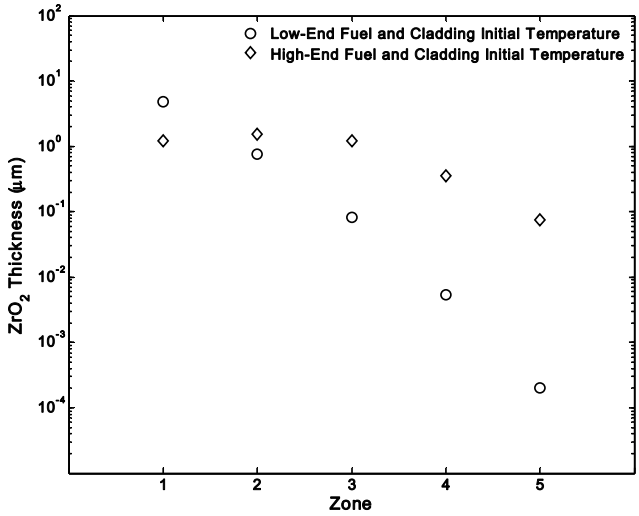

Figure A4-3 ZrO_2 layer thickness formed during cladding oxidation for 17.4 moles of residual water, 0.1-percent cladding failure, exponential decomposition of the water in 4.77 years, low- and high-end SNF and cladding initial temperature, and thermal decay constant of 0.023

However, the trend is not observed in the Case 4 (linear in 71.62 years) data. This is attributed to the slower rate of radiolysis in the case in which the residual water linearly decomposes in 71.62 years. For the low-end temperature condition, the cladding cools and no appreciable amount of oxidation occurs beyond 20 years; however, an appreciable amount of cladding oxidation continues beyond 20 years for the high-end initial temperature condition of SNF and cladding.

A4.4.1.2 Cladding Failure

The cladding failure of 0.01 and 0.1 percent do not significantly affect cladding oxidation. This trend is observed for Cases 1 to 4. The cladding failure is used to determine the number of exposed SNF pellets in the canister. Thus, higher cladding failure results in a greater number of exposed SNF pellets. However, this does not significantly affect the extent of cladding oxidation because the amount of oxygen needed to oxidize an SNF pellet is much smaller than the total amount of oxygen radiolysis generates. For example, only 0.013 moles of oxygen are needed to completely oxidize an SNF pellet from UO_2 to U_3O_8, whereas the amount of oxygen generated by radiolysis is 2.75, 8.7, and 27.5 moles for the residual water amounts of 5.5, 17.4, and 55 moles, respectively.

A4.4.1.3 Radiolysis Kinetics

Uncertainty in radiolysis kinetics affects the extent of cladding oxidation by 1 to 5 micrometers, which is insignificant compared to the extent of cladding oxidation in the reactor. The integration model data indicate that radiolysis kinetics affects the cladding oxidation in the case of slower radiolysis kinetics. For example, the data listed in Tables A10-1 and A10-2 for Cases 1 and 2 (i.e., exponential and linear in 4.77 years), respectively, indicate that selection of either exponential or linear decomposition of the residual water in 4.77 years does not significantly affect the extent of cladding oxidation. However, the extent of cladding oxidation when the decomposition period is extended to 71.62 years is significantly affected by the radiolysis kinetics.

The data from Cases 3 and 4 (i.e., exponential and linear in 71.62 years, 55 moles of water, 0.1-percent cladding failure, and the low-end SNF and cladding initial temperature condition) are used to show the effect of linear and exponential decomposition of the residual water in 71.62 years on the cladding oxidation. Figure A4-4(a) presents these data. As seen in the figure, the cladding is oxidized more for Zones 1 and 2 when the kinetic model for decomposition of residual water is exponential rather than linear. However, no difference in the ZrO_2 thickness is noted for Zones 3, 4, and 5. This observation is attributed to the compound effect of the SNF temperature, oxygen generation rate, and amount of available oxygen in a zone. When water decomposes via exponential kinetics, more oxygen is available within the first 10 years after storage than when water decomposes via linear kinetics. The cladding oxidation in Zones 3, 4, and 5 depends on temperatures, whereas in Zones 1 and 2 the cladding oxidation depends on the rate of oxygen generation and the amount of available oxygen. Because more oxygen is generated with exponential kinetics and more oxygen becomes available, greater oxidation of cladding occurs in Zones 1 and 2 compared to the linear kinetics.

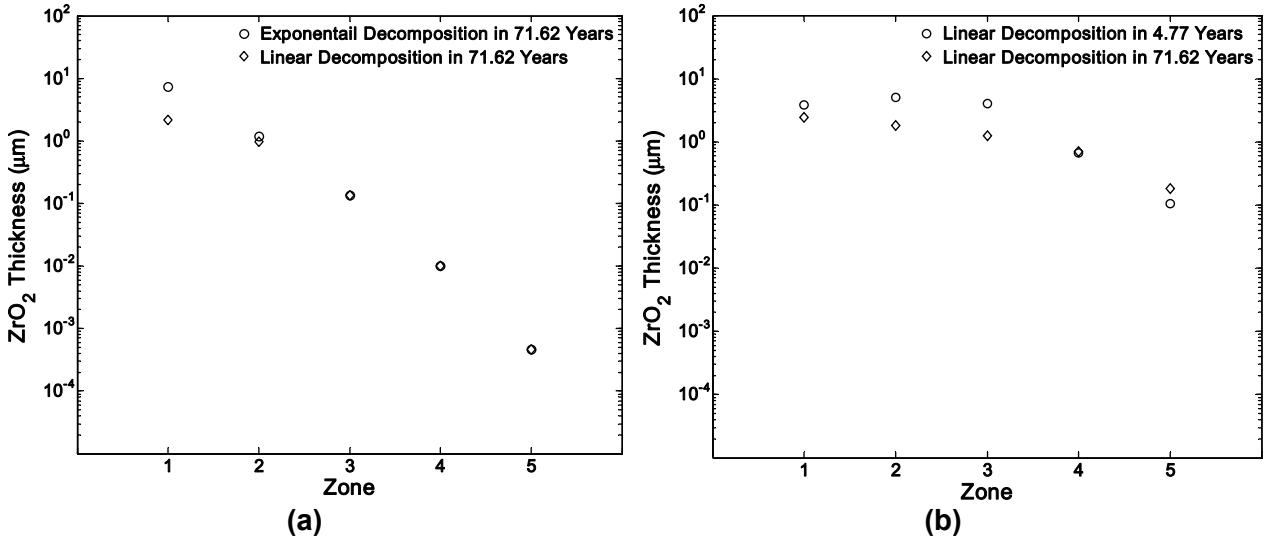

Figure A4-4 (a) Cases 3 and 4 (i.e., exponential and linear in 71.62 years) cladding oxidation data for 55 moles of water, 0.1-percent cladding failure, and low-end SNF and cladding initial temperatures to highlight the effect of radiolysis model. (b) Cases 2 and 4 (i.e., linear in 4.77 and 71.62 years) cladding oxidation data for 55 moles of water, 0.1-percent cladding failure, and high-end SNF and cladding initial temperatures to highlight the effect of decomposition periods on cladding oxidation.

The cladding oxidation data for Cases 1 and 3 (i.e., exponential in 4.77 and 71.62 years), indicate that that there is little or no difference in cladding oxide thickness when the water decomposes via exponential kinetics either in 4.77 or 71.62 years. More pronounced differences are observed when Cases 2 and 4 (i.e., linear in 4.77 and 71.62 years), cladding oxidation data for 55 moles of water, 0.1-percent cladding failure, and high-end SNF and cladding initial temperatures are selected. Figure A4-4(b) presents these data graphically. As seen in the figure, the ZrO_2 thickness in Zones 1, 2, and 3 is greater for the decomposition period of 4.77 than for 71.62 years. This is a result of the compound effect of temperature and the availability of oxygen. When more oxygen is available at higher temperature and the rate of cladding oxidation is controlled by the availability of the oxygen, more oxidation occurs for the shorter decomposition period (i.e., 4.77 years).

A4.4.1.4 Water Amount

It is observed that more cladding oxidation occurs for higher amounts of residual water. This trend is observed for Cases 1 to 4 and is independent of cladding failure. For example, in Case 1 for the low-end SNF and cladding temperatures, the cladding oxide thickness increased from 1.24 μm (4.87×10^{-5} in.) to 7.32 μm (2.88×10^{-4} in.) for the Zone 1 exposed cladding when the residual water amount was increased from 5.5 to 55 moles. The same trend is observed in Cases 2, 3, and 4. If the water amount is less than 5.5 moles, the extent of cladding oxidation will be less.

A4.4.1.5 Thermal Decay Constant

The value of thermal decay constant (i.e., of a in Equation A4-6), affects the extent of cladding oxidation. Table A4-7 lists the cladding oxidation data for Case 5 (i.e., linear in 71.62 years) and a equal to 0.064 in Equation A4-6, to highlight the effect of the thermal decay constant. The data are for low-end SNF and cladding initial temperatures, cladding failure of 0.1 percent, radiolysis kinetics controlled by linear decomposition of residual water in 71.62 years, water amount of 17.4 moles, and oxygen diffusion through grain boundaries. The value of the thermal decay constant varies. The data indicate that more cladding oxidation occurs with a lower value thermal decay constant (i.e., a equal to 0.023 in Equation A4-6) than with a higher value of thermal decay constant (i.e., a equal to 0.064 in Equation A4-6) in all five zones. This is expected because cladding temperature remains higher for a longer time with the lower value of thermal decay constant. Hence, more cladding is oxidized.

A4.4.1.6 Mode of Oxygen Diffusion

Table A4-8 lists the cladding oxidation data for Case 6 to highlight the effect of the mode of oxygen diffusion through exposed SNF pellets. The listed data are for low-end SNF and cladding initial temperatures, cladding failure of 0.1 percent, radiolysis kinetics of exponential decomposition in 4.77 years, 17.4 moles of residual water, and thermal decay constant equal to 0.023. The mode by which oxygen diffuses through the exposed SNF pellet varies.

It is observed that there is less than a 10-percent difference in the two values of the oxide layer thickness in each zone. The ZrO_2 thickness is slightly less for the oxygen diffusion through grain boundaries compared to the fragment surface because slightly more oxygen is consumed by the SNF when oxygen diffuses through the fuel.

Table A4-7 Cladding Oxidation Simulation Data for Case 5 (Linear Decomposition of Residual Water in 71.62 Years, Low-End SNF and Cladding Initial Temperatures, 17.4 Moles of Residual Water, Cladding Failure of 0.1 Percent, and Variable Values of Decay Constant)		
Zone	**Cladding Oxides Layer Thickness (μm) (mil) for Thermal Decay Constant Value of 0.023**	**Cladding Oxides Layer Thickness (μm) (mil) for Thermal Decay Constant Value of 0.064**
1	7.70×10^{-1} (3.03×10^{-2})	2.74×10^{-1} (1.07×10^{-2})
2	4.57×10^{-1} (1.79×10^{-2})	1.63×10^{-1} (6.41×10^{-3})
3	1.36×10^{-1} (5.35×10^{-3})	4.90×10^{-2} (1.82×10^{-3})
4	1.03×10^{-2} (4.05×10^{-4})	3.95×10^{-3} (1.55×10^{-4})
5	4.38×10^{-4} (1.72×10^{-5})	1.81×10^{-4} (7.12×10^{-6})

Table A4-8 SNF Oxidation Simulation Data for Case 6 (Low-End SNF and Cladding Initial Temperatures, Cladding Failure of 0.1 Percent, Exponential Decay of Residual Water in 4.77 Years, Water Amount of 17.4 Moles, Decay Constant Value of 0.023, and Variable Mode of Oxygen Diffusion)		
Zone	**Cladding Oxide Layer Thickness (μm) (mil) for Oxygen Diffusion Through Grain Boundaries of Each Exposed SNF Pellet**	**Cladding Oxide Layer Thickness (μm) (mil) for Oxygen Diffusion Through Exposed Surfaces of SNF Pellet Fragments**
1	4.80 (1.88×10^{-1})	4.92 (1.93×10^{-1})
2	7.58×10^{-1} (2.98×10^{-2})	7.78×10^{-1} (3.06×10^{-2})
3	8.23×10^{-2} (3.24×10^{-3})	8.45×10^{-2} (3.32×10^{-3})
4	5.44×10^{-3} (2.14×10^{-4})	5.56×10^{-3} (2.18×10^{-4})
5	2.03×10^{-4} (7.99×10^{-6})	1.83×10^{-4} (7.20×10^{-6})

A4.4.2 Spent Nuclear Fuel Oxidation

A4.4.2.1 Spent Nuclear Fuel and Cladding Initial Temperatures

The SNF oxidation data from Case 1 (exponential in 4.77 years) are extracted to illustrate the temperature effect. Table A4-9 lists the SNF oxidation data for low- and high-end SNF temperatures conditions, 0.1-percent cladding failure, exponential decomposition of the residual water in 4.77 years, 5.5 moles of water, oxygen diffusing through grain boundaries, and decay constant equal to 0.023.

The listed data of Case 1 indicate that more of the exposed SNF is oxidized at the low-end temperature condition than for the high-end condition. It is noted that the UO_{2+x} phase in

Zones 3 and 4 for the low-end condition is $UO_{2.4}$, whereas the UO_{2+x} phase is U_3O_8 in the two zones for the high-end temperature condition. An examination of the Case 2 (linear radiolysis kinetics in 4.77 years) data for 5.5 moles of water also indicates the same trend.

To further examine this trend, Table A4-10 lists the data from the four cases for 0.1-percent cladding failure. The mass of various UO_{2+x} phases formed is added in the canister with the five zones. The listed data indicate that more of the exposed SNF is oxidized for 5.5 moles of residual water at the low-end temperature condition in the four cases. Similarly, more SNF is oxidized for 17.4 moles of the residual water at the low-end condition in Cases 1, 2, and 3. In Case 4, more SNF oxidation occurs for 17.4 moles for the high-end temperature condition.

Table A4-9 Mass of UO_{2+x} Phase and Extent of Oxidation for Exponential Decomposition of Residual Water in 4.77 Years, 0.1-Percent Cladding Failure, 5.5 Moles of Water, Oxygen Diffusing through Grain Boundaries, and Decay Constant Equal to 0.023

Zone	Low-End SNF and Cladding Initial Temperature		High-End SNF and Cladding Initial Temperature	
	Mass of UO_{2+x} Phase (oz)	Extent of Oxidation*	Mass of UO_{2+x} Phase (oz)	Extent of Oxidation*
1	68.2 g (2.40 oz) of U_3O_8	100% to U_3O_8, 100% to U_3O_8	2.4 g (0.08 oz) of U_3O_8	10.4% to U_3O_8, 0
2	68.2 g (2.40 oz) of U_3O_8	100% to U_3O_8, 100% to U_3O_8	2.4 g (0.08 oz) of U_3O_8	10.4% to U_3O_8, 0
3	49.2 g (1.73 oz) of $UO_{2.4}$	100% to $UO_{2.4}$, 60.0% to $UO_{2.4}$	2.6 g (0.09 oz) of U_3O_8	11.4% to U_3O_8, 0
4	10.0 g (0.34 oz) of $UO_{2.4}$	44.7% to $UO_{2.4}$, 0	68.2 g (2.40 oz) of U_3O_8	100% to U_3O_8, 100% to U_3O_8

* Extent of Oxidation: This column provides information on the percentage of exposed SNF pellets that have undergone oxidation to a particular UO_{2+x} phase in the canister. The extent of oxidation is separately calculated for the directly exposed SNF pellets and SNF pellets in the crack length, plus a 6-cm (2.36-cm) area of a failed rod not directly exposed. The extent of oxidation values for the directly exposed SNF pellets and the adjacent SNF pellets, not directly exposed, are separated by a comma.

Table A4-10 Mass of UO_{2+x} Phase for Different Water Amount under Cases 1 to 4 (The Data Are for 0.1-Percent Cladding Failure; the SNF Oxidation Data for the Five Zones Are Added)

Case Number	Low-End SNF and Cladding Initial Temperatures			High-End SNF and Cladding Initial Temperatures		
	Combined Mass of UO_{2+x} Phase (oz) for Water Amount (moles)			Combined Mass of UO_{2+x} Phase (oz) for Water Amount (moles)		
	5.5	17.4	55	5.5	17.4	55
1 (exponential in 4.77 years)	136.4 g (4.8 oz) of U_3O_8 and 59.2 g (2.1 oz) of $UO_{2.4}$	136.5 g (4.8 oz) of U_3O_8 and 79.2 g (2.8 oz) of $UO_{2.4}$	136.6 g (4.8 oz) of U_3O_8 and 86.9 g (3.1 oz) of $UO_{2.4}$	75.6 g (2.7 oz) of U_3O_8	153.3 g (5.4 oz) of U_3O_8	268.3 g (9.5 oz) of U_3O_8

Table A4-10 Mass of UO_{2+x} Phase for Different Water Amount under Cases 1 to 4 (The Data Are for 0.1-Percent Cladding Failure; the SNF Oxidation Data for the Five Zones Are Added) (continued)

Case Number	Low-End SNF and Cladding Initial Temperatures			High-End SNF and Cladding Initial Temperatures		
	Combined Mass of UO_{2+x} Phase (oz) for Water Amount (moles)			Combined Mass of UO_{2+x} Phase (oz) for Water Amount (moles)		
	5.5	17.4	55	5.5	17.4	55
2 (linear in 4.77 years)	72.0 g (2.5 oz) of U_3O_8 and 78.8 g (2.8 oz) of $UO_{2.4}$	136.4 g (4.8 oz) of U_3O_8 and 79.0 g (2.8 oz) of $UO_{2.4}$	136.4 g (4.8 oz) of U_3O_8 and 86.9 g (3.1 oz) of $UO_{2.4}$	9.4 g (0.3 oz) of U_3O_8 and 0.5 g (0.02 oz) of $UO_{2.4}$	92.0 g (3.2 oz) of U_3O_8	199.8 g (7.0 oz) of U_3O_8
3 (exponential in 71.62 years)	4.0 g (0.14 oz) of U_3O_8 and 131.9 g (4.6 oz) of $UO_{2.4}$	100.1 g (3.5 oz) of U_3O_8 and 122.2 g (4.3 oz) of $UO_{2.4}$	136.4 g (4.8 oz) of U_3O_8 and 86.9 g (3.1 oz) of $UO_{2.4}$	7.5 g (0.26 oz) of U_3O_8 and 4.5 g (0.16 oz) of $UO_{2.4}$	24.1 g (0.84 oz) of U_3O_8 and 76.9 g (2.7 oz) of $UO_{2.4}$	183.9 g (6.5 oz) of U_3O_8 and 68.5 g (2.4 oz) of $UO_{2.4}$
4 (linear in 71.62 years)	0.6 g (0.02 oz) of U_3O_8 and 214.1 g (7.6 oz) of $UO_{2.4}$	2.6 g (0.09 oz) of U_3O_8 and 86.5 g (7.5 oz) of $UO_{2.4}$	83.1 g (2.9 oz) of U_3O_8 and 136.6 g (4.8 oz) of $UO_{2.4}$ and 51.9 g (1.8 oz) of UO_3	2.2 g (0.08 oz) of U_3O_8 and 58.1 g (2.1 oz) of $UO_{2.4}$	6.9 g (0.24 oz) of U_3O_8 and 149.3 g (5.3 oz) of $UO_{2.4}$	51.4 g (1.9 oz) of U_3O_8 and 214.9 g (7.6 oz) of $UO_{2.4}$

The data in Table A4-9 are for the four zones in which SNF is exposed under Case 1. The data in Table A4-10 are obtained by adding the SNF oxidation data for the four zones under Cases 1 through 4. For the 55 moles of residual water, more SNF is oxidized for the high-end temperature condition in Cases 1 and 3 (exponential radiolysis kinetics in 4.77 and 71.62 years). In Case 2 (linear radiolysis kinetics in 4.77 years), more SNF is oxidized for the low-end condition. In addition, more SNF is oxidized to U_3O_8 phase for the high-end temperature condition in Cases 1, 2, and 3. In Case 4 (linear radiolysis kinetics in 71.62 years), the amount of oxidized SNF for the low- and high-end conditions is comparable. However, it is noted that more U_3O_8 forms for the low-end condition.

The SNF oxidation in a zone of the canister is affected by the availability of oxygen and the rate of cladding and SNF oxidation. The unused oxygen from colder zones is transferred to the hotter zones in the integration model. For the low-end SNF initial temperatures of SNF and cladding, more unused oxygen is transferred from the colder zones to the hotter zones compared to the high-end SNF initial temperatures of SNF and cladding. This result in a greater extent of oxidation of the exposed SNF in the hotter zones for the low-end temperature condition compared to the high-end temperature condition. However, more of the exposed SNF for the high-end condition tends to be oxidized to U_3O_8 because a sufficient amount of oxygen is available in the model calculation. This occurs when the residual water decomposes either through exponential or linear radiolysis kinetics in 4.77 years or through exponential radiolysis kinetics in 71.62 years. When the residual water decomposes via linear radiolysis kinetics in 71.62 years, a compound effect of cladding oxidation rate, SNF oxidation rate, and the amount of available oxygen determine the extent of SNF oxidation. In the integration model, the available oxygen is divided between SNF and cladding according to surface area proportions

(see Equations A4-12 and A4-13). When more oxygen is available during a time step in a zone, the additional oxygen is allocated to SNF oxidation.

A4.4.2.2 Cladding Failure

A greater amount of SNF is exposed to radiolysis-generated oxygen when the cladding failure is 0.1 percent as compared to 0.01 percent. Only SNF pellets in Zone 1 are exposed to oxygen for a cladding failure of 0.01 percent, whereas SNF pellets in Zones 1 through 4 are exposed to oxygen for a cladding failure of 0.1 percent. Thus, more SNF gets oxidized when the cladding failure is greater. To illustrate the effect of cladding failure on the extent of oxidation of SNF pellets exposed in Zone 1, the data are extracted from the first four cases, as listed in Table A4-11. The data indicate that there is less than a 20-percent change in the extent of SNF oxidation for the two cladding failure conditions when other parameters are the same. This trend is observed in the data for all four cases. These data also indicate that the higher value of cladding failure does not affect the extent of SNF oxidation in different zones. This is because a very small amount of oxygen is needed to oxidize an SNF pellet compared to the total oxygen generated by radiolysis whether there are 5.5, 17.4, or 55 moles of water.[3]

A4.4.2.3 Radiolysis Kinetics

To examine the effect of radiolysis kinetics on SNF oxidation, the data from Cases 1, 2, and 4 were extracted and are listed in Table A4-12. The compiled data are for low-end SNF and cladding initial temperatures, 0.1-percent cladding failure, 17.4 moles of water, oxygen diffusion through grain boundaries, and a thermal decay constant equal to 0.023.

Table A4-11 Effect of Cladding Failure Rate on SNF Oxidation for Zone 1 Exposed SNF Pellets (The SNF Oxidation Data Are Extracted from the First Four Cases and Are for Low-End SNF and Cladding Initial Temperatures)

Water Amount	Mass of UO_{2+x} (oz) Phase for Cladding Failure of 0.1%				Mass of UO_{2+x} (oz) Phase for Cladding Failure of 0.01%			
(Moles)	Case 1	Case 2	Case 3	Case 4	Case 1	Case 2	Case 3	Case 4
5.5	68.2 g (2.40 oz) of U_3O_8	3.6 g (0.13 oz) of U_3O_8	2.0 g (0.07 oz) of U_3O_8 and 1.5 g (0.05 oz) of $UO_{2.4}$	2.4 g (0.0847 oz) of U_3O_8	68.3 g (2.40 oz) of U_3O_8	4.4 g (0.16 oz) of U_3O_8	2.0 g (0.07 oz) of U_3O_8 and 5.8 g (0.20 oz) of $UO_{2.4}$	0.5 g (0.02 oz) of U_3O_8 and 26.2 g (0.92 oz) of $UO_{2.4}$
17.4	68.3 g (2.40 oz) of U_3O_8	68.2 g (2.40 oz) of U_3O_8	0.5 g (0.02 oz) of U_3O_8 and 25.3 g (0.90 oz) of $UO_{2.4}$	2.0 g (0.07 oz) of U_3O_8 and 65.1 g (2.30 oz) of $UO_{2.4}$	68.3 g (2.40 oz) of U_3O_8	68.2 g (2.40 oz) of U_3O_8	32.3 g (1.14 oz) of U_3O_8 and 35.3 g (1.24 oz) of $UO_{2.4}$	2.0 g (0.07 oz) of U_3O_8 and 65.1 g (2.30 oz) of $UO_{2.4}$
55	68.4 g (2.41 oz) of U_3O_8	68.2 g (2.41 oz) of U_3O_8	68.2 g (2.40 oz) of U_3O_8	68.2 g (2.40 oz) of U_3O_8	68.4 g (2.41 oz) of U_3O_8	68.4 g (2.41 oz) of U_3O_8	68.2 g (2.40 oz) of U_3O_8	68.2 g (2.40 oz) of U_3O_8

[3] Preliminary qualitative analysis shows that a 1-percent cladding failure rate could lead to higher SNF oxidation when significant amounts of residual water undergo relatively fast decomposition via radiolysis.

Table A4-12 Compilation of Cases 1, 2, 3, and 4 Simulation Data for Identification of Radiolysis Kinetics Effect on SNF Oxidation (The Selected Data Are for Low-End SNF and Cladding Initial Temperatures, 0.1-Percent Cladding Failure, 17.4 Moles of Residual Water, Oxygen Diffusion through Grain Boundaries, and Thermal Decay Constant Equal to 0.023)

	Radiolysis Model							
	Exponential in 4.77 Years		Linear in 4.77 Years		Exponential in 71.62 Years		Linear in 71.62 Years	
Zone	Mass of UO_{2+x} Phase (oz)	Extent of Oxidation*	Mass of UO_{2+x} Phase (oz)	Extent of Oxidation*	Mass of UO_{2+x} Phase (oz)	Extent of Oxidation*	Mass of UO_{2+x} Phase (oz)	Extent of Oxidation*
1	68.3 g (2.40 oz) of U_3O_8	100% to U_3O_8, 100% to U_3O_8	68.2 g (2.40 oz) of U_3O_8	100% to U_3O_8, 100% to U_3O_8	31.8 g (1.12 oz) of U_3O_8 and 35.7 g (1.26 oz) of $UO_{2.4}$	100% to U_3O_8, 20% to U_3O_8 and 80% to $UO_{2.4}$	2.0 g (0.07 oz) of U_3O_8 and 65.1 g (2.30 oz) of $UO_{2.4}$	8.8% to U_3O_8 and 91.2% to $UO_{2.4}$, 100% to $UO_{2.4}$
2	68.2 g (2.40 oz) of U_3O_8	100% to U_3O_8, 100% to U_3O_8	68.2 g (2.40 oz) of U_3O_8	100% to U_3O_8, 100% to U_3O_8	68.2 g (2.40 oz) of U_3O_8	100% to U_3O_8, 100% to U_3O_8	0.6 g (0.02 oz) of U_3O_8 and 63.2 g (2.22 oz) of $UO_{2.4}$	2.6% to U_3O_8 and 97.4% to $UO_{2.4}$, 97.5% to $UO_{2.4}$
3	67.1 g (2.36 oz) of $UO_{2.4}$	100% to $UO_{2.4}$, 100% to $UO_{2.4}$	67.1 g (2.36 oz) of $UO_{2.4}$	100% to $UO_{2.4}$, 100% to $UO_{2.4}$	67.1 g (2.36 oz) of $UO_{2.4}$	100% to $UO_{2.4}$, 100% to $UO_{2.4}$	67.1 g (2.36 oz) of $UO_{2.4}$	100% to $UO_{2.4}$, 100% to $UO_{2.4}$
4	12.1 g (0.43 oz) of $UO_{2.4}$	54.1% to $UO_{2.4}$, 0	11.8 g (0.42 oz) of $UO_{2.4}$	52.7% to $UO_{2.4}$, 0	19.4 g (0.68 oz) of $UO_{2.4}$	86.7% to $UO_{2.4}$, 0	18.6 g (0.65 oz) of $UO_{2.4}$	83.2% to $UO_{2.4}$, 0

* Extent of Oxidation: This column provides information on the percentage of exposed SNF pellets that have undergone oxidation to a particular UO_{2+x} phase in the canister. The extent of oxidation is calculated separately for the directly exposed SNF pellets and SNF pellets in the crack length, plus a 6-cm (2.36-in.) area of a failed rod not directly exposed. The extent of oxidation values for the directly exposed SNF pellets and the adjacent SNF pellets, not directly exposed, are separated by a comma.

This study noted that the extent of oxidation differs for Zone 4 exposed SNF pellets when the radiolysis model is changed from exponential to linear for the decomposition period of 4.77 years (i.e., Cases 1 and 2). The difference in the extent of oxidation is less than 10 percent. This indicates that, when the residual water decomposes relatively soon compared to the storage period, the type of radiolysis kinetic model (i.e., either linear or exponential) does not significantly affect the extent of SNF oxidation. Between the four cases, the extent of oxidation for the Zones 3 and 4 exposed SNF pellets is nearly the same. The cladding oxidation in Zones 3 and 4 is negligible compared to Zones 1 and 2 because of the lower temperatures. Therefore, most of the available oxygen in Zones 3 and 4 is used to oxidize fuel.

This study also noted that the extent of oxidation is significantly different for exposed SNF pellets in Zones 1 and 2 when the radiolysis model is changed from exponential to linear for the decomposition period of 71.62 years (i.e., Cases 3 and 4). Residual water decomposes slowly with the decomposition period of 71.62 years compared to 4.77 years. More oxygen is generated in the first 20 years for the exponential model compared to the linear model. This results in more oxygen being available to oxidize fuel.

The compiled data for linear radiolysis in 4.77 and 71.62 years indicate that the extent of oxidation increases for exposed pellets in Zone 4 when the decomposition period is increased from 4.77 to 71.62 years. Moreover, the oxide phase in exposed pellets in Zones 1 and 2 shifts from U_3O_8 to $UO_{2.4}$. For example, 68.2 g (2.40 oz) of U_3O_8 forms in Zone 1 with linear radiolysis in 4.77 years, whereas only 2.0 g (0.07 oz) of U_3O_8 forms in Zone 1 with linear radiolysis in 71.62 years. The same trend is observed for exposed SNF pellets in Zone 2. This trend occurs because of the slower rate of oxygen generation during linear radiolysis in 71.62 years compared to linear radiolysis in 4.77 years. The slower rate of oxygen generation results in a greater amount of $UO_{2.4}$ forming with the slower radiolysis kinetic in the integration model.

A4.4.2.4 Water Amount

The data compiled in Table A4-11 also illustrate the effect of water amount on SNF oxidation. The SNF oxide amount increases as the water amount increases because the amount of oxygen produced by radiolysis also increases with increasing water amount. This trend is observed for the first four cases. For example, the data in Table A4-10 for Case 1 and the low-end SNF and cladding temperatures specify that the amount of oxidized SNF is 136.4 g (4.8 oz) of U_3O_8 and 59.2 g (2.1 oz) of $UO_{2.4}$ for 5.5 moles of the residual water. The oxidized SNF amount increases to 136.6 g (4.8 oz) of U_3O_8 and 86.9 g (3.1 oz) of $UO_{2.4}$ for the same set of conditions in Case 1, but for 55 moles of residual water. This trend is also observed for the data from Cases 2, 3, and 4 listed in Table A4-10, which clearly indicates that increasing the amount of residual water increases the extent of SNF oxidation.

A4.4.2.5 Thermal Decay Constant

The simulation data for Cases 3 and 5 are used to examine the effect of the thermal decay constant on SNF oxidation. Table A4-13 lists these data. The key differences between the two cases are the extent of oxidation and the UO_{2+x} phase. As noted in the table, the extent of oxidation for Zone 4 SNF pellets is greater when the higher value of the decay constant is used. However, no difference is observed in the extent of oxidation for the Zones 1, 2, and 3 exposed SNF pellets between the two cases.

The data also indicate that more U_3O_8 forms with the lower value of the decay constant in Zones 1 and 2, whereas more $UO_{2.4}$ and UO_3 forms with the higher values of the decay constant. This is expected because exposed SNF in Zones 1 and 2 remains at a higher temperature for a longer time with a lower value of the decay constant. The higher temperature of the SNF results in formation of more U_3O_8 in Zones 1 and 2 for the lower value of the thermal decay constant.

A4.4.2.6 Mode of Oxygen Diffusion

The simulation data for Case 6 are used to examine the effect of the mode of oxygen diffusion. Table A4-14 presents the data from Case 6. As noted in the table, the extent of oxidation for each zone decreases significantly when oxygen diffuses through the fragment surface instead of along and through the grain boundaries. This is attributed to the decrease in surface area available for oxidation per pellet. When oxygen diffuses through grain boundaries and each grain is being oxidized simultaneously, the calculated surface area for SNF oxidation is 0.299 m^2 (3.22 ft^2) per pellet, whereas when oxygen diffuses through the surface area of each fragment, the effective surface area available for SNF oxidation is 0.002 m^2 (0.022 ft^2) per pellet. This decrease in surface area directly affects the extent of oxidation.

Table A4–13 SNF Oxidation Simulation Data for Case 5 (Low-End SNF and Cladding Initial Temperatures, 0.1-Percent Cladding Failure, Exponential Decomposition of Residual Water in 71.62 Years, 17.4 Moles of Residual Water, Oxygen Diffusion through Grain Boundaries, and Variable Values of Decay Constant)

	Decay Constant Equal to 0.023		Decay Constant Equal to 0.064	
Zone	UO_{2+x} Mass (oz)	Extent of Oxidation*	UO_{2+x} Mass (oz)	Extent of Oxidation*
1	31.8 g (1.12 oz) of U_3O_8 and 35.7 g (1.26 oz) of $UO_{2.4}$	100% to U_3O_8, 20% to U_3O_8, and 80% to $UO_{2.4}$	0.7 g (0.02 oz) of U_3O_8 and 34.0 g (1.2 oz) of $UO_{2.4}$, 33.6 g (1.2 oz) of UO_3	3.1% to U_3O_8 and 96.7% to $UO_{2.4}$, 26% to $UO_{2.4}$, and 74% to UO_3
2	68.2 g (2.40 oz) of U_3O_8	100% to U_3O_8, 100% to U_3O_8	0.2 g (0.008 oz) of U_3O_8 and 27.3 g (0.96 oz) of $UO_{2.4}$, 41.0 g (1.4 oz) of UO_3	0.9% to U_3O_8 and 99.1% to $UO_{2.4}$,11.5% to $UO_{2.4}$, and 88.5% to UO_3
3	67.1 g (2.36 oz) of $UO_{2.4}$	100% to $UO_{2.4}$, 100% to $UO_{2.4}$	32.2 g (1.1 oz) of $UO_{2.4}$ and 36.2 g (1.3 oz) of UO_3	100% to $UO_{2.4}$, 21.8% to $UO_{2.4}$, and 78.2% to UO_3
4	19.4 g (0.68 oz) of $UO_{2.4}$	86.7% to $UO_{2.4}$, 0	10.6 g (0.37 oz) of $UO_{2.4}$ and 58.6 g (2.1 oz) of UO_3	47.4% to U_3O_8 and 52.6% to $UO_{2.4}$, 100% to UO_3

* Extent of Oxidation: This column provides information on the percentage of exposed SNF pellets that have undergone oxidation to a particular UO_{2+x} phase in the canister. The extent of oxidation is calculated separately for the directly exposed SNF pellets and SNF pellets in the crack length, plus a 6-cm (2.36-in.) area of a failed rod not directly exposed. The extent of oxidation values for the directly exposed SNF pellets and the adjacent SNF pellets, not directly exposed, are separated by a comma.

Table A4-14 SNF Oxidation Simulation Data for Case 6 (Exponential Decomposition of Residual Water in 4.77 Years, Low-End SNF and Cladding Initial Temperatures, 17.4 Moles of Residual Water, 0.1-Percent Cladding Failure, Thermal Decay Constant of 0.023, and Variable Mode of Oxygen Diffusion)

	Oxygen Diffusing through Grain Boundaries		Oxygen Diffusing through Each Fragment Surface	
Zone	UO_{2+x} Mass (oz)	Extent of Oxidation*	UO_{2+x} Mass (oz)	Extent of Oxidation*
1	68.3 g (2.40 oz) of U_3O_8	100% to U_3O_8, 100% to U_3O_8	3.3 g (0.12 oz) of U_3O_8	14.5% to U_3O_8, 0
2	68.2 g (2.40 oz) of U_3O_8	100% to U_3O_8, 100% to U_3O_8	1.2 g (0.04 oz) of U_3O_8 and 0.07 g (0.002 oz) of $UO_{2.4}$	5.3% to U_3O_8 and 0.3% to $UO_{2.4}$, 0
3	67.1 g (2.36 oz) of $UO_{2.4}$	100% to $UO_{2.4}$, 100% to $UO_{2.4}$	0.4 g (0.013 oz) of $UO_{2.4}$	1.8% to $UO_{2.4}$, 0
4	12.1 g (0.43 oz) of $UO_{2.4}$	54.1% to $UO_{2.4}$, 0	0.08 g (0.003 oz) of $UO_{2.4}$	0.4% to $UO_{2.4}$, 0

* Extent of Oxidation: This column provides information on the percentage of exposed SNF pellets that have undergone oxidation to a particular UO_{2+x} phase in the canister. The extent of oxidation is calculated separately for the directly exposed SNF pellets and SNF pellets in the crack length, plus a 6-cm (2.36-in.) area of a failed rod not directly exposed. The extent of oxidation values for the directly exposed SNF pellets and the adjacent SNF pellets, not directly exposed, are separated by a comma.

A4.4.3 Residual Oxygen

The residual oxygen is defined as radiolysis-generated oxygen, but is not consumed in the SNF and cladding oxidation. Figure A4-5(a) presents the oxygen production and consumption data for a set of Case 4 (linear in 71.62 years) conditions. As seen in the figure, the generated oxygen amount increases linearly with time. The generated oxygen is predominantly consumed by the cladding and SNF only during the first few decades. The difference between the generated and consumed oxygen during the analyzed storage period of 300 years is the residual oxygen which remains in the canister. The net residual oxygen amount is the difference between the produced and consumed oxygen at the end of storage period.

The simulation data for Cases 1 to 4 are used to estimate the net amount of residual oxygen. Table A4-15 lists the net residual oxygen amounts for each case. An examination of the Case 1 data indicates that the residual oxygen is left in the canister for 55 moles of residual water under the low-end SNF and cladding initial temperature condition only. The residual oxygen amounts for the Case 3 conditions include low-end SNF and cladding initial temperatures and 17.4 and 55 moles of residual water. In Case 4, residual oxygen exists for every combination of the conditions, which include cladding failure, residual water amount, and low- and high-end SNF and cladding temperatures.

The residual oxygen is left in the cask when SNF and cladding are too cold to react with oxygen. The listed data in Table A4-15 indicate that the cladding failure does not significantly affect the residual moles of oxygen. In fact, the difference between the moles of residual oxygen for the two values of cladding failure is less than 10 percent. The residual oxygen increases with increasing moles of residual water and with the decomposition period.

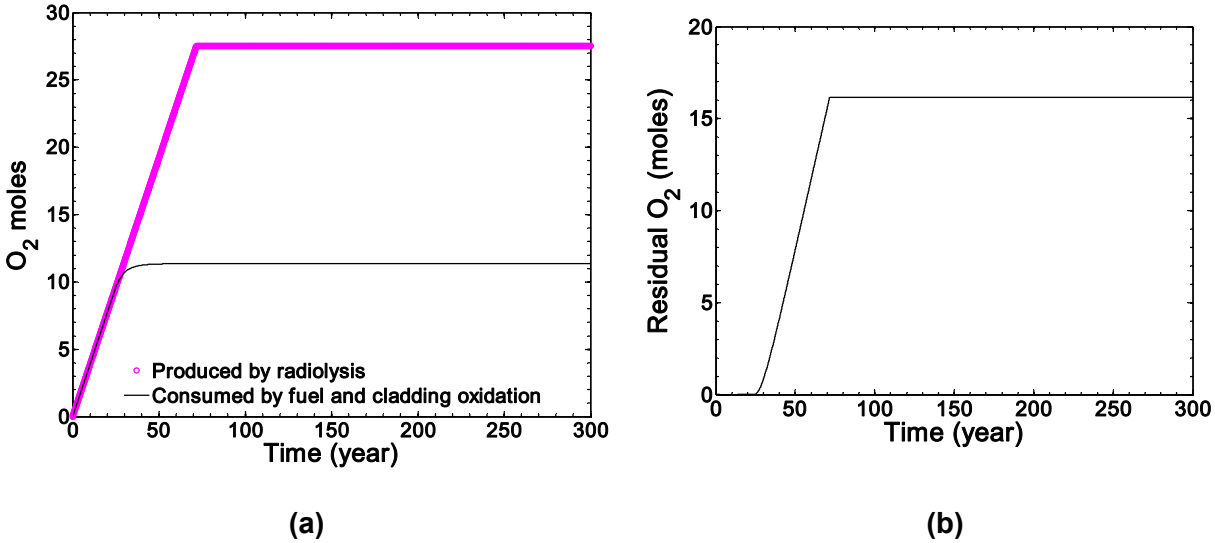

Figure A4-5 (a) Moles of oxygen produced and consumed by SNF and cladding oxidation and (b) residual oxygen amount as a function of time for linear decomposition in 71.62 years, high-end SNF and cladding initial temperatures, 55 moles of residual water, 0.1-percent cladding failure, decay constant equal to 0.023, and oxygen diffusion through grain boundaries. The net residual moles of oxygen are determined by calculating the difference between the produced and consumed moles at the end of the storage period.

Table A4-15 Net Residual Oxygen Amount in Moles for Cases 1, 2, 3, and 4 Conditions*																
	Case 1 (Exponential Decomposition in 4.77 Years)				Case 2 (Linear Decomposition in 4.77 Years)				Case 3 (Exponential Decomposition in 71.62 Years)				Case 4 (Linear Decomposition in 71.62 Years)			
Residual Water Amount (moles)	Low-End SNF and Cladding Initial Temperatures		High-End SNF and Cladding Initial Temperatures		Low-End SNF and Cladding Initial Temperatures		High-End SNF and Cladding Initial Temperatures		Low-End SNF and Cladding Initial Temperatures		High-End SNF and Cladding Initial Temperatures		Low-End SNF and Cladding Initial Temperatures		High-End SNF and Cladding Initial Temperatures	
	Cladding Failure		Cladding Failure		Cladding Failure		Cladding Failure		Cladding Failure		Cladding Failure		Cladding Failure		Cladding Failure	
	0.1%	0.01%	0.1%	0.01%	0.1%	0.01%	0.1%	0.01%	0.1%	0.01%	0.1%	0.01%	0.1%	0.01%	0.1%	0.01%
5.5	0	0	0	0	0	0	0	0	0	0	0	0	1.7	1.7	1.1	1.1
17.4	0	0	0	0	1.2	1.1	0	0	0.6	0.6	0	0	6.1	6.1	4.3	4.4
55	14.3	14.4	0	0	14.3	14.4	0	0	14.2	14.3	0	0	21.7	21.8	16.1	16.2
* Net residual oxygen amount is defined as the difference between the produced and consumed oxygen at the end of the analyzed storage period (i.e., 300 years).																

A4.4.4 Flammability Evaluation

The cladding is not expected to absorb the radiolysis-generated hydrogen because the produced hydrogen would be in molecular form. This results from the presence of the oxide layer film on the cladding surface and decreasing temperature of the cladding (see Section 4.4.1 for additional details). According to the flammability criterion specified in NUREG-1609, "Standard Review Plan for Transportation Packages for Radioactive Material," issued March 1999 (NRC, 1999), the volume fraction of any flammable gas should be less than 5 percent.

Because hydrogen is flammable, its mole fraction is calculated as a function of backfill pressure and radiolysis kinetics. Mole fraction is representative of volume fraction in a closed canister of a dry storage cask system. To evaluate flammability of the canister environment, it is assumed that the canister was backfilled with helium at room temperature. Furthermore, it is assumed that the physical properties of helium, hydrogen, and oxygen can be described by the ideal gas law inside the canister environment. Figure A4-6(a) presents the data on mole fraction of hydrogen versus residual water amount for two values of backfill pressure of helium—1 and 5 atm (14.7 and 73.5 lb/in.^{2}). Figure A4-6(b) presents the data on mole fraction of hydrogen considering the amount of residual oxygen in the cask.

The data presented in Figure A4-6(a) are calculated assuming that no residual oxygen exists in the cask, whereas the data in Figure A4-6(b) are calculated considering the residual oxygen values listed in Table A4-15 for the linear decay of residual water in 71.62 years and low-end SNF and cladding temperatures. As seen in the figures, the hydrogen mole fraction is more than 5 percent for 1 atm (14.7 lb/in.^{2}) backfill pressure irrespective of the residual oxygen amount. However, the hydrogen mole fraction is more than 5 percent for 5 atm (73.5 lb/in.^{2}) backfill pressure only when the residual water amount is 55 moles. The presence of residual oxygen slightly decreases the hydrogen mole fraction.

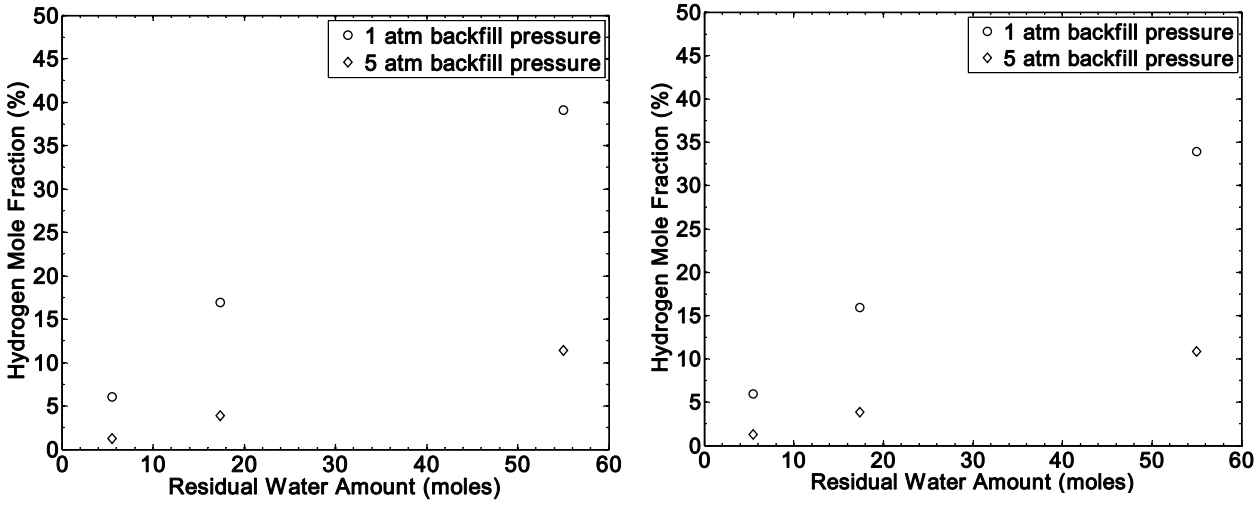

Figure A4-6 Hydrogen mole fraction versus moles of residual water for 1 and 5 atm helium backfill pressure. (a) No residual oxygen and (b) residual oxygen data in Table A4-15 for linear decay of residual water in 71.62 years and low-end SNF and cladding initial temperatures and 0.1-percent cladding failure.

The presence of oxygen is necessary for hydrogen to become flammable; however, no criterion exists that specifies the ratio of oxygen to hydrogen needed for the flammability of hydrogen with helium as an inert gas. Zlochower and Green (2009) conducted experiments to determine oxygen concentration limits for the flammability of hydrogen in the presence of nitrogen as an inert gas. The limiting oxygen concentration is defined as the minimum amount of oxygen that can support flame propagation and lead to explosion.

Zlochower and Green (2009) determined that the limiting oxygen concentration is close to 5 mole percent for a hydrogen mole fraction varying between 4 and 76 mole percent. It is assumed that the limiting oxygen concentration value Zlochower and Green (2009) determined applies to hydrogen mixed with helium as an inert gas. The amount of oxygen needed to achieve the criterion of 5 mole percent in the canister is estimated using the following equation:

$$\frac{n_{oxygen}}{n_{oxygen} + n_{hydrogen} + n_{helium}} = 0.05 \quad \text{(A4-18)}$$

where n_{helium} denotes moles of helium in the canister. The moles of helium in the canister are calculated using the ideal gas law as follows:

$$n_{helium} = \frac{PV}{RT} \quad \text{(A4-19)}$$

where P is equal to either 1 or 5 atm (14.7 or 73.5 lb/in.^{2}), V is equal to canister void volume (i.e., 2,100 L (74.2 ft^3), and T is equal to 298 Kelvin (K)). The value of T is equal to 298 K (77 degrees Fahrenheit (°F)) because the backfill pressure is measured at room temperature, which is assumed to be 25 degrees Celsius (°C) (77 °F).

According to Equation A4-18, the oxygen concentration exceeds 5 mole percent only when the residual oxygen is more than 4.8, 5.4, and 7.4 moles for 5.5, 17.4, and 55 moles of residual water, respectively, and the backfill pressure is 1 atm. Similarly, at a backfill pressure of 5 atm (73.5 lb/in.^{2}), the oxygen concentration exceeds 5 mole percent when residual oxygen is more than 22.8, 24.4, and 25.7 moles for 5.5, 17.4, and 55 moles of the residual water, respectively. Note that these values of oxygen amounts are for a 2,100-L (555 gallons (gal)) canister void volume and backfill pressure measured at room temperature.

The data indicate that conditions for flammability are met for 55 moles of residual water and 1 atm (14.7 lb/in,^{2}) backfill pressure (in the presence of ignition), irrespective of the temperature and radiation conditions considered in this scoping analysis. The data also indicate that the canister environment would meet the conditions of flammability when 17.4 moles of residual water undergo radiolysis via linear decomposition in 71.62 years, given the low-end SNF and cladding initial temperature condition and 1 atm (14.7 lb/in.^{2}) backfill pressure. The conditions of flammability are never met when backfill pressure is 5 atm (73.5 lb/in.^{2}) and the residual water amount is 55 moles or less.

A4.5 Spent Nuclear Fuel and Cladding Oxidation Simulation Data for Cases 1 to 4

Tables A4-16 to A4-19, respectively, list the cladding oxidation simulation data of the integration model for Cases 1 to 4. Similarly, Tables A4-20 to A4-23, respectively, list the SNF oxidation simulation data for Cases 1 to 4. Table A4-4 describes Cases 1 to 4.

Table A4-16 Cladding Oxidation Data for Case 1 (Exponential Decomposition of the Residual Water in 4.77 Years)

Zone	Low-End SNF and Cladding Initial Temperature: Cladding Oxide Layer Thickness in μm (mil) for Moles of the Water			High-End SNF and Cladding Initial Temperature: Cladding Oxide Layer Thickness in μm (mil) for Moles of the Water			Cladding Failure
	5.5	17.4	55	5.5	17.4	55	
1	1.24 (4.87×10^{-2})	4.80 (1.89×10^{-1})	7.32 (2.88×10^{-1})	3.84×10^{-1} (1.51×10^{-2})	1.22 (4.78×10^{-2})	7.03 (2.77×10^{-1})	0.1
2	3.09×10^{-1} (1.22×10^{-2})	7.58×10^{-1} (2.98×10^{-2})	1.19 (4.67×10^{-2})	3.85×10^{-1} (1.52×10^{-2})	1.53 (6.02×10^{-2})	5.36 (2.11×10^{-1})	0.1
3	5.12×10^{-2} (2.01×10^{-3})	8.23×10^{-2} (3.24×10^{-3})	1.36×10^{-1} (3.53×10^{-3})	4.18×10^{-1} (1.65×10^{-2})	1.23 (4.86×10^{-2})	1.95 (7.66×10^{-2})	0.1
4	4.77×10^{-3} (1.88×10^{-4})	5.44×10^{-3} (2.14×10^{-4})	1.00×10^{-2} (3.95×10^{-4})	2.54×10^{-1} (1.00×10^{-2})	3.52×10^{-1} (1.39×10^{-2})	4.41×10^{-1} (1.74×10^{-2})	0.1
5	1.89×10^{-4} (7.4×10^{-6})	2.03×10^{-4} (8.00×10^{-6})	4.63×10^{-4} (1.82×10^{-5})	6.21×10^{-2} (2.45×10^{-3})	7.53×10^{-2} (2.96×10^{-3})	8.69×10^{-2} (3.42×10^{-3})	0.1
1	1.33 (5.22×10^{-2})	4.88 (1.92×10^{-1})	7.32 (2.88×10^{-1})	3.84×10^{-1} (1.51×10^{-2})	1.22 (4.78×10^{-2})	7.21 (2.84×10^{-1})	0.01
2	3.15×10^{-1} (1.24×10^{-2})	7.71×10^{-1} (3.03×10^{-2})	1.19 (4.67×10^{-2})	3.86×10^{-1} (1.52×10^{-2})	1.61 (6.32×10^{-2})	5.36 (2.11×10^{-1})	0.01
3	5.15×10^{-2} (2.03×10^{-3})	8.37×10^{-2} (3.29×10^{-3})	1.36×10^{-1} (3.53×10^{-3})	4.55×10^{-1} (1.79×10^{-2})	1.23 (4.86×10^{-2})	1.94 (7.66×10^{-2})	0.01
4	4.57×10^{-3} (1.80×10^{-4})	5.53×10^{-3} (2.18×10^{-4})	1.00×10^{-2} (3.95×10^{-4})	2.48×10^{-1} (9.77×10^{-2})	3.51×10^{-1} (1.38×10^{-2})	4.41×10^{-1} (1.74×10^{-2})	0.01
5	1.89×10^{-4} (7.45×10^{-6})	2.03×10^{-4} (8.00×10^{-6})	4.63×10^{-4} (1.82×10^{-5})	6.21×10^{-2} (2.45×10^{-3})	7.53×10^{-2} (2.96×10^{-3})	8.69×10^{-2} (3.42×10^{-3})	0.01

Table A4-17 Cladding Oxidation Data for Case 2 (Linear Decomposition of the Residual Water in 4.77 Years)

Zone	Low-End SNF and Cladding Initial Temperatures: Cladding Oxide Layer Thickness in μm (mil) for Moles of Water			High-End SNF and Cladding Initial Temperatures: Cladding Oxide Layer Thickness in μm (mil) for Moles of Water			Cladding Failure
	5.5	17.4	55	5.5	17.4	55	
1	6.29×10^{-1} (2.48×10^{-2})	3.98 (1.57×10^{-1})	7.32 (2.88×10^{-1})	3.84×10^{-1} (1.51×10^{-2})	1.22 (4.78×10^{-2})	3.84 (1.51×10^{-1})	0.1
2	6.66×10^{-1} (2.62×10^{-2})	7.23×10^{-1} (2.85×10^{-2})	1.19 (4.67×10^{-2})	3.85×10^{-1} (1.52×10^{-2})	1.22 (4.78×10^{-2})	5.04 (2.00×10^{-1})	0.1
3	7.76×10^{-2} (3.06×10^{-3})	7.82×10^{-2} (3.08×10^{-3})	1.36×10^{-1} (5.35×10^{-3})	3.85×10^{-1} (1.52×10^{-2})	1.44 (5.65×10^{-2})	4.02 (1.59×10^{-1})	0.1
4	5.11×10^{-3} (2.01×10^{-4})	5.10×10^{-3} (2.05×10^{-4})	1.00×10^{-2} (3.95×10^{-4})	4.26×10^{-1} (1.62×10^{-2})	7.08×10^{-1} (2.79×10^{-2})	6.65×10^{-1} (2.60×10^{-2})	0.1
5	1.64×10^{-4} (6.48×10^{-6})	1.66×10^{-4} (6.54×10^{-6})	4.63×10^{-4} (1.82×10^{-5})	1.04×10^{-1} (4.08×10^{-2})	1.04×10^{-1} (4.08×10^{-3})	1.04×10^{-1} (4.08×10^{-3})	0.1
1	7.11×10^{-1} (2.80×10^{-2})	4.16 (1.64×10^{-1})	7.32 (2.88×10^{-1})	3.84×10^{-1} (1.51×10^{-2})	1.22 (4.78×10^{-2})	3.84 (1.51×10^{-1})	0.01
2	6.78×10^{-1} (2.67×10^{-2})	7.35×10^{-1} (2.89×10^{-2})	1.19 (4.67×10^{-2})	3.86×10^{-1} (1.52×10^{-2})	1.22 (4.78×10^{-2})	5.09 (2.00×10^{-1})	0.01
3	7.74×10^{-2} (3.05×10^{-3})	7.96×10^{-2} (3.14×10^{-3})	1.36×10^{-1} (5.35×10^{-3})	3.87×10^{-1} (1.52×10^{-2})	1.49 (5.87×10^{-2})	4.05 (1.59×10^{-1})	0.01
4	5.06×10^{-3} (1.99×10^{-4})	5.21×10^{-3} (2.05×10^{-4})	1.00×10^{-2} (3.95×10^{-4})	4.27×10^{-1} (1.68×10^{-2})	6.60×10^{-1} (2.60×10^{-2})	6.60×10^{-1} (2.60×10^{-2})	0.01
5	1.64×10^{-4} (6.48×10^{-6})	1.70×10^{-4} (6.70×10^{-6})	4.63×10^{-4} (1.82×10^{-5})	1.04×10^{-1} (4.08×10^{-3})	1.04×10^{-1} (4.08×10^{-3})	1.04×10^{-1} (4.08×10^{-3})	0.01

Table A4-18 Cladding Oxidation Data for Case 3 (Exponential Decomposition of the Residual Water in 71.62 Years)

Zone	Low-End SNF and Cladding Initial Temperatures: Cladding Oxide Layer Thickness in μm (mil) for Moles of Water			High-End SNF and Cladding Initial Temperatures: Cladding Oxide Layer Thickness in μm (mil) for Moles of Water			Cladding Failure
	5.5	17.4	55	5.5	17.4	55	
1	4.65×10^{-1} (1.83×10^{-2})	3.54 (1.39×10^{-1})	7.37 (2.90×10^{-1})	3.84×10^{-1} (1.51×10^{-2})	1.22 (4.80×10^{-2})	3.95 (1.55×10^{-1})	0.1
2	7.17×10^{-1} (2.82×10^{-2})	1.19 (4.68×10^{-2})	1.19 (4.68×10^{-2})	3.85×10^{-1} (1.51×10^{-2})	1.22 (4.80×10^{-2})	4.27 (4.68×10^{-1})	0.1
3	1.36×10^{-1} (5.35×10^{-3})	1.36×10^{-1} (5.35×10^{-3})	1.36×10^{-1} (5.35×10^{-3})	3.85×10^{-1} (1.51×10^{-2})	1.31 (5.15×10^{-2})	4.51 (1.77×10^{-1})	0.1
4	1.01×10^{-2} (3.97×10^{-4})	1.00×10^{-2} (3.93×10^{-4})	1.00×10^{-2} (3.93×10^{-4})	4.13×10^{-1} (1.62×10^{-2})	1.06 (4.17×10^{-2})	1.11 (4.37×10^{-2})	0.1
5	4.34×10^{-4} (1.70×10^{-5})	4.39×10^{-4} (1.72×10^{-5})	4.63×10^{-4} (1.82×10^{-5})	1.80×10^{-1} (7.08×10^{-3})	1.80×10^{-1} (7.08×10^{-3})	1.80×10^{-1} (7.08×10^{-3})	0.1
1	4.87×10^{-1} (1.91×10^{-2})	3.65 (1.43×10^{-1})	7.36 (2.89×10^{-1})	3.84×10^{-1} (1.51×10^{-2})	1.22 (4.80×10^{-2})	3.98 (1.56×10^{-1})	0.01
2	7.44×10^{-1} (2.92×10^{-2})	1.19 (4.68×10^{-2})	1.19 (4.68×10^{-2})	3.86×10^{-1} (1.51×10^{-2})	1.23 (4.84×10^{-2})	4.31 (1.69×10^{-1})	0.01
3	1.36×10^{-1} (5.35×10^{-3})	1.36×10^{-1} (5.35×10^{-3})	1.36×10^{-1} (5.35×10^{-3})	3.88×10^{-1} (1.52×10^{-2})	1.33 (5.23×10^{-2})	4.55 (1.79×10^{-1})	0.01
4	9.99×10^{-3} (3.93×10^{-4})	9.99×10^{-3} (3.93×10^{-4})	1.00×10^{-2} (3.93×10^{-4})	4.13×10^{-1} (1.62×10^{-2})	1.05 (4.13×10^{-2})	1.10 (4.33×10^{-2})	0.01
5	4.38×10^{-4} (1.72×10^{-5})	4.39×10^{-4} (1.72×10^{-5})	4.63×10^{-4} (1.82×10^{-5})	1.80×10^{-1} (7.08×10^{-3})	1.80×10^{-1} (7.08×10^{-3})	1.80×10^{-1} (7.08×10^{-3})	0.01

Table A4-19 Cladding Oxidation Data for Case 4 (Linear Decomposition of the Residual Water in 71.62 Years)							
	Low-End SNF and Cladding Initial Temperatures			High-End SNF and Cladding Initial Temperatures			
	Cladding Oxide Layer Thickness in μm for (mil) Moles of Water			Cladding Oxide Layer Thickness in μm (mil) for Moles of Water			
Zone	5.5	17.4	55	5.5	17.4	55	Cladding Failure
1	2.75×10^{-1} (1.08×10^{-2})	7.70×10^{-1} (3.03×10^{-2})	2.14 (8.42×10^{-2})	3.07×10^{-1} (1.20×10^{-2})	8.70×10^{-1} (3.42×10^{-2})	2.43 (9.56×10^{-2})	0.1
2	1.80×10^{-1} (7.08×10^{-3})	4.57×10^{-1} (1.79×10^{-2})	9.75×10^{-1} (3.83×10^{-2})	2.46×10^{-1} (9.68×10^{-3})	6.72×10^{-1} (2.64×10^{-2})	1.79 (7.04×10^{-2})	0.1
3	8.75×10^{-2} (3.44×10^{-3})	1.36×10^{-1} (5.35×10^{-3})	1.36×10^{-1} (5.35×10^{-3})	1.93×10^{-1} (7.59×10^{-3})	5.00×10^{-1} (1.96×10^{-2})	1.24 (4.88×10^{-2})	0.1
4	1.12×10^{-2} (4.40×10^{-4})	1.03×10^{-2} (4.05×10^{-4})	1.01×10^{-2} (3.97×10^{-4})	1.40×10^{-1} (5.51×10^{-3})	3.29×10^{-1} (1.29×10^{-2})	6.98×10^{-1} (2.74×10^{-2})	0.1
5	4.38×10^{-4} (1.72×10^{-5})	4.38×10^{-4} (1.72×10^{-5})	4.63×10^{-4} (1.82×10^{-5})	8.51×10^{-2} (3.35×10^{-3})	1.55×10^{-1} (6.10×10^{-3})	1.80×10^{-1} (7.08×10^{-3})	0.1
1	2.82×10^{-1} (1.11×10^{-2})	7.90×10^{-1} (3.11×10^{-2})	2.18 (8.58×10^{-2})	3.11×10^{-1} (1.22×10^{-2})	8.79×10^{-1} (3.46×10^{-2})	2.46 (9.68×10^{-2})	0.01
2	1.85×10^{-1} (7.28×10^{-3})	4.77×10^{-1} (1.87×10^{-2})	9.97×10^{-1} (3.92×10^{-2})	2.49×10^{-1} (9.80×10^{-3})	6.78×10^{-1} (2.66×10^{-2})	1.81 (7.12×10^{-2})	0.01
3	9.10×10^{-2} (3.58×10^{-3})	1.36×10^{-1} (5.35×10^{-3})	1.36×10^{-1} (5.35×10^{-3})	1.95×10^{-1} (7.67×10^{-3})	5.06×10^{-1} (1.99×10^{-2})	1.26 (4.96×10^{-2})	0.01
4	9.99×10^{-3} (3.93×10^{-4})	9.99×10^{-3} (3.93×10^{-4})	1.00×10^{-2} (3.93×10^{-4})	1.40×10^{-1} (5.51×10^{-3})	3.30×10^{-1} (1.29×10^{-2})	6.99×10^{-1} (2.75×10^{-2})	0.01
5	4.38×10^{-4} (1.72×10^{-5})	4.38×10^{-4} (1.72×10^{-5})	4.63×10^{-4} (1.82×10^{-5})	8.51×10^{-2} (3.35×10^{-3})	1.55×10^{-1} (6.10×10^{-3})	1.80×10^{-1} (7.08×10^{-3})	0.01

Table A4-20 SNF Oxidation Simulation Data for Case 1 (Exponential Decomposition of the Residual Water in 4.77 Years)

Zone	Low-End SNF and Cladding Initial Temperatures						High-End SNF and Cladding Initial Temperatures						Cladding Failure
	Moles of Water												
	5.5		17.4		55		5.5		17.4		55		
	UO_{2+x} Mass (oz)	Extent of Oxidation*	UO_{2+x} Mass (oz)	Extent of Oxidation*	UO_{2+x} Mass (oz)	Extent of Oxidation*	UO_{2+x} Mass (oz)	Extent of Oxidation*	UO_{2+x} Mass (oz)	Extent of Oxidation*	UO_{2+x} Mass (oz)	Extent of Oxidation*	
1	68.2 g (2.40 oz) of U_3O_8	100% to U_3O_8, 100% to U_3O_8	68.3 g (2.40 oz) of U_3O_8	100% to U_3O_8, 100% to U_3O_8	68.4 g (2.41 oz) of U_3O_8	100% to U_3O_8, 100% to U_3O_8	2.4 g (0.08 oz) of U_3O_8	10.4% to U_3O_8, 0	7.5 g (0.26 oz) of U_3O_8	32.8% to U_3O_8, 0	63.5 g (2.24 oz) of U_3O_8	100% to U_3O_8, 89.7% to U_3O_8	0.1%
2	68.2 g (2.40 oz) of U_3O_8	100% to U_3O_8, 100% to U_3O_8	68.2 g (2.40 oz) of U_3O_8	100% to U_3O_8, 100% to U_3O_8	68.2 g (2.40 oz) of U_3O_8	100% to U_3O_8, 100% to U_3O_8	2.4 g (0.08 oz) of U_3O_8	10.4% to U_3O_8, 0	9.4 g (0.33 oz) of U_3O_8	41.4% to U_3O_8, 0	68.4 g (2.41 oz) of U_3O_8	100% to U_3O_8, 100% to U_3O_8	0.1%
3	49.2 g (1.73 oz) of $UO_{2.4}$	100% to $UO_{2.4}$, 60.0% to $UO_{2.4}$	67.1 g (2.36 oz) of $UO_{2.4}$	100% to $UO_{2.4}$, 100% to $UO_{2.4}$	67.1 g (2.36 oz) of $UO_{2.4}$	100% to $UO_{2.4}$, 75.9% to $UO_{2.4}$	2.6 g (0.09 oz) of U_3O_8	11.4% to U_3O_8, 0	69.3 g (2.44 oz) of U_3O_8	100% to U_3O_8, 100% to U_3O_8	68.2 g (2.40 oz) of U_3O_8	100% to U_3O_8, 100% to U_3O_8	0.1%
4	10.0 g (0.34 oz) of $UO_{2.4}$	44.7% to $UO_{2.4}$, 0	12.1 g (0.43 oz) of $UO_{2.4}$	54.1% to $UO_{2.4}$, 0	19.8 g (0.70 oz) of $UO_{2.4}$	47.5% to $UO_{2.4}$, 0	68.2 g (2.40 oz) of U_3O_8	100% to U_3O_8, 100% to U_3O_8	68.2 g (2.40 oz) of U_3O_8	100% to U_3O_8, 100% to U_3O_8	68.2 g (2.40 oz) of U_3O_8	100% to U_3O_8, 100% to U_3O_8	0.1%
1	68.3 g (2.40 oz) of U_3O_8	100% to U_3O_8, 100% to U_3O_8	68.3 g (2.40 oz) of U_3O_8	100% to U_3O_8, 100% to U_3O_8	68.4 g (2.41 oz) of U_3O_8	100% to U_3O_8, 100% to U_3O_8	2.4 g (0.08 oz) of U_3O_8	10.4% to U_3O_8, 0	7.5 g (0.26 oz) of U_3O_8	32.8% to U_3O_8, 0	65.8 g (2.32 oz) of U_3O_8	100% to U_3O_8, 97.4% to U_3O_8	0.01%

* Extent of Oxidation: This column provides information on the percentage of exposed SNF pellets that have undergone oxidation to a particular UO_{2+x} phase in the canister. The extent of oxidation is calculated separately for the directly exposed SNF pellets and SNF pellets in the crack length, plus a 6-cm (2.36-in.) area of a failed rod not directly exposed. The extent of oxidation values for the directly exposed SNF pellets and the adjacent SNF pellets, not directly exposed, are separated by a comma.

Table A4-21 SNF Oxidation Simulation Data for Case 2 (Linear Decomposition of the Residual Water in 4.77 Years)

Zone	Low-End SNF and Cladding Initial Temperatures						High-End SNF and Cladding Initial Temperatures						Cladding Failure
	Moles of Water												
	5.5		17.4		55		5.5		17.4		55		
	UO_{2+x} Mass (oz)	Extent of Oxidation*	UO_{2+x} Mass (oz)	Extent of Oxidation*	UO_{2+x} Mass (oz)	Extent of Oxidation*	UO_{2+x} Mass (oz)	Extent of Oxidation*	UO_{2+x} Mass (oz)	Extent of Oxidation*	UO_{2+x} Mass (oz)	Extent of Oxidation*	
1	3.6 g (0.13 oz) of U_3O_8	16% to U_3O_8, 0	68.2 g (2.40 oz) of U_3O_8	100% to U_3O_8, 100% to U_3O_8	68.2 g (2.41 oz) of U_3O_8	100% to U_3O_8, 100% to U_3O_8	2.4 g (0.09 oz) of U_3O_8	10.4% to U_3O_8, 0	7.5 g (0.26 oz) of U_3O_8	32.8% to U_3O_8, 0	24.4 g (0.86 oz) of U_3O_8	100% to U_3O_8, 3.7% to U_3O_8	0.1%
2	68.2 g (2.40 oz) of U_3O_8	100% to U_3O_8, 100% to U_3O_8	68.2 g (2.40 oz) of U_3O_8	100% to U_3O_8, 100% to U_3O_8	68.2 g (2.40 oz) of U_3O_8	100% to U_3O_8, 100% to U_3O_8	2.4 g (0.09 oz) of U_3O_8	10.4% to U_3O_8, 0	7.5 g (0.26 oz) of U_3O_8	41.4% to U_3O_8, 0	39.1 g (1.37 oz) of U_3O_8	100% to U_3O_8, 36% to U_3O_8	0.1%
3	67.1 g (1.73 oz) of $UO_{2.4}$	100% to $UO_{2.4}$, 100% to $UO_{2.4}$	67.1 g (2.36 oz) of $UO_{2.4}$	100% to $UO_{2.4}$, 100% to $UO_{2.4}$	67.1 g (2.36 oz) of $UO_{2.4}$	100% to $UO_{2.4}$, 75.9% to $UO_{2.4}$	2.4 g (0.09 oz) of U_3O_8	10.4% to U_3O_8, 0	8.8 g (0.31 oz) of U_3O_8	38.7% to U_3O_8, 0	68.2 g (2.40 oz) of U_3O_8	100% to U_3O_8, 100% to U_3O_8	0.1%
4	11.6 g (0.34 oz) of $UO_{2.4}$	44.7% to $UO_{2.4}$, 0	11.8 g (0.42 oz) of $UO_{2.4}$	52.7% to $UO_{2.4}$, 0	19.8 g (0.70 oz) of $UO_{2.4}$	47.5% to $UO_{2.4}$, 0	2.3 g (0.08 oz) of U_3O_8	10.1% to U_3O_8, 0	68.2 g (2.40 oz) of U_3O_8	100% to U_3O_8, 100% to U_3O_8	68.2 g (2.40 oz) of U_3O_8	100% to U_3O_8, 100% to U_3O_8	0.1%
1	4.4 g (0.16 oz) of U_3O_8	19.4% to U_3O_8, 0	68.2 g (2.40 oz) of U_3O_8	100% to U_3O_8, 100% to U_3O_8	68.4 g (2.41 oz) of U_3O_8	100% to U_3O_8, 100% to U_3O_8	2.4 g (0.09 oz) of U_3O_8	10.4% to U_3O_8, 0	7.5 g (0.26 oz) of U_3O_8	32.8% to U_3O_8, 0	24.4 g (0.86 oz) of U_3O_8	100% to U_3O_8, 3.7% to U_3O_8	0.01%

* Extent of Oxidation: This column provides information on the percentage of exposed SNF pellets that have undergone oxidation to a particular UO_{2+x} phase in the canister. The extent of oxidation is calculated separately for the directly exposed SNF pellets and SNF pellets in the crack length, plus a 6-cm (2.36-in.) area of a failed rod not directly exposed. The extent of oxidation values for the directly exposed SNF pellets and the adjacent SNF pellets, not directly exposed, are separated by a comma.

Table A4–22 SNF Oxidation Simulation Data for Case 3 (Exponential Decomposition of the Residual Water in 71.62 Years)

Zone	Low-End SNF and Cladding Initial Temperatures						High-End SNF and Cladding Initial Temperatures						Cladding Failure
	Moles of Water												
	5.5		17.4		55		5.5		17.4		55		
	UO_{2+x} Mass g (oz)	Extent of Oxidation*	UO_{2+x} Mass g (oz)	Extent of Oxidation*	UO_{2+x} Mass g (oz)	Extent of Oxidation*	UO_{2+x} Mass g (oz)	Extent of Oxidation*	UO_{2+x} Mass g (oz)	Extent of Oxidation*	UO_{2+x} Mass g (oz)	Extent of Oxidation*	
1	2.0 g (0.07 oz) of U_3O_8 and 1.5 g (0.05 oz) of $UO_{2.4}$	8.8% to U_3O_8 and 6.7% to $UO_{2.4}$, 0	31.8 g (1.12 oz) of U_3O_8 and 35.7 g (1.26 oz) of $UO_{2.4}$	100% to U_3O_8, 20% to U_3O_8 and 80% to $UO_{2.4}$	68.2 g (2.40 oz) of U_3O_8	100% to U_3O_8, 100% to U_3O_8	2.3 g (0.08 oz) of U_3O_8 and 0.1 g (0.003 oz) of $UO_{2.4}$	10.1% to U_3O_8 and 0.5% to $UO_{2.4}$, 0	7.2 g (0.25 oz) of U_3O_8 and 0.4 g (0.014 oz) of $UO_{2.4}$	31.7% to U_3O_8 and 1.8% to $UO_{2.4}$, 0	23.0 g (0.81 oz) of U_3O_8 and 25.6 g (0.90 oz) of $UO_{2.4}$	100% to U_3O_8, 0.6% to U_3O_8 and 57.2% to $UO_{2.4}$	0.1%
2	2.0 g (0.07 oz) of U_3O_8 and 44.3 g (1.56 oz) of $UO_{2.4}$	8.8% to U_3O_8 and 91.2% to $UO_{2.4}$, 53.4% to $UO_{2.4}$	68.2 g (2.40 oz) of U_3O_8	100% to U_3O_8, 100% to U_3O_8	68.2 g (2.40 oz) of U_3O_8	100% to U_3O_8, 100% to U_3O_8	2.2 g (0.08 oz) of U_3O_8 and 0.3 g (0.01 oz) of $UO_{2.4}$	9.7% to U_3O_8 and 1.3% to $UO_{2.4}$, 0	7.0 g (0.25 oz) of U_3O_8 and 0.9 g (0.03 oz) of $UO_{2.4}$	30.8% to U_3O_8 and 4.0% to $UO_{2.4}$, 0	24.6 g (0.87 oz) of U_3O_8 and 42.9 g (1.51 oz) of $UO_{2.4}$	100% to U_3O_8 and 4.1% to $UO_{2.4}$, 95.9% to $UO_{2.4}$	0.1%
3	67.1 g (2.36 oz) of $UO_{2.4}$	100% to $UO_{2.4}$, 100% to $UO_{2.4}$	67.1 g (2.36 oz) of $UO_{2.4}$	100% to $UO_{2.4}$, 100% to $UO_{2.4}$	67.1 g (2.36 oz) of $UO_{2.4}$	100% to $UO_{2.4}$, 100% to $UO_{2.4}$	1.9 g (0.07 oz) of U_3O_8 and 0.7 g (0.03 oz) of $UO_{2.4}$	8.4% to U_3O_8 3.1% to $UO_{2.4}$, 0	6.4 g (0.22 oz) of U_3O_8 and 12.0 g (10.42 oz) of $UO_{2.4}$	28.2% to U_3O_8 and 53.7% to $UO_{2.4}$, 0	68.2 g (2.40 oz) of U_3O_8	100% to U_3O_8, 100% to U_3O_8	0.1%
4	19.1 g (0.67 oz) of $UO_{2.4}$	85.4% to $UO_{2.4}$, 0	19.4 g (0.68 oz) of $UO_{2.4}$	86.7% to $UO_{2.4}$, 0	19.8 g (0.69 oz) of $UO_{2.4}$	88.6% to $UO_{2.4}$, 0	1.1 g (0.04 oz) of U_3O_8 and 3.4 g (0.12 oz) of $UO_{2.4}$	4.8% to U_3O_8 and 15.2% to $UO_{2.4}$, 0	3.5 g (0.12 oz) of U_3O_8 and 63.6 g (2.24 oz) of $UO_{2.4}$	15.4% to U_3O_8 and 84.6% to $UO_{2.4}$, 100% to $UO_{2.4}$	68.2 g (2.40 oz) of U_3O_8	100% to U_3O_8, 100% to U_3O_8	0.1%
1	2.0 g (0.07 oz) of U_3O_8 and 5.8 g (0.20 oz) of $UO_{2.4}$	8.8% to U_3O_8 and 25.9% to $UO_{2.4}$, 0	32.3 g (1.14 oz) of U_3O_8 and 35.3 g (1.24 oz) of $UO_{2.4}$	100% to U_3O_8, 21% to U_3O_8 and 79% to $UO_{2.4}$	68.2 g (2.40 oz) of U_3O_8	100% to U_3O_8, 100% to U_3O_8	2.3 g (0.08 oz) of U_3O_8 and 0.1 g (0.003 oz) of $UO_{2.4}$	10.1% to U_3O_8 and 0.5% to $UO_{2.4}$, 0	7.2 g (0.25 oz) of U_3O_8 and 0.4 g (0.014 oz) of $UO_{2.4}$	31.7% to U_3O_8 and 1.8% to $UO_{2.4}$, 0	23.1 g (0.81 oz) of U_3O_8 and 25.9 g (0.91 oz) of $UO_{2.4}$	100% to U_3O_8, 0.8% to U_3O_8 and 57.9% to $UO_{2.4}$	0.01%

* Extent of Oxidation: This column provides information on the percentage of exposed SNF pellets that have undergone oxidation to a particular UO_{2+x} phase in the canister. The extent of oxidation is calculated separately for the directly exposed SNF pellets and SNF pellets in the crack length, plus a 6-cm (2.36-in.) area of a failed rod not directly exposed. The extent of oxidation values for the directly exposed SNF pellets and the adjacent SNF pellets, not directly exposed, are separated by a comma.

Table A4–23 SNF Oxidation Simulation Data for Case 4 (Linear Decomposition of the Residual Water in 71.62 Years)

Zone	Low-End SNF and Cladding Initial Temperatures						High-End SNF and Cladding Initial Temperatures						Cladding Failure
	Moles of Water												
	5.5		17.4		55		5.5		17.4		55		
	UO_{2+x} Mass (oz)	Extent of Oxidation*	UO_{2+x} Mass (oz)	Extent of Oxidation*	UO_{2+x} Mass (oz)	Extent of Oxidation*	UO_{2+x} Mass (oz)	Extent of Oxidation*	UO_{2+x} Mass (oz)	Extent of Oxidation*	UO_{2+x} Mass (oz)	Extent of Oxidation*	
1	0.5 g (0.02 oz) of U_3O_8 and 25.3 g (0.90 oz) of $UO_{2.4}$	2.2% to U_3O_8 and 97.8% to $UO_{2.4}$, 7.6% to $UO_{2.4}$	2.0 g (0.07 oz) of U_3O_8 and 65.1 g (2.30 oz) of $UO_{2.4}$	8.8% to U_3O_8 and 91.2% to $UO_{2.4}$, 100% to $UO_{2.4}$	68.2 g (2.40 oz) of U_3O_8	100% to U_3O_8, 100% to U_3O_8	0.9 g (0.03 oz) of U_3O_8 and 17.0 g (0.60 oz) of $UO_{2.4}$	4% to U_3O_8 and 76% to $UO_{2.4}$, 0	2.9 g (0.10 oz) of U_3O_8 and 48.0 g (1.69 oz) of $UO_{2.4}$	12.8% to U_3O_8 and 87.2% to $UO_{2.4}$, 63.6% to $UO_{2.4}$	36.9 g (0.13 oz) of U_3O_8 and 30.7 g (1.73 oz) of $UO_{2.4}$	100% to U_3O_8, 31.2% to U_3O_8 and 68.8% to $UO_{2.4}$	0.1%
2	0.2 g (0.007 oz) of U_3O_8 and 20.4 g (0.72 oz) of $UO_{2.4}$	0.9% to U_3O_8 and 91.2% to $UO_{2.4}$, 0	0.6 g (0.02 oz) of U_3O_8 and 63.2 g (2.22 oz) of $UO_{2.4}$	2.6% to U_3O_8 and 97.4% to $UO_{2.4}$, 97.5% to $UO_{2.4}$	14.9 g (0.53 oz) of U_3O_8 and 52.4 g (1.85 oz) of $UO_{2.4}$	65.6% to U_3O_8 and 34.4% to $UO_{2.4}$, 100% to $UO_{2.4}$	0.7 g (0.03 oz) of U_3O_8 and 14.5 g (1.73 oz) of $UO_{2.4}$	3% to U_3O_8 and 64.8% to $UO_{2.4}$, 0	2.2 g (0.08 oz) of U_3O_8 and 36.9 g (1.30 oz) of $UO_{2.4}$	9.7% to U_3O_8 and 90.3% to $UO_{2.4}$, 37.3% to $UO_{2.4}$	11.1 g (0.13 oz) of U_3O_8 and 56.2 g (1.73 oz) of $UO_{2.4}$	48.9% to U_3O_8 and 51.1% to $UO_{2.4}$, 100% to $UO_{2.4}$	0.1%
3	20.2 g (0.71 oz) of $UO_{2.4}$	90.3% to $UO_{2.4}$, 0	67.1 g (2.36 oz) of $UO_{2.4}$	100% to $UO_{2.4}$, 100% to $UO_{2.4}$	67.1 g (2.36 oz) of $UO_{2.4}$	100% to $UO_{2.4}$, 100% to $UO_{2.4}$	0.4 g (0.13 oz) of U_3O_8 and 13.2 g (0.51 oz) of $UO_{2.4}$	1.8% to U_3O_8 and 59% to $UO_{2.4}$, 0	1.4 g (0.05 oz) of U_3O_8 and 31.4 g (1.11 oz) of $UO_{2.4}$	6.2% to U_3O_8 and 93.8% to $UO_{2.4}$, 23.2% to $UO_{2.4}$	4.8 g (0.17 oz) of U_3O_8 and 64.2 g (1.73 oz) of $UO_{2.4}$	21.1% to U_3O_8 and 78.9% to $UO_{2.4}$, 100% to $UO_{2.4}$	0.1%
4	16.4 g (0.58 oz) of $UO_{2.4}$	70.3% to $UO_{2.4}$, 0	18.6 g (0.65 oz) of $UO_{2.4}$	83.2% to $UO_{2.4}$, 0	17.0 g (0.60 oz) of $UO_{2.4}$ and 51.9 g (1.83 oz) of UO_3	76% to $UO_{2.4}$ and 24% to $UO_{2.4}$, 100% to UO_3	0.1 g (0.003 oz) of U_3O_8 and 13.3 g (0.47 oz) of $UO_{2.4}$	0.4% to U_3O_8 and 59.5% to $UO_{2.4}$, 0	0.4 g (0.13 oz) of U_3O_8 and 32.9 g (1.73 oz) of $UO_{2.4}$	1.9% to U_3O_8 and 98.2% to $UO_{2.4}$, 38.5% to $UO_{2.4}$	1.5 g (0.05 oz) of U_3O_8 and 65.6 g (2.31 oz) of $UO_{2.4}$	6.6% to U_3O_8 and 93.4% to $UO_{2.4}$, 100% to $UO_{2.4}$	0.1%
1	0.5 g (0.02 oz) of U_3O_8 and 26.2 g (0.92 oz) of $UO_{2.4}$	2.2% to U_3O_8 and 97.8% to $UO_{2.4}$, 9.6% to $UO_{2.4}$	2.0 g (0.07 oz) of U_3O_8 and 65.1 g (2.30 oz) of $UO_{2.4}$	8.8% to U_3O_8 and 91.2% to $UO_{2.4}$, 100% to $UO_{2.4}$	68.2 g (2.40 oz) of U_3O_8	100% to U_3O_8, 100% to U_3O_8	0.9 g (0.03 oz) of U_3O_8 and 17.4 g (0.61 oz) of $UO_{2.4}$	4% to U_3O_8 and 77.8% to $UO_{2.4}$, 0	2.9 g (0.014 oz) of U_3O_8 and 48.9 g (1.72 oz) of $UO_{2.4}$	12.8% to U_3O_8 and 87.2% to $UO_{2.4}$, 65.6% to $UO_{2.4}$	38.8 g (1.37 oz) of U_3O_8 and 28.9 g (1.02 oz) of $UO_{2.4}$	100% to U_3O_8, 35.4% to U_3O_8 and 64.6% to $UO_{2.4}$	0.01%

* Extent of Oxidation: This column provides information on the percentage of exposed SNF pellets that have undergone oxidation to a particular UO_{2+x} phase in the canister. The extent of oxidation is calculated separately for the directly exposed SNF pellets and SNF pellets in the crack length, plus a 6-cm (2.36-in.) area of a failed rod not directly exposed. The extent of oxidation values for the directly exposed SNF pellets and the adjacent SNF pellets, not directly exposed, are separated by a comma.

A5. HYDROGEN ABSORPTION BY CLADDING AND DEGRADATION OF INTERNAL STRUCTURAL MATERIALS AS A RESULT OF RESIDUAL WATER

This section presents the results of analyses of hydrogen absorption by cladding and corrosion of cask internal structures from various degradation modes. The analyses are used to develop an understanding of the extent of damage to various cask internal structural components.

A5.1 Hydrogen Absorption by Cladding

Zirconium, like other metals, such as titanium, niobium, tantalum, and palladium, exothermically absorbs hydrogen under some conditions. The zirconium-based cladding material exposed to coolant water during reactor operations would absorb hydrogen. The concentration of absorbed hydrogen in the cladding material ranges from 100 to 600 parts per million (ppm) (Mardon et al., 1997), mainly depending on temperature, SNF burnup, and material type. This hydrogen absorption process during reactor operation is depicted in the form of sequences of chemical reactions shown in Figure A5-1. As seen in the figure, water first reacts with the zirconium in the cladding material. This results in release of atomic hydrogen. A fraction of the released atomic hydrogen is absorbed by the cladding, while that remaining is released as hydrogen gas. The fraction of atomic hydrogen absorbed is also known as the hydrogen uptake fraction and is denoted by the symbol x in Figure A5-1. Depending on the cladding alloy, it ranges from 10 to 20 percent. The solubility of hydrogen in zirconium is highly temperature dependent, with increased solubility at higher temperatures (Pfeif et al., 2010). As the cladding cools during extended storage, the solubility of hydrogen may be exceeded and hydride precipitates may form.

The analyses presented in Section A2 indicate that radiolysis of residual water generates hydrogen. This radiolysis-generated hydrogen is expected to be predominantly in the molecular form, which can be dissociated on the cladding surface and absorbed into cladding by the simplified Equation A5-1 without showing the detailed absorption mechanism as follows:

$$Zr + H_2\,(gas) \rightarrow Zr\text{-}2H\,(absorbed) \qquad (A5\text{-}1)$$

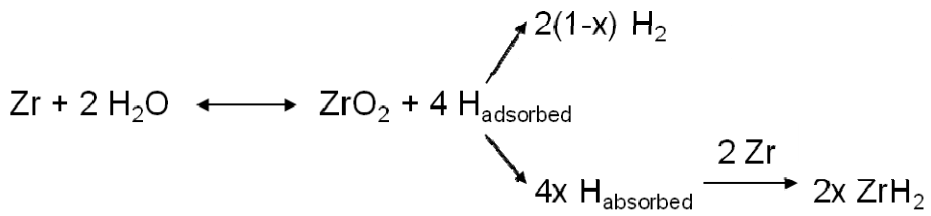

Figure A5-1 Sequence of chemical reactions depicting zirconium reaction with water, release of hydrogen gas, and absorption of hydrogen by zirconium

It is known that the amount of hydrogen absorbed follows Sievert's law, which increases with hydrogen partial pressure and temperature (Steinbrück, 2004). Based on this fact, researchers developed the gaseous method to charge hydrogen into cladding material. But this method

often operates at elevated temperatures (e.g., 300 or 400 degrees Celsius (°C)) (Racine et al., 2005) to enhance hydrogen absorption.

It is reported that the hydrogen solubility in zirconium oxide is very low (10^{-5} to 10^{-4} moles of hydrogen per mole oxide) (Miyake et al., 1999). Consequently, the oxide film significantly impedes hydrogen absorption by the substrate (Steinbrück, 2004). In practice, the oxide film is often removed by sanding and pickling in strong acidic solution before hydrogen charging to facilitate hydrogen entry. The discussion presented in Section A3.1 indicated that the SNF cladding is covered by oxide film formed from reactor operation. During extended storage, this oxide film is expected to impede molecular hydrogen entry into the cladding.

However, hydrogen could be absorbed by the cladding through the process shown in Figure A5-1 when water directly reacts with cladding. This would occur when water contacting the cladding material is either in the liquid phase or the RH is above a threshold value and the cladding temperature is sufficiently high. The threshold RH value is assumed to be 20 percent based on the similarity in thermodynamic and practical nobility between zirconium and aluminum, as discussed in Section A3.1.5.

The RH inside the cask is a function of (1) SNF and cladding temperatures, (2) water amount, and (3) the rate of radiolysis. RH data as a function of these three factors were generated from the integration model, as summarized in Table A5-1.

The information listed in Table A5-1 indicates that the RH values would briefly exceed 20 percent in Zone 5 only for 17.4 and 55 moles of water, low-end SNF and cladding initial temperatures, and the following three radiolysis models: (1) exponential decomposition in 4.77 years, (2) linear decomposition in 4.77 years, and (3) exponential decomposition in 71.62 years. RH values are expected to exceed 20 percent in several zones for the radiolysis kinetic model of linear decomposition in 71.62 years.

First discussed is the effect of RH values exceeding 20 percent in Zone 5 for low-end SNF and cladding initial temperatures and for the three kinetic models: (1) exponential decomposition in 4.77 years, (2) linear decomposition in 4.77 years, and (3) exponential decomposition in 71.62 years. The cladding surface area that would be exposed in Zone 5 is approximately 11.1 m^2 (119.5 ft^2) (see Table A4-6). The temperature of the SNF and cladding in Zone 5 would vary between 375 and 370 Kelvin (K) (215.6 and 206.6 degrees Fahrenheit (°F)) for the first 5 years after storage begins, and 375 and 355 K (215.6 and 179.6 °F) for the first 16 years after storage begins (see Figure A1-12 in Section A1). Considering this, it can be assumed that the cladding temperature in Zone 5 is 375 K (215.6 °F) for the first 16 years when RH exceeds 20 percent. The amount of water that would react with the exposed cladding in Zone 5 at 375 K (215.6 °F) as a function of time is calculated, and data are presented in Figure A5-2. As seen in the figure, the maximum water amount that could react with exposed cladding in Zone 5 in 16 years after storage begins is less than 6×10^{-4} moles.

Table A5-1 Summary of the RH Data Generated from the Integration Model (The Data Are Summarized as a Function of Radiolysis Kinetic Model, Low- and High-End SNF and Cladding Initial Temperatures, and Water Amount with a Thermal Decay Constant of 0.023)

Radiolysis Kinetic Model	Low-End SNF and Cladding Initial Temperatures			High-End SNF and Cladding Initial Temperatures		
	Water Amount (Moles)			Water Amount (Moles)		
	5.5	17.4	55	5.5	17.4	55
Exponential Decomposition in 4.77 Years	RH does not exceed 20% in any zone. See Figure A5-7(a).	Maximum RH of 23.6% in Zone 5. This value decreases to below 20% less than 1.5 years after storage begins. See Figure A5-7(b).	Maximum RH of 75% in Zone 5. This value decreases below 20% less than 4 years after storage begins. See Figure A5-7(c).	RH does not exceed 20% value in any zone. See Figure A5-11(a).	RH does not exceed 20% value in any zone. See Figure A5-11(b).	RH does not exceed 20% value in any zone. See Figure A5-11(c).
Linear Decomposition in 4.77 Years	RH does not exceed 20% in any zone. See Figure A5-8(a).	Maximum RH of 23.6% in Zone 5. This value decreases to below 20% less than 1.5 years after storage begins. See Figure A5-8(b).	Maximum RH of 75% in Zone 5. This value decreases below 20% less than 4 years after storage begins. See Figure A5-8(c).	RH does not exceed 20% in any zone. See Figure A5-12(a).	RH does not exceed 20% value in any zone. See Figure A5-12(b).	RH does not exceed 20% value in any zone. See Figure A5-12(c).
Exponential Decomposition in 71.62 Years	RH does not exceed 20% in any zone. See Figure A5-9(a).	Maximum RH of 23.6% in Zone 5. This value decreases to below 20% less than 2 years after storage begins. See Figure A5-9(b).	Maximum RH of 75% in Zone 5. This value decreases to below 20% less than 16 years after storage begins. See Figure A5-9(c).	RH does not exceed 20% in any zone. See Figure A5-13(a).	RH does not exceed 20% value in any zone. See Figure A5-13(b)	RH does not exceed 20% value in any zone. See Figure A5-13(c)
Linear Decomposition in 71.62 Years	RH does not exceed 20% in any zone. See Figure A5-10(a).	RH remains above 20% in Zones 4 and 5. See Figure A5-3(a) for additional information.	RH exceeds 20% in Zones 3, 4, and 5. See Figure A5-3(b) for additional information.	RH does not exceed 20% value in any zone. See Figure A5-14(a).	RH does not exceed 20% value in any zone. See Figure A5-14(b).	RH exceeds 20% in Zones 4 and 5. See Figure A5-5 for additional information.
Figures A5-7 to A5-14 at the end of this section present detailed data.						

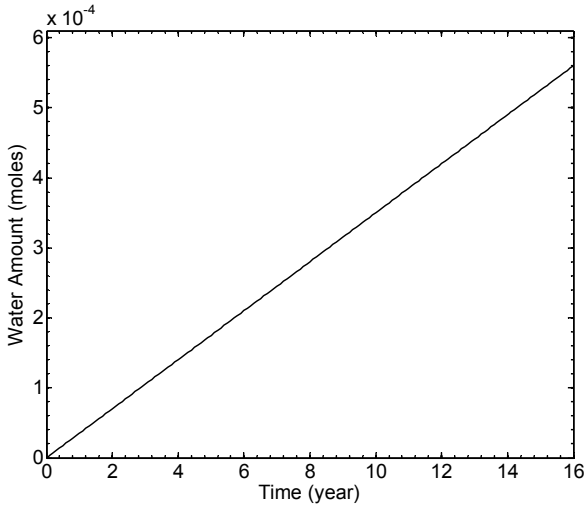

Figure A5-2 Water amount in moles that would react with exposed cladding in Zone 5 as a function of time

Assuming a cladding thickness of 0.8 mm (3.1×10^{-2} in.) and a water amount of 6×10^{-4} moles, the maximum amount of atomic hydrogen that could be absorbed by the cladding would be 6×10^{-4} moles. This would yield an increase in hydrogen concentration of approximately 24 parts per billion (ppb) in the cladding material assuming the hydrogen uptake fraction is 100 percent. Thus, hydrogen absorption by cladding is not a concern for the three radiolysis models.

The following discussion concerns the effect of RH values exceeding 20 percent in different zones for both low- and high-end SNF and cladding initial temperatures and the kinetic model of linear radiolysis in 71.62 years. Figures A5-3(a) and (b), respectively, present the RH profile for low-end SNF and cladding initial temperatures and 17.4 and 55 moles of residual water.

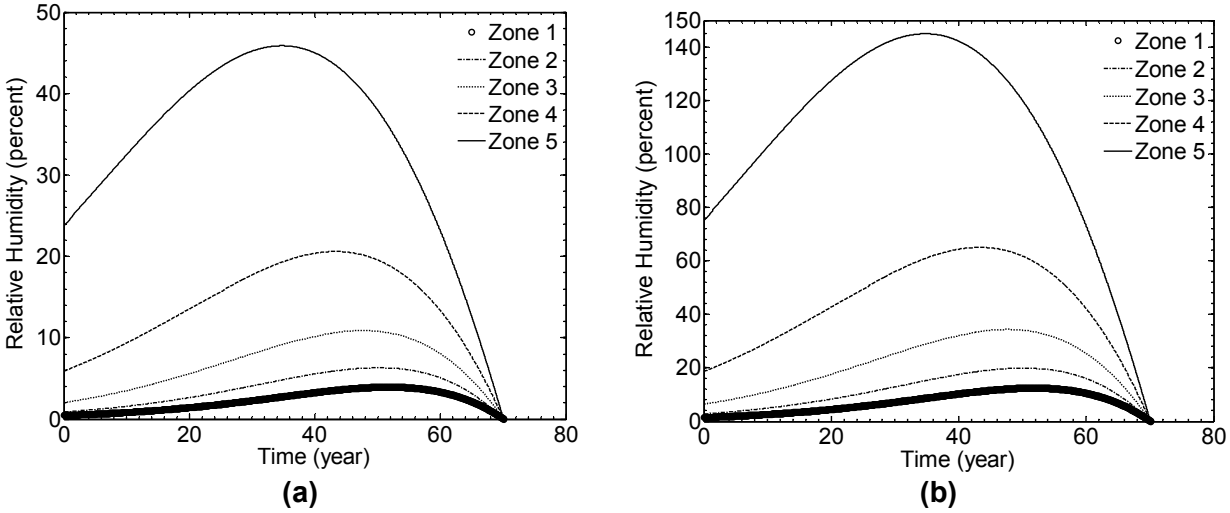

Figure A5-3 RH as a function of time for the radiolysis kinetic model of linear decay in 70 years and low-end SNF and cladding initial temperatures in different zones inside canister of the dry storage cask system. (a) 17.4 moles of residual water and (b) 55 moles of residual water. Above 100 percent represents saturation.

As seen in Figure A5-3(a), the RH in Zone 5 is greater than 20 percent until 62 years after storage begins, and the RH in Zone 4 exceeds 20 percent after 38 years of storage and remains at more than 20 percent for the next 10 years. The extrapolation of information presented in Figure A5-2 indicates that the cladding in Zone 5 would, at most, react with 2.4×10^{-3} moles of water, and there would be corresponding increases in hydrogen concentration of approximately 100 ppb in the cladding material. Moreover, the SNF and cladding temperatures in Zone 4 after 38 years of storage are below 375 K (215.6 °F) but above 350 K (170.6 °F) up to 50 years after storage. The cladding surface area in Zone 4 is approximately 72.5 m^2 (780.4 ft^2) (see Table A4-6). Using the information presented in Figure A5–2 and the cladding surface area in Zone 4, the maximum amount of water that could directly react with the cladding is 2.5×10^{-3} moles. This would result in increases of hydrogen concentration of approximately 15 ppb in the Zone 4 cladding material.

As seen in Figure A5-3(b), the RH in Zones 3, 4, and 5 is higher than 20 percent. Specifically, RH in Zone 5 is higher than 20 percent until 68 years after storage begins. Moreover, the RH in Zone 4 exceeds 20 percent until 66 years after storage begins, and the RH in Zone 3 exceeds 20 percent after 21 years of storage and remains above 20 percent for the next 40 years. The RH in Zone 2 is close to 20 percent but does not exceed 20 percent. The analysis presented for Zone 5 based on the RH profile in Figure A5-3(a) can be applied for the zones for the RH profile in Figure A5-3(b).

These results indicate that exposed cladding in Zone 5 would not be expected to absorb more than 2.4×10^{-3} moles of hydrogen and, as a result, the hydrogen concentration would not exceed 100 ppb in the Zone 5 cladding material. Figure A5–4 indicates the amount of water that could react with cladding in Zones 3 and 4 given the RH and temperature profile. The amount of water is approximately equal to 0.06 and 0.05 moles for Zones 3 and 4, respectively. This amount of water would result in an increase in hydrogen concentration by 0.13 and 0.3 ppm for the cladding in Zones 3 and 4, respectively.

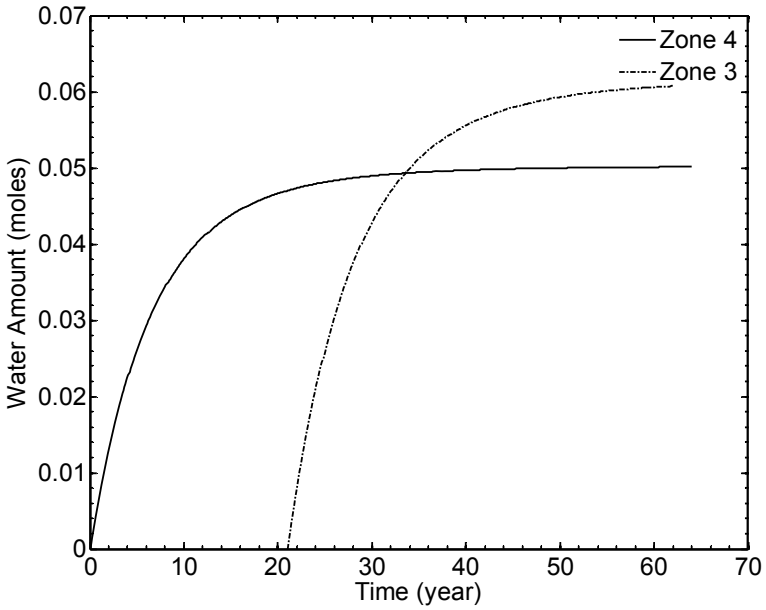

Figure A5–4 Temperature versus water amount in moles that would react with exposed cladding in Zones 3 and 4 given the RH profiles presented in Figure A5-3(b)

Figure A5-5 illustrates the RH profile for high-end SNF and cladding initial temperatures and 55 moles of residual water. As seen in the figure, the RH in Zone 5 exceeds 20 percent after 24 years of storage and remains above 20 percent for the next 28 years. Moreover, the RH in Zone 4 exceeds 20 percent after 46 years of storage and remains above 20 percent for the next 8 years. The cladding temperature in Zone 5 when the RH exceeds 20 percent is expected to range from 475 to 325 K (395.6 to 125.6 °F). Similarly, the cladding temperature in Zone 4 when RH exceeds 20 percent is expected to be in the range of 390 to 380 K (243.6 to 224.6 °F). Considering this, the cladding material in Zones 5 and 4 would at most react with 3.0×10^{-3} and 2.0×10^{-3} moles of water, respectively. This would result in an increase in hydrogen concentration by 120 and 12 ppb in Zones 5 and 4, respectively.

The analysis presented in this section, which is based on information found in the literature, indicates that the presence of the oxide film is expected to impede the absorption of the molecular form of hydrogen generated from radiolysis of the residual water. During storage, the decreasing temperature further reduces the likelihood of hydrogen entry. Under the conditions in which the RH is above 20 percent, cladding directly reacts with moisture or liquid water. The analysis of RH and temperature from the integration model shows that the amount of hydrogen absorbed by the cladding during extended storage is significantly less than preexisting dissolved hydrogen in the cladding resulting from reactor operations, even assuming that the hydrogen uptake fraction is 100 percent.

Therefore, absorption of additional hydrogen by cladding from residual water is not a concern. However, as this study did not conduct detailed radiolysis modeling, uncertainty remains regarding

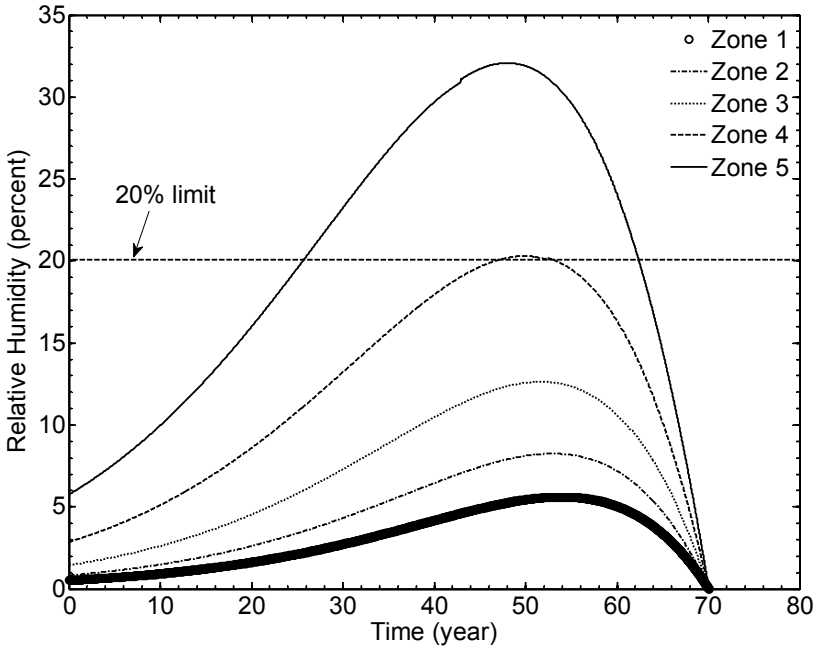

Figure A5-5 RH as a function of time for the radiolysis kinetic model of linear decomposition in 71.62 years, high-end SNF and cladding initial temperatures and 55 moles of residual water in different zones inside canister of the dry storage cask system

the radiolysis products of the residual water (e.g., hydrogen radicals may be produced from radiolysis and may have a different entry mechanism). In addition, radiolysis could also affect the cladding oxide film, which could also lead to uncertainty in the hydrogen absorption analysis.

A5.2 Degradation of Internal Structural Materials

This section discusses corrosion of internal structural materials by residual water and describes the different structural materials used in various canisters. The section also discusses the degradation of those materials by residual water and radiolysis-generated chemical species.

Aqueous corrosion could occur in vapor when the RH is greater than a threshold value. For internal structural components, the threshold value of greater than 20 percent is used for corrosion to occur. The following section describes an assessment made assuming that the RH is high enough for vapor corrosion or vapor condensation. In the early period of storage, the RH is usually below 20 percent.

A5.2.1 Internal Structural Materials

The materials inside the canister primarily include the canister internal wall, SNF basket, neutron absorber materials, shielding materials, cladding, and spacer grid materials used in SNF assemblies.

A5.2.1.1 Canister

Canisters are typically composed of stainless steel materials and are sealed by welding. The materials used for metallic cask vessels are typically nodular cast iron, carbon steel, low-alloy steel, forged steel, and stainless steel (NWTRB, 2010).

A5.2.1.2 Spent Nuclear Fuel Basket

The SNF basket assembly consists of the SNF basket and neutron absorbers. Examples of neutron absorber materials used in the SNF basket assemblies include metal matrix composites, such as boron carbide/aluminum matrix, that may be clad in aluminum (e.g., BORAL) and castable borated shielding (e.g., borated resins) (NWTRB, 2010). In some cases, neutron-absorbing materials are incorporated directly into the basket material (e.g., borated stainless steel). Materials typically used for the SNF basket include SS304 with boron, 6061–T651 aluminum, SA 705 Type 630 stainless steel, Inconel, SA 516 Gr 70, and 479 stainless steel (NWTRB, 2010). SNF baskets also have heat-conducting elements, which are made of aluminum alloys.

A5.2.1.3 Spent Nuclear Fuel Assembly

Zirconium-based alloys are used as cladding materials. Each SNF assembly also has spacer grids, which are made of Inconel alloys. The guide tubes for PWR assemblies and assembly channels for BWR assemblies are typically made from zirconium alloy, similar to cladding.

A5.2.2 Degradation Mechanisms

The following sections discuss degradation of the various internal structural materials from general corrosion, localized corrosion, SCC, galvanic corrosion, shadow corrosion, and

hydrogen-induced damage. These corrosion modes, except for general corrosion, are expected to commence when a fraction of the residual water condenses in the canister. The analysis presented in the previous section indicates that a fraction of the residual water could condense when relatively slow radiolytic decomposition of the residual water occurs and SNF and cladding temperatures are sufficiently low. The next section provides additional details on the range of canister environments that would lead to condensation of the residual water and the effect of the various degradation mechanisms on the internal structural components.

A5.2.2.1 General Corrosion

The SNF basket, neutron absorbers, and SNF assembly materials may be subject to general corrosion in the presence of moisture and aqueous solution. The rate and extent of corrosion will depend on temperature and RH. The corrosion rate of aluminum and carbon steel is expected to be higher than stainless steel and Inconel alloy in the canister environment.

The literature reports experimental data on corrosion rates of stainless steel and neutron absorber materials (Fix et al., 2004; EPRI, 2006; He et al., 2011). Typically, conventional stainless steel is reported to have higher corrosion rates than the metallic neutron absorber material. Tests conducted at 60, 75, and 90 °C (140, 167, and 194 °F) in humid air for borated stainless steel showed that the general corrosion rates were less than 600 nanometers per year (nm/yr) (0.024 mil/yr) (He et al., 2011). Based on the highest corrosion rate, 0.18 mm (7.1×10^{-3} in.) of material will be consumed in 300 years. However, the metal corrosion could be lower in the cask during storage because of the limited amount of water and low RH in the earlier period. The general corrosion rate of an Inconel alloy as a result of humid air is expected to be on the order of 25 nm/yr (10^{-3} mil/yr) (Van Rooyen and Copson, 1968). Based on this rate, the corrosion over 300 years would degrade a 7.5-μm (0.30×10^{-4} in.) layer of any structure made of Inconel alloy. The literature indicates that the humid air corrosion rate of carbon steel is expected to range from 8 to 30 μm/yr (0.32 to 1.2 mil/yr) under ambient conditions (Kucera, 1988). This would yield a penetration depth of 2.4 to 9 mm (0.09 to 0.35 in.) on structures made of carbon steel; however, the limited amount of water would constrain the extent of damage to the structures. Based on Baumann (2010), the humid air corrosion rate of pure aluminum is approximately 0.1 μm/yr (4×10^{-3} mil/yr) under ambient conditions. This corrosion rate would yield a penetration depth of 30 μm (1.2×10^{-3} in.) on structures made of pure aluminum. The humid air corrosion rate of aluminum-based alloys is not expected to differ significantly from pure aluminum (Baumann, 2010). Hence, the penetration depth of structures made of aluminum-based alloys would be close to that of pure aluminum.

Any aqueous solution would form when water condenses. Water may condense when RH is at 100 percent. This could occur for certain combinations of radiolysis kinetic models, cladding and SNF temperature profiles, and amounts of residual water. Analyses presented in the previous section indicate that water would condense when the 55 moles of residual water undergo linear decay in 71.62 years (see Figure A5-3(b)). The amount of water that would condense is approximately 1 mole in Zone 5. The condensed water would be saturated with oxygen and may contain other oxidizing species, such as hydrogen peroxide. Calculations were conducted using the validated OLI Systems software (Pabalan, 2009) to estimate the corrosion rate of carbon steel, SS304, pure aluminum, and Alloy 600 in a 1 and 5 weight-percent (wt%) H_2O_2 aqueous solution saturated with oxygen at 25, 75, and 125 °C (77, 167, and 257 °F). Alloy 600 is selected as a representative nickel-based alloy. Table A5-2 lists the corrosion rate data.

The listed data indicate that the corrosion rates of carbon steel in a 1 and 5 wt% H_2O_2 aqueous solution saturated with oxygen are the highest. The damage to any structural material from general corrosion in aqueous solutions will be limited by the amount of solution and by the spread of the solution on the structure surface. For example, if 1 mole of either a 1 or 5 wt% H_2O_2 solution is evenly spread over the 1-m^2 (10.8-ft^2) surface of a carbon steel structure, it would result in a corrosion penetration depth of 4.7 μm (2×10^{-4} in.). Note that this value is independent of the corrosion rate data listed in Table A5-2. The data listed in Table A5-2 and this analysis for carbon steel indicate that degradation of structural materials from general corrosion in aqueous solutions inside the storage canister is expected to be too small to be a concern.

Table A5-2 Corrosion Rate Data for Carbon Steel, SS304, Pure Aluminum, and Alloy 600 in a 1 and 5 Wt% H_2O_2 Aqueous Solution Saturated with Oxygen at 25, 75, and 125 °C (77, 167, and 257 °F)

Temperature °C (°F)	Corrosion Rate (μm/yr) in 1 wt% H_2O_2 Solution				Corrosion Rate (μm/yr) in 5 wt% H_2O_2 Solution			
	Carbon Steel	SS304	Pure Aluminum	Alloy 600	Carbon Steel	SS304	Pure Aluminum	Alloy 600
25 (77)	602	2.5	0.6	0.13	534	2.6	0.7	0.13
75 (167)	625	6.1	1.5	0.05	564	6.2	2.1	0.10
125 (257)	1300	12.2	4.9	1.3	1237	12.4	7.3	2.6

A5.2.2.2 Localized Corrosion

Localized corrosion either in the form of pitting or crevice corrosion would occur only when an aqueous solution is present. Localized corrosion would initiate when the corrosion potential is greater than the repassivation potential (Shukla et al., 2008). Researchers used the OLI Systems software to calculate corrosion and repassivation potentials for carbon steel, SS304, pure aluminum, and Alloy 600 in a 1 and 5 wt% H_2O_2 aqueous solution saturated with oxygen at 25, 75, and 125 °C (77, 167, and 257 °F). Table A5-3 lists the corrosion and repassivation potential data for the 1 wt% H_2O_2 aqueous solution. Table A5-4 lists the data for the 5 wt% H_2O_2 aqueous solution.

The data presented in Tables A5-3 and A5-4 indicate that the corrosion potential is always lower than the repassivation potential for the four metals in the 1 and 5 wt% H_2O_2 aqueous solutions. These data indicate that localized corrosion of the structural component materials is not likely from residual water.

Table A5-3 Calculated Corrosion and Repassivation Potentials for Carbon Steel, SS304, Pure Aluminum, and Alloy 600 in a 1 wt% H_2O_2 Aqueous Solution Saturated with Oxygen at 25, 75, and 125 °C (77, 167, and 257 °F)

Temperature °C (°F)	Corrosion Potential (mV) with Respect to Standard Hydrogen Electrode				Repassivation Potential (mV) with Respect to Standard Hydrogen Electrode			
	Carbon Steel	SS304	Pure Aluminum	Alloy 600	Carbon Steel	SS304	Pure Aluminum	Alloy 600
25 (77)	−470	302	−185	338	>2,000	>2,000	>2,000	>2,000
75 (167)	−496	265	−406	316	>2,000	>2,000	>2,000	>2,000
125 (257)	−499	261	−628	322	>2,000	>2,000	>2,000	>2,000

Table A5-4 Calculated Corrosion and Repassivation Potentials for Carbon Steel, SS304, Pure Aluminum, and Alloy 600 in a 5 wt% H_2O_2 Aqueous Solution Saturated with Oxygen at 25, 75, and 125 °C (77, 167, and 257 °F)								
	Corrosion Potential (mV) with Respect to Standard Hydrogen Electrode				Repassivation Potential (mV) with Respect to Standard Hydrogen Electrode			
Temperature °C (°F)	Carbon steel	SS304	Pure Aluminum	Alloy 600	Carbon Steel	SS304	Pure Aluminum	Alloy 600
25 (77)	−477	302	−170	357	>2,000	>2,000	>2,000	>2,000
75 (167)	−498	265	−402	298	>2,000	>2,000	>2,000	>2,000
125 (257)	−500	263	−626	300	>2,000	>2,000	>2,000	>2,000

Localized damage to the neutron-absorbing material BORAL in the form of blistering (EPRI, 2006) has been observed. A postulated mechanism for blister formation is based on water entering the material during SNF loading operations from the SNF pool to a dry storage cask. Water could enter through open porosity at the edges. During dry storage at elevated temperatures, water contacting the internal surfaces of interconnected pores causes internal corrosion and produces Al_2O_3 and hydrogen gas. The volume change associated with Al_2O_3 formation causes the pores to close, thus entrapping hydrogen and water in the core of the neutron-absorbing material. Subsequent formation of hydrogen or heating of trapped hydrogen, or both, cause internal pressure buildup and material deformation. As temperature decreases during extended storage, this process decreases, which in turn decreases the likelihood of the basket's structural integrity for very long-term storage being affected.

A5.2.2.3 Shadow Corrosion Effects on the Spent Nuclear Fuel Rods

Galvanic corrosion in the form of shadow corrosion could be caused by a mismatch between cladding and spacer-grid materials. Cladding is made of zirconium-based alloy, and spacer grids are made of Inconel alloys. In addition, the cladding material could be covered with a crud layer deposit during reactor operations.

An electrochemical cell may form when water condenses in an opening between an SNF rod and a spacer grid and contacts both materials. The standard electrode potential for zirconium and ZrO_2 in aqueous solution at 25 °C (77 °F) is approximately 1.6 V_{SHE} (the subscript "SHE" stands for standard hydrogen electrode). Similarly, the standard electrode potentials for chromium and nickel are equal to −0.74 and −0.23 V_{SHE}, respectively, at 25 °C (77 °F) (Bard and Faulkner, 1980). This information indicates that zirconium would get oxidized into zirconium ion during the shadow corrosion, and oxidizing species, such as oxygen and hydrogen peroxide in aqueous solution, would get reduced. Thus, the extent of damage would depend on the amount of oxidants present in the condensed water. The oxidation of zirconium and reduction of oxidizing species would occur according to the chemical reactions given by the following equations:

$$Zr \rightarrow Zr^{4+} + 4e^- \quad \text{(A5-2)}$$

$$H_2O_2 + 2e^- \rightarrow 2OH^- \quad \text{(A5-3)}$$

$$O_2 + 2H_2O + 4e^- \rightarrow 4OH^- \quad \text{(A5-4)}$$

According to these equations, reduction of 1 mole of hydrogen peroxide would result in oxidation of 0.5 mole of zirconium. Similarly, a reduction of 1 mole of oxygen would result in oxidation of 1.0 mole of zirconium. The amount of hydrogen peroxide and oxygen in 1 mole of a 5 wt% H_2O_2 solution saturated with oxygen at 25 °C (77 °F) and 1 atm (14.7 lb/in.^{2}) is 0.03 and 8.0×10^{-6} moles, respectively. The corresponding amount of zirconium that could be oxidized is 1.5×10^{-2} moles, which is equivalent to 1.37 g (0.05 oz). The corresponding volume of the zirconium cladding material is approximately 0.25 cm^3 (8.8×10^{-6} ft^3). The depth of penetration on the cladding would depend on the spread of the condensed water. However, it is expected that condensed water would not be localized and would spread over a large surface area. Therefore, even if shadow corrosion were to occur, it is unlikely to result in throughwall cracks on cladding because of the limited amount of oxidants.

A5.2.2.4 Galvanic Corrosion

The previous discussion addressed galvanic corrosion in the form of shadow corrosion between Inconel alloy and zirconium-based cladding materials. This section discusses galvanic corrosion between a combination of carbon steel, stainless steel, and pure aluminum and estimates the extent of damage attributable to galvanic couples of carbon and stainless steels, carbon steel and pure aluminum, and stainless steel and pure aluminum. Galvanic corrosion would occur when two dissimilar metals are in physical contact and a layer of aqueous solution covers both metals. Oxidation of the active (i.e., less noble) metal would occur, whereas reduction reactions would take place at the nobler metal surface. Nobility of a metal in a metal couple can be determined by analyzing the corrosion potential values. Corrosion potential values of various alloys in flowing seawater (Shukla, 2008) are used to infer the relative nobility of the canister materials during extended storage. The environmental condition primarily affecting the nobility is corrosion potential driven by chemistry, oxygen level, and temperature of water. Table A5-5 lists the corrosion potentials of carbon steel, various stainless steel types, and aluminum-based alloys.

The alloy or metal with the lower corrosion potential value in a metal couple would undergo oxidation. Therefore, if galvanic corrosion is occurring between carbon steel and any type of stainless steel, carbon steel would undergo oxidation. Similarly, an aluminum alloy would undergo oxidation when galvanic corrosion occurs between an aluminum alloy and stainless steel, and carbon steel would undergo oxidation in a galvanic couple between carbon steel and stainless steel.

The dissolution of iron will be the predominant chemical reaction in the oxidation of the carbon steel and is expressed by the following equation:

$$Fe \rightarrow Fe^{2+} + 2e^- \qquad \text{(A5-4)}$$

Similarly, the dissolution of aluminum will be the predominant chemical reaction in the oxidation of an aluminum-based alloy and is expressed by the following equation:

$$Al \rightarrow Al^{3+} + 3e^- \qquad \text{(A5-5)}$$

Table A5-5 Corrosion Potentials of Various Alloys in Flowing Seawater	
Alloy	**Corrosion Potential (mV) With Respect to Standard Hydrogen Electrode**
Stainless Steel: Type 316 and 317	100 to 240
Stainless Steel: Types 302, 304, 321, 347	120 to 170
Carbon Steel	−159 to −360
Aluminum Alloys	−460 to −660

The extent of these reactions would depend on the availability of the oxidizing species in the condensed water. As discussed in the previous section, the amount of hydrogen peroxide and oxygen in 1 mole of a 5 wt% H_2O_2 solution saturated with oxygen at 25 °C (77 °F) and 1 atm is 0.03 and 8.0×10^{-6} moles, respectively. This amount of oxidizing species could oxidize 3.0×10^{-2} moles of iron and 2.0×10^{-2} moles of aluminum. This corresponds to 1.7 g (0.06 oz) of iron and 0.54 g (0.02 oz) of aluminum. These values are small compared to the mass of materials used in building a storage canister. This analysis indicates that, while galvanic corrosion may occur inside a canister as a result of residual water, the extent of damage to structural materials would be insignificant.

A5.2.2.5 Stress-Corrosion Cracking

SCC of the structural components made of carbon steel and stainless steel in a dry storage cask system is of primary concern because SCC may lead to cracks and compromise the integrity of internal components. SCC of Inconel and aluminum-based alloys could also occur, but is not considered to be risk significant. SCC of Inconel and aluminum-based alloys would not lead to any throughwall cracks in a canister. For this reason, the following discussion centers on SCC of carbon steel and stainless steel in the internal environment of a dry storage canister.

SCC would occur when susceptible materials with sufficient tensile stresses are exposed to a chemical environment. Residual tensile stresses are expected to be present from the welding process that is used during construction of a dry storage canister and internal components. Regarding the chemical environment, the literature indicates that various types of stainless steels are prone to SCC, even in high-purity demineralized water, at the temperatures of BWRs, typically 290 °C (554 °F) (Kain, 2011). This observation is attributed to the presence of dissolved oxygen and other oxidizing species in the pure water (Kain, 2011) of a BWR. Parallel information regarding carbon steel is not available in the literature. If stainless steel is susceptible to SCC, it can be reasonably assumed that carbon steel is also susceptible to SCC in the cask internal environment (Ciaraldi, 1992; King, 2007). However, RH near 290 °C (554 °F) is well below the threshold RH of aqueous corrosion even without radiolysis. There are no data at lower temperatures of higher RH. Therefore, it is difficult to support the susceptibility of stainless steel and carbon steel to SCC.

A5.2.2.6 Hydrogen-Absorption-Induced Damage

In an extended storage environment, most of the hydrogen is generated from radiolysis of the residual water. The subsequent absorption of hydrogen into the metal matrix can affect and may degrade the mechanical properties of the stainless steel basket and canister when the absorbed hydrogen concentration exceeds a critical hydrogen concentration in the metal matrix.

Okada (1977) reported that the critical hydrogen concentration dissolved in the iron matrix needs to be 10 ppm to cause appreciable mechanical degradation by blistering and cracking.

The hydrogen concentration in alpha iron was estimated to be 0.9 ppb at room temperature in contact with 0.1 MPa (14.5 lb/in.^{2}) H_2 atmospheres according to Sievert's law. With increasing temperature, the concentration can increase following the Arrhenius relationship. Oriani (1970) estimated that the maximum hydrogen concentration in iron was less than 1 ppm at 300 °C (572 °F) with 8 MPa (1,160.3 lb/in.^{2}) of H_2 pressure. This information indicates the hydrogen absorption in any ferrous-based alloy is expected to be insignificant.

Hydrogen could also be absorbed when water directly reacts with a metal, as depicted for zirconium in Figure A5-1. The canister internals could corrode when the RH exceeds the threshold value of 60 percent for the case of carbon steel (Vernon, 1935). The cathodic reaction from the steel corrosion process produces hydrogen, and some of the hydrogen is absorbed by carbon steel. Once absorbed, hydrogen can diffuse within the steel and interact with traps and other defects within the material. However, hydrogen absorption efficiency is known to range between 0.0002 and 0.016 percent even during aggressive discharging under oxide-film-free conditions at a pH of 2.6 (Gajek and Zakroczymski, 2005). The efficiency is even further decreased at the neutral pH. The hydrogen concentration measurement results show that, in a neutral pH, the concentrations ranged from approximately 0.01 to 0.1 ppm when carbon steel was immersed in a number of solutions saturated with 0.01 MPa (1.45 lb/in.^{2}) of hydrogen sulfide (H_2S) at 25 °C (77 °F) (Yamakawa and Nishimura, 1999). In another study, King (2009) reported that the maximum hydrogen concentration in iron under aqueous corrosion conditions is 0.01 ppm.

Although the critical concentration observed under more severe experimental conditions (e.g., acidic, aggressive discharging with H_2S, high temperature, and high pressure) may exceed 10 ppm, hydrogen concentrations under the relatively benign conditions expected for dry storage would be much lower. Another factor that can inhibit the absorption of hydrogen is the oxide film formed on the steel surface that acts as a diffusion barrier, as summarized in King (2009). Considering this information, it is concluded that hydrogen absorption by the canister internals is not a concern.

A5.3 Relative Humidity Data

Figures A5-6 to A5-13 present the RH data generated using the integration models for Cases 1 to 4.

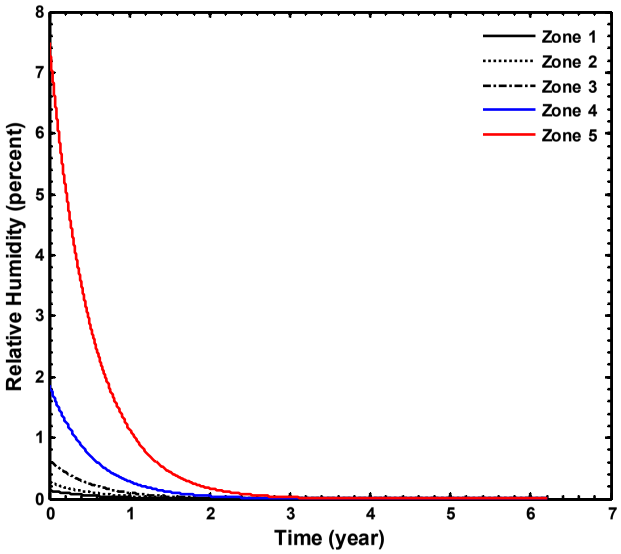

(a) 5.5 moles

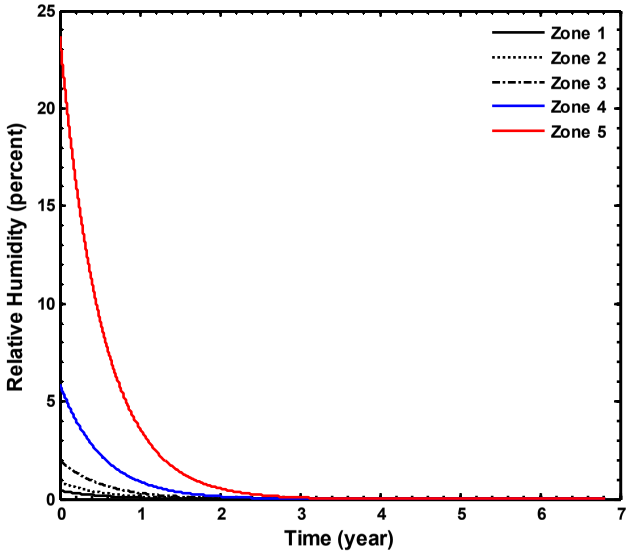

(b) 17.4 moles

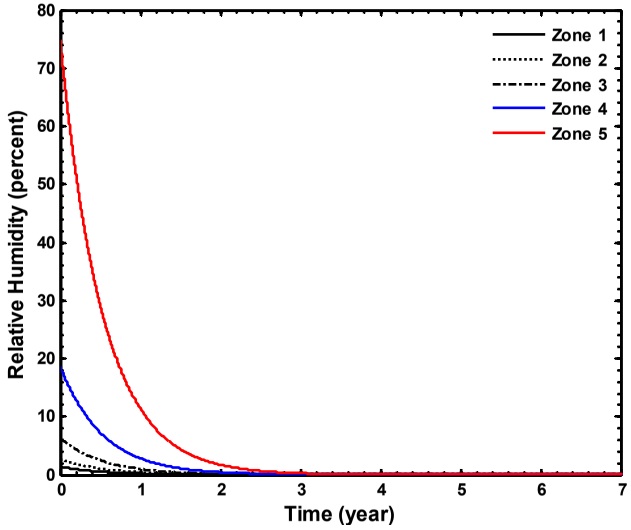

(c) 55 moles

Figure A5-6 RH profiles for exponential decomposition in 4.77 years, low-end temperature condition, and (a) 5.5, (b) 17.4, and (c) 55 moles of residual water

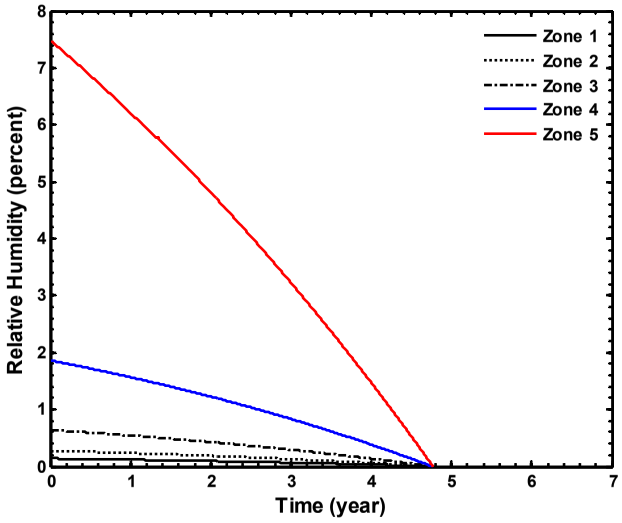

(a) 5.5 moles

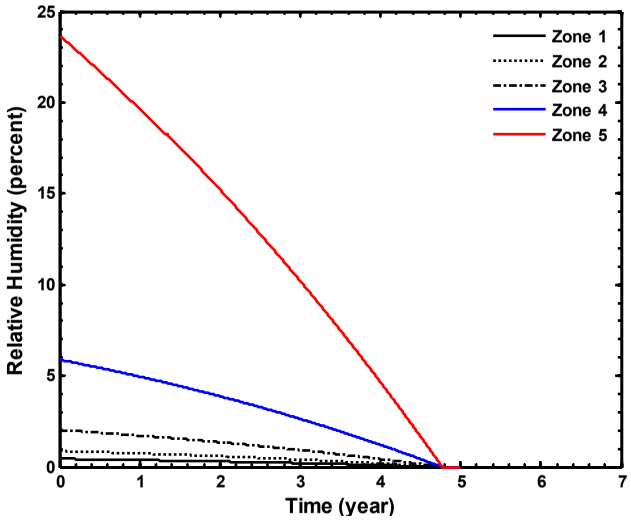

(b) 17.4 moles

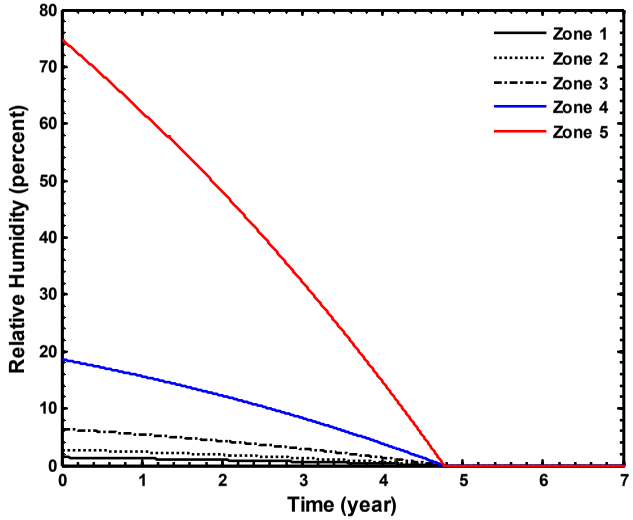

(c) 55 moles

Figure A5-7 RH profiles for linear decomposition in 4.77 years, low-end temperature condition, and (a) 5.5, (b) 17.4, and (c) 55 moles of residual water

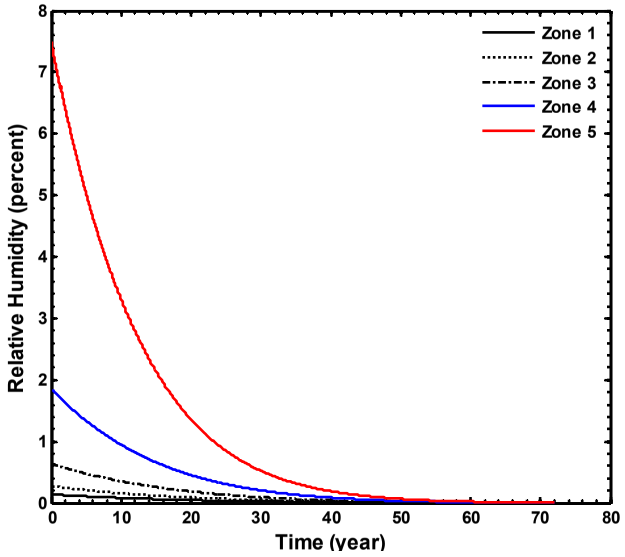

(a) 5.5 moles

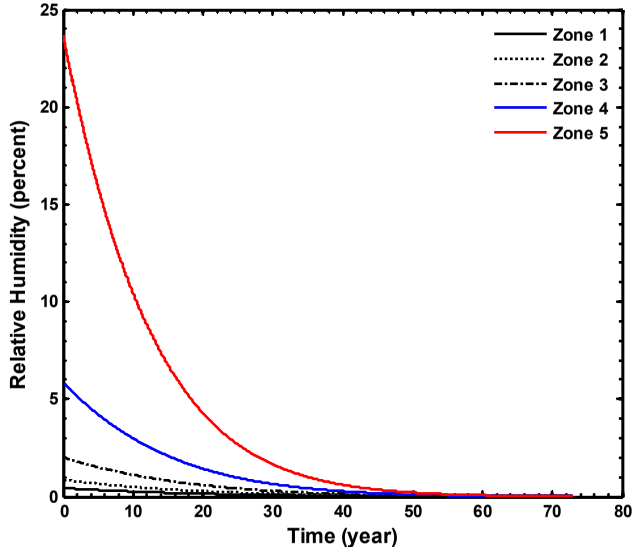

(b) 17.4 moles

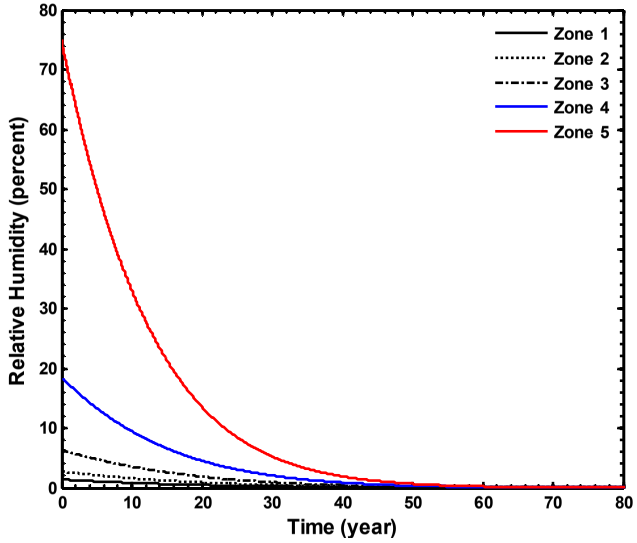

(c) 55 moles

Figure A5-8 RH profiles for exponential decomposition in 71.62 years, low-end temperature condition, and (a) 5.5, (b) 17.4, and (c) 55 moles of residual water

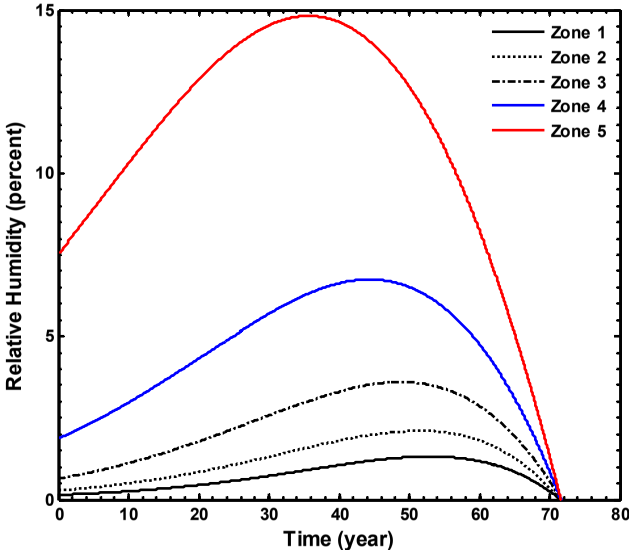

(a) 5.5 moles

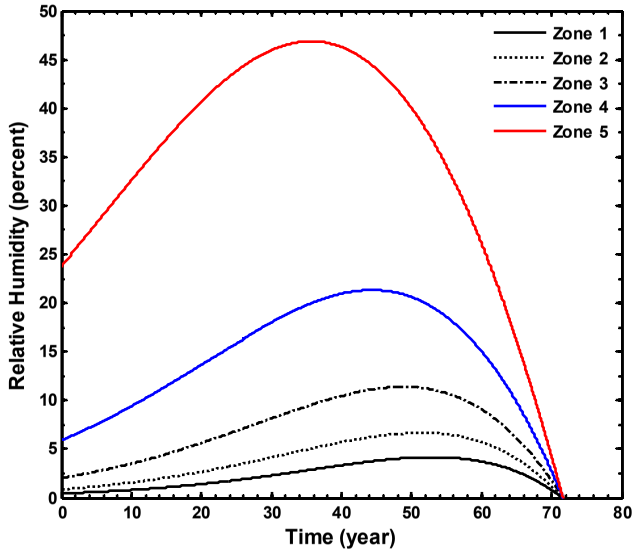

(b) 17.4 moles

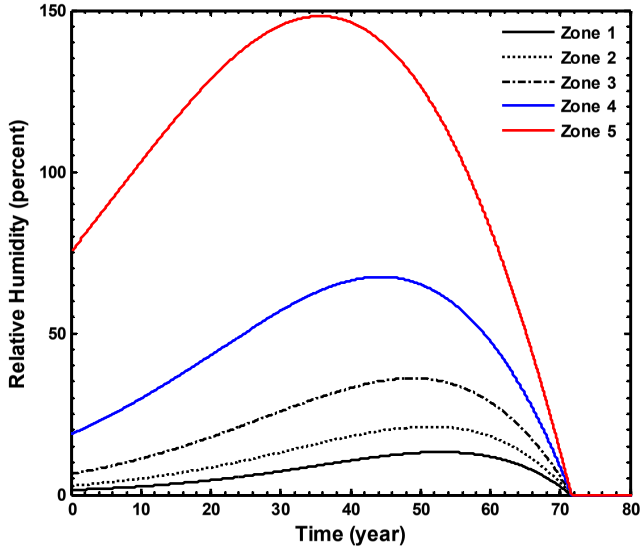

(c) 55 moles

Figure A5-9 RH profiles for linear decomposition in 71.62 years, low-end temperature condition, and (a) 5.5, (b) 17.4, and (c) 55 moles of residual water

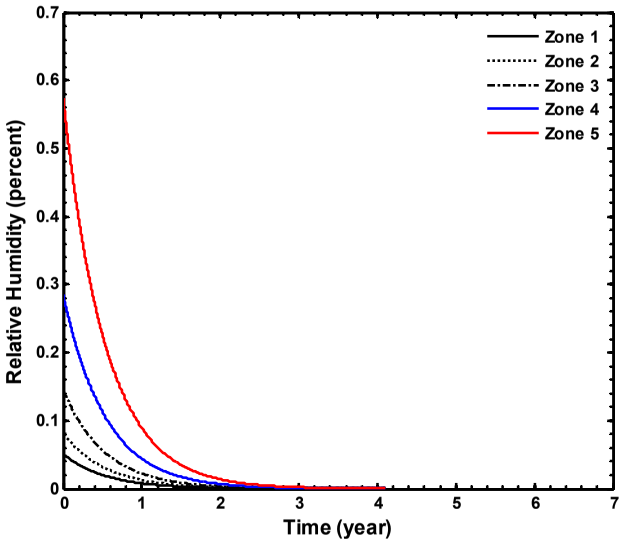

(a) 5.5 moles

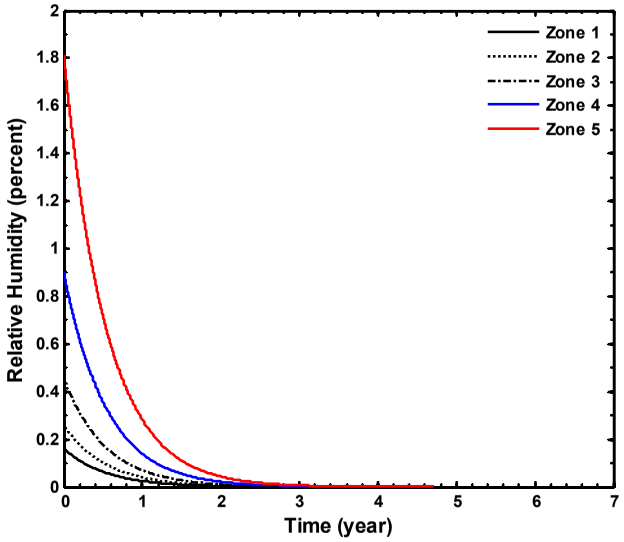

(b) 17.4 moles

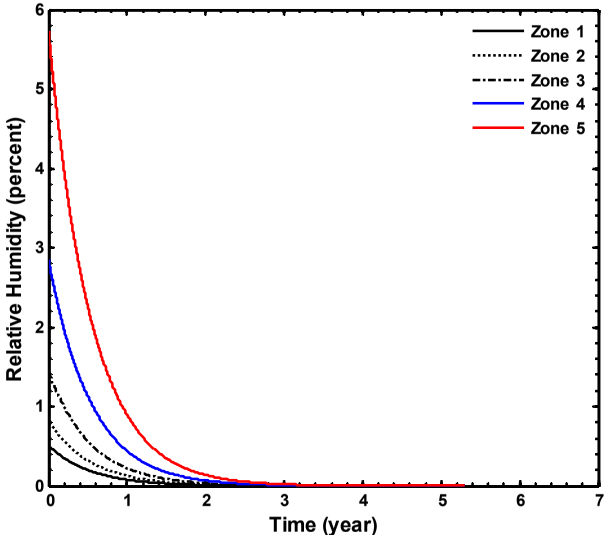

(c) 55 moles

Figure A5-10 RH profiles for exponential decomposition in 4.77 years, high-end temperature condition, and (a) 5.5, (b) 17.4, and (c) 55 moles of residual water

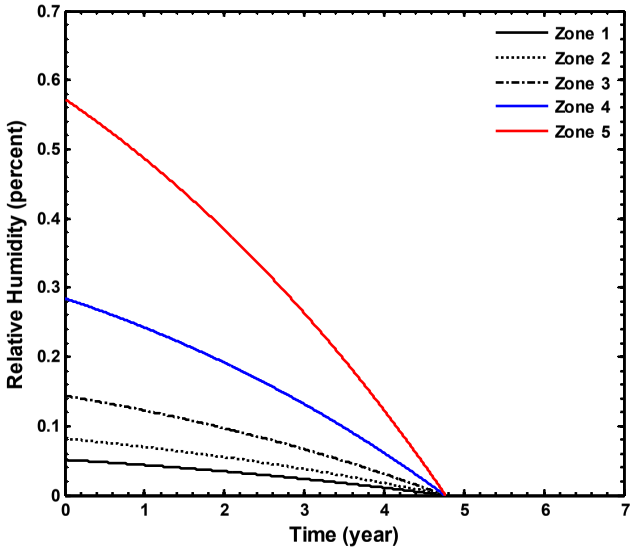

(a) 5.5 moles

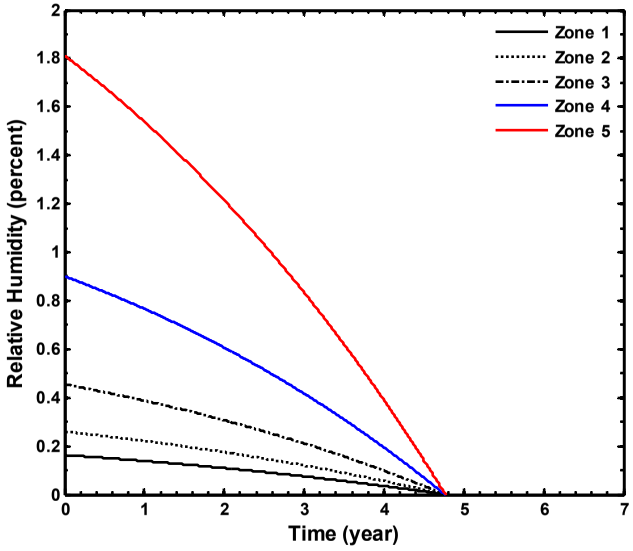

(b) 17.4 moles

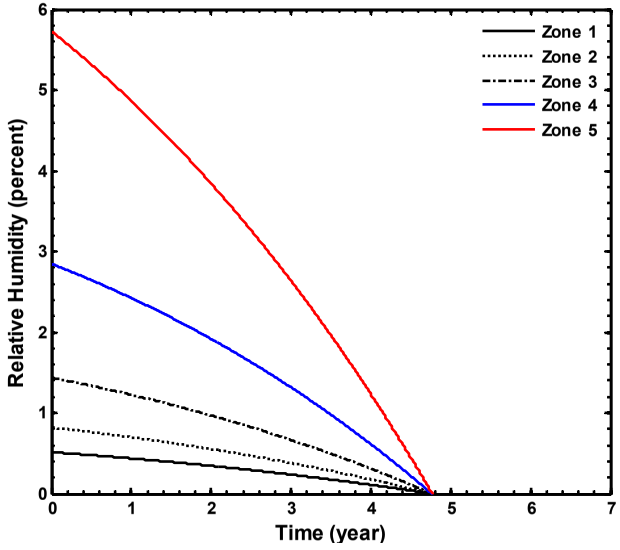

(c) 55 moles

Figure A5-11 RH profiles for linear decomposition in 4.77 years, high-end temperature condition, and (a) 5.5, (b) 17.4, and (c) 55 moles of residual water

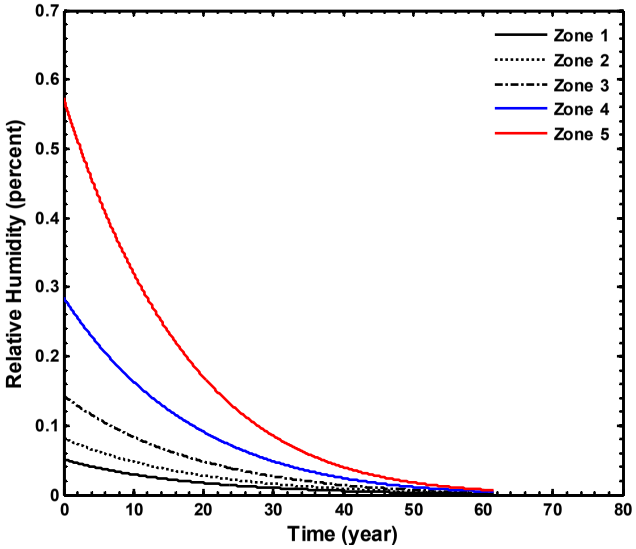

(a) 5.5 moles

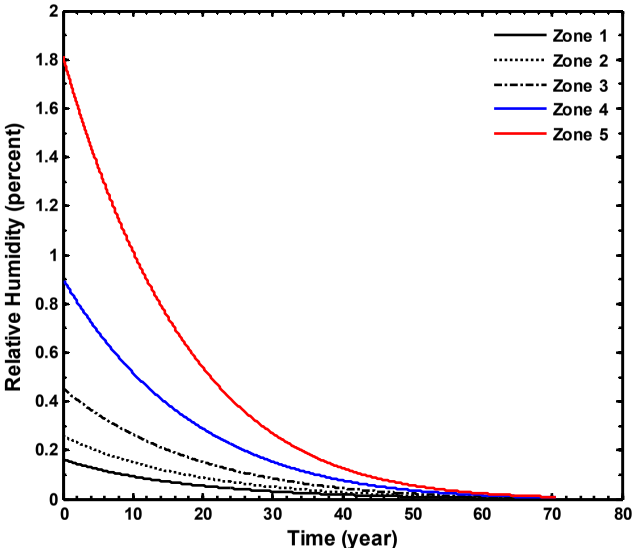

(b) 17.4 moles

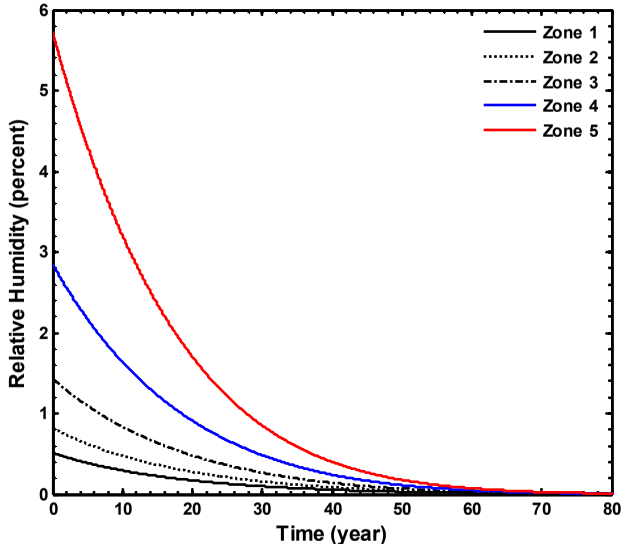

(c) 55 moles

Figure A5-12 RH profiles for exponential decomposition in 71.62 years, high-end temperature condition, and (a) 5.5, (b) 17.4, and (c) 55 moles of residual water

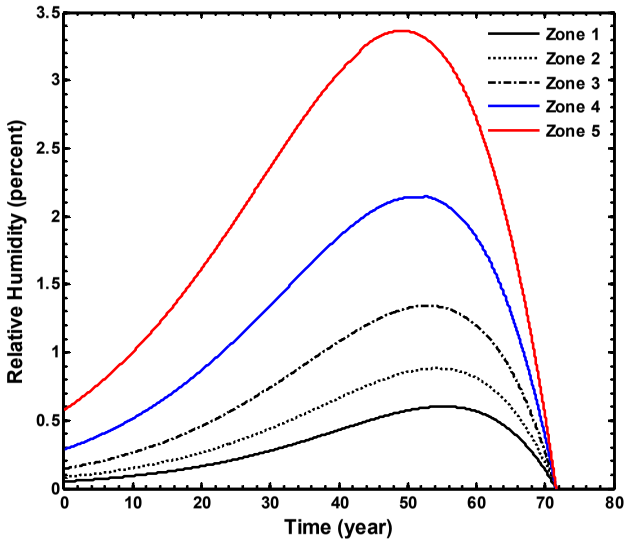

(a) 5.5 moles

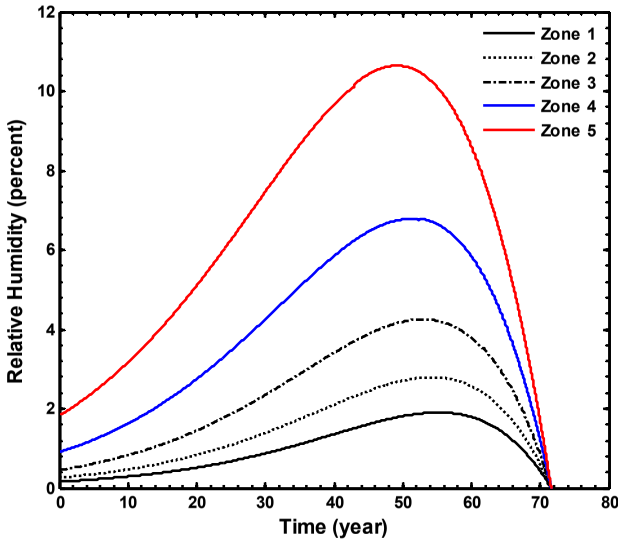

(b) 17.4 moles

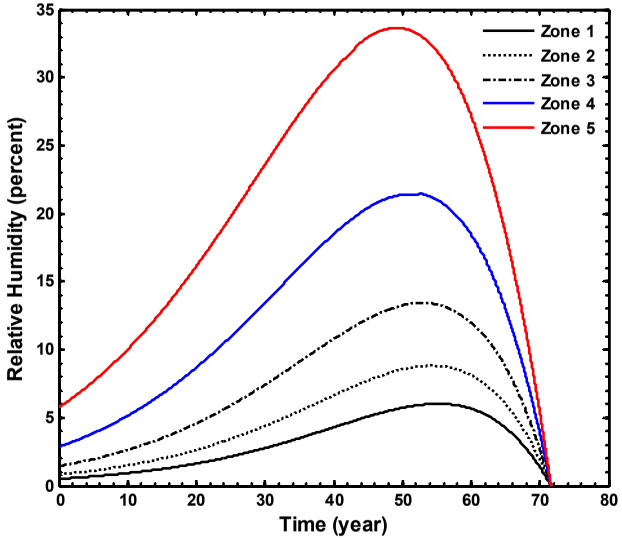

(c) 55 moles

Figure A5-13 RH profiles for linear decomposition in 71.62 years, high-end temperature condition, and (a) 5.5, (b) 17.4, and (c) 55 moles of residual water

A6. PERSPECTIVES ON THE POTENTIAL IMPACT OF INCOMPLETE DRYING ON CRITICALITY SAFETY MARGINS

One of the important safety requirements for dry cask storage systems is maintaining subcriticality for the stored SNF assemblies. For the case of incomplete cask drying, several considerations are important for criticality safety margins, including (1) the impact of water (a moderating material for neutrons) directly on system reactivity and (2) the potential corrosive effects of water on system components, which could impact their performance for safety-related functions. To carry out an initial assessment of these considerations, the researchers used a qualitative approach. For this effort, several references were reviewed to develop insight into the potential impacts on system reactivity from the presence of water and potential degraded states for dry cask storage system components, including NUREG/CR-6835, "Effects of Fuel Failure on Criticality Safety and Radiation Dose for Spent Fuel Casks," issued in 2003 (Elam et al., 2003), and Povetko et al. (2008). From these works, several scenarios can provide examples for bounding scenarios and their impact on the criticality safety margin if severe degradation occurred.

For systems containing fissionable material, measurement of criticality safety is often assessed using the effective neutron multiplication factor (referred to as k-effective). For a critical system, the value of k-effective is equal to one (by definition), and the rate of neutrons being produced is equal to the number of neutrons absorbed (potentially leading to fission) or lost through other means. For a subcritical system, the k-effective value is less than one; therefore, fewer neutrons are produced than consumed or lost from the system. The system reactivity, the fractional departure from criticality, is defined as $\rho = (k-1)/k$, where k is the k-effective for a finite system. The change in the reactivity that is introduced by the change in the system can be quantified as a change in k-effective (Δk-effective) or in $\Delta\rho$. For assessment of criticality safety, a model of the system performance sensitivity analysis is commonly constructed by varying material types, their respective properties (i.e., density), and system geometry. For example, models often assume fresh (unirradiated) SNF because it would have a higher contribution to system reactivity than irradiated fuel (e.g., SNF). For criticality safety, the model often includes several conservative assumptions to ensure that model uncertainties are accounted for and the real system would remain subcritical. Typically, an additional safety margin is maintained to further ensure that any unaccounted for uncertainties would not lead to an unexpected critical state under predicted conditions.

For dry storage environments, maintaining subcriticality is achieved through favorable geometry and the use of permanently fixed neutron-absorbing materials. For a dry cask storage system, this is done using an SNF basket assembly. The SNF basket assembly consists of the SNF basket and neutron absorbers. The SNF basket provides a rigid structure that ensures that the SNF assemblies maintain their intended geometry. The neutron-absorbing materials remove neutrons from the system and thus contribute to lowering the system's k-effective value. The most commonly used neutron absorber materials for criticality control in dry storage are borated stainless steel alloys, borated aluminum alloys, and boron carbide aluminum alloy composites (e.g., BORAL™) (ASTM International, 2007; EPRI, 2006). Materials typically used for the SNF basket include SS304 with boron, 6061-T651 Al, SA 705 Type 630 stainless steel, Inconel, SA 516 Gr 70, and 479 stainless steel (NWTRB, 2010).

An important consideration in criticality safety is the exclusion of moderating material, (i.e., water), which can increase the system's k-effective value. For the case of a dry cask

storage system under normal operating conditions, there is, by design, exclusion of moderating material in the dry, inert confinement environment. However, because there is potential for incomplete drying of the canister, some residual water from cask loading and storage in the SNF pool may be present in the form of liquid or vapor, which could contribute to decreasing criticality safety margins. Further, the presence of water in the canister and resulting radiolysis products could cause degradation of canister components. Degradation of components that are important to safety could lead to a loss of their intended function and contribute to an increase in system k-effective. An additional concern may be degradation that leads to rupture of the SNF cladding. Such an event could lead to relocation of the SNF and contribute to a change in system k-effective. For example, residual water present from incomplete drying of SNF may oxidize the SNF matrix at defective cladding, increasing the SNF matrix volume. This will in turn impose stress on the defective cladding, resulting in cladding unzipping and rupture.

In NUREG/CR-6835 (Elam et al., 2003), the authors assessed several scenarios for criticality safety in dry storage casks. These scenarios were developed using several assumptions for the criticality model, using fresh SNF (more reactive for criticality), and assuming that both the canister internal volume and the gap space between cladding and SNF were filled with water (moderator). Although many of the scenarios assessed in NUREG/CR-6835 go beyond credible conditions (unlikely to occur) for realistic dry cask environments, the scenarios were designed to be bounding for those expected under licensing conditions. For the present assessment of incomplete drying, NUREG/CR-6835 may also be considered bounding for many of the scenarios that could be feasible from incomplete drying. The assessment reported in NUREG/CR-6835 included results for models of the Holtec HI-STAR dry cask loaded with the MPC-24 and the MPC-68 canisters. In these models, the MPC-24 canister was assumed to be loaded with 4-percent enriched PWR SNF, and the MPC-68 canister was assumed to be loaded with 4.5-percent enriched BWR fuel. For several of the scenarios, an SNF basket-cell model was developed and used for each specific cask design to simplify modeling (e.g., a single SNF basket channel and assembly was modeled with radially reflected boundary conditions for tracked radiation). For those cases, the validity of using the basket-cell model was verified with the full cask model. The subsequent discussion considers the following two scenarios from NUREG/CR-6835 (Elam et al, 2003):

- Scenario 1—An individual SNF rod collapse results in rods being absent from the assembly lattice.

- Scenario 3—A collapse of SNF rods form zones of optimum-moderate SNF pellets.

Elam et al. considered several additional scenarios in NUREG/CR-6836 (Elam et al., 2003); however, for brevity, the present discussion only includes those considered most relevant. For the case of loss of SNF from an SNF rod (e.g., as a result of cladding unzipping), the scenarios presented in NUREG/CR-6835 (Elam et al., 2003) provide some insights for the impact on criticality margins. For example, for Scenario 1, the contribution of missing rods from an assembly to the calculated k-effective is assessed. The SNF rods in assemblies are generally spaced such that the array of assembly forms is undermoderated. Removal of a single or multiple rods (e.g., from collapse of the SNF rod) could result in the vacated space being filled with moderator (such as water). However, the scenario does not account for relocation of the SNF (the SNF rods are removed from the model). For the case of a single SNF rod, the contribution to the calculated k-effective was modeled for removal from every rod position. The maximum contribution observed for removal of a single rod was small—0.0013 for the MPC-24 model and 0.0036 for the MPC-68 model.

For removal of multiple SNF rods, Elam et al. examined a select number of permutations of removed rods in NUREG/CR-6835 (Elam et al., 2003) (specifically those expected to contribute more significantly to a change in k-effective). The contribution to the change in k-effective was shown to be less than 0.015 for both the MPC-24 and MPC-68 models. This scenario demonstrates that the collapse of a single rod (or possibly a few rods) may not make a large contribution to k-effective. It is also clear that the position of the SNF rods can be important, especially for multiple SNF rods, which could make a more significant contribution. For example, SNF rods near an assembly center or in a diagonal orientation with guide tubes (or water holes) had the largest positive effect on k-effective (Elam et al., 2003).

Scenario 3 in NUREG/CR-6835 (Elam et al., 2003) was used to examine a case in which SNF rubble could form and may provide some insight for the present discussion for bounding the case of a failure of multiple, adjacent SNF rods followed by relocation of fuel. For this scenario, the SNF assembly hardware and cladding were assumed to be removed (disintegrated) from all of the SNF assemblies and the SNF pellets were spaced in optimally moderated arrays within their respective SNF basket channels. As expected, this scenario resulted in a large contribution to increasing k-effective. The maximum contribution to k-effective in this case was 0.0563 for the MPC-24 and 0.1149 for the MPC-68 canisters. This case may represent a bounding range for scenarios that could be expected from incomplete drying. However, although the scenario for SNF rubble uses a number of very conservative assumptions, the SNF basket and neutron absorbers are intact and included in the model. Therefore, evaluation of specific degradation conditions, scenarios, cask designs, and loading may require detailed modeling to ensure that all potential bounding conditions are considered.

For consideration of potential degradation of neutron-absorbing materials, Povetko et al. (2008) provides some insight into the effect of a loss of neutron-absorbing materials on the system reactivity. In this work, the authors examined the effect of removing neutron absorber panels on reactivity for several canister designs. Their work considered canisters containing SNF baskets with and without flux traps. The canisters were assumed fully flooded. Fresh SNF with enrichments of 4.2 and 5 weight-percent (wt%) U-235 was examined. The assessment included separate modeling of SNF baskets that utilize BORAL and borated stainless steel Neutronit A978 plates (with 1.1 wt% boron content). The results of the Povetko et al. (2008) analysis showed that, for the modeled casks that had flux traps, removal of two or four BORAL neutron absorber plates had a negligible effect on k-effective because the calculated change in reactivity was less than the calculation uncertainties. For the canister without flux traps, the neutronic reactivity effect of removed plates ranged from 0.8 to 5 percent for the cases with two to six BORAL and Neutronit plates removed (Povetko et al., 2008). The authors concluded that the effect of SNF enrichment on reactivity increase, for the values of 4.2 and 5 wt% U-235 considered, was small and that the effect for BORAL was 1.6 to 2 times higher than for Neutronit.

For the present discussion, Povetko et al. (2008) yield several important insights. First, for SNF baskets that have flux traps, there may be some margin for degradation of neutron absorbers; however, it should be cautioned that this would depend on the particular cask design and SNF characteristics, among other factors. If detailed quantification of an expected degradation effect is needed, a thorough analysis of the particular design and condition is recommended. For casks without flux traps, removal of the panels may contribute to a significant reduction in safety margin depending on the neutron-absorbing material and the size and geometry of the affected area. However, the scenarios in Povetko et al. (2008) considered complete removal of neutron absorber panels, which would constitute removal of a large quantity of neutron-absorbing material and may require a significant quantity of degradation. Given the quantity of material

removed in the cases Povetko et al. (2008) considered, their results and cases may be bounding for many potential scenarios. However, if a large quantity of degradation was expected for a particular scenario, a detailed analysis taking into account the specific materials used and geometries considered is recommended.

With regard to the effect of the presence of 55 moles of water (approximately 1 L (0.26 gal) of liquid water at standard temperature and pressure), it is not expected that this would contribute significantly to the k-effective because of the relatively small quantity of water in the canister volume. For example, the present assessment assumes the interior of the canister confinement to be approximately 2.1 m^3 (74 ft^3). Using this assumption, a fully flooded cask would contain a much larger quantity of water—roughly 2,100 L (546 gal) (neglecting displacement by SNF assemblies, the SNF basket, and other internal components). Although cask designs do vary and calculated values of k-effective will differ as a result of variations in geometry (e.g., SNF basket dimensions and presence of flux traps), materials, and SNF assembly characteristics, the base case models of the Holtec HI-STAR dry cask reported in NUREG/CR-6835 (Elam et al., 2003) are representative of many cask systems. Furthermore, several fairly conservative assumptions have been made in the models for calculation of k-effective. In NUREG/CR-6835 (Elam et al., 2003), the two baseline models of the Holtec HI-STAR dry cask are loaded with the MPC-24 (4-percent enriched PWR fuel) and MPC-68 (4.5-percent enriched BWR fuel) canisters. The models include loading with fresh SNF and fully flooded conditions, including water in the SNF cladding gap. The k-effective for both of the models of the full cask were shown to be 0.9369 and 0.9358, respectively, for the MPC-24 and the MPC-68 models. For these conservative base case designs, the fully flooded cask models remain subcritical.

The present discussion has focused on a review of available literature to develop insights into the potential impact of incomplete drying on criticality safety margins. In general, based on the limited degradation expected for dry cask storage system components and absorption of hydrogen by SNF cladding from residual water, as discussed in Section A5, a significant impact on criticality safety is not anticipated. The presence of up to 55 moles of water is not expected to contribute significantly to the criticality concerns because of the relatively small quantity of water in the canister volume. Therefore, criticality is not expected to be a concern if significant degradation of cask system components does not occur. The cases considered in NUREG/CR-6835 (Elam et al., 2003) and Povetko et al. (2008) provide some examples for bounding scenarios and their impact on the criticality safety margin if severe degradation were to occur. If specific degradation mechanisms are identified or if the expected safety margins are exceeded by the bounding cases, development of more detailed models would likely be required to address each potential issue.

A7. REFERENCES

Ahn, T. NUREG-1565, "Dry Oxidation and Fracture of LWR Spent Fuels." Washington, DC: U.S. Nuclear Regulatory Commission. 1996. ADAMS Accession No. ML040150720.

American National Standards (ANSI) and American Nuclear Society (ANS). "Neutron and Gamma-Ray Fluence-to-Dose Factors." ANSI/ANS-6.1.1-1991. ANSI: Washington DC, ANS: La Grange Park, IL. 1991.

Araya, P.E. and M. Greiner. "Two-Dimensional Simulations of Natural Convection/Radiation Heat Transfer for BWR Assembly within Isothermal Enclosure." *Packaging, Transport, Storage and Security of Radioactive Materials*. Vol. 18, No. 3. pp. 171–179. 2007.

Arkhipov, O.P., A.O. Verkhovskaya, S.A. Kabakchi, and A.N. Ermakov. "Development and Verification of a Mathematical Model of the Radiolysis of Water Vapor." *Atomic Energy*. Vol. 103, No. 5. pp. 870–874. 2007.

Arya, M.S. and M. Keyhani. "Convective Heat Transfer in a Sealed Storage Cask Containing Spent-Fuel Canisters." *Nuclear Science and Engineering*. Vol. 105. pp. 391–403. 1990.

ASTM International. "Standard Practice for Qualification and Acceptance of Boron Based Metallic Neutron Absorbers for Nuclear Criticality Control for Dry Cask Storage Systems and Transportation Packaging." ASTM C1671-07. West Conshohocken, PA: ASTM International. 2007.

Ausloos, P., ed. *Fundamental Processes in Radiation Chemistry.* Hoboken, NJ: Wiley Interscience Publications. 1968. (Chapter 5, "Inorganic Gases," A.R. Anderson).

Bahney, R.H. and T.L. Lotz. "Spent Nuclear Fuel Effective Thermal Conductivity Report." Las Vegas, NV: TRW Environmental Safety Systems, Inc. 1996.

Bailey, J.C. and M. Tokar. NUREG/CR-3001, PNL-4342, "Fuel Performance Annual Report for 1981." Washington, DC: U.S. Nuclear Regulatory Commission. December 1982.

Bard, A.J. and L.R. Faulkner. *Electrochemical Methods, Fundamentals and Applications*. New York City, NY: John Wiley & Sons. 1980.

Bare, W.C. and L.D. Torgerson. "Dry Cask Storage Characterization Project Phase I: CASTOR V/21 Cask Opening and Examination." INEEL/EXT-01-00183. Idaho Falls, ID: Idaho National Engineering and Environmental Laboratory. 2001.

Baumann, K. "Aluminum and Aluminum Alloys." *Corrosion Resistance of Aluminum and Aluminum Alloys*. M. Schütze, D. Wieser, and R. Bender, eds. New York City, NY: John Wiley & Sons. 2010.

Brach, E.W. Approval of Interim Staff Guidance Memorandum No. 11, "Cladding Considerations for the Transportation and Storage of Spent Fuel, Rev. 3." Memorandum dated November 17, 2003, to NRC Spent Fuel Project Office Staff Members. 2003. ADAMS Accession No. ML033230281.

Billot, P., P. Beslu, A. Giodano, and J. Thomazel. "Development of a Mechanistic Model To Assess the External Corrosion of the Zircaloy Claddings in PWRs." Presented at the Zirconium in the Nuclear Industry: 8th International Symposium. L.F.P. Van Swam and C.M. Eucken, eds. ASTM STP 1023. Philadelphia, PA: ASTM International. pp. 165–184. 1989.

Bruno, J. and R.C. Ewing. "Spent Nuclear Fuel." *Elements*. Vol. 2. pp. 343–349. 2006.

BSC. "Release Fractions for Spent Nuclear Fuel and High-Level Waste." 000-00C-MGRO-03400-000-00A. Las Vegas, NV: Bechtel SAIC Company, LLC. 2007.

BSC. "Commercial Spent Nuclear Fuel Handling in Air Study." 000-30R-MGR0-00700-000-000. Las Vegas, NV: Bechtel SAIC Company, LLC. 2005.

BSC. "Dose Rate Calculation for the 21-PWR UCF Waste Package." CAL-UDC-NU-000002, Rev. 01. ACC: MOLES.20000223.0507. Las Vegas, NV: Bechtel SAIC Company, LLC. 2001a. ADAMS Accession No. ML040550509.

BSC. "Gamma and Neutron Radiolysis in the 21-PWR Waste Package." CAL-MGR-NU-000006, Rev. 00. Las Vegas, NV: Bechtel SAIC Company, LLC. 2001b.

Cannan, R.E. and D.E. Klein. "A Numerical Investigation of Natural Convection Heat Transfer within Horizontal Spent-Fuel Assemblies." *Nuclear Technology*. Vol. 123, No. 2. pp. 193–208. 1998.

Causey, R.A., D.F. Cowgill, and R.H. Nilson. "Review of the Oxidation Rate of Zirconium Alloys." SAND2005–6006. Albuquerque, NM: Sandia National Laboratories. 2005.

Cheng, B.C., D. Smith, E. Armstrong, K. Tunage, and G. Bond. "Water Chemistry and Fuel Performance in LWRs." *Proceedings of the 2000 International Topical Meeting on Light Water Reactor Fuel Performance, Park City, UT, April 10–13, 2000*. Published on CD-ROM. La Grange Park, IL: American Nuclear Society. 2000.

Ciaraldi, S.W. "Stress-Corrosion Cracking of Carbon and Low-Alloy Steels." *Stress Corrosion Cracking*. R.H. Jones, eds. Materials Park, OH: ASM International. pp. 41–61. 1992.

Cohen & Associates. "Effectiveness of Fuel Rod Cladding as an Engineered Barrier in the Yucca Mountain Repository." Contract No. 68D70073. Washington, DC: U.S. Environmental Protection Agency. 1999.

Cornstock, R.J., G. Shoenberger, and G.P. Sabol. "Influence of Processing Variables and Alloy Chemistry on the Corrosion Behavior of ZIRLO Nuclear Fuel Cladding." *Proceedings of the Zirconium in the Nuclear Industry: 11th International Symposium*. E.R. Bradley and G.P. Sabol, eds. ASTM STP 1295. West Conshohocken, PA: ASTM International. pp. 710–725. 1996.

Cox, B. "Degradation of Zirconium Alloys in Water Cooled Reactors." Presented at the 3rd International Symposium on Environmental Degradation of Materials in Nuclear Power Systems-Water Reactors. Warrendale, PA: The Metallurgical Society. pp. 65–76. 1988.

Cox, B. "Oxidation of Zirconium and its Alloys." *Advances in Corrosion Science and Technology*. M. Fontana and R.W. Staehle, eds. New York City, NY: Plenum Press. 1976.

Cox, B. "Some Effects of Pressure on the Oxidation of Zircaloy-2 in Steam and Oxygen." *Journal of the Less Common Metals*. Vol. 5. pp. 325–336. 1963.

CRWMS M&O. "Initial Cladding Condition." ANL-EBS-MD-000048, Rev. 00 ICN 01. Las Vegas, NV: Civilian Radioactive Waste Management Systems, Management and Operations. 2000.

Daalgard, S.B. "Long-Term Corrosion and Hydriding of Zircaloy-4 Fuel Clad in Commercial Pressurized Water Reactors with Forced Convective Heat Transfer." Extended Abstracts of the Electrochemical Society. Vol. 76-1, No. 31. p. 82. 1976.

Das, K., D. Basu, J. Solis, and Z. Zigh. "Computational Fluid Dynamics Modeling Approach to Evaluate VSC-17 Dry Storage Cask Thermal Designs." Presentation at Experimental Validation and Application of CFD and CMFD Codes to Nuclear Reactor Safety Issues Meeting. CFD4NRS3. September 14–16, 2010. Washington, DC. 2010.

Das, K., D. Basu, and K. Axler. "Validation of Modeling Approach To Evaluate Transportation, Aging, and Disposal Canister Thermal Designs." San Antonio, TX: Center for Nuclear Waste Regulatory Analyses. 2008.

Duriez, C., T. Dupont, B. Schmet, and F. Enoch. "Zircaloy-4 and M57 High Temperature Oxidation and Nitriding in Air." *Journal of Nuclear Materials*. Vol. 380. pp. 30–45. 2008.

Dyce, I.H. "Corrosion of Zircaloy Fuel Cladding: The Influence of High Heat Fluxes." Nuclear Engineering. Vol. 9, No. 98. pp. 253–255. 1964.

Einziger, R.E. and J.A. Cook. "Behavior of Breached Light Water Reactor Spent Fuel Rods in Air and Inert Atmospheres at 229 °C." *Nuclear Technology*. Vol. 69. pp. 55–71. 1985.

Einziger, R.E. and R.V. Strain. "Behavior of Breached Pressurized Water Reactor Spent-Fuel Rods in an Air Atmosphere between 250 and 360 °C." *Nuclear Technology*. Vol. 75. pp. 82–95. 1986.

Einziger, R.E., L.E. Thomas, H.C. Buchanan, and R.B. Stout. "Oxidation of Spent Fuel in Air At 175 to 195 °C." *Journal of Nuclear Materials*. Vol. 190. pp. 53–60. 1992.

Elam, K.R., J.C. Wagner, C.V. Parks, and C.J. Withee. NUREG/CR-6835, "Effects of Fuel Failure on Criticality Safety and Radiation Dose for Spent Fuel Casks." Washington, DC: U.S. Nuclear Regulatory Commission. 2003.

EPRI. "Spent Fuel Transportation Applications—Assessment of Cladding Performance, A Synthesis Report—Final Report." EPRI-TR-1015048. Palo Alto, CA: Electric Power Research Institute. 2007.

EPRI. "Handbook of Neutron Absorber Materials for Spent Nuclear Fuel Transportation and Storage Applications." 2006 Edition. Palo Alto, CA: Electric Power Research Institute. 2006.

EPRI. "Dry Cask Storage Characterization Project—Final Report." Palo Alto, CA: Electric Power Research Institute. 2002.

EPRI. "Oxidation of Spent Fuel between 250 and 360 °C." EPRI NP-4524. Palo Alto, CA: Electric Power Research Institute. 1986.

Fix, D.V., J.C. Estill, L.L. Wong, and R.B. Rebak. "General and Localized Corrosion of Austenitic and Borated Stainless Steels in Simulated Concentrated Ground Waters." Vol. 483. Washington, DC: American Society of Mechanical Engineers, Pressure Vessels and Piping Division. pp. 121–130. 2004.

Fluent, Inc. "FLUENT7 Theory Guide." Version 6.3. Lebanon, NH: Fluent, Inc. 2007a.

Fluent, Inc. "FLUENT7User Manual." Version 6.3. Lebanon, NH: Fluent, Inc. 2007b.

Gajek, A. and T. Zakroczymski. "Long-Lasting Hydrogen Evolution on and Hydrogen Entry into Iron in an Aqueous Solution." *Journal of Electroanalytical Chemistry*. Vol. 578. pp. 171–182. 2005.

Garde, A.M. "Enhancement of Aqueous Corrosion of Zircaloy-4 Due to Hydride Precipitation at the Metal-Oxide Interface." *Proceedings of the Zirconium in the Nuclear Industry: 9th International Symposium.* C.M. Eucken and A.M. Garde, eds. ASTM STP 1132. West Conshohocken, PA: ASTM International. pp. 566–594. 1991.

Garzarolli, F., W. Jung, H. Schoenfeld, A.M. Garde, G.W. Parry, and P.G. Smerd. "Waterside Corrosion of Zircaloy Fuel Rods." EPRI NP-2789. Palo Alto, CA: Electric Power Research Institute. 1982.

Ghali, E. *Corrosion Resistance of Aluminum and Magnesium Alloys: Understanding, Performance and Testing*. Hoboken, NJ: John Wiley & Sons, Inc. 2010.

Guipponi, C., N. Millard-Pinard, N. Bérerd, E. Serris, M. Pijolat, V. Peres, and V. Wasselin-Trupin. "Modification of Oxidized Zircalloy-4 Surface in Contact with Radiolysed Wet Air." *Nuclear Instruments and Methods in Physics Research*. B 272. pp. 222–226. 2012.

Hanson, B.D. "The Burnup Dependence of Light Water Reactor Spent Fuel Oxidation." PNL–11929. Richland, WA: Pacific Northwest National Laboratory. 1998.

Hastings, I.J., E. Missan, A.M. Ross, J.R. Kelm, R.J. Chenier, D.H. Rose, and J. Novak. "Postirradiation Behavior of UO_2 Fuel: Fragments at 175 to 275 °C in Air." *Nuclear Technology*. Vol. 68. pp. 40–47. 1985.

He, X., T. Ahn, and T. Sippel. "Corrosion of Borated Stainless Steel in Water and Humid Air." San Antonio, TX: Center for Nuclear Waste Regulatory Analyses. 2011. ADAMS Accession No. ML112490365. 2011.

Heng, X., G. Zuying, and Z. Zhiwei. "A Numerical Investigation of Natural Convection Heat Transfer in Horizontal Spent Fuel Storage Cask." *Nuclear Engineering and Design*. Vol. 213. pp. 59–65. 2002.

Herranz, L.E. and F. Feria. "Spent Fuel Rod Splitting due to UO_2 Oxidation During Dry Storage: Assessment of the Database." *Progress in Nuclear Energy*. Vol. 51. pp. 201–206. 2009.

Hillner, E. "Corrosion of Zirconium-Base Alloys: An Overview." Presented at the Zirconium in the Nuclear Industry—3rd International Symposium. A.L. Lowe, Jr. and G.W. Parry, eds. ASTM STP 633. Philadelphia, PA: ASTM International. pp. 211–235. 1977.

Hillner, E., D.G. Franklin, and J.D. Smee. "The Corrosion of Zircaloy-Clad Fuel Assemblies in a Geological Repository Environment." WAPD–3173. West Miffin, PA: Bettis Atomic Power Laboratory. 1994.

Jenks, G.H. "Radiolysis and Hydrolysis in Salt-Mine-Brines." ORNL-TM-3717. Oak Ridge, TN: Oak Ridge National Laboratory. 1972.

Kain, V. "Chapter 5: Stress Corrosion Cracking in Stainless Steels." In *Stress Corrosion Cracking: Theory and Practice*. V.S. Raja and T. Shoji, eds. Cambridge, England: Woodhead Publishing. pp. 199–244. 2011.

Keenan, J.H., F.G. Keyes, P.G. Hill, and J.G. Moore. "Steam Tables: Thermodynamic Properties of Water, Including Vapor, Liquid, and Solid Phases." Somerset, NJ: John Wiley & Sons. pp. 5.12. 1969.

King, F. "Hydrogen Effects on Carbon Steel Used Fuel Containers." NWMO TR-2009-29. Toronto, Ontario, Canada: Canada Nuclear Waste Management Organization. 2009.

King, F. "Overview of a Carbon Steel Container Corrosion Model for a Deep Geological Repository in Sedimentary Rock." NWMO TR-2007-01. Toronto, Ontario, Canada: Nuclear Waste Management Organization. 2007.

Kohli, R., D. Stahl, V. Pasupathi, A.B. Johnson, and E.R. Gilbert. "The Behavior of Breached Boiling Water Reactor Fuel Rods on Long-Term Exposure to Air and Argon at 598 K." *Nuclear Technology.* Vol. 69. pp. 186–197. 1985.

Kucera, V. "The Effect of Acidification on Corrosion of Structures and Cultural Property." *Acidification in Tropical Countries*. H. Rodhe and R. Herrera, eds. New York City, NY: John Wiley & Sons. 1988.

Lam, R.S., R.L. Sindelar, and H.B. Peacock. "Vapor Corrosion of Aluminum Cladding Alloys and Aluminum-Uranium Fuel Materials in Storage Environments (U)." WSRC-TR-97-0120. Aiken, SC: Westinghouse Savannah River Company. 1997.

Lee, J.C., W.S. Choi, K.S. Bang, K.S. Seo, and S.Y. Yoo. "Thermal-Fluid Flow Analysis and Demonstration Test of a Spent Fuel Storage System." *Nuclear Engineering and Design*. Vol. 239. pp. 551–558. 2009.

Lewis, M. A. and D. W. Warren. "The Use of Additives for Reducing Hydrogen Yield in Mortar Containing Slag and Chloride Salt." *Scientific Basis for Nuclear Waste Management XIII, Symposium Proceedings 176*. V. M. Oversby and P. W. Brown, eds. Pittsburgh, PA: Materials Research Society. pp. 53-60. 1990.

Locke, D.H. "Review of Experience with Water Reactor Fuels—1968–1973." *Nuclear Engineering and Design*. Vol. 33. pp. 94–124. 1974.

Lombardo, N.J., J.M. Cuta, T.E. Michener, D.R. Recot, and C.L. Wheeler. "COBRA-SFS: A Thermal Hydraulic Analysis Computer Code, Volume III: Validation Assessments." PNL-6049, UC-85. Richland, WA: Pacific Northwest Laboratory. 1986.

Manzel, R. and C.T. Walker. "EPMA and SEM of Fuel Samples from PWR Rods with an Average Burnup of Around 100 MWd/kgHM." *Journal of Nuclear Materials*. Vol. 301. pp. 170–182. 2002.

Mardon, J.P., D. Charquet, and J. Senevant. "Influence of Composition and Fabrication Process on Out-of-Pile and In-Pile-Properties of M57 Alloy." *Proceedings of the Zirconium in the Nuclear Industry: 12th International Symposium*. G.P. Sabol and G.T. Moan, eds. ASTM STP 1354. West Conshohocken, PA: ASTM International. pp. 505–524. 2000.

Mardon, J.P., G. Garner, P. Beslu, D. Charquet, and J. Senevat. "Update on the Development of Advanced Zirconium Alloys for PWR Fuel Rod Claddings." *Proceedings of the 1997 International Topical Meeting on LWR Fuel Performance, Portland, OR, March 2–6, 1997*. La Grange Park, IL: American Nuclear Society. pp. 405–412. 1997.

McCann, R.A. and P.S. Lowery. "HYDRA-II: A Hydrothermal Analysis Computer Code Volume III: Verification and Validation Assessments." PNL–6206, UC-85. Richland, WA: Pacific Northwest Laboratory. 1987.

McEachern, R.J. and P. Taylor. "A Review of the Oxidation of Uranium Dioxide at Temperatures below 400 °C." *Journal of Nuclear Materials*. Vol. 254. pp. 87–121. 1998.

McKinnon, M.A. "Spent Fuel Integrity during Dry Storage." *Proceedings from the Institute of Nuclear Materials Management 36th Annual Meeting, Palm Desert, CA, July 9–12, 1995*. Deerfield, IL: Institute of Nuclear Materials Management. 1995.

McKinnon, M.A. and V.A. DeLoach. "Spent Nuclear Fuel Storage: Performance Tests and Demonstrations." PNL-8451 and UC-510. Richland, WA: Pacific Northwest Laboratory. 1993.

McKinnon, M.A. and A.L. Doherty. "Spent Nuclear Fuel Storage—Performance Tests and Demonstrations." PNNL-11576 and UC-810. Richland, WA: Pacific Northwest National Laboratory. 1997.

McKinnon, M.A., R.E. Dodge, R.C. Schmitt, L.E. Eslinger, and G. Dineen. "Performance Testing and Analyses of the VSC-17 Ventilated Concrete Cask." TR-100305. Palo Alto, CA: Electric Power Research Institute. 1992.

Meyer, R.O. "NRC Activities Related to High Burnup, New Cladding Types, and Mixed-Oxide Fuel." *Proceedings of the 2000 International Topical Meeting on Light Water Reactor SNF Performance, Park City, UT, April 10–13, 2000*. Published on CD-ROM. La Grange Park, IL: American Nuclear Society. 2000.

Miyake, M., M. Uno, S. Yamanaka. "On the Zirconium-Oxygen-Hydrogen Ternary System." *Journal of Nuclear Materials*. Vol. 270. pp. 233–241. 1999.

Nakamura, J. M. Hashimoto, T. Ottomo, and S. Kawasaki. "Effects of Oxygen Partial Pressure on Oxidation of Zircaloy." *Journal of Nuclear Materials*. Vol. 200. pp.256-264. 1993.

Nishino, Y., M. Endo, E. Ibe, and T. Yasuda. "Formation and Dissolution of Oxide Film on Zirconium Alloys in 288 °C Pure Water under γ-ray Irradiation." *Journal of Nuclear Materials*. Vol. 248. pp. 292–298. 1997.

Novak, J., I.J. Hastings, E. Mizzan, and R.J. Chenier. "Postirradiation Behavior of UO_2 Fuel: Elements at 220 to 250 °C in Air." *Nuclear Technology*. Vol. 63. pp. 254–265. 1983.

NRC. Interim Staff Guidance–1, "Classifying the Condition of Spent Nuclear Fuel for Interim Storage and Transportation Based on Function." Rev. 2. Washington, DC: U.S. Nuclear Regulatory Commission. 2007.

NRC. NUREG-1609, "Standard Review Plan for Transportation Packages for Radioactive Material." Washington, DC: U.S. Nuclear Regulatory Commission. March 1999.

NWTRB. "Evaluation of the Technical Basis for Extended Dry Storage and Transportation of Used Nuclear Fuel." Washington, DC: U.S. Nuclear Waste Technical Review Board. 2010.

Okada, H. "Stress Corrosion Cracking and Hydrogen Cracking of Structural Steels." In *Proceedings, Stress Corrosion Cracking and Hydrogen Embrittlement of Iron Base Alloys, NACE-5.* Houston, TX: NACE International. pp. 124–134. 1977.

Oriani, R.A. "The Diffusion and Trapping of Hydrogen in Steel." *Acta Metallurgica*. Vol. 18. pp. 147–157. 1970.

Pabalan, R.T. "Software Validation Test Plan and Report For OLI Analyzer Version 3.0." San Antonio, TX: Center for Nuclear Waste Regulatory Analyses. 2009.

Peplow, D.E. "Monte Carlo Shielding Analysis Capability with MAVRIC." *Nuclear Technology.* Vol. 174. p. 289. 2011.

Peters, H.R. "Improved Characterization of Aqueous Corrosion Kinetics of Zircaloy-4." Presented at the Zirconium in the Nuclear Industry: 6th International Symposium. D.G. Franklin and R.B. Adamson, eds. ASTM STP 824. Philadelphia, PA: ASTM International. pp. 507–518. 1984.

Pfeif, E.A., A.N. Lasseigne, K. Krzywosz, E.V. Mader, B. Mishra, and D.L. Olson. "Characterization of Hydrogen Content in Zircaloy-4 Nuclear Fuel Cladding." CP1211. *Review of Quantitative Nondestructive Evaluation*. Vol. 29. D.O. Thompson and D.E. Chimenti, eds. American Institute of Physics. pp. 1,317–1,324. 2010.

Povetko, O., S. Whaley, and A. Kouznetsov. "Neutronic Reactivity Effect of Removed Neutron Absorber Plates." Presentation to the ASTM C26—Nuclear Fuel Cycle C260300 Subcommittee on Neutron Absorber Materials, Washington, DC, June 24, 2008. Washington, DC: U.S. Nuclear Regulatory Commission. 2008. ADAMS Accession No. ML081760149.

Racine, A., M. Bornert, C.S. Catherine, C. Cappelaere. "Experimental Investigation of Strain, Damage and Failure of Hydrided Zircaloy-4 with Various Hydrides Orientations." *18th International Conference on Structural Mechanics in Reactor Technology*. Beijing, China, August 7–12, 2005. SmiRT 18. 2005.

Radulescu, G. "Radiation Transport Evaluations for Repository Science." ORNL/LTR-2011/294. Oak Ridge, TN: Oak Ridge National Laboratory. 2011.

Rondinella, V. and T. Wiss. "The High Burnup Structure in Nuclear Fuel." *Materials Today*. Vol. 13, No. 12. pp. 24–32. 2010.

Rothman, A.J. "Potential Corrosion and Degradation Mechanisms of Zircaloy Cladding on Spent Nuclear in a Tuff Repository." UCID-20172. Livermore, CA: Lawrence Livermore National Laboratory. 1984.

Sabol, G.P., R.J. Comstock, R.A. Weiner, P. Larouere, and R.N. Stanutz. "In-Reactor Corrosion Performance of ZIRLO and Zircaloy-4." *Proceedings of the Zirconium in the Nuclear Industry: 10th International Symposium.* ASTM–STP–1425. A.M. Garde and E.R. Bradley, eds. West Conshohocken, PA: American Society for Testing and Materials. pp. 724–744. 1994.

Saji, G., "Degradation of Aged Plants by Corrosion: 'Long Cell Action' in Unresolved Corrosion Issues." *Nuclear Engineering and Design*. Vol. 239. pp. 1,591–1,613. 2009.

Shukla, P. "Thermodynamics of Corrosion and Potentiometric Methods for Measuring Localized Corrosion." *Techniques for Corrosion Monitoring*. L. Yang, ed. Cambridge, England: Woodhead Publishing. pp. 156–186. 2008.

Shukla, P.K., R. Pabalan, T. Ahn, L. Yang, X. He, and H. Jung. "Cathodic Capacity of Alloy 22 in the Potential Yucca Mountain Repository Environment." *Proceedings of the CORROSION 2008 Conference, Corrosion in Nuclear Systems Symposium, New Orleans, LA, March 16–20, 2008*. Paper No. 08583. Houston, TX: NACE International. 2008.

Sowden, R.G. "Radiolytic Problems in Water Reactors." *Journal of Nuclear Materials.* Vol. 8. pp. 81–101. 1963.

Stehle, H., W. Kaden, and R. Manzel. "External Corrosion of Cladding in PWRs." *Nuclear Engineering and Design*. Vol. 33. pp. 155–169. 1975.

Steinbrück, M. "Hydrogen Absorption by Zirconium Alloys at High Temperatures." *Journal of Nuclear Materials*. Vol. 334. pp. 58–64. 2004.

Stout, R. and H. Leider. "Preliminary Waste Form Characteristics Report." Version 1.0. UCRL-ID-108314. Livermore, CA: Lawrence Livermore National Laboratory. 1984.

Suzuki, M. and S. Kawasaki. "Oxidation of Zircaloy Cladding in Air." *Journal of Nuclear Materials*. Vol. 140. pp. 32–43. 1986.

Takeda, H., M. Wataru, K. Shirai, and T. Saegusa. "Heat Removal Verification Tests Using Concrete Casks under Normal Condition." *Nuclear Engineering and Design*. Vol. 238. pp. 1,196–1,205. 2008.

Taylor, P., D.D. Wood, and D.G. Owen. "Microstructures of Corrosion Films on UO_2 Fuel Oxidized in Air-Steam Mixtures at 225 °C." *Journal of Nuclear Materials*. Vol. 223. pp. 316–320. 1995.

Taylor, P., D.D. Wood, A.M. Duclos, and D.G. Owen. "Formation of Uranium Trioxide Hydrates on UO_2 Fuel in Air-Steam Mixtures near 200 °C." *Journal of Nuclear Materials*. pp. 70–75. 1989.

Thomas, L. E., R. E. Einziger, and H. C. Buchanan. "Effect of Fission Products on Air Oxidation of LWR Spent Fuel." *Journal of Nuclear Materials.* Vol. 201. pp. 310–319. 1993.

Thomas, L.E., R.E. Einziger, and R.E. Woodley. "Microstructural Examination of Oxidized Spent Fuel by Transmission Electron Spectroscopy." *Journal of Nuclear Materials.* Vol. 166. pp. 243–251. 1989.

Van der Linde, A. "Calculation of the Safe Life Time Expectancy of Zirconium Alloy Canning in the Fuel Elements of the NERO Reaction." RCN Report 41. Petten, The Netherlands: Reactor Centrum. 1965.

Van Rooyen, D. and H.R. Copson. "Metal Corrosion in the Atmosphere." Report No. STP 435. West Conshohocken, PA: ASTM International. 1968.

Van Swam, L.F., G.M. Bain, W.C. Dey, D.D. Davis, and H. Heckermann. "BWR and PWR Fuel Performance at High Burnup." *Proceedings of the 1997 International Topical Meeting on LWR Performance, Portland, OR, March 2–6, 1997*. La Grange Park, IL: American Nuclear Society. pp. 3–10. 1997.

Vernon, W.H.J. "A Laboratory Study of the Atmospheric Corrosion of Metals: Part II—Iron: The Primary Oxide Film and Part III—The Secondary Product or Rust (Influence of Sulphur Dioxide, Carbon Dioxide, and Suspended Particles on the Rusting of Iron)." *Transactions of the Faraday Society*. Vol. 31. pp. 1,668–1,700. 1935.

Wasywich, K.M., W.H. Hocking, D.W. Shoesmith, and P. Taylor. "Differences in Oxidation Behavior of Used CANDU Fuel during Prolonged Storage in Moisture-Saturated Air and Dry Air at 150 °C." *Nuclear Technology*. Vol. 104. pp. 309–329. 1993.

Wataru, M., H. Takeda, K Shirai, and T. Saegusa. "Thermal Hydraulic Analysis Compared With Tests of Full Scale Concrete Casks." *Nuclear Engineering and Design*. Vol. 238. pp. 1,213–1,219. 2008.

Wilson, H.W., H.F. Menke, H. Kunishi, R.S. Miller, and L.R. Scherpereel. "Westinghouse Fuel Performance in Today's Aggressive Plant Operating Environment." *Proceedings of the 1997 International Topical Meeting on LWR Fuel Performance, Portland, OR, March 2–6, 1997*. La Grange Park, IL: American Nuclear Society. pp. 23–30. 1997.

Woo, O., G. McDougall, R. Hutcheon, V. Urbanic, M. Griffiths, and C. Coleman. "Corrosion of Electron-Irradiated Zr-2.5Nb and Zircaloy-2." ASTM STP1354. *Proceedings of the Zirconium in the Nuclear Industry: 12th International Symposium.* West Conshohocken, PA: ASTM International. 2000.

Yamakawa, K. and R. Nishimura. "Hydrogen Permeation of Carbon Steel in Weak Alkaline Solution Containing Hydrogen Sulfide and Cyanide Ion." *Corrosion*. Vol. 55. pp. 24–30. 1999.

Zigh, G. and J. Solis. "Computational Fluid Dynamics Best Practice Guidelines in the Analysis of Storage Dry Casks." *Proceedings of the Waste Management 2008 Symposia, Phoenix, AZ, February 24–28, 2008. Phoenix, AZ*: WM Symposia. 2008.

Zlochower, I.A. and G.M. Green. "The Limiting Oxygen Concentration and Flammability Limits of Gases and Gas Mixtures." *Journal of Loss Prevention in the Process Industries*. Vol. 22, No. 4. pp. 499–505. 2009.